

Structure-function relationships of cobalt and manganese oxides as catalysts for (photo-) electrochemical water splitting

vorgelegt von
Dipl.-Ing.
Philipp Hillebrand
geb. in Bozen

von der Fakultät II – Mathematik und Naturwissenschaften
der Technischen Universität Berlin
zur Erlangung des akademischen Grades

Doktor der Ingenieurwissenschaften
- Dr. Ing -

genehmigte Dissertation.

Promotionsausschuss:

Vorsitzender:	Prof. Dr. Martin Lerch
Gutachter:	Prof. Dr. Sebastian Fiechter
Gutachter:	Prof. Dr. Peter Strasser
Gutachter:	Dr. Wolfram Calvet

Datum der wissenschaftlichen Aussprache: 10. September 2015

Berlin 2015

Kurzfassung

Die photoelektrochemische Wasserspaltung ist ein vielversprechendes neuartiges Verfahren zur Produktion von nachhaltigem und schadstofffreiem Wasserstoff, der als chemischer Energieträger eingesetzt werden kann. Ein Kernpunkt für die erfolgreiche Entwicklung dieser Technologie ist die Verfügbarkeit effizienter Katalysatoren bei der Sauerstoffentwicklung (oxygen evolution reaction, OER) an der Anode des Systems.

In dieser Arbeit werden Kobalt- und Manganoxide als günstige und leicht verfügbare Katalysatoren für die OER in basischem Ambiente beschrieben. Auf FTO elektrochemisch abgeschiedenes amorphes Kobaltoxid (CoO_x), welches sich einfach herstellen lässt und kein Tempern benötigt, bildete dabei den Schwerpunkt. Durch Tempern bildet sich kristallines Co_3O_4 , welches jedoch weniger aktiv ist als die amorphe Phase. Bei Manganoxid ist die kristalline $\alpha\text{-Mn}_2\text{O}_3$ Phase am aktivsten. Sie ist durch zum Teil stark verzerrte $[\text{MnO}_6]$ -Koordinationsoktaeder und unterschiedliche interatomare Bindungsabstände gekennzeichnet. Für ihre Synthese musste die galvanostatisch abgeschiedene Schicht auf 500°C erhitzt werden. Es wird angenommen, dass die Vielzahl der energetisch leicht unterschiedlichen Bindungszustände an der Oberfläche für die hohe Aktivität der beiden Phasen verantwortlich ist. Überspannungen von 370 bzw. 360 mV bei 10 mA/cm^2 wurden für CoO_x und $\alpha\text{-Mn}_2\text{O}_3$ erreicht, was mit den besten Werten aus der Literatur für diverse Katalysatoren vergleichbar ist¹.

Zur Klärung der Fragestellung, ob sich ein Bezug zwischen der Menge an auf der Elektrode abgeschiedenem Kobaltoxid und der katalytischen Aktivität (Überspannung) herstellen lässt, wurde CoO_x mit unterschiedlichen Ladungsmengen abgeschieden und elektrochemisch charakterisiert. Dabei führte die systematische Erhöhung der abgeschiedenen Ladung, welche ein Maßstab für die Menge an Katalysator ist, zu einer steigenden katalytischen Leistung. Dieser Effekt wurde auf Mikroporosität in den Katalysatorschichten zurückgeführt, welche in elektronenmikroskopischen Abbildungen sichtbar wird. Differentielle elektrochemische Massenspektroskopie (DEMS) konnte einen klaren Bezug zwischen dem beobachteten faradayschen Strom bei hohen anodischen Potentialen und der Sauerstoffentwicklung herstellen. In schlecht gepufferten neutralen Lösungen konnte dagegen mittels DEMS eine Versauerung in den Poren des Materials nachgewiesen werden, welche die OER behindert. Generell ist die Aktivität in neutralen Medien deutlich schlechter als in stark basischen.

Mit Hilfe der Methode der in-line Synchrotron-Photoelektronenspektroskopie (SXPS) konnten die Oberflächenzustände von CoO_x - und $\alpha\text{-Mn}_2\text{O}_3$ -Elektroden nach Kontakt mit dem Elektrolyten und nach Polarisation mit verschiedenen anodischen Spannungen untersucht werden. CoO_x zeigte dabei eine partielle Oxidation von Co^{2+} zu Co^{3+} , überraschenderweise aber kein Co^{4+} , welches durch elektrochemische Messungen und Literaturangaben zu erwarten gewesen wäre. Durch in-situ UV/Vis Messungen wurde ein deutlicher elektrochromer Effekt als Funktion der angelegten Spannung beschrieben und Hinweise auf die Präsenz von Co^{4+} gefunden. Relaxationsphänomene beweisen die Instabilität der Co^{4+} Ionen nach Entfernen der Probe aus dem Elektrolyten, ein Grund für deren Fehlen in den SXPS Spektren. $\alpha\text{-Mn}_2\text{O}_3$ dagegen zeigte einen deutlichen Mn^{4+} Anteil im SXPS, nachdem die Probe mit einem Potential im OER Bereich belastet wurde. Dieser Unterschied in der Stabilität des tetravalenten Zustandes könnte ein Hinweis auf unterschiedliche Reaktionsmechanismen bei der Wasseroxidation an der Phasengrenze Elektrode/Elektrolyt sein.

Abstract

Photoelectrochemical water splitting represents a promising route for producing sustainable and potentially cheap hydrogen as an alternative energy carrier to replace fossil fuels. However, several scientific and technological challenges are still to be solved. One of the key issues is the availability of high efficient catalysts for the oxygen evolution reaction (OER) at the anode side of the system, to minimize energetic losses in the process of charge transfer.

In this work cobalt and manganese oxides were investigated as cheap and abundant catalysts for the OER in alkaline media. The main focus was put on electrochemically deposited cobalt oxide (CoO_x) on FTO substrates, which is easy to fabricate and does not need the application of high temperatures to form the catalyst. On the contrary, annealing of the as-deposited amorphous thin films has led to the formation of crystalline spinel phase Co_3O_4 correlated to a decrease in activity. In the manganese oxide system on the other hand, crystalline $\alpha\text{-Mn}_2\text{O}_3$, which formed after annealing the galvanostatically deposited film at 500°C in air, showed the best catalytic performance. This material is characterized by (partially) strongly distorted $[\text{MnO}_6]$ coordination octahedrons with a wide gamut of different interatomic bonding distances. It is assumed that the availability of various kinds of energetically slightly different binding sites at the surface of amorphous CoO_x and crystalline $\alpha\text{-Mn}_2\text{O}_3$ is responsible for the high catalytic activity. Overpotentials of 370 and 360 mV at 10 mA/cm^2 have been achieved for CoO_x and $\alpha\text{-Mn}_2\text{O}_3$, respectively, which are comparable to the best catalysts based on abundant transition metal compounds¹.

In the synthesis of CoO_x electrodes, a systematic increase of the charge during film formation, which is a measure for the amount of the deposited catalyst, had a pronounced effect on the catalytic performance. This behavior was attributed to microporosity of the films, which is supported by TEM imaging. Differential electrochemical mass spectroscopy (DEMS) confirmed that the faradaic current at anodic potentials above 1.5 V (RHE) is related to oxygen evolution. Measurements in buffered aqueous solutions at pH7 revealed acidification inside the pores, if the buffer concentration is too low. In general, the activity at neutral pH is significantly lower compared to alkaline media.

In-line synchrotron X-ray photoelectron spectroscopy (SXPS) was applied to study the surface state of CoO_x and $\alpha\text{-Mn}_2\text{O}_3$ after the application of different anodic potentials. CoO_x showed a partial oxidation of Co^{2+} to Co^{3+} at moderate potentials, but no Co^{4+} was detected in the OER potential range. This was surprising, since electrochemical experiments and literature data strongly suggest the formation of Co^{4+} . In-situ UV/Vis measurements showed a pronounced electrochromic effect and gave further evidence for the appearance of Co^{4+} at potentials above 1.5 V. Furthermore, UV/Vis studies provided indications for the instability of Co^{4+} , if the potential is removed, which is the reason for not appearing in the X-ray spectra. Instead, $\alpha\text{-Mn}_2\text{O}_3$ showed a clear share of Mn^{4+} after application of a potential in the OER regime. This difference in stability of the tetravalent oxidation state is interpreted as a sign for a possible different oxygen evolution reaction mechanism at the electrode/electrolyte interface.

Danksagung

An dieser Stelle möchte ich mich bei jenen Menschen bedanken, die mich in den letzten Jahren fachlich und menschlich bei der Erstellung dieser Arbeit unterstützt haben.

Zunächst möchte ich mich herzlich bei Prof. Sebastian Fiechter für die Betreuung meiner Arbeit und die Unterstützung in allen wissenschaftlichen Belangen bedanken. Er war stets ansprechbar und hilfsbereit. Durch seinen Enthusiasmus für die Wissenschaft entstanden sehr anregende Diskussionen die oftmals weit über das wissenschaftliche Thema hinausgingen und mir vielfach neue Blickwinkel eröffneten. Außerdem bedanke ich mich für seine Verbesserungsvorschläge und die Anfertigung des Gutachtens.

Prof. Peter Strasser von der TU Berlin und Dr. Wolfram Calvet vom Helmholtz-Zentrum Berlin möchte ich für die Erstellung ihrer Gutachten danken. Außerdem bedanke ich mich bei Prof. Martin Lerch für die Übernahme des Vorsitzes in der Prüfungskommission.

Für seine Hilfestellung in allen Belangen der Elektrochemie danke ich Peter Bogdanoff, der mit seinem schier unendlichen Fachwissen so manches Rätsel lösen konnte und immer mit Rat und Tat zur Seite stand. Alejandra Ramírez danke ich für die Bereitstellung der Syntheseroute für die Manganoxide, sowie für die gute Zusammenarbeit auf dem Gebiet.

Bei Stefanie Bierwirth, Fatwa Abdi, Matthias May und Michael Kanis möchte ich mich für die Unterstützung bei den XPS Messungen in Adlershof bedanken. Ein besonderer Dank geht hierbei auch an Dr. Wolfram Calvet, der mich bei den vielen technischen Problemen mit der SoLIAS sehr unterstützt hat. Bei Fatwa Abdi möchte ich mich außerdem für die Unterstützung bei den UV/Vis Messungen bedanken.

Für die TEM und REM Querschnittspräparation, sowie für die TEM Bilder bedanke ich mich herzlich bei Ulrike Bloeck, die das erst möglich gemacht hat. Außerdem geht ein spezieller Dank an Stefanie Bierwirth, die mit viel Geduld und Hingabe meinen sich ständig ändernden Wünschen bei den REM Aufnahmen nachkam.

Bei Diana Stellmach bedanke ich mich für die moralische, seelische und leibliche (Schokolade) Fürsorge in den letzten Jahren. Ihr Weggang riss ein tiefes Loch in die Arbeitsgruppe.

Schließlich geht ein ganz besonderes Dankeschön an Sophie Jancke, die mir in den letzten Monaten der Arbeit in allen möglichen Belangen sehr geholfen hat. Ohne sie wäre die Arbeit vermutlich nicht rechtzeitig fertig geworden.

Außerdem danke ich allen Mitgliedern des Instituts für Solare Brennstoffe für das nette und freundschaftliche Arbeitsklima und auch außerhalb des Instituts haben mich meine Eltern, Brüder und Freunde immer toll unterstützt und mich durch die Doktorandenzeit begleitet.

Zum Schluss möchte ich mich bei meiner kleinen Familie bedanken, die mich tapfer aushält und mich nach Kräften unterstützt. Bei meiner Frau Anja dafür, dass sie mir immer gut zuredet, wenn ich Zweifel habe und meinem Sohn Max für seine bloße Existenz; das allein macht das Leben schon schön.

Table of contents

1. Broader context and motivation	1
2. Theoretical background	5
2.1. Electrochemical basics	5
2.2. The oxygen evolution reaction (OER)	9
2.2.1. Theoretical considerations	9
2.2.2. Catalysts for the oxygen evolution reaction	11
2.2.3. Cobalt Oxide	12
2.2.4. Manganese Oxide	13
3. Experimental section	15
3.1. Sample preparation	15
3.2. Analysis methods	17
3.2.1. Electrochemistry	17
3.2.1.1. Cyclic voltammetry (CV)	17
3.2.1.2. Differential electrochemical mass spectroscopy (DEMS)	20
3.2.2. Spectroscopic methods	21
3.2.2.1. In-line synchrotron X-ray photoelectron spectroscopy (SXPS)	21
3.2.2.2. UV/Vis spectroscopy	26
3.2.3. Other methods	27
3.2.3.1. X-ray diffraction (XRD)	27
3.2.3.2. Scanning electron microscopy (SEM)	27
3.2.3.3. Transmission electron microscopy (TEM)	27
4. Results and discussion	29
4.1. Cobalt Oxide	29

4.1.1.	Influence of preparation parameters on the catalytic activity	29
4.1.1.1.	Deposition potential.....	29
4.1.1.2.	Composition of the deposition solution.....	35
4.1.1.3.	Substrate.....	38
4.1.1.4.	Temperature	45
4.1.2.	CoO _x films as oxygen evolution catalysts	53
4.1.2.1.	Dependence of OER activity on the deposited amount of CoO _x	53
4.1.2.2.	Film thickness.....	57
4.1.2.3.	Determination of the electrochemically active surface area (ECASA).....	60
4.1.2.4.	Magnitude of the reduction peaks	65
4.1.2.5.	Kinetics.....	68
4.1.2.6.	Influence of the electrolyte	73
4.1.2.7.	Differential electrochemical mass spectroscopy (DEMS)	78
4.1.2.8.	Stability of CoO _x electrodes	81
4.1.3.	Spectroscopic analysis	87
4.1.3.1.	In-line SXPS	87
4.1.3.2.	In-situ UV/Vis	95
4.2.	Manganese Oxide	103
4.2.1.	Catalytic activity	103
4.2.2.	In-line SXPS	105
5.	Summary and final remarks.....	111
6.	Appendix.....	117
6.1.	References	117
6.2.	List of figures	133
6.3.	List of tables.....	139
6.4.	List of publications	141

1. Broader context and motivation

Sufficient supply of the world's population with energy is one of the key challenges in the 21st century. Since the industrial revolution, the demand for energy increased by orders of magnitude related to a growing world population and its augmented industrial activities. Most scenarios predict a continuously enhanced energy need in the next decades. In 2010, the primary energy demand worldwide was in the range of 481-506 EJ (Exa Joule = 10^{18} Joule)²⁻⁴ and assuming „business as usual“, where no significant political impacts on the energy issue are expected, the numbers will grow to about 750 EJ in 2035⁵ and 1069 EJ in 2050³. Roughly 83% of this enormous amount of energy is expected to be provided by fossil fuels (coal, natural gas, oil), which corresponds to burning a lake of oil half the size of Lake Constance (Bodensee) in Germany every year. Severe and incalculable economic risks are related to this dependence on fossil fuels, manifested e.g. in the currently extremely underrated oil price of about 60 USD per barrel (April 2015). At the latest when the gigantic speculative bubble⁶ caused by hydraulic fracturing („fracking“) in the United States collapses in a few years, a significant increase of the oil price can be expected with tremendous consequences for the world economy.

Besides economic issues, strongly increased emissions of CO₂, methane, fine dust, mercury and other heavy metals from producing and burning fossil fuels have affected the global climate and the health of people living close to power plants. In fact, atmospheric CO₂ concentration has never been higher than today (approx. 400 ppm) in the last 800 000 years (Figure 1.1, left graph) and is still rapidly increasing^{7,8}. A much more pronounced greenhouse effect is predicted for the future⁹ and up to the current state of knowledge a global temperature increase of maximum 2°C until 2100 can, if at all, only be achieved if fundamental and rapid action is taken to minimize emission of greenhouse gases⁸. Global warming of 2°C is widely accepted to be the limit for the ability to handle its environmental consequences.

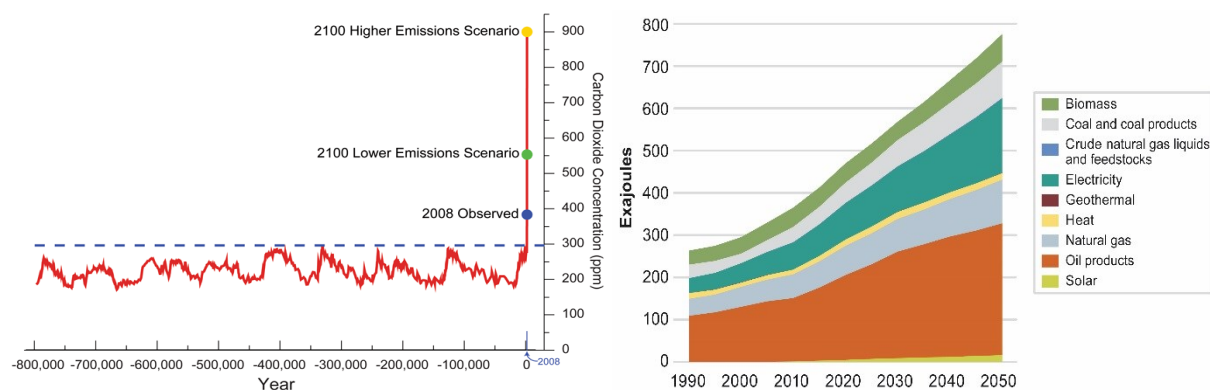


Figure 1.1: (left) Global atmospheric CO₂ concentration in ppm over the last 800 000 years. Source: Ref. ¹⁰. (right) Global final energy demand from 1990 to 2050 in EJ by source of energy under a “business as usual” scenario. Source: Ref. ³.

International initiatives have tried to put the problem on the agenda and several governments have started to pass laws and develop strategies for reducing CO₂ emissions, but opposition of economy and conservative pressure groups is strong. Furthermore, most efforts are focused mainly on the decarbonization of electricity production, which is reflected by the recent sensational technological progress in photovoltaics and wind energy systems. However, as the right diagram in Figure 1.1 shows, less than 20% of the total energy is consumed in form of electricity. The vast majority consists of fuels for transportation, industry and heating, based on coal, natural gas and oil products like gasoline. Consequently, even for Germany, who claims to be a pioneer in climate protection policy, the International Energy Agency (IEA) estimated the share of carbon free renewable energies on the total primary energy mix in 2011 to be about 3% only¹¹.

To address the core of the energy problem, an alternative and carbon free chemical fuel has to be found, which can be stored, transported and converted into heat, motion or electricity on a large scale and thus replace fossil fuels. It is not surprising, also in consideration of the topic of this thesis, that the top candidate is molecular hydrogen (H₂). This idea is not new. Already in 1874, Jules Verne thought about a society based on “the elements of water, hydrogen and oxygen”¹². In fact, hydrogen brings all qualities to build a whole economy on it. It is one of the most abundant elements on earth and readily available in form of water. Due to its low molecular mass, the gravimetric energy density outperforms all fossil fuel by at least a factor of three (see Table 1.1). Furthermore, storing and transportation issues have been largely solved in the last years and the low volumetric energy density can be overcome by storing H₂ under high pressure (up to 700 bar), by liquidation (cryo-storage), by chemical bonds (e.g. metal hydrates) or by physisorption at high-surface area metal organic frameworks (MOFs) or in clathrate hydrate cages⁷. In addition, it is also possible to convert H₂ into other (carbon neutral) fuels, such as methane, methanol or diesel using CO₂ as carbon source and the well-established reverse water-gas shift reaction and Fischer-Tropsch-synthesis. This has the advantage that the already existing infrastructure for transport, distribution and consumption can be used.

Table 1.1: Gravimetric and volumetric energy densities of different fuels (at 1 bar). Source: Ref. 7.

Fuel	Energy density	
	Gravimetric (MJ/kg)	Volumetric (MJ/L)
Coal	24	–
Wood	16	–
Gasoline (petrol)	44	35
Diesel	46	37
Methanol	20	18
Natural gas	54	0.036
Hydrogen	143	0.011

Even though H₂ seems to be the ideal fuel for a sustainable energy supply in the future, there is still a fundamental problem to be solved. H₂ does not appear on earth in its molecular form, it has to be extracted from compounds. Today, most hydrogen is produced by steam reforming from natural gas. While this procedure is the most economic one, it does not solve the CO₂ problem as large amounts of CO₂ are emitted during the process.

The second main possibility to generate hydrogen is the electrolysis of water¹³ according to the reaction:



Only if the necessary energy comes from renewable energy sources without emission of CO₂, the electrochemical production of H₂ makes sense. Attempts have been made to use electricity from PV or wind power for electrolysis (“power-to-gas”), but up to now this procedure is too expensive to be competitive.

Another approach is the use of solar radiation energy to directly split water and generate hydrogen in a photoelectrochemical cell (PEC)^{7,14}. Among others, the so called “artificial leaf”¹⁵ represents a possible design for such a photoelectrochemical device. It consists of one or more PV cells to provide the necessary current and voltage and a set of directly attached electrodes, where well suited catalysts optimize the electrochemical reaction. In contrast to commercial electrolyzers, the current densities at such a device would be in the order of $\geq 10 \text{ mA/cm}^2$ ($\geq 10\%$ efficiency of PV * 100 mW/cm² radiation power), which is a relatively low value, increasing the needed photoactive area. If one considers the current energy demand of 500 EJ/a an area of at least 240 000 km² is needed to be covered with PECs (considering 10 hours of direct sunlight per day, which is even for deserts a rather optimistic supposition). By 2050, the necessary photoactive area is expected to increase to a size of more than 500 000 km². This seems to be far beyond any realistic feasibility, but on the other hand it is less than 3.5% of the world’s desert area. Still, the challenge is enormous and there is no alternative to a significant reduction of mankind’s energy demand to meet the climate goals.

A key issue for developing efficient PECs is the reduction of energy losses at the anode side of the system, where O₂ is released. The so-called oxygen evolution reaction (OER) involves the transfer of four electrons to produce one O₂ molecule, which leads to significant overpotentials to be applied for achieving acceptable reaction rates. Today, the most efficient OER catalysts are RuO₂ and IrO₂, which both contain expensive and rare elements. A coating of all the photoactive area mentioned above with only 100 nm of catalyst would result in the need of over 500 tons of Ir or 260 tons of Ru by 2050. With a current price of 17 600 (Ir)¹⁶ and 1 500 €/kg (Ru)¹⁷, respectively, neither of these oxides is applicable for large scales.

Cobalt and manganese oxides represent two possible alternatives to noble metal oxides. They are up to four orders of magnitude cheaper (Co: 26.4 €/kg¹⁸, Mn: 2 €/kg¹⁹), abundant and relatively easy accessible. But although their high catalytic activity is known for many years, several questions about the catalytic mechanism are still open.

In this work, cobalt and manganese oxide thin films were synthesized and characterized as alternative catalysts with a possible application in photoelectrochemical devices with “artificial leaf” design in superstrate configuration²⁰. The synthesis method of choice was electrochemical deposition, because it allows in principle to deposit the desired catalyst directly onto the back contact of the solar cells and is an easy and reliable method, which does not necessarily need the application of elevated temperatures.

The main focus of the thesis was to understand the relations between composition, crystallinity, film thickness, surface state and OER activity, respectively. The major part of the experiments was carried out on amorphous cobalt oxide which was studied intensively using electrochemical methods to understand its working principles.

In the second part, also spectroscopic analysis methods were applied. By using in-line synchrotron photoelectron spectroscopy (SXPS) the composition and oxidation states of the surface of cobalt and manganese oxide, respectively, were investigated in dependence of the applied anodic potentials and commonalities as well as differences have been evaluated. Furthermore, in-situ UV/Vis measurements gave direct insights into potential dependent transitions during and after potential cycling in the anodic regime.

2. Theoretical background

2.1. Electrochemical basics

In this chapter the electrochemical background is briefly reviewed regarding electrochemical water splitting and the oxygen evolution reaction. Much more detailed information can be found in standard textbooks^{21–23}.

When Alessandro Volta published his invention of the “electric pile” (the first battery) in 1800, the impact on the scientific community was tremendous. For the first time a steady DC current of tunable magnitude could be produced and the scientific field of electrochemistry was born. Despite Volta did not understand the chemistry behind his invention, it pioneered the development for Ohm’s and Faraday’s laws, the discovery of the relationship between electricity and magnetism and much more²⁴. While trying to reproduce the “electric pile” W. Nicholson and A. Carlisle observed the electrochemical splitting of water into hydrogen and oxygen, finding immediately a first application of Volta’s achievement. However, already in 1789 two Dutchmen, A. Paets van Troostwijk and J. R. Deiman, were the first to discover that upon electric discharge water could be decomposed into “combustible air” and “life-giving air”^{25–27}. With the development of the first fuel cell²⁸ in 1838 by W. R. Grove and C. F. Schönbein, respectively, the energetic cycle was closed and hydrogen as energy carrier started to attract attention.

Energetics

Water splitting is an uphill reaction, which means that it will not occur spontaneously and one has to introduce energy into the system separate water into its elements. This can be done e.g. thermally (thermolysis) or by using electric power (electrolysis).

An electrochemical cell for water electrolysis consists of two electrodes immersed into an aqueous electrolyte. If one applies a potential difference between the two electrodes, which is high enough to overcome the decomposition voltage E_d and all kinetic barriers, oxygen will be evolved at the anode, while hydrogen will be produced at the cathode according to:

Acid media (pH0):	Anode:	$2 \text{H}_2\text{O} \rightarrow \text{O}_2(\text{g}) + 4 \text{H}^+ + 4\text{e}^-$	$E^0 = 1.23 \text{ V (NHE)}$
	Cathode:	$4 \text{H}^+ + 4\text{e}^- \rightarrow 2 \text{H}_2 (\text{g})$	$E^0 = 0 \text{ V (NHE)}$
	Overall:	$2 \text{H}_2\text{O} \rightarrow 2 \text{H}_2 (\text{g}) + \text{O}_2 (\text{g})$	$E_d = 1.23 \text{ V}$
Alkaline media (pH14):	Anode:	$4 \text{OH}^- \rightarrow \text{O}_2(\text{g}) + 2 \text{H}_2\text{O} + 4\text{e}^-$	$E^0 = 0.404 \text{ V (NHE)}$
	Cathode:	$4 \text{H}_2\text{O} + 4\text{e}^- \rightarrow 2 \text{H}_2 (\text{g}) + 4 \text{OH}^-$	$E^0 = -0.826 \text{ V (NHE)}$
	Overall:	$2 \text{H}_2\text{O} \rightarrow 2 \text{H}_2 (\text{g}) + \text{O}_2 (\text{g})$	$E_d = 1.23 \text{ V}$

The different anodic and cathodic reactions for acid and alkaline media come from the radically different concentrations (and activities) of H^+ and OH^- ions by a factor of 10^{14} for pH0 and pH14, respectively. At neutral pH7, both pathways can be expected to occur simultaneously but due to the dissociation constant of water ($[H^+] * [OH^-] = 10^{-14}$), the overall concentration of reaction educts is seven orders of magnitude smaller than in strong acid or alkaline media. This is one of the reasons, why electrolysis runs best in acid or basic solutions. Furthermore, in neutral electrolytes the pH value has to be stabilized by a buffering agent to prevent local pH shifts close to the electrodes (see reaction equations).

The equilibrium potentials E^0 are given with respect to the normal hydrogen electrode (NHE) in the same electrolyte. The shift in the potential values is a consequence of the Nernst equation as follows for standard conditions:

$$E^0 = E^{00} + \frac{R*T}{n*F} * \ln \frac{a_{ox}}{a_{red}} = E^{00} + \frac{8.314*298}{1*96485} * 2.303 * \log \frac{a_{H^+}}{a_{H_2}(=1)} = E^{00} - 0.059 * pH \quad (2)$$

In this equation E^0 is the equilibrium potential, E^{00} is the standard equilibrium potential, R , T , F and n are the universal gas constant, the absolute temperature, the Faraday constant and the number of transferred electrons per ion and a_{ox} and a_{red} are the activity of the oxidized and reduced species. From the equation it can be seen that the equilibrium potential of H^+/H_2 shifts to lower values by 59 mV per unit pH. Likewise, the equation can be written for OH^-/O_2 . Thus, to compare the catalytic activity of different catalysts in different electrolytes, one should refer the potential to the reversible hydrogen electrode (RHE), which accounts the pH dependent potential shift.

The Gibbs free energy, which has to be provided per mole of water to be split (see equation 1) can be calculated by:

$$\Delta G = -nFE_0 = -(2)*96485*(-1.23) = +237 \frac{kJ}{mol} \quad (3)$$

In this equation E_0 is the potential difference between cathode (reduction) and anode (oxidation) and equal to $-E_d$. Now, there seems to be a mismatch between the Gibbs free energy (i.e. the process-initiating work) needed to split water and the energy density of hydrogen, which is given in Table 1.1 and corresponds to 286 kJ/mol. This disagreement can be solved by considering that ΔG is also given by

$$\Delta G = \Delta H - T\Delta S = 286 - 298*(0.13(H_2) + 0.5*0.205(O_2) - 0.07(H_2O_{(l)})) = 237 \frac{kJ}{mol} \quad (4)$$

In this equation ΔH is the standard enthalpy of formation of water and ΔS is the entropy change during the reaction. This means that the thermodynamic decomposition potential E_d of 1.23 V does not account for the entropy change caused by the transition of liquid water into H_2 and O_2 in the gas phase. This energy comes from the ambience in the form of heat. An ideal electrolysis

cell, which runs at 1.23 V would cool down very fast and the reaction would stop. If one takes the entropy change into account the so called thermoneutral potential of 1.48 V has to be taken to split water into its elements. However, in a photoelectrochemical cell more than enough heat is provided by the sun, which can be used by the system, such that for practical use, E_d is the potential of reference. Nevertheless, the thermoneutral potential is often taken for calculating solar to hydrogen efficiencies as it leads to higher numbers.

Overpotential

To run an electrochemical reaction into any direction, the equilibrium potential E^0 has to be left. If we consider our water splitting reaction, one can think of an electrochemical cell with two electrodes, on which H_2 and O_2 gas are bubbled through the aqueous electrolyte, respectively. If one connects an electric load in between the electrodes, current will flow from the hydrogen side to the oxygen side and the equilibrium potential will decrease (this is the case for a fuel cell). But if one applies an external potential sufficiently higher than the equilibrium potential, current will flow from the oxygen side to the hydrogen side and water from the electrolyte will be decomposed into H_2 and O_2 (electrolysis). Deviation from E^0 to either side is called overpotential η . So, on one hand η is required for electrochemical reactions to occur in the first place, on the other hand it always represents energy loss, as it diminishes the energy output of a fuel cell and it increases the energy input for an electrolysis system.

The relation of overpotential η to current density j for an ideal electrochemical cell under standard conditions is given by the Butler-Volmer equation:

$$j = j_A + j_C = j_0 * \left\{ e^{\frac{\alpha * n * F}{R * T} * \eta} - e^{\frac{-(1-\alpha) * n * F}{R * T} * \eta} \right\} \quad (5)$$

Here, j_A and j_C are the anodic and the cathodic current density, j_0 is the exchange current density, α is the charge transfer coefficient and n , F , R and T are the number of electrons involved in the electrochemical reaction, the Faraday constant, the universal gas constant and the absolute temperature, respectively. Thus, the current density is always a mixture between anodic and cathodic reaction currents. However, for a high anodic overpotential the cathodic term becomes negligible and vice versa. The charge transfer coefficient α is a measure for the effect of anodic potential change on the activation energy of the reaction. Anodic reactions are most effective if α is close to 1, cathodic reactions run fastest if α is close to 0. In experiments α values around 0.5 are frequently found.

For overpotentials above ca. 25 mV one can plot the logarithm of the current density versus the overpotential according to the equation (anodic case):

$$\lg j = \lg j_0 + \frac{\alpha * n * F}{2.3 * R * T} * \eta = \lg j_0 + \frac{1}{B} * \eta \quad (6)$$

From the linear extrapolation of the curve one can calculate j_0 and B (i.e. the Tafel slope, which is the increase in η per decade of j). Exchange current density and Tafel slope are the two most important kinetic parameters for characterizing the activity of a catalyst.

The overpotential is composed of three portions. (I) The electron transfer overpotential is related to the actual electrochemical reaction. It depends on the kind of reaction, activation energies and number of transferred electrons. (II) The diffusion overpotential is caused by an insufficiently fast supply of educts (e.g. OH^-) to or removal of products (e.g. O_2) from the electrode. The formation of gas bubbles at the surface of the electrode, “blocking” some of the active area is a special case of diffusion overpotentials. This phenomenon usually occurs at high current densities, when the reaction rates are very fast. (III) Reaction overpotentials are associated with slow chemical reactions before or after the charge transfer reaction. This can be e.g. adsorption or desorption processes.

As will be discussed in the next chapter, the overpotentials required for the OER to run at satisfying rates are rather large. Big commercial electrolyzers face that problem with harsh reaction conditions (120°C, 40 wt.% KOH, 30-50 bar)²⁹ to improve kinetics, but for photoelectrochemical devices (PEC) this is not possible. Understanding, development, optimization and application of materials catalyzing the OER are therefore indispensable.

2.2. The oxygen evolution reaction (OER)

In this chapter, the oxygen evolution reaction will be discussed briefly and the relevant issues will be addressed. For more in-depth information about the chemistry and catalysis of this very important reaction the interested reader is referred to more comprehensive reviews published elsewhere^{30–32}.

The oxygen evolution reaction from water is one of the most fundamental reactions in nature. With the process of photosynthesis, green plants, algae and cyanobacteria use solar radiation to form hydrocarbons from CO₂ and water. As a side product O₂ is released to the ambience and basically all O₂ in the current atmosphere comes from this process. The OER takes place in photosystem II (PSII), which is a large protein complex with a catalytic center consisting of a Mn₃CaO₄ cluster linked to a fourth Mn by a mono-μ-oxo bridge³³. Energetically, water oxidation occurs via a complex cascade reaction and is incredibly efficient. Generations of scientists have worked on the elucidation of the reaction mechanism and today it is one of the best studied chemical reactions^{34–36}.

However, the transfer of the principles of the biological OER in PSII to an electrochemical cell with inorganic catalysts is not trivial. Despite intensive research for several decades, a catalyst material, which allows electrochemical water oxidation at overpotentials well below 300 mV has not been found yet.

2.2.1. Theoretical considerations

The release of one O₂ molecule from two molecules of water requires the transfer of four electrons from the electrolyte (i.e. OH⁻ in the alkaline and H₂O in the acidic case, respectively) to the anode. It is very unlikely that all four electrons can be transferred simultaneously and experimental results as well as theoretical calculations strongly suggest that the OER occurs in at least four steps, transferring one electron at a time. If so, the formation of transition states is unavoidable and represents the key factor in understanding and optimizing catalysts. Several reaction pathways have been proposed based on kinetic experimental data³⁰ (Tafel slope, j_0 , reaction order etc.) and, more recently, also relying upon density functional theory (DFT) calculations^{37–39} and advanced in-situ techniques⁴⁰. However, since transition states usually have rather short life times and are hard or impossible to detect spectroscopically, it was tried to find universal descriptors expressing the catalytic activity of different materials. In an early attempt Trasatti⁴¹ plotted the experimentally determined overpotential versus the enthalpy of transition of the oxide from a lower to a higher oxidation state. A volcano shaped relation was found. Compounds, which form very stable higher oxides will bind the transition state too strong, such that the release of O₂ becomes the rate determining step (left branch). On the other hand, if the transition enthalpy is too large, intermediate states will not be stabilized and water discharge

2. Theoretical background

becomes limiting^{41,42}. This gives a first idea of how systematic materials research could be carried out for finding new materials for OER catalysis, despite the fact that this graph represents only a first approximation, since several experimental parameters (e.g. real surface area and Tafel slope) are not taken into account.

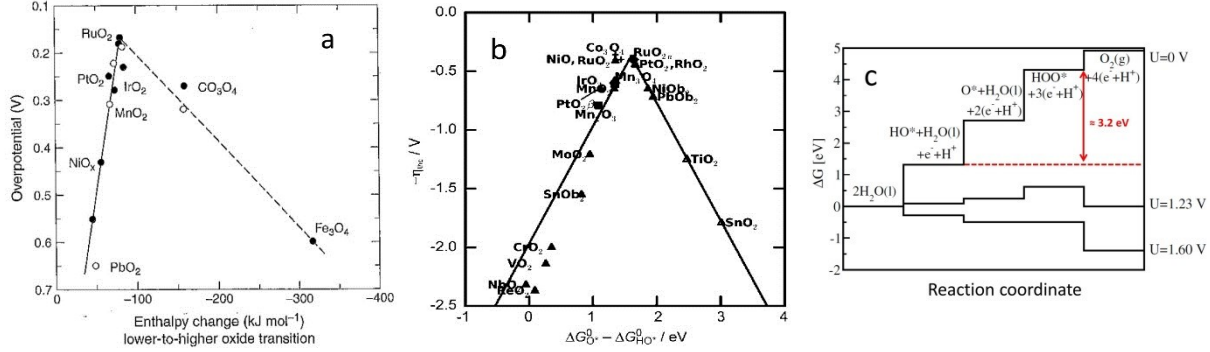


Figure 2.1: (a) Volcano plot based on Trasatti⁴¹ linking overpotential with transition enthalpy. Source: Ref. ⁴². (b) Volcano plot using the difference in binding energy between the $-O^*$ and the $-OH^*$ transition state as descriptor. Source: Ref. ³⁸. (c) Free energy diagram of intermediates during OER at $-O^*$ covered RuO_2 for different potentials. Source: Ref. ³⁹.

The significant increase of computational power in recent years opened new possibilities for DFT calculations on reaction energetics. For the hydrogen evolution reaction, a clear and experimentally provable relation between the free energy of hydrogen adsorption ΔG_H and catalytic activity was found, leading to a volcano plot with Pt at the top⁴³. The OER, involving four electrons, is a considerably more complex task, though. Rossmeisl et al.^{38,39} and Koper⁴⁴ elaborated detailed DFT and thermodynamic studies on the OER at metal oxides. For an ideal catalyst the reaction free energy ΔG_{OER} is given by the thermodynamic equilibrium potential with all elementary reaction steps having the same ΔG :

$$\Delta G_{OER} = \Delta G_{OH^*} + \Delta G_{O^*} + \Delta G_{OOH^*} + \Delta G_{O_2} = 4 * 1.23 eV = 4.92 eV \quad (7)$$

Such a catalyst would start with oxygen evolution at potentials just above 1.23 V as ΔG becomes downhill for all reaction steps. However, for a great variety of oxides the authors found a constant difference of about 3.2 eV (instead of 2.46 eV) between the binding energies of the $-OH^*$ and the $-OOH^*$ transition states, independent of the absolute binding energy of $-O^*$ in between them (see an example in Figure 2.1c). This “scaling relation” leads inescapably to a theoretical overpotential η_{the} of at least 0.2 – 0.4 V for real catalysts, since it is determined by the transition state with the highest ΔG . In fact, no material is known to show oxygen evolution below these values. Knowing this, the difference in ΔG between the $-O^*$ and $-OH^*$ transition state can be taken as descriptor for catalytic activity resulting in a volcano plot with its maximum at about 1.6 eV, placing $-O^*$ energetically right in the middle between $-OH^*$ and $-OOH^*$ (Figure 2.1b), but still far away from $\eta_{the} = 0 V$. Compounds, which bind oxygen ($-O^*$) too strong will have their rate limiting reaction in step 3, forming $-OOH^*$ (left branch), whereas oxides, which bind oxygen too

weakly, have their bottleneck in the formation of $-O^*$ (right branch) in step 2. Manganese oxide is found on the strong binding leg of the volcano plot, while new results placed cobalt oxide on the weak binding site of the graph³⁷. For significant improvements in OER catalysis this “scaling relation” has to be overcome. A first effort has been published recently⁴⁵, where RuO_2 has been modified with Ni and Co.

2.2.2. Catalysts for the oxygen evolution reaction

In contrast to the hydrogen evolution reaction, the OER occurs at potentials where basically all metals are covered with a thin oxide film and thus the metal oxide is the active phase^{41,44,46}. This is the reason why e.g. Pt is not a very good OER catalyst even though for the oxygen reduction reaction it is one of the most active materials. Transition metals are able to readily change their oxidation state, which is a fundamental property for electrocatalysis, since it always includes electron transfer from one species to another and charge balance has to be maintained. Therefore OER catalysts are usually based transition metal oxides. IrO_2 and RuO_2 have shown the highest catalytic activity towards OER and especially RuO_2 is very well characterized³⁰. However, both compounds consist of very expensive and rare noble metals and are no option for the use in a large scale application. For classical alkaline electrolysis therefore, steel, Ni or Ni-Co-spinels are used as anodes and harsh reaction conditions are applied to improve kinetics.

Even though catalysis of OER is one of the bottlenecks for developing photoelectrochemical cells for solar water splitting, no standards for experimental work, as it is e.g. the case for photovoltaics, have been established yet. Recently, there has been some effort to introduce a standard protocol for characterizing HER and OER catalysts for PECs^{1,47}, but still a wide variety of electrochemical setup parameters and benchmarking characteristics are reported. For instance, several definitions of turnover frequencies (TOF) are used for the description of a catalyst's activity. This can be defined e.g. as O_2 molecules per second and active surface site, per total amount of catalyst atom⁴⁷, per gram of catalyst, per surface area unit, per nanocluster⁴⁸ or also possible per € of catalyst material. Moreover, the overpotential at which the TOF is measured frequently varies between different studies, which makes comparison of experimental results challenging.

Furthermore, a crucial parameter, the real surface area, is not easily accessible and no standard method is available to estimate the roughness of a catalyst. Comparison of the apparent current density may be interesting considering the application of a catalyst in a device, but for fundamental research the real current density, which represents the intrinsic activity is of greater importance. This becomes striking if one takes into account that the preparation parameters can significantly alter the apparent catalytic activity by e.g. increasing the surface area and/or porosity, preferring a certain surface modification or improving the contact to the substrate. An example can be given regarding Ni-Co-oxide, which frequently is described as more active than cobalt oxide and nickel oxide. A systematic study by Trotochaud et. al⁴⁹ however, showed that

the intrinsic catalytic activity is related to the Ni portion in the compound and the increased apparent activity most probably related an increased surface area.

In recent years a growing interest in cheap and abundant alternatives for RuO₂ and IrO₂ emerged for the application in PECs. The most studied compounds are based on cobalt oxide, manganese oxide and nickel oxide, but especially iron-nickel-oxide appeared as very highly active towards the OER^{49,50}. Furthermore, mild synthesis routes⁵¹ have been investigated, which is of particular importance, if the catalyst should be deposited on possibly rather sensitive photoabsorbers or PV devices.

2.2.3. Cobalt Oxide

Cobalt oxide is a typical first row transition metal oxide. Due to the ability of transition metals to stabilize more than one oxidation state, several different types of cobalt oxides and cobalt hydroxides are known. The thermodynamically stable form between room temperature and 900°C is spinel type Co₃O₄⁵², but also the metastable rock salt CoO compound can be synthesized relatively easy by annealing in reducing atmosphere⁵³. Co₃O₄ contains mixed valences of cobalt ions with Co³⁺ occupying half of the octahedral sites and Co²⁺ sitting in one eighth of the tetrahedral sites of the cubic close-packed oxygen lattice⁵⁴. The synthesis and/or characterization of Co₂O₃ has also been reported sometimes, but Chuang et al.⁵⁵ showed that nominal Co₂O₃ shows the same XPS features as Co₃O₄ and concluded that Co₂O₃ might not be available under ambient conditions. Similar information are found elsewhere⁵⁴. Likewise, the synthesis and isolation of CoO₂ has not been reported yet (to the best of the author's knowledge).

Besides the oxides also different hydroxides such as Co(OH)₂ and Co(OOH) are known. Benson et al.⁵⁶ identified in an early work already three different types of cobalt oxyhydroxides. The complexity of the cobalt oxygen system has later be confirmed by potential cycling experiments of Co metal in alkaline solutions, showing several transitions within the anodic potential regime below the onset of the oxygen evolution reaction^{57,58}.

Cobalt oxide, cobalt hydroxide and mixed compounds containing cobalt and oxygen are typically used as electrochemical supercapacitors⁵⁹, for electrochromic devices⁶⁰, in energy storage systems such as Li-ion batteries⁶¹, as gas sensors⁶² and for heterogeneous catalysis³².

The electrocatalytic activity of cobalt oxide has been known for many decades. Already in 1950 electrochemical experiments on the oxidation of cobalt metal in alkaline solution have been carried out⁶³ and showed oxygen evolution. Hundreds of papers have been published over the years reporting the synthesis and electrochemical characterization of active cobalt oxides and mixed compounds containing Ni, Cu, Li, La and others^{64–70} to name just a few. The preparation methods used for fabrication of the OER electrodes were predominantly thermal decomposition

of usually $\text{Co}(\text{NO}_3)_2$ ^{64,71–73}, but also sol-gel routes^{66,68,74–77}, spray pyrolysis^{65,78,79}, wet chemical⁴⁹ and electrodeposition^{80–83}.

With the growing interest in photoelectrochemical application of OER catalysts, mild synthesis methods, eliminating the need for elevated temperatures became very interesting. In 2008 Kanan and Nocera⁸⁴ could synthesize an amorphous, highly active catalyst by simple electrochemical deposition from a phosphate buffer solution. In numerous studies structure, composition and working principles were investigated^{85–89} leading to a comprehensive picture of the catalyst consisting of octahedrally coordinated Co^{3+} ions interconnected by di-oxo bridges^{85,90} and the Co^{4+} being produced during oxygen evolution⁸⁸. This catalyst has successfully been applied in several photoelectrochemical cells to reduce OER overpotentials^{91–93}. Using the right scaffold for the deposition of this catalyst, tremendous current densities have been achieved at rather low overpotentials⁹⁴.

With the new field of application in photoelectrochemical devices or for direct photocatalytic water splitting^{95,96} the efforts to develop highly active OER catalysts has increased significantly and new methods of synthesis^{51,97} and in-situ investigations⁴⁰ allowed significant improvements in activity and understanding of the OER on cobalt oxide based catalysts.

2.2.4. Manganese Oxide

The various available manganese oxides, who comprise e.g. MnO_2 , Mn_3O_4 and Mn_2O_3 , are another group of OER catalysts based transition metal oxides, which attracted much attention in recent years. Their fundamental activity has been demonstrated very well by nature with the active center of photosystem II (see above). Several groups have synthesized calcium manganese oxide powders and thin films to mimic the catalytic center of PS II^{98–100}. However, it turned out that in an inorganic approach manganese oxide without the presence of calcium in the investigated compound are more active towards the OER^{101–104,96}, stable over a broad pH range¹⁰⁵ and also applicable as bifunctional catalyst for both OER and the oxygen reduction reaction (ORR)^{101,106}. Intensive structural studies and in-situ investigations have been carried out to elucidate the working principles of manganese oxide catalysts, finding commonalities with the active center in PSII^{103,107–109}.

Especially the bixbyite structure of nanostructured $\alpha\text{-Mn}_2\text{O}_3$, which is structurally distinguished by regular and distorted $[\text{MnO}_6]$ octahedrons interlinked in a complex network¹¹⁰ as well as nanostructured $\beta\text{-MnO}_2$ have been described as being extraordinary active binary electrocatalysts in the process of oxygen evolution^{101,102}. Also in our working group some efforts on manganese oxide and calcium manganese oxide have been done in the past and showed promising results concerning activity and stability of thin film electrocatalysts^{100,111–114}.

3. Experimental section

3.1. Sample preparation

Cobalt Oxide

Cobalt oxide (CoO_x) catalyst thin films were prepared via electrochemical deposition following a modified protocol of Casella and Di Fonzo⁸³. In the standard procedure, 12 mM of $\text{CoCl}_2 \cdot 6 \text{H}_2\text{O}$ (Merck, p. A.) and 12 mM of D-gluconic acid sodium salt (Merck, p. S.) as complexing agent were dissolved in aqueous solution containing 1 M KOH. D-gluconic acid sodium salt is known to be a very powerful chelating agent for masking metal ions in strongly alkaline solutions and usually forms dimeric complexes¹¹⁵. The solution has a dark greenish color and is stable for about 12 hours, before $\text{Co}(\text{OH})_2$ slowly starts to precipitate as black powder. This precipitation reduces the concentration of Co^{2+} ions and consequently deposition rates decrease with time. Therefore, the deposition solution was freshly prepared for every series of samples.

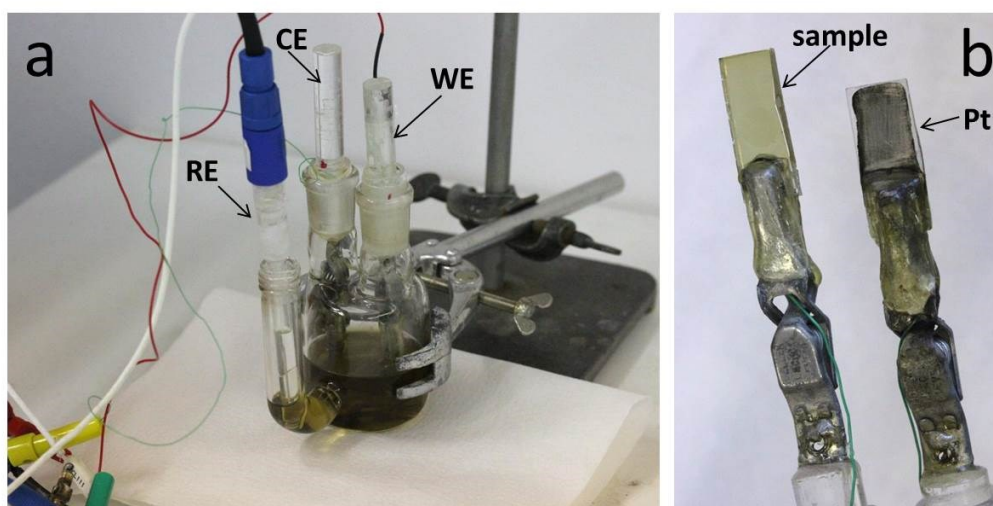
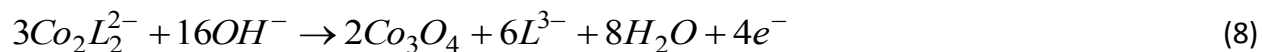


Figure 3.1: Electrochemical cell for sample preparation in operation mode (a) and working (sample) and counter (Pt) electrodes outside the cell (b). WE, CE and RE denote working, counter and reference electrode, respectively.

Electrochemical deposition was carried out in a self-designed three electrode electrochemical cell (Figure 3.1) with the substrate as working, Pt foil as counter and a commercial Ag/AgCl reference electrode (Radiometer Analytical, $E_R = 0.204 \text{ V vs. RHE}$). The standard substrate was FTO coated glass (Pilkington), but also Au, Ti and Co foils (Goodfellow) were used. For the deposition procedure a potentiostatic voltage of usually 1.4 V vs. RHE was applied between working and reference electrode and the resulting deposition current was recorded by the potentiostat (Versastat 3, Princeton Applied Research). After a defined deposition time or after a particular charge (usually 1 C/cm^2) has passed the electrochemical cell the deposition was stopped and a homogeneous brownish film was obtained. During the deposition process the solution was

neither stirred nor bubbled with any gases. Before characterization, the samples were usually dried in air at room temperature. Some samples were furthermore annealed in air at temperatures up to 450°C after the deposition. Their color turned into black upon the heat treatment to form spinel type crystalline Co₃O₄. Several of the deposition parameters were varied to find the best preparation conditions. The results are given in chapter 4.1.1.

The following reaction equation has been proposed for the deposition of CoO_x⁸³:



Co₂L₂²⁻ denotes the dimeric complex formed between the Co²⁺ ions and the gluconate chelating agent. It has been further suggested that the deposition of cobalt oxide onto the substrate might occur in a multistep mechanism¹¹⁶, but the single steps have not been clarified in detail yet. However, this equation has been used as basis for calculations of film thickness and amount of deposited Co (see chapter 4.1.2.2).

Manganese Oxide

Manganese oxide films¹¹² were deposited at pH 7 from a 1:1 mixture of two solutions containing 0.5 M MnSO₄ (Merck, ACS standard) and 0.5 M Na₂SO₄ (Sigma Aldrich, 98%), respectively¹¹⁷. Storing these solutions for long periods of time did not cause any observable changes. For the electrochemical deposition, FTO/glass was again used as substrate, while a Pt-wire and a commercial Hg/HgSO₄ electrode (Radiometer Analytical, E_R = 0.640 V vs. RHE) acted as counter and reference electrode, respectively. During the deposition N₂ was gently bubbled through the solution. A constant current of 0.25 mA/cm² was applied for 25 min in order to achieve a brown homogeneous MnO_x film, which was amorphous in its pristine state. After a heat treatment at 500°C for 1 hour in air, the amorphous film converted into crystalline α-Mn₂O₃, while annealing at 600°C for 1 hour in N₂-atmosphere resulted in the formation of the spinel-type Mn₃O₄ phase.

3.2. Analysis methods

3.2.1. Electrochemistry

Electrochemical measurements represent a major tool in this work to characterize the synthesized catalysts. In this chapter, the applied electrochemical experiments and methods with the relevant parameters are briefly described. A more detailed description of the techniques can be found elsewhere^{22,118,119}.

3.2.1.1. Cyclic voltammetry (CV)

Cyclic voltammetry is one of the most frequently used electrochemical measurement techniques. It allows a thermodynamic and kinetic examination of electrode processes as a function of applied potential and time. In a standard experiment a dynamic potential is constantly increased with a defined speed (scan rate or sweep rate) towards the upper vertex potential (anodic scan) and subsequently decreased until the lower vertex potential is reached (cathodic scan). The current flow generated by the system is simultaneously recorded. The experimental parameters are therefore the size of the vertex potentials, the scan rate and the number of scans. In electrocatalysis this experiment provides information about the activity of a catalyst (onset potential and shape of the catalytic current curve), electrode surface processes (e.g. oxidation or reduction, their kinetics and reversibility), the double layer capacitance (current as function of the scan rate), the stability of the electrode (current as function of the number of scans) and much more. A typical CV diagram with its most important features labeled is shown in Figure 3.2a.

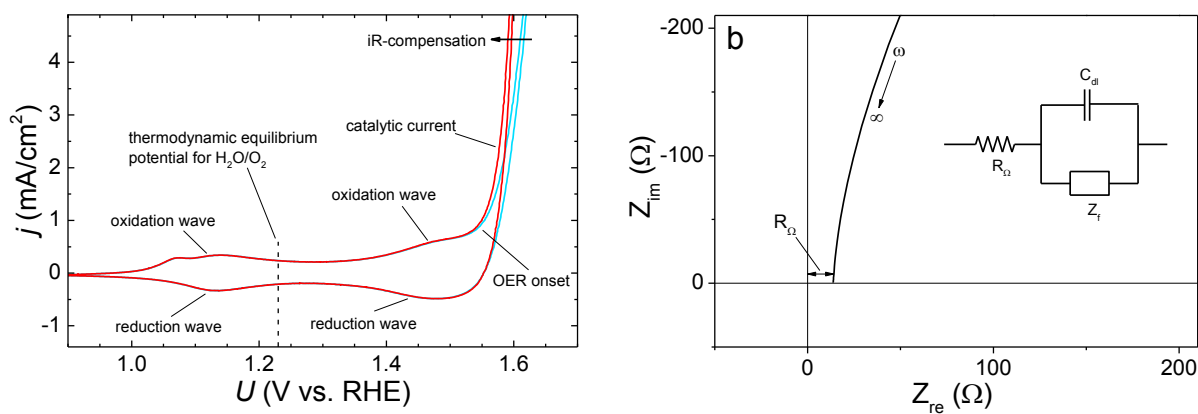


Figure 3.2: (a): Typical CV diagram of a CoO_x electrode with the most important features labeled. The red line represents the iR-corrected current curve, while the blue line depicts the current density as function of the applied potential without any iR-compensation. (b): Typical impedance spectrum of a CoO_x electrode, with the setup resistance R_{Ω} labeled. The Randles equivalent circuit is schematically illustrated on the right hand side of the graph.

iR- compensation

A very important issue for the characterization of electrocatalysts is the so called compensation for the iR-drop. The iR-drop is a potential decrease caused by ohmic resistance within the electrochemical cell (wires, substrate, electrolyte etc.), which leads to the fact that the potential at the electrode/electrolyte interface is smaller than the applied potential from the potentiostat and consequently the current response does not correspond exactly to the applied potential. In order to make the results of an electrochemical measurement independent of the measurement setup and thus comparable to other results, one should try to eliminate this iR-drop.

The potential drop ΔU can be determined by the following equation:

$$\Delta U = U_{\text{applied}} - U_{\text{real}} = i \cdot R_{\Omega} \quad (9)$$

In this equation, U_{applied} (V) is the potential applied to the setup by the potentiostat, U_{real} (V) is the actual potential at the sample surface, i (A) is the absolute current at U_{applied} and R_{Ω} (Ω) is the setup resistance. It becomes obvious from the equation that ΔU is directly proportional to the absolute current i , which is also assigned in Figure 3.1a.

The setup resistance R_{Ω} should be minimized, e.g. by using very conductive substrates and/or by placing the reference electrode very close to the sample surface. The magnitude of R_{Ω} can be estimated by impedance spectroscopy. Figure 3.1b shows the high frequency end of a typical impedance spectrum of a CoO_x electrode and the so called Randles equivalent circuit, which represents the electrochemical half-cell with the sample as working electrode. It consists of the double layer capacitance C_{dl} and the general sample impedance Z_f of the sample connected in parallel and furthermore an ohmic series element, which represents the setup resistance R_{Ω} . At very high frequencies ω the resistance of C_{dl} becomes zero and the whole impedance signal can be attributed to R_{Ω} . Thus, the offset of the high frequency end of the impedance spectrum has been taken for the iR-compensation. Typical values were in the range from 10 to 20 Ω .

Experimental

The CV measurements in this work were, if not mentioned otherwise, conducted in a self-designed electrochemical cell in a three electrodes arrangement. The samples were mounted into the cell and contacted as working electrode (WE) with a gold wire. After mounting the top of the cell, only a defined spot of the film electrode with an area of 0.31 cm^2 was in contact with the electrolyte (measurement spot), which allows the precise calculation of the current density. About 7 ml of electrolyte, usually 1 M KOH, were added to the cell. A platinum wire acted as counter electrode (CE), while a commercial Ag/AgCl reference electrode (Radiometer Analytical, $E_R = 0.204$ V vs. RHE) was used as a point of reference (RE). Potential application with a scan rate of usually 10 mV/s and current recording were carried out using a Versastat 3 potentiostat (Princeton Applied Research). All potentials in this work are given with respect to the reversible

hydrogen electrode (RHE). Figure 3.3 shows two photographs of the unmounted (left) and the mounted electrochemical cell (right), including the electrodes.

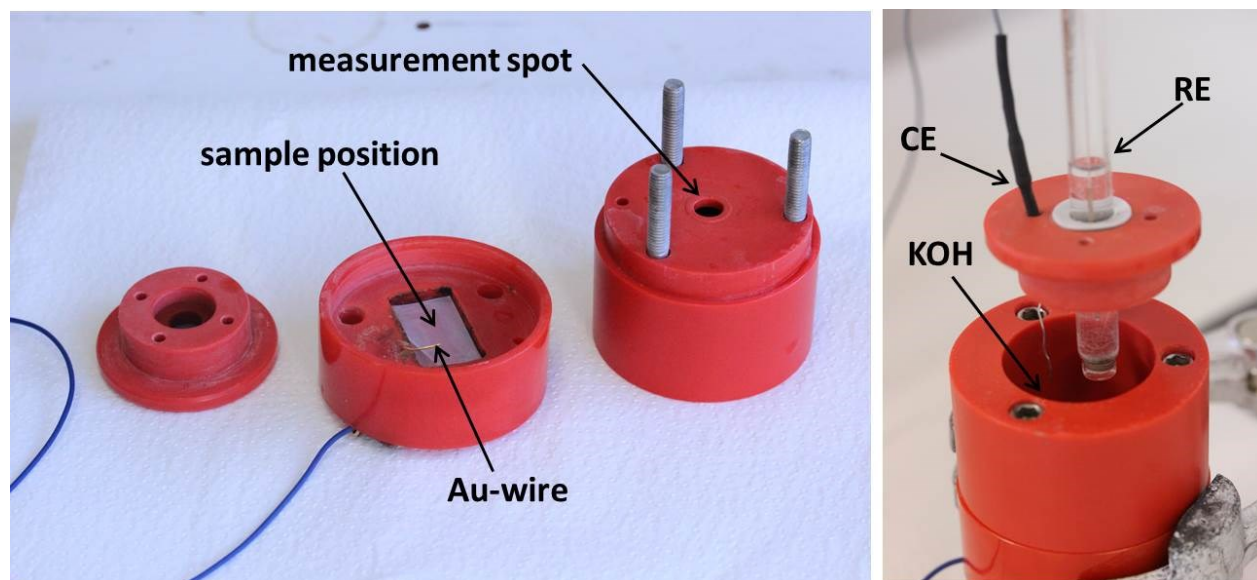


Figure 3.3: Photographs of the unmounted (left) and mounted electrochemical cell (right).

In addition to CV diagrams also potentiostatic and galvanostatic experiments were carried out. For the former, a constant potential has been applied to the sample and the corresponding current was recorded as a function of time. This experiment can be used, among others, to gain information about the stability of the catalyst and for constructing Tafel plots (see 4.1.2.5). In the latter experiments, a constant current density is set by the potentiostat and the potential necessary to achieve this current density is recorded over time. These measurements are useful for benchmarking and stability estimations as well.

3.2.1.2. Differential electrochemical mass spectroscopy (DEMS)

A very special version of CV measurements is known as differential electrochemical mass spectroscopy (DEMS). The setup consists of an electrochemical cell (three electrode configuration), which is connected to a mass spectrometer (Balzers; QMI 420, QME 125, QMA 125 with 90° off axis Secondary Electron Multiplier) over a gas permeable hydrophobic membrane and allows in-situ detection of reaction products like O_2 , while the applied potential is cycled^{120,121}. In that way one can test if the exponential current increase after passing a certain anodic potential (OER onset) actually leads to the production of O_2 or if possible corrosion of the catalyst takes place. A schematic illustration of the setup is given in Figure 3.4. The sample is placed upside down onto the gas permeable membrane so that an electrolyte film of only a few hundred μm remains in between the catalyst surface and the membrane. Gases, which are produced at the surface of the sample, diffuse through the thin electrolyte film, cross to some extend the membrane and can be detected by the mass spectrometer. To ensure that the gas signal corresponds to the applied potential the scan rate of the CV measurements was set to 2 mV/s, to give the gas sufficient time to reach the mass spectrometer. Furthermore, the electrochemical cell was purged with argon to get rid of any residual or dissolved gases in the electrolyte.

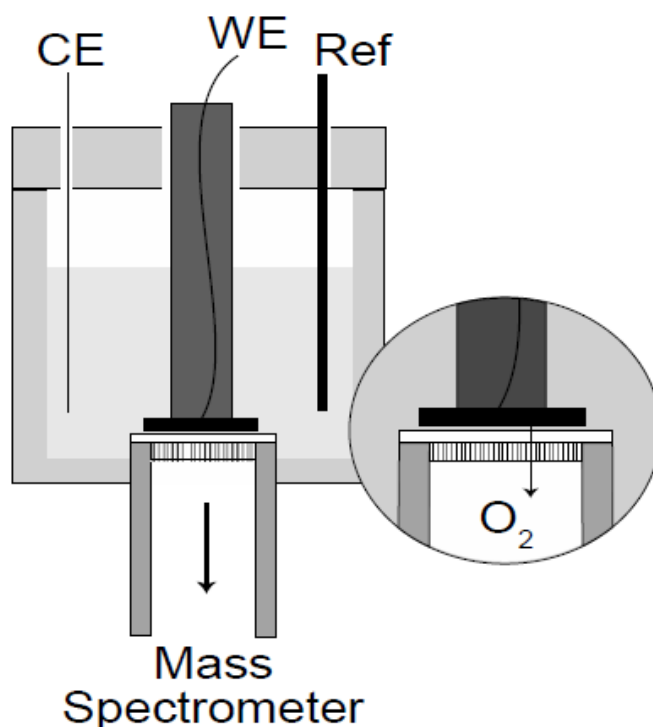


Figure 3.4: Schematic illustration of a DEMS setup. The sample is turned upside down onto the gas permeable membrane where O_2 can diffuse through it and be analyzed in the mass spectrometer. The diagram has been taken from Ref. ¹¹¹.

3.2.2. Spectroscopic methods

3.2.2.1. In-line synchrotron X-ray photoelectron spectroscopy (SXPS)

Besides electrochemistry the second emphasis of this work lays on photoelectron spectroscopy (XPS). A very comprehensive textbook about this technique can be found in Ref. ¹²², a more compact, but well written overview of the principles and main applications is given by Ref. ¹²³. A short introduction into the topic will be given in this chapter.

Photoelectron spectroscopy is based on the photoelectric effect, which was discovered by Albert Einstein, who was rewarded for its correct explanation with the Nobel Prize in 1921. Briefly, an X-ray photon of known energy hits the sample and interacts with a core electron of one of the sample's atoms or ions, which leads to the ejection of this now called photoelectron (see Figure 3.5a). The X-ray photon transfers its energy to the electron, which uses part of the photon energy to overcome its specific binding energy and converts the rest into kinetic energy. One can write this relation as:

$$KE = h\nu - BE - \phi_s \quad (10)$$

where KE is the kinetic energy of the photoelectron, $h\nu$ is the energy of the X-ray photon, BE is the binding energy of the photoelectron and ϕ_s is the work function of the spectrometer, which plays a role due to the electrical contact of the sample with the spectrometer and is usually known. After the photoelectron ejection, the atom/ion is in the $(n-1)$ state and has an electron hole at its core shell. Accordingly, one electron of an outer shell will drop into that core hole (Figure 3.5b) to minimize the energy of the system. The energy released by this relaxation process is either emitted as X-ray photon (X-ray fluorescence) or transferred to another outer electron leaving the atom/ion as Auger electron (Figure 3.5c). If the X-ray photon energy and the work function of the spectrometer are known and the kinetic energy is measured by the spectrometer one can easily calculate the binding energy of the photoelectron.

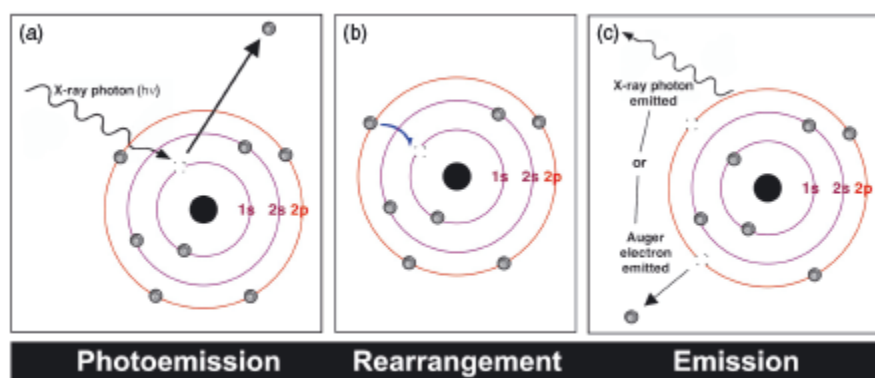


Figure 3.5: (a): An X-ray photon interacts with a core electron, transfers its energy and leads to the ejection of a photoelectron from the n -electron initial state. (b): The ion, now in the $(n-1)$ state reorganizes its electrons to a lower energy state by dropping an electron from an outer shell into the vacant core hole. (c): The excess energy from the process in (b) is released from the ion either by X-ray photon emission (X-ray fluorescence) or by emission of an Auger electron from an outer shell. Source: Ref. ¹²³

As every element contains a different number of protons in the atomic nucleus, the binding energies of the inner electrons (core electrons) are very distinct for every element and can be used for their identification. Moreover, not only the nature of the element, but also its oxidation state and/or its binding properties can frequently be detected by analyzing the chemical shift to higher or lower binding energies. Relaxation processes can influence the binding energy and cause a shift as well, which is e.g. the case for cobalt. Usually, the binding energy increases with oxidation state, but because of the higher relaxation energy of the $(n-1)$ state of Co^{3+} , its binding energy shifts slightly to lower values compared to Co^{2+} . Furthermore, some spectral features, like shake-up satellites can appear (and be used for analysis), due to interactions of the photoelectrons with the outer electron shell. Since the kinetic energy of all emitted electrons is measured by the spectrometer, also Auger electrons are detected and produce peaks in the spectrum. Their kinetic energy, however, is element specific and independent of the X-ray photon energy. Thus, in the binding energy scale, the position of the Auger peaks changes for different X-ray photon energies relative to the photoelectron peaks, according to equation (10). In some cases, Auger and photoelectron peaks overlap and make analysis difficult or impossible. Therefore, most laboratory XPS systems contain two or more metallic anodes in the X-ray gun (usually Al, Mg and/or Ag), to produce X-rays of different energies.

Peak fitting

In many cases the resolution of the spectrometer is not high enough to resolve clear peaks for every species present in the sample. Then, mathematical peak fitting can be a powerful tool to gain deeper information about the kind and amount of the contributions building up the measured peak. However, one has to be careful with the parameters for the fit, as every measured spectrum can be fitted if enough peaks and degrees of freedom are enabled, even though there might be no physical justification for the peaks. Further information about the composition of the sample and spectral features of the elements like reported binding energies, shake-up satellites, chemical shifts etc. are indispensable for a good peak fit. In this work the software Unifit 2013 (Unifit Scientific Software GmbH) was used for peak fitting

Surface sensitivity

The most interesting part of an electrocatalyst is its interface to the electrolyte, because catalysis takes place right there. XPS is a very surface sensitive characterization method and principally well suited for investigations on the composition of a sample surface. The reason for the surface sensitivity of XPS is based on the very short mean free path length of free electrons inside a solid. While X-rays of about 1000 eV penetrate 1000 nm or more into the sample, electrons of the same energy can only travel below 10 nm. This means that only photoelectrons generated very close

to the surface can escape the solid and contribute to the peak without being scattered or absorbed. Photoelectrons that lose energy by interacting with other atoms, e.g. by inelastic scattering, might still be able to leave the sample, but will contribute to the unspecific spectral background. Figure 3.6 shows the dependence of the mean free path lengths of electrons on their kinetic energy for different metals. As one can see there is a global minimum at about 50 to 100 eV. The sampling depth is usually said to be three times the mean free path lengths, where 95% of the signal is generated.

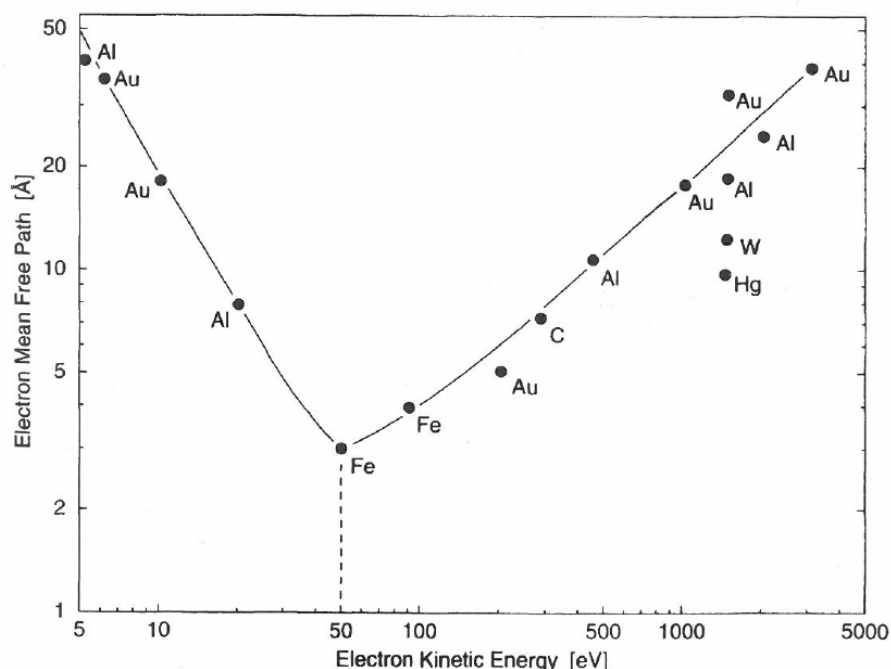


Figure 3.6: Electron mean free path length as function of their kinetic energy for various metals. Source: Ref ¹²².

Regular laboratory XPS setups contain metal anodes as X-ray source, which produce radiation of a defined energy. Tuning the surface sensitivity is thus very limited or not possible at all. Besides its much higher brilliance, synchrotron radiation has a continuous spectrum over several orders of magnitude and allows adjusting the incident X-ray energy to any desired value. In order to measure as surface sensitive as possible, one should choose an energy of about 50 eV higher than the expected binding energy of the peak of interest. The sampling depth should then be around 1 nm only. For many, especially porous samples (like electrocatalysts) a strong secondary electron tail generated by inelastic scattered photoelectrons becomes striking at low electron kinetic energies. Peaks in this range therefore might have a very bad signal to noise ratio and a compromise between surface sensitivity and signal clarity has to be found. The measurements in this work were conducted with X-ray photon energies about 100 to 150 eV higher than the binding energy of interest.

Experimental

In-line synchrotron X-ray photoelectron spectroscopy experiments were carried out at the U49/2 beamline at Bessy II in Berlin Adlershof using the SoLIAS endstation (Solid-Liquid-Interface-Analysis-System, provided by the Technical University Darmstadt). The endstation consists of a photoelectron spectrometer with a Phoibos 150 analyzer (Specs), a large UHV system with different separable chambers and an attached electrochemical cell (Figure 3.7a). The electrochemical cell is composed of a three dimensional “glass cross”, which was held under inert N₂ atmosphere. A small glass pipe, which contains the reservoir of the electrolyte (1 M KOH), a counter (Pt-wire) and a reference electrode (commercial Ag/AgCl) entered the glass cross from one side (Figure 3.7b). The sample of about 1 cm² size was mounted onto a molybdenum XPS sample holder and was electrically contacted using a two component silver filled epoxy adhesive (Elecolit 323 A+B). On top of the sample the silver adhesive was isolated from the electrolyte with a nonconductive epoxy adhesive. A molybdenum spacer ensured that the electrolyte did not get in contact with the sample holder. The sample holder was placed on an UHV transfer bar, turned upside down and contacted with a platinum wire from the back side (Figure 3.7c). The electrical circuit was closed by bringing the sample’s surface (i.e. the catalytically active thin film electrode) in contact with an electrolyte droplet from the glass pipe.

The electrochemical measurements were conducted as follows: First an impedance spectrum was recorded with a Versastat 3 potentiostat (Princeton Applied Research) to determine the setup resistance. Typical values were between 150 and 180 Ω. This high resistance was attributed to the setup geometry with its large distance between the working (sample) and the reference electrode, the non-ideal electrical contacts and so on. Subsequently, a constant anodic potential was applied to the sample and after the current had stabilized, which happened typically after 1 to 2 minutes, the electrode film was quickly removed from the electrolyte by pulling back the transfer bar, while the potential was still kept. Then, residual electrolyte was washed from the sample surface with deionized water and the electrode was dried in an N₂ gas flow using a gas nozzle. Finally, the electrode was transferred into the UHV system of the SoLIAS for surface analysis. In that order, the surface of one and the same sample could be studied with XPS after the application of different potentials and transferred back and forward from the XPS chamber into the electrochemical environment without contact to the ambient atmosphere.

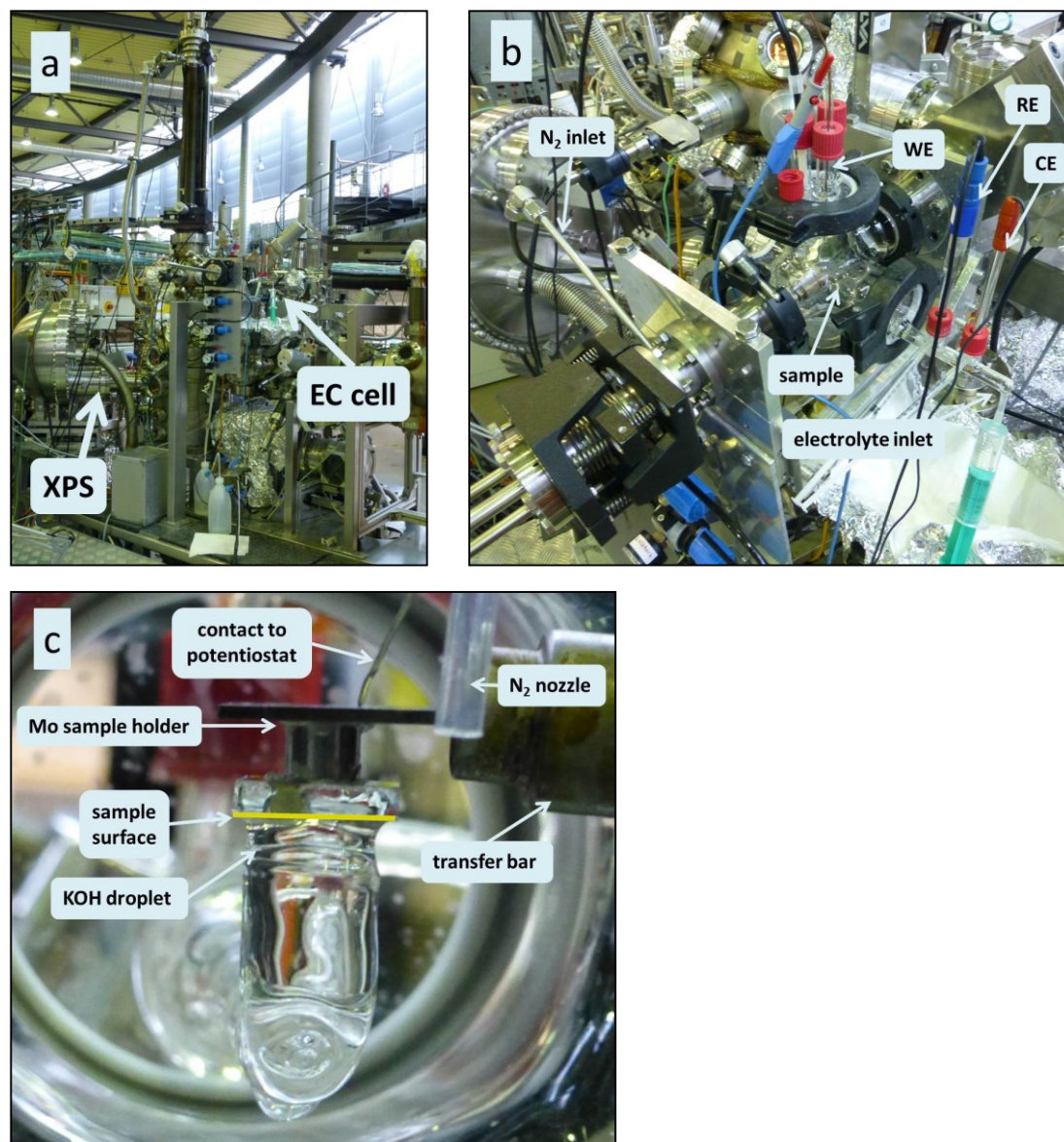


Figure 3.7: (a): Photograph of the SoLIAS endstation at Bessy II. (b): Electrochemical cell ("glass cross") attached to the UHV system of the SoLIAS, with all relevant components. (c): Sample in contact with the electrolyte (KOH) inside the electrochemical cell.

3.2.2.2. UV/Vis spectroscopy

To investigate the electrochromic effect of cobalt oxide, in-situ UV/Vis spectroscopy was performed. In a typical experiment, the sample was mounted into an electrochemical cell, which allowed light transmittance through the sample to be recorded behind the cell. A schematic illustration of the setup is given in Figure 3.8. The electrochemical cell consisted of the sample as working and a Pt-wire as counter electrode together with a Ag/AgCl reference electrode (Radiometer Analytical, $E_R = 0.204$ V vs. RHE) and 1 M KOH as electrolyte. A DH-2000-BAL deuterium and halogen lamp (Mikropack) was used as light source and a Maya 2000 PRO spectrometer (Oceanoptics) recorded the spectra behind the sample.

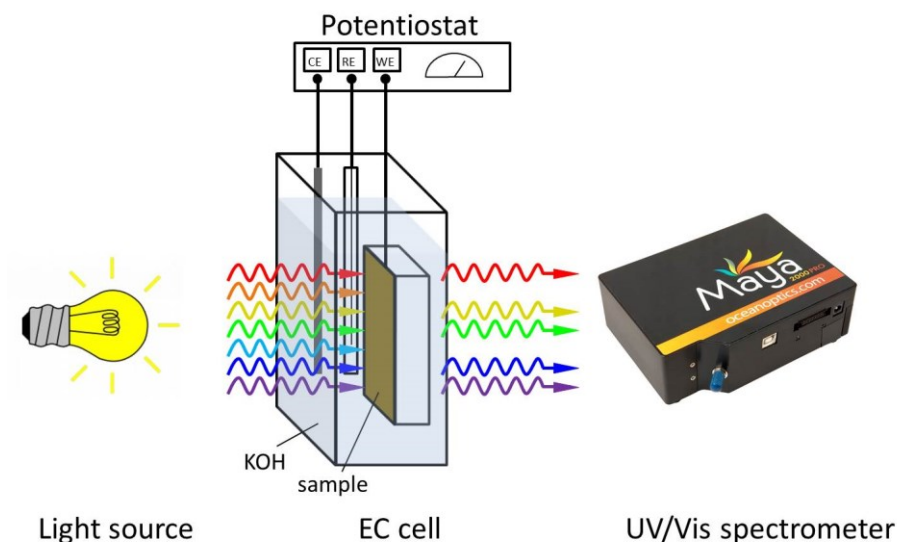


Figure 3.8: Schematic illustration of the in-situ UV/Vis spectroscopy measurement setup.

Only relative transmittance changes were studied during the experiments. Therefore, a reference transmittance spectrum was taken of the sample before any potential was applied. All following spectra were divided by the reference spectrum to find relative changes in light transmittance as a function of the applied potential (Versastat 3, Princeton Applied Research) and the wave length of the light. The transmitted light was integrated for 5, 0.5 and 60 seconds for CV, potentiostatic and relaxation measurements, respectively (see section 4.1.3.2).

3.2.3. Other methods

3.2.3.1. X-ray diffraction (XRD)

The crystallinity and crystal structure of some samples was measured using X-ray diffraction. The thin films were placed in the X-ray diffractometer and measured in grazing incidence mode with an incident radiation angle of 1° . The X-rays had the wave length of $\lambda = 1.5418 \text{ \AA}$ (Cu-K α radiation). The step size was set to 0.02° and the acquisition time was 10 seconds (manganese oxide samples) and 25 seconds (cobalt oxide samples) per step, respectively.

X-ray diffraction is based on Bragg's law:

$$n * \lambda = 2d * \sin\theta \quad (11)$$

where n is a positive integer, λ is the wave length of the incident radiation (\AA), d is the lattice plane distance (\AA) and θ is the angle of the incident radiation based on the considered lattice plane. Measuring under grazing incident conditions the position of X-ray beam has been kept constant and the energy dispersive detector has scanned the selected 2θ range. For those angles θ , where Bragg's law is fulfilled, a part of the radiation is diffracted and can be detected. In this geometry diffractograms of thin films can be recorded. A Bruker D8 Advance diffractometer equipped with a Sol-X detector has been used in this work. To analyze the taken diffractograms, reference files from the Joint Committee on Powder Diffraction Standards (JCPDS-NBS) have been used to identify the crystal structure of crystallized parts in the layers.

3.2.3.2. Scanning electron microscopy (SEM)

Scanning electron microscopy was applied to investigate the surface morphology and the thickness of the catalyst thin films. A LEO Gemini 1530 microscope was used for that purpose. The electrons were accelerated with 5 kV towards the sample and signals were recorded in the InLense detector mode. For cross section imaging the samples were cut, glued onto a sample holder with epoxy resin and polished until a thin and smooth cross section was achieved.

3.2.3.3. Transmission electron microscopy (TEM)

Transmission electron microscopy allows evaluation of thin films on an atomic scale. In this work cobalt oxide thin films have been examined with a CM 12 microscope (Philips). The system has a LaB₆-cathode as electron source and an acceleration voltage of 120 kV was used. For the investigations the samples were cut into small pieces, embedded into epoxy resin and again cut into disks of 0.5 mm thickness. Then, the samples are polished mechanically and in an ion beam until a film thickness of a few monolayers was obtained in order to allow electrons to pass through the thinned cross section.

4. Results and discussion

4.1. Cobalt Oxide

The main part of this work is devoted to the investigation of electrodeposited cobalt oxide thin films. Special attention is directed to the synthesis of samples avoiding elevated temperatures in the preparation route, in order to make them suitable for a potential application in a photoelectrochemical cell (PEC) consisting of a PV device directly connected to highly active and abundant electrocatalysts for the hydrogen (HER) and oxygen evolution reaction (OER), respectively. This is necessary, because thin film amorphous/microcrystalline silicon solar cells may not sustain annealing temperatures above 170°C. The work on such “artificial leaf” type structures is one focus of the activities in our research group^{20,124,125}.

In the first chapter the influence of different synthesis parameters like deposition potential, substrate material and annealing temperature, on the activity of the cobalt oxide thin films towards the OER is described. This is followed by a more detailed view onto the OER itself, considering, amongst others, stability, the influence of pH and the relation of surface area and catalyst volume towards the activity of the catalyst, respectively. In the last chapter spectroscopic methods such as in-line synchrotron radiation photoelectron spectroscopy and in-situ UV/Vis spectroscopy are applied to gain more insights into the working principles of the cobalt oxide thin films.

4.1.1. Influence of preparation parameters on the catalytic activity

In this chapter it is investigated how different parameters of the sample preparation process, e.g. deposition potential, precursor concentration and annealing temperature, influence the activity of the cobalt oxide catalysts towards the OER. The utilized anodic electrochemical deposition procedure⁸³ turned out to be a simple, reproducible and very robust method for synthesizing catalyst thin films on a conductive substrate. If not mentioned otherwise the samples were deposited at room temperature onto FTO/glass substrates at a potential of 1.4 V vs. RHE from a solution containing 12 mM CoCl₂, 12 mM Na-gluconate and 1 M KOH (standard parameters).

4.1.1.1. Deposition potential

The applied electrical potential is the driving force in the process of electrochemical deposition and therefore expected to have a major impact on the properties of the deposited films¹²⁶. To elucidate the effects of the deposition potential on the cobalt oxide thin films, magnitude and type of the applied potential were varied in a systematic way.

Film deposition at constant potentials

In a first step, constant deposition potentials in the range from 1.1 to 1.8 V (RHE) were impressed on FTO/glass substrates and the corresponding current density was recorded. As shown in Figure 4.1 the current density gradually increases with increasing potential, which was expected due to the higher energy input. The dark blue line at the bottom of the graph represents the current density at a potential of 1.1 V, which is located a little below the oxidation potential of the Co^{2+} ions under this conditions and consequently results in no current flow or film deposition, respectively. Starting from 1.5 V (yellow line) the differences in current density become larger and larger with increasing potential. For reasons of better illustration the line for 1.8 V, which is in the range of 7-8 mA/cm^2 , is not shown in the graph. This larger current increase is mostly attributed to oxygen evolution on the just formed catalyst, which becomes more important the higher the potential is. Another possible side reaction is the direct oxidation of the sodium gluconate complex to d-arabinose. But due to the high potential required for that reaction, this effect can be neglected^{116,127,128}. However, the current densities e.g. at 1.7 V do not achieve the same values as in the CV diagrams (see Figure 4.3), recorded in pure 1 M KOH after deposition. This might seem inconsistent at a first view, but can be explained by the fact that for the deposition processes no iR-correction was made. Owing to the relatively high absolute current flow during the deposition of a 2 cm^2 sample, already a small resistance value of $15\text{-}20^\circ\Omega$, coming from electrolyte and substrate, can diminish the applied potential at the electrode/electrolyte interface by a fairly large amount. Therefore, the given potential values have to be seen as “nominal” deposition potential, especially at values above 1.5 V. The small current peak in the first seconds of the deposition at 1.6 and 1.7 V is attributed to charging of the double layer capacitor of the substrate, which occurs very rapid at high potentials.

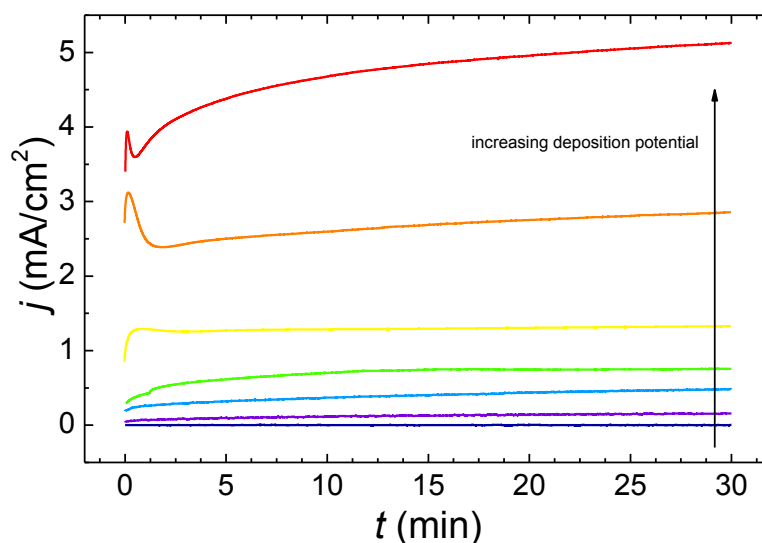


Figure 4.1: Deposition current density j as function of deposition time t at different applied deposition potentials from 1.1 V (dark blue, bottom curve) to 1.7 V vs. RHE (red, top curve) in steps of 0.1 V.

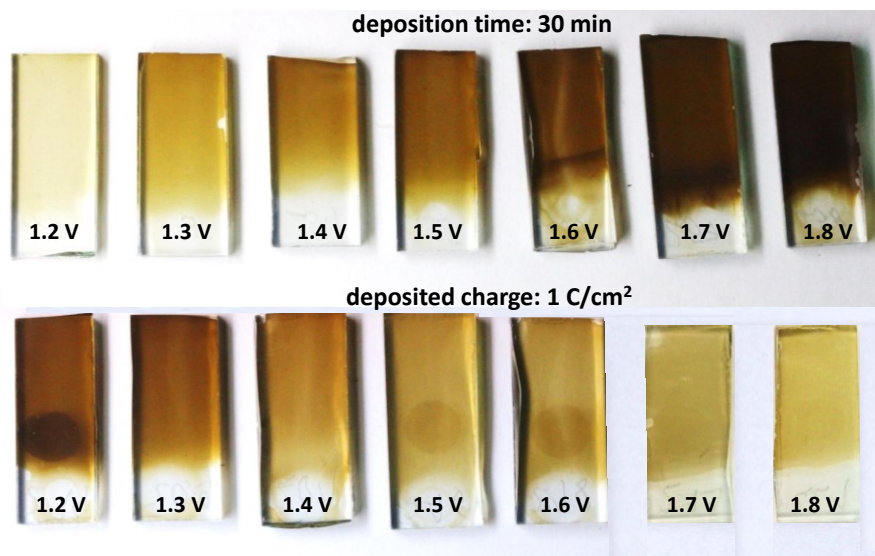


Figure 4.2: Photograph of samples deposited at different deposition potentials. Top row: samples were deposited for 30 minutes, bottom row: samples were deposited until a total charge of 1 C/cm^2 had been recorded.

Figure 4.2 shows a photograph of samples deposited at different potentials. The samples in the upper row have all been deposited for the same period (30 minutes), while the deposition of the samples at the bottom was stopped after a charge of 1 C/cm^2 has crossed the interface between substrate and electrolyte. The opposing trend of the two groups is striking. Samples deposited for 30 minutes become darker (and thus thicker) the higher the applied potential is; the deposition rate increases. On the other hand, the deposition efficiency decreases with increasing potential and is highest for 1.2 V (bottom row). This is again explained by competitive reactions, like the OER, which consume a higher fraction of the current flow the higher the nominal applied voltage is. Interestingly, no threshold is visible for the color changes, indicating that the OER is possibly not the only source of reduced film growth.

After the deposition, the samples were dried at room temperature in air and their activity towards the OER was evaluated using cyclic voltammetry. As depicted in Figure 4.3 the opposing trends of the two different groups of samples (see Figure 4.2) are also visible in the catalytic activity. If the deposition time is kept constant, a higher deposition potential leads to a lower OER overpotential (a), while at a constant deposition charge the sample with the lowest deposition potential has the best activity (b).

However, it is not entirely correct to speak of higher or lower activity when comparing the samples within the two groups. Activity describes the intrinsic ability of a material to catalyze a certain reaction, independent of any geometric factors. As can already be seen from the photograph in Figure 4.2 some samples are darker (thicker) than others. This is exactly reflected in the CV diagrams. Thicker samples have lower overpotentials at 10 mA/cm^2 than thinner ones. In the traditional view of (electro-) catalysis, it is not the thickness or the amount of catalyst, but

the surface area that is crucial for a low overpotential, if two samples of the same chemical composition are compared, as it is the surface where the catalytic reaction takes place. A closer look to the oxidation/reduction waves at around 1.5 V in Figure 4.3 shows that the current density increases as the samples become thicker. A higher current density at an oxidation/reduction wave is an indicator for higher surface area (i.e. porosity), because the oxidation/reduction of the catalyst happens at the interfaces with the electrolyte. A higher surface area brings more ions in direct contact to the electrolyte and allows them to be oxidized or reduced. The same is true for the OER. A larger surface area or increased porosity offers more catalytically active centers for the reaction to take place and consequently results in larger faradaic currents and lower overpotentials. Transferring that knowledge to Figure 4.3 the logical interpretation is that together with the thickness of the samples also the surface area (roughness) and/or porosity should increase and enable a better catalytic performance, while the intrinsic activity of the active centers (i.e. their turnover frequency) remains constant. In terms of overvoltage the effect is relatively small, but when the current density at a certain overpotential is compared between the samples, the difference can be as big as an order of magnitude.

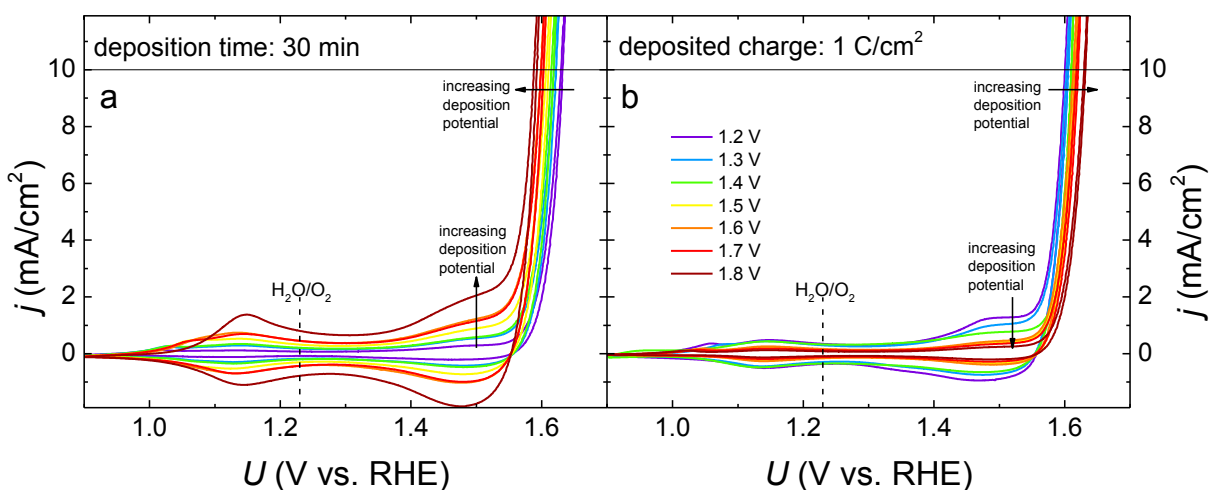


Figure 4.3: Cyclovoltammograms (CV diagrams) of cobalt oxide electrodes deposited at different deposition potentials for 30 minutes (a) and deposited until a charge of 1 C/cm² has passed the electrode (b), respectively. The diagrams show opposing trends for the activity of the two series of samples. Measurements were carried out in 1 M KOH (pH 14) at a scan rate of 10 mV/s.

In Figure 4.4 the overpotential at the current density of 10 mA/cm² is given as a function of the deposition potential. This current density is frequently used as benchmark for comparing the performance of catalysts towards the OER⁴⁷. Again the opposing trends of the two groups of samples are visible. As mentioned above the effect of the deposition potential on the OER overpotential is rather small. Compared to the literature, however, these values of around 370 to 380 mV are among the lowest known for cobalt oxides⁶⁹ and comparable to the most active OER catalysts based on abundant transition metals^{49,50} under alkaline conditions. From Figure 4.4 it

can also be seen that the samples with constant deposition charge (red) deviate less from the interpolated line than those deposited for 30 minutes (blue). This is attributed to the fact that the deposition of a constant charge is less dependent on experimental factors like the quality of the electrical contacts and the substrate, which can influence the deposition current density and thus the deposition rate significantly. Especially the FTO substrates turned out to deviate considerably in their conductive properties¹²⁹.

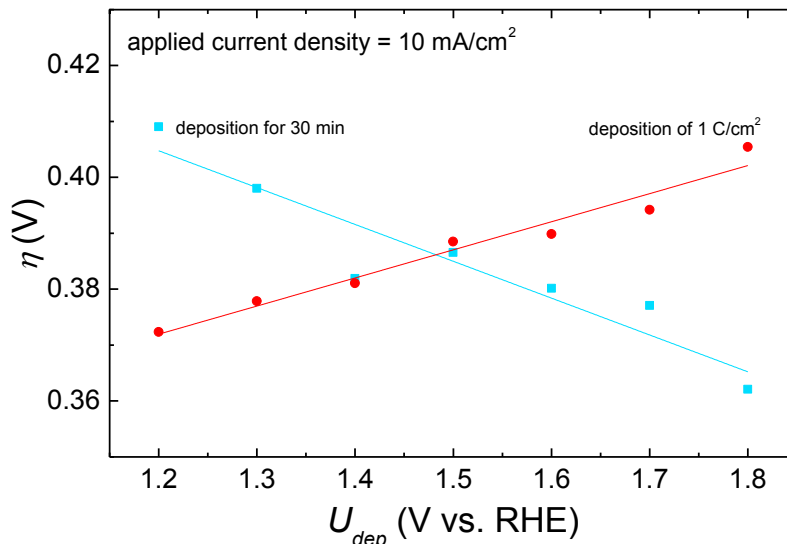


Figure 4.4: Overpotential η , recorded at the current density of 10 mA/cm² in 1 M KOH as function of the deposition potential U_{dep} for the two group of samples with constant deposition time of 30 min (blue) and constant deposition charge of 1 C/cm² (red), respectively.

Film deposition at cycled potentials

In addition to the deposition at a constant potential, some samples were prepared by cycling the potential in the range between 0.7 and 1.8 V (RHE). Figure 4.5a shows the cyclovoltammograms of every 10th deposition cycle. The growth of the film can be followed by the increasing capacitive current density in the range from 1.15 to 1.55 V. It is not possible to distinguish from this graph between the fractions of the current that contributes to the actual deposition of the cobalt oxide film, the capacitive current that is related to the cycling of the potential and the oxidation/reduction current belonging to redox processes in the film. However, after 100 cycles the samples have the same color than the ones deposited at a constant potential of 1.4 V. Therefore it is assumed that a similar amount of cobalt oxide was deposited.

This is confirmed by the CV diagram in Figure 4.5b. There is no significant difference between the samples deposited by potential cycling and the samples deposited at 1.4 V with a deposited charge of 1 C/cm². The differences in the current density between the CV diagrams during deposition (a) and for characterization (b) is explained by the different scan rate of 100 and 10 mV/s, respectively, and by the missing iR-compensation in (a).

Apparently, the influence of magnitude and type of applied potential is very limited, if the actual deposited charge is in the same range. Yet, it is easier to control the deposition at low constant potentials and therefore all further investigations were conducted on samples deposited at 1.4 and 1.2 V, respectively.

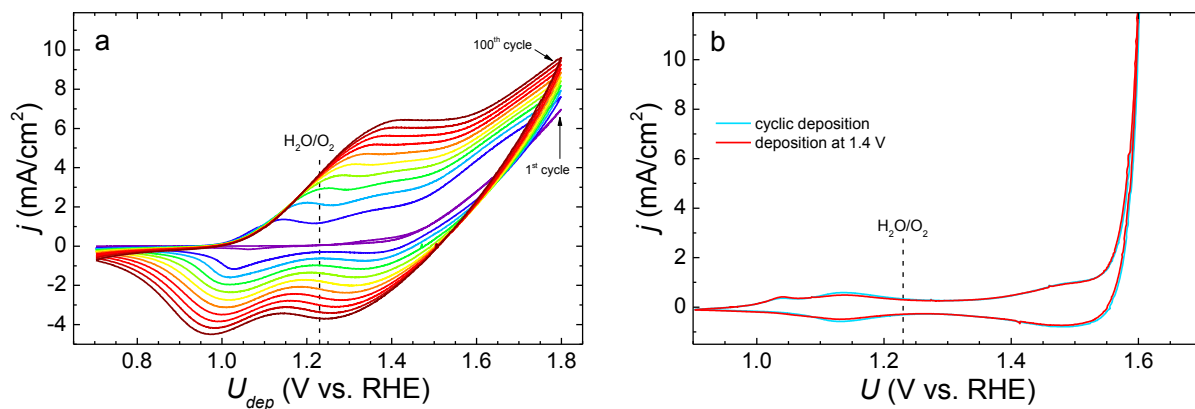


Figure 4.5: (a) Current density j vs. deposition potential U_{dep} recorded during the deposition of CoO_x on an FTO/glass substrate. The lines represent the 1st, 10th, 20th, 30th, 40th, 50th, 60th, 70th, 80th, 90th and 100th cycle at a scan rate of 100 mV/s. (b) CV diagram of a sample deposited with cyclic potential (blue) in comparison to a sample deposited at the potential of 1.4 V and a deposited charge of 1 C/cm². CV measurements in (b) have been corrected for the iR-drop and were carried out in 1 M KOH (pH 14) at a scan rate of 10 mV/s.

4.1.1.2. Composition of the deposition solution

In the next step it was investigated whether and how the composition of the deposition solution influences the synthesis and OER activity of the CoO_x films. Therefore, the concentration of Co^{2+} and OH^- ions was varied by at least one order of magnitude. Furthermore, the nature of the counter anion of Co^{2+} was changed by using different salts as cobalt source. All samples were deposited at 1.4 V (RHE) for 30 minutes or with a deposition charge of 1 C/cm², respectively.

Co^{2+} concentration

The concentration of Co^{2+} ions in the solution was varied by two orders of magnitude, from 1.2 mM to 120 mM. Of course, to prevent the precipitation of presumably Co(OH)_2 also the complexing agent Na-gluconate had to be adopted in the same way. In Figure 4.6a the deposition current density of the samples is illustrated. As expected, the current density for a 120 mM sample (blue) is much higher than for samples deposited from a 12 mM (green) and a 1.2 mM solution (red), but not directly proportional to the amount of Co^{2+} ions, which can be interpreted as a diffusion limitation of migrating Co^{2+} ions at higher concentrations. This is illustrated by the fact that the current increase from 1.2 to 12 mM Co^{2+} is roughly by a factor of 4 to 5, while from 12 to 120 mM Co^{2+} only a doubling of the current density is noticeable. The deposition of all samples was stopped after a deposition charge of 1 C/cm² has been achieved.

Subsequently, the OER activity was measured in 1 M KOH using cyclic voltammetry to evaluate any differences in the electrocatalytic behavior (Figure 4.6b). Besides some minor changes in extent and position of the first small oxidation wave at around 1.0 V (red line), no effect of the Co^{2+} concentration on the overpotential at the current density of 10 mA/cm² has been observed. It can be concluded that the amount of Co^{2+} ions in the deposition solution influences the growth velocity of the layer, but not the structure or morphology of the electrode films, since the OER performance remains unchanged in the current voltage plots.

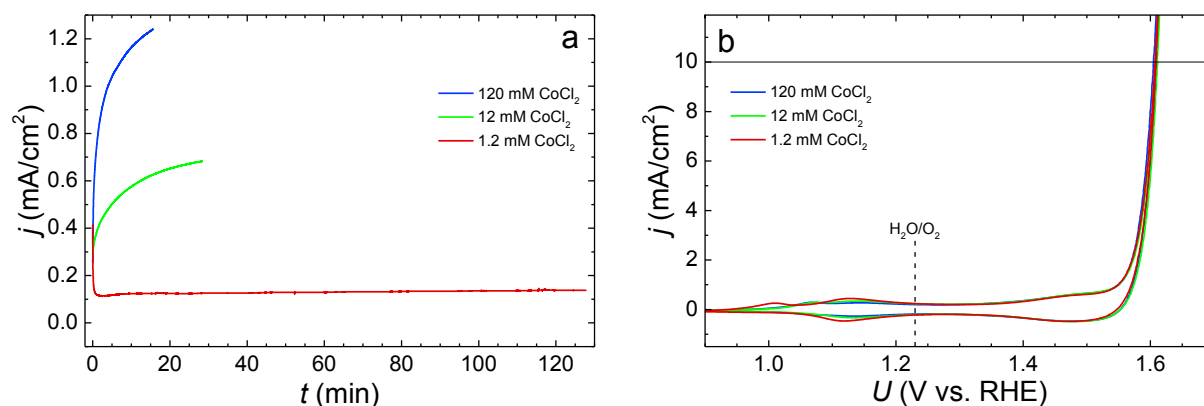


Figure 4.6: Deposition current density j vs. time t (a) and related cyclovoltammograms (b) of samples deposited from solutions containing different Co^{2+} concentrations. The deposited charge for all samples was 1 C/cm² at 1.4 V (RHE). CV measurements have been corrected for the iR-drop and were carried out in 1 M KOH (pH 14) at a scan rate of 10 mV/s.

Type of anion

To check whether the activity of the CoO_x catalyst can be influenced by the type of anion that accompanies the Co^{2+} cations in the deposition solution, several cobalt salts have been used to synthesize the samples. From Figure 4.7 it is evident that the type of anion plays no role in film formation. The minor differences in the deposition current density in the left figure (a) are attributed to experimental factors like small deviations in quality of the electric contacts and conductivity of the substrates, which influence setup resistance (iR) and current density, respectively. The CV diagrams in the right figure (b) show an almost perfect match of all curves throughout the whole investigated potential range and an entire independence of the used cobalt salt. This is not surprising, since it is expected that the D-gluconic acid sodium salt (Na-gluconate) forms a rather stable $\text{L}_2\text{Co}_2^{2-}$ complex, which isolates the Co^{2+} ions from contact with any other part of the deposition solution. Therefore, nature, size and charge of the anion should not influence the deposition process, as long as they are electrochemically inactive and don't decompose (competitive side reactions!) at the deposition potential, which is not the case with the tested cobalt salts.

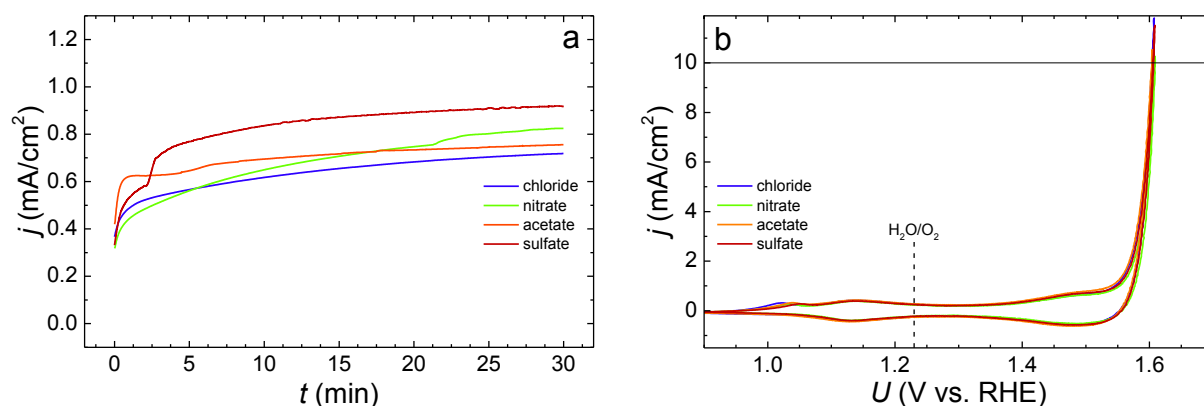


Figure 4.7: Deposition current density j over time t (a) and CV diagrams (b) of samples deposited from solutions containing different cobalt salts. The deposition time was 30 minutes at 1.4 V (RHE). CV measurements have been corrected with respect to the iR -drop and were carried out in 1 M KOH (pH 14) at a scan rate of 10 mV/s.

KOH concentration

Another parameter, which might have an influence on the properties of the catalyst thin film, is the concentration of KOH in the deposition solution. It has been reported that the loading of the substrate surface is heavily depending on the amount of base during the deposition⁸³. In fact, the deposition rate is coupled to the KOH concentration as can be seen in Figure 4.8a. This is ascribed to the increasing conductivity of the solution with higher KOH concentrations and thus a faster transport of Co^{2+} ions to the substrate. However, the overpotential at 10 mA/cm² (see Figure 4.8b) is not influenced by this, if the deposited charge is kept constant. Besides small deviations in the magnitude of the oxidation/reduction waves all the samples have a very similar current-voltage

behavior. Furthermore, also the film thickness is independent from the pH value and the conductivity of the electrolyte. As conclusion it can be stated again that only the speed of film formation is influenced by the KOH concentration in the deposition solution, not the properties of the film itself.

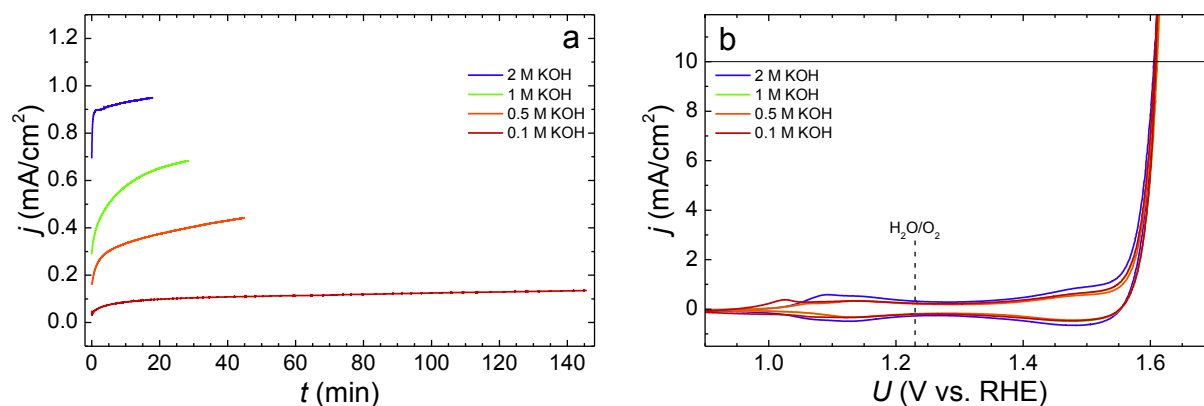


Figure 4.8: Deposition current density j over time t (a) and CV diagrams (b) of samples deposited from solutions containing different KOH concentrations. The deposited charge was 1 C/cm^2 at 1.4 V (RHE). CV measurements have been corrected with respect to the iR-drop and were carried out in 1 M KOH (pH 14) at a scan rate of 10 mV/s .

4.1.1.3. Substrate

The substrate, which carries the catalyst thin film, undoubtedly plays a crucial role for deposition, structure and catalytic activity of the material. This has been studied intensively in the past^{116,130,81}. To evaluate the influence of the substrate on the properties of the catalyst, CoO_x films have been deposited at 1.4 V (RHE) on FTO/glass, Au, Ti, Co and ITO/PET. The corresponding deposition current densities are summarized in Figure 4.9. To make sure that only the top side of the conductive metallic substrates is coated with catalyst, the back side was isolated from the deposition solution using adhesive tape. Obviously, the type of substrate influences the deposition rate and partly big differences in the deposition current density can be noticed. This cannot be explained by the missing iR correction for the deposition potential, because all metal electrodes have a very similar setup resistance (i.e. the resistance of substrate, electrolyte and electric contacts), which is given in Table 4.1. It is more likely that the different surfaces possess different adsorption energies for the $\text{Co}_2\text{L}_2^{2-}$ complex in the solution (see chapter 3.1) and facilitate (Au) or impede (Ni) adsorption and decomposition of the precursor complex at a given potential. From Table 4.1 it is also evident that the main part of the setup resistance of the CoO_x film deposited on FTO comes from the electrical resistance of the FTO film itself, because the electrolyte is the same for all substrates in the table and the values for the metals are much lower.

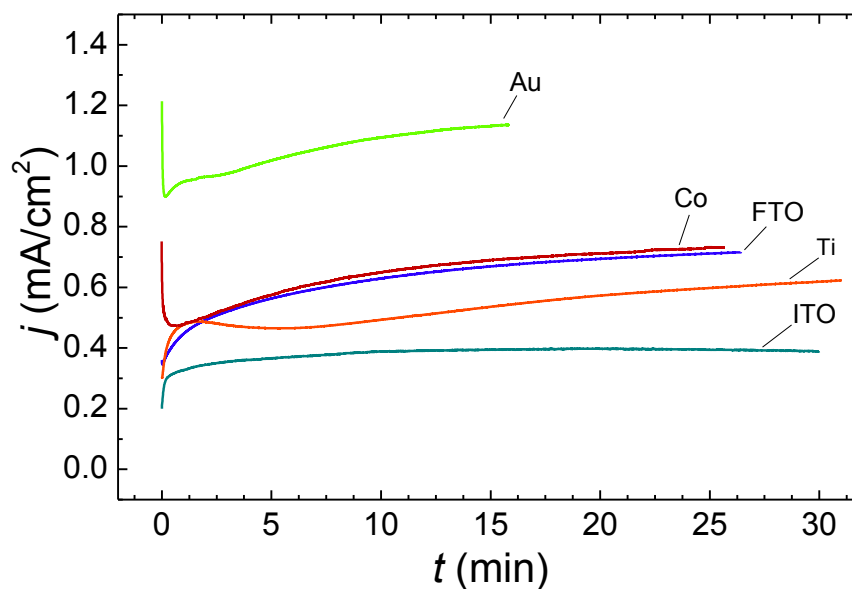


Figure 4.9: Current density j over time t during the deposition of CoO_x films on different substrates at a potential of 1.4 V (RHE) until a charge of 1 C/cm² has passed the electrode, except for the ITO sample, where a film was deposited for 30 min.

4. Results and discussion

Table 4.1: Setup resistance and capacitance for samples deposited on different substrates. The resistance values have been taken from the high frequency end of electrochemical impedance measurements at open circuit conditions and the capacitance was calculated from the capacitive current values at different scan rates at 1.27 V (RHE).

Substrate	Setup resistance (Ω)	Capacitance (mF/cm ²)
FTO	13.0	18.5
Au	3.5	100
Ti	3.2	n/a
Co	2.7	51

A photograph of CoO_x films deposited on different substrate materials is depicted in Figure 4.10. The large differences in the optical appearance of the films are obvious. First of all the color of the films varies from a bright brown to black. On the one hand this might be caused by the different color and transparency of the substrates, but on the other hand it could also be an evidence for structural and/or morphological differences between the samples. Secondly, it can also be seen that the thin cobalt oxide layer is not uniformly covering the substrate surface and parts of the substrate are still visible under the thin film. This is most evident for the Au-sample, where the typical golden color of the substrate is still visible. Thirdly, the homogeneity differs markedly between the FTO sample and the ones deposited on metallic substrates. While the former film is very uniformly covering the substrate with a rather clear border to the upper, blank part, the films on the metallic substrates are quite inhomogeneous. The sample deposited on an ITO coated flexible PET foil is not shown in the picture, because the CoO_x film would indeed form but not adhere tightly enough to the ITO to sustain any electrochemical measurement and just peel off. This might be one of the reasons for the very low current density observed during its deposition. It has to be stated that ITO/PET substrates are not suited for this kind of CoO_x deposition. Electrochemical deposition of cobalt oxide films on ITO have been shown to work out under different experimental conditions^{84,87}.

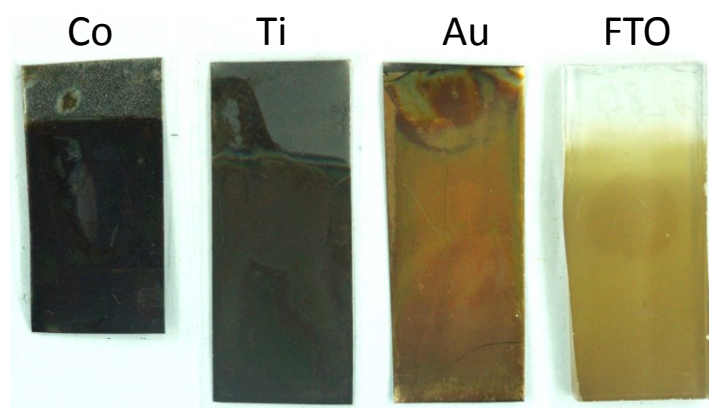


Figure 4.10: Photograph of CoO_x films deposited on different substrates.

Figure 4.11 shows SEM images of the CoO_x films deposited on FTO, Au, Ti and Co. As was already suspected considering the different deposition rates in Figure 4.10 the appearance of the films varies strongly. The only property all samples have in common is that the substrate is not fully covered by a dense cobalt oxide film and partly large areas of the support remain blank. Greatest similarity can be seen between the FTO- and the Au-sample. Both consist of more or less isolated islands of CoO_x , which appear to have a rough surface area, even more pronounced for the Au-sample. It is supposed that the formation of the islets is caused by “shrinking cracks” during the drying process of the samples after deposition. This is a common phenomenon often described in literature^{84,131,132}. The substrate is well visible in both cases between the film patches and differs strongly in its structure. The FTO substrate is easily identifiable by its typical granular shape of SnO_2 crystallites, with a grain size in the range of about 100 nm. The gold support in the upper right SEM image in Figure 4.11 (bright areas) on the other hand has particle sizes, which are smaller than for FTO. The appearance of the CoO_x patches, however, seems to be similar.

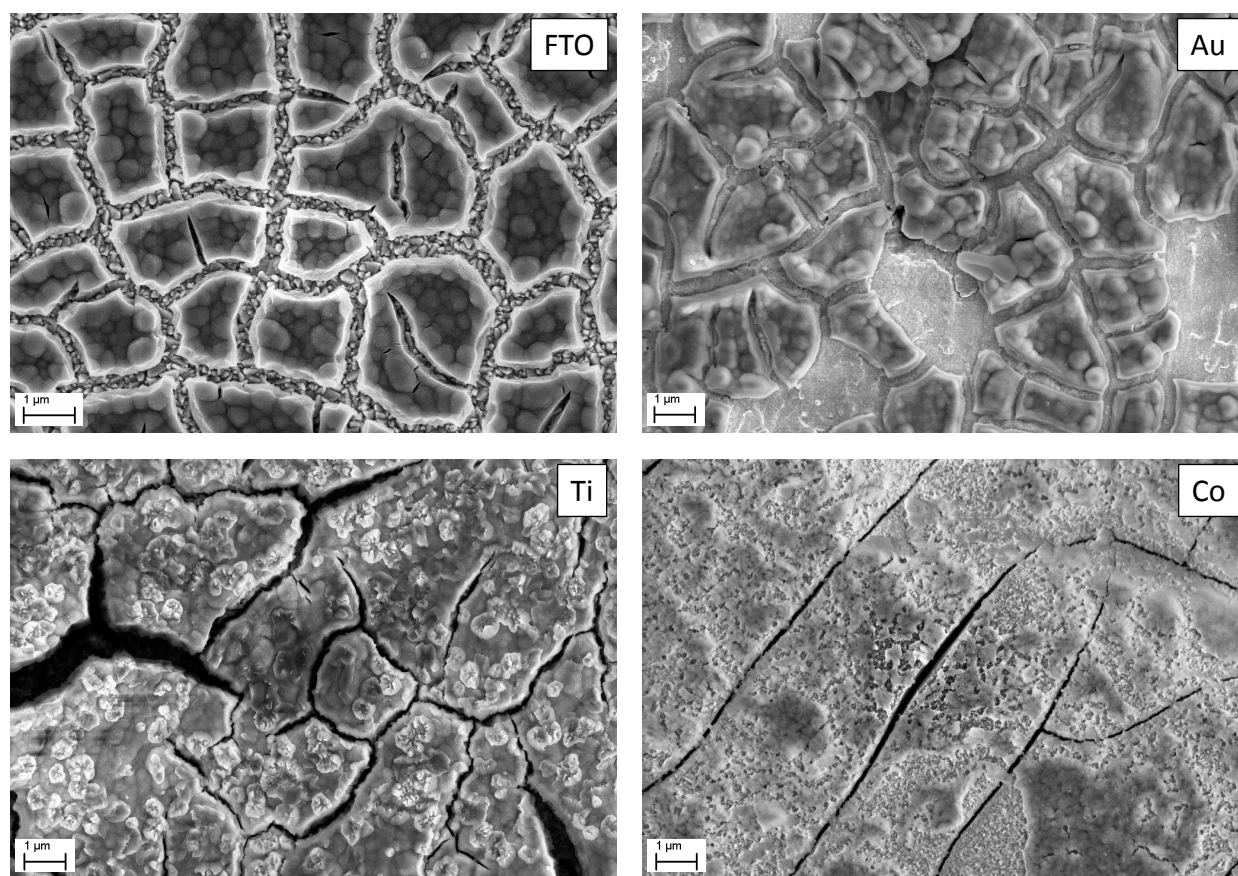


Figure 4.11: SEM images of CoO_x films on different substrates. Top left: Isolated CoO_x patches with high surface area on a FTO support, which is visible in between the islands. Top right: CoO_x on Au forming similar structures as on FTO. The bright areas show the blank substrate. Bottom left: CoO_x on a Ti-substrate does not form films, but rose-like structures. Bottom right: Loose and not uniformly covering network of CoO_x on a Co substrate.

A CoO_x film deposited on a Ti support, however, formed a more or less continuous film, but with large cracks as the SEM image on the bottom left side of Figure 4.11 shows. In addition, randomly distributed bud-like structures with dimensions in the order of around 100 to 300 nm are formed on top of the cracked film. The conductivity of these structures is low, which can be recognized by them appearing blurred in the SEM image. This way of film formation seems not to be optimal, because the catalytic activity of the Ti-sample is very low compared to the films on the other substrates, as the results of the electrochemical analysis show.

The film deposited on a Co substrate consists, in contrast to the Au- and FTO-sample, of a loosely connected network of porous CoO_x film with elongated cracks in between. The morphology of the film is quite different compared to the other samples and the features of the film, like pores and islets, are smaller. The reason for this different appearance might be caused by the fact that cobalt metal is not inert under the applied experimental conditions and reacts with the forming film and/or oxidizes, influencing the structure and growth of the deposited film. The substrate itself is characterized by a microroughness comparable to the Au substrate as can be seen on the brighter areas in between the cobalt oxide network.

The evaluation of the catalytic performance towards the OER can exemplarily be seen in Figure 4.12. To exclude that a higher or lower activity has its origin in just a higher or lower amount of catalyst on the substrate, the deposition of all samples was stopped after a charge of 1 C/cm^2 has passed the electrode/electrolyte interface. In that order, the effect of the varying deposition rates was eliminated regarding the activity of the samples. At first view, the big qualitative difference between the current-voltage behavior of the Ti-sample and the others is striking. The very low catalytic activity of this sample has to be referred to the formation of insulating oxides¹¹⁶. In fact, CoO is known for being insulating and inhibiting the catalytic activity⁵⁸ and Ti passivates very easily to TiO_2 at the surface⁵⁴, which could be responsible for a bad charge carrier transfer from the catalyst to the substrate.

In contrast to that, the cobalt oxide films deposited on FTO, Au and Co show a similar high activity towards the OER with overpotentials of 380 mV and below at 10 mA/cm^2 . Also the shape of the curves is similar to one another with two oxidation/reduction features at around 1.1 to 1.15 V (RHE) and 1.5 V, respectively. This is surprising because especially the film on the Co substrate has a different morphology compared to films grown on FTO and Au (see Figure 4.11). In conclusion, this signalizes that the morphology of the catalyst film plays a minor role for the overall activity and that material composition, crystallinity and intrinsic activity are very similar for the CoO_x films deposited on Co, Au and FTO substrates, despite their different morphology. Still, there are some differences between the samples regarding the capacitive currents in the lower potential range before the onset of the OER. The Co- and especially the Au-sample have higher capacitive current densities between 1.0 and 1.5 V, which is an indication for a higher surface roughness of the films. A closer look to the black lines in the diagrams shows that also for the blank substrates a higher capacitive current can be observed for the metals. This is consistent

with the higher surface area for the metal substrates found in the SEM pictures in Figure 4.11. It is reasonable to assume that the higher microroughness of the metal substrates Au and Co leads to a film growth, which results in higher active surface areas and consequently slightly lower overpotentials for the deposited CoO_x films.

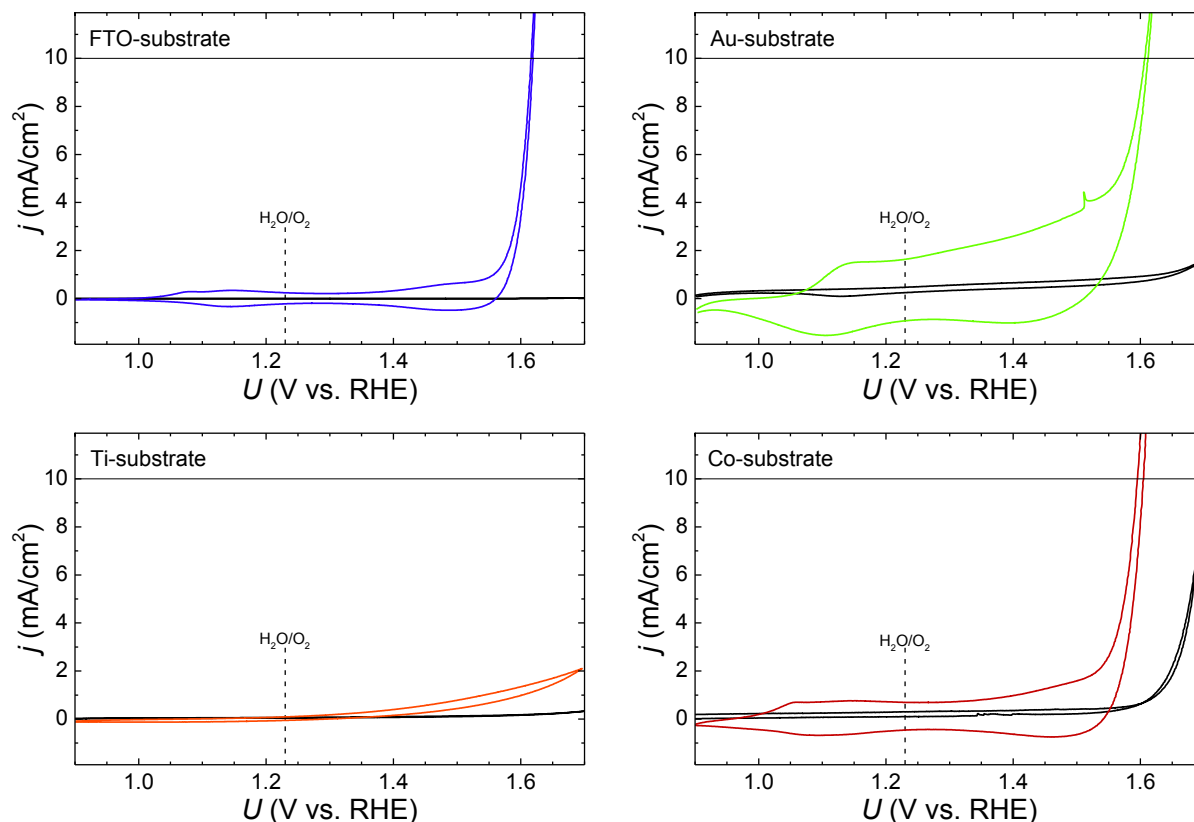


Figure 4.12: CV diagrams of CoO_x films deposited on different substrates at 1.4 V (RHE) until the charge of 1 C/cm² has passed the electrochemical cell. The CVs of the corresponding blank substrates are given by black line scans. CV measurements have been corrected for the iR-drop and were carried out in 1 M KOH (pH 14) at a scan rate of 10 mV/s.

As explained in more detail in Chapter 4.1.2.3, it is not trivial to find a suited potential range for determining the double layer capacitance of the CoO_x films from the slope of the plotted current density versus the scan rate of the voltammograms. Nevertheless, in Figure 4.13a it has been exemplarily tried to compare the capacitance of an FTO-, Au- and Co-sample at 1.27 V, a potential that lies in between the two oxidation features. The double layer capacitance is then given by the arithmetic mean of the anodic (positive) and cathodic (negative) branch of the diagram. The values summarized in Table 4.1 may not be suited to calculate the absolute surface area of the films⁴⁷ and to compare them to literature values, but it should be possible to use them for an „internal“ evaluation since the only difference between the sample is the substrate material. As obvious from Figure 4.13a, the Au-sample has by far the highest double layer capacitance. But the linear fit of the anodic current densities has a quite strong deviation from ideality ($R^2 = 0.979$),

while all the other interpolations are acceptable. To explain this, it has to be considered that the Au substrates consisted of a 150 nm Au film, which was vacuum-deposited on a Ti sheet. Before the electrodeposition of the CoO_x film, the Au substrates were not cleaned in an ultrasonic bath to prevent the Au film from peeling off. Therefore, it is possible that the oxidation of residual organic contaminations on the surface of the uncoated parts of the Au substrates influence the current response during the anodic CV scan. This effect becomes weaker the more often the sample is cycled and as can be seen from the top green line, the points at 5, 10 and 20 mV/s, which were recorded first, are slightly higher than the interpolation while the value at 100 mV/s, which was the last one to be recorded, is located slightly below. This is taken as evidence for the gradual decomposition of organic contaminations during the CVs. Even though this might lead to a systematic error in the measurements, the effect of the error is considered to be relatively small and the deviated values for the capacitance reasonable.

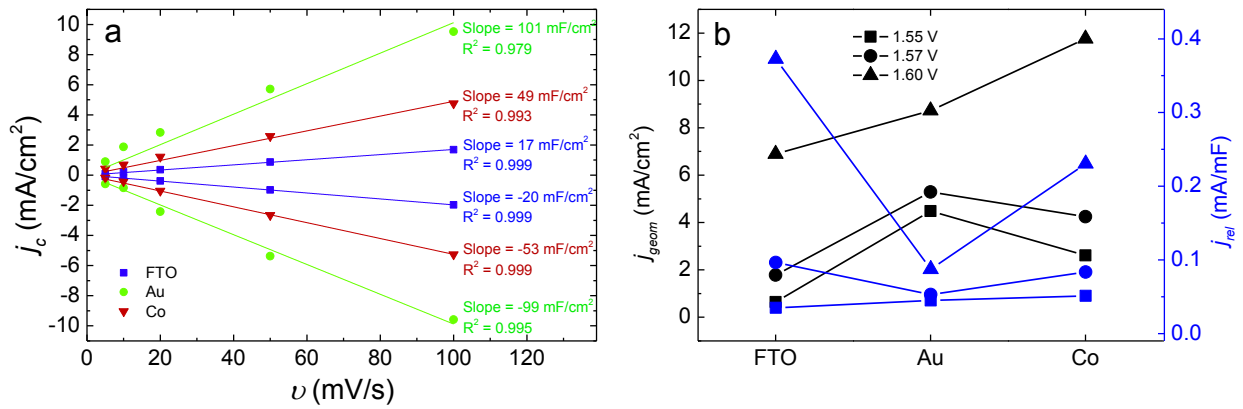


Figure 4.13: (a) Capacitive current density j_c vs. scan rate v for CoO_x on FTO, Au and Co recorded at 1.27 V (RHE) to determine the double layer capacitance of the samples. (b) Geometric current density j_{geom} (black) at 1.55 V (squares), 1.57 V (circles) and 1.60 V (triangles) in comparison with the relative current density j_{rel} (blue), which has been normalized for the double layer capacitance.

In Figure 4.13b the apparent geometric current density j_{geom} of the samples at 1.55 V, 1.57 V and 1.60 V is compared with a relative current density j_{rel} , which was calculated by dividing the geometric current density by the capacitance of the sample. This is based on the assumption that the calculated double layer capacitance is directly proportional to the active surface area in contact with the electrolyte and that the samples show no significant qualitative differences in their capacitive behavior throughout the investigated potential range. By no means, one can expect this approach to be an absolute method to compare catalysts, since it is limited to samples of equal composition. But a qualitative comparison of the actual intrinsic activity of the CoO_x films in dependence of the substrate should be possible.

A clear trend is noticeable in the diagram regarding the activity of the samples. At potentials below the onset of the OER (1.55 V) the j_{rel} of all three substrate types is constant (blue squares), which was expected since no significant faradaic current contributes to the overall current

density. However, if the potential rises above the onset of the OER (1.60 V, blue triangles), j_{rel} of the FTO-sample increases dramatically compared to the Au- and the Co-sample, while the j_{geom} (black lines) is the lowest one. This is interpreted in that way that CoO_x on FTO catalyzes the OER much more efficiently per unit surface area than the same film on Co and especially on Au, which shows almost no increase in the relative current density despite the higher applied potential. In contrast to reports on the benefit of Au as substrate¹³⁰ and as incorporated nanoparticles¹³³ for the intrinsic activity of cobalt oxide towards the OER, no such effect of the Au support could be observed here. It has to be stated though that the investigated films in this work were much thicker compared to the layers from the literature, which possibly superimposes any benefits from the strong electronegativity of Au. Furthermore, factors like bubble formation and/or detachment as well as diffusion limitations and surface accessibility are not considered in this experiments, but they can be seen as inherent film characteristics, which are hard to control in the deposition process as the results of the former chapters showed.

In conclusion it can be stated that the type of substrate indeed has a strong influence on deposition rate, morphology and catalytic activity of CoO_x electrocatalysts. FTO/glass as substrate has been identified as the most reliable support, because the CoO_x films are formed in a very homogeneous, stable and reproducible way and due to the transparency of the substrate a first simple optical quality check is possible. Also, the CV characteristics are reasonably good in absolute values and the very best of all substrates, when the double layer capacitance is taken into account to calculate the relative current density per unit surface area. Cobalt oxide films deposited on Co and Au substrates show similar good catalytic activities but have drawbacks in film quality (homogeneity) and electrochemical reproducibility. Furthermore, the metallic substrates, most of all Co, tend to participate in the electrocatalytic reactions, which is not acceptable for any investigations on the actual cobalt oxide catalyst. Ti would be a very convenient substrate for the application of cobalt oxide as OER catalyst in a photoelectrochemical device²⁰, but the electrochemical results in this chapter show that film growth and electrocatalytic activity are very poor on Ti as substrate. Therefore, all further investigations were conducted on FTO/glass substrates.

4.1.1.4. Temperature

A further important parameter for the synthesis of CoO_x electrocatalysts is the annealing temperature after electrodeposition. So far, all samples in this work have been characterized without any heat treatment. To investigate the influence of elevated temperatures on crystallinity, morphology and catalytic activity of CoO_x towards the OER, a series of samples was deposited from the standard deposition solution (see chapter 3.1) onto FTO/glass substrates at 1.4 V (RHE) for 30 minutes. After the deposition the samples were annealed for 1 h in air at temperatures between 100 and 450°C and were then characterized using XRD, SEM and electrochemical methods.

Figure 4.14 shows typical X-ray diffractograms of a set of CoO_x films after annealing at different temperatures and a blank FTO/glass substrate as reference (bottom line). Obviously, all the films are very thin and/or not fully covering the FTO substrate, since the reflexes from the substrate are the most prominent ones¹¹². Besides the FTO signals no further features can be observed in the diffractograms of the samples annealed at temperatures below 300°C. Even measurements under grating incidence conditions with an incident radiation angle of 1° and a very long acquisition time of 25 s per step could not resolve any signals related to the CoO_x films. These samples are therefore considered to be amorphous.

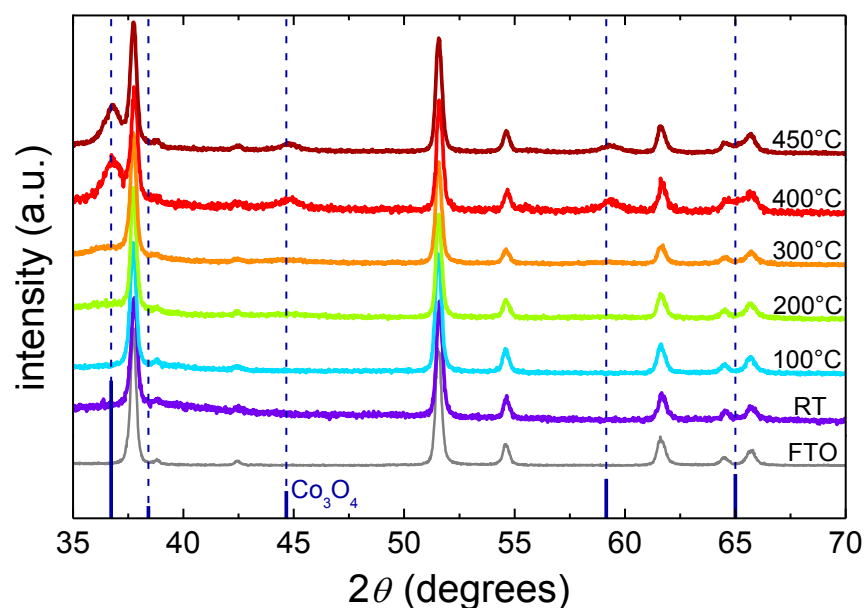


Figure 4.14: X-ray diffractograms of electrodeposited cobalt oxide films after annealing at different temperatures. The spinel type Co_3O_4 phase appears at annealing temperatures of 300°C and higher. At 450°C no further change in the diffractogram can be observed and the crystallization process is considered to be completed.

At the annealing temperature of 300°C (orange line) additional diffraction lines appear, albeit very weak and broad in shape. They become more pronounced at 400°C. These features correspond

to the 311 (36.73°), 222 (38.42°), 400 (44.66°), 511 (59.15°) and 440 (65.00°) lines of the Co_3O_4 spinel structure (JCPDS file # 80-1542). Between the diffractograms at 400°C and at 450°C no further changes can be observed. It is concluded that the amorphous structure of the as-deposited samples is transferred into the crystalline Co_3O_4 spinel phase at temperatures above 300°C. The crystallization process is completed at 400°C. From the full width at half maximum a mean particle size of the films in the range of 5 nm can be calculated using the Scherrer equation.

The photograph in Figure 4.15 shows some samples after annealing at different temperatures. Interestingly, already a temperature of 200°C the color of the CoO_x film changes markedly from bright brown to dark brown. The darkening continues with increasing temperatures until an almost completely black film is formed at 450°C. This finding is somehow contradictory to the XRD results above and suggests that already at temperatures below 300°C morphological and/or changes in the crystallinity take place. From the yellowish brown color of the layer deposited at room temperature and annealed at 100°C it can be concluded that the oxide films should have semiconducting properties. The color change can then be explained by a structural change or by introduction of color centers in the process of heat treatment. The increasing concentrations of these centers could be associated with an increasing number of states in the band gap leading to a more and more metallic character of the film. However, as shown later, the conductivity of the films decrease (see Figure 4.17) after heat treatment. Therefore, the observed color change is a hint for a fundamental change of the electronic structure oxidizing the amorphous CoO_x film to Co_3O_4 .

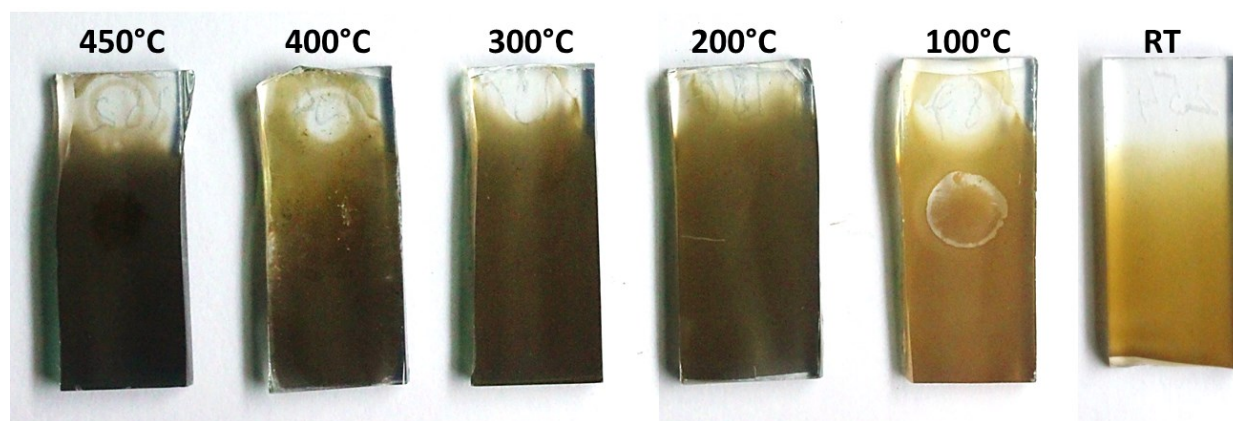


Figure 4.15: Photograph of CoO_x films annealed at different temperatures.

The typical current-voltage behavior of the same samples is exemplarily illustrated in Figure 4.16. In this diagram, only the potential range below the onset of the OER is shown and particular attention should be turned to the oxidation/reduction waves, which are marked with Roman numerals. Samples, which were annealed at maximum 100°C (violet and blue lines) have three oxidation waves at around 1.02 V (I_a), 1.15 V (II_a) and 1.50 V (III_a), but only two corresponding reduction features at around 1.13 (II_c) and 1.50 V (III_c), respectively. The redox pairs II and III

have been assigned in the literature to the transitions from $\text{Co}^{2+} \leftrightarrow \text{Co}^{3+}$ and from $\text{Co}^{3+} \leftrightarrow \text{Co}^{4+}$, respectively^{112,83,116,81,134,135,80}. The third oxidation wave at 1.5 V appears shortly before the onset of the OER and can therefore be considered as an activation step of the catalyst^{79,112}. Furthermore, the oxygen evolution reaction is expected to occur on a fully oxidized Co^{4+} surface¹³⁶. It is not trivial to identify the species involved in the redox processes because many different cobalt oxides may appear in the anodic potential range and have to be considered, such as CoO , $\text{Co}(\text{OH})_2$, Co_3O_4 , Co_2O_3 , CoOOH and CoO_2 . A set of possible redox reaction equations is summarized in Table 4.2. Some of the depicted reactions have their electrode equilibrium potentials below the investigated potential range (No. 1-4), but still several redox couples have to be taken into account and match the observed redox features in the CV diagram very well. Especially the reactions No. 6 and No. 9 have been considered often in the literature^{74,83,116,81,134,136}. The high number of possible reactions shows the complexity of the cobalt oxide/hydroxide system under anodic potential conditions in the alkaline regime.

Table 4.2: Redox couples, half-cell reactions and corresponding electrode equilibrium potentials of cobalt oxide/hydroxide under anodic potential conditions in alkaline solution. Data have been derived from Ref ⁵⁸.

No.	Redox couple	Half-cell reaction	Electrode potential (V vs. RHE)
1	CoO/Co₃O₄	$3 \text{ CoO} + 2 \text{ OH}^- \rightarrow \text{Co}_3\text{O}_4 + \text{H}_2\text{O} + 2 \text{ e}^-$	0.555
2	Co(OH)₂/Co₃O₄	$3 \text{ Co(OH)}_2 + 2 \text{ OH}^- \rightarrow \text{Co}_3\text{O}_4 + 4 \text{ H}_2\text{O} + 2 \text{ e}^-$	0.732
3	CoO/CoOOH	$\text{CoO} + \text{OH}^- \rightarrow \text{CoOOH} + \text{e}^-$	0.752
4	Co(OH)₂/CoOOH	$\text{Co(OH)}_2 + \text{OH}^- \rightarrow \text{CoOOH} + \text{H}_2\text{O} + \text{e}^-$	0.870
5	CoO/CoO₂	$\text{CoO} + 2 \text{ OH}^- \rightarrow \text{CoO}_2 + \text{H}_2\text{O} + 2 \text{ e}^-$	1.119
6	Co₃O₄/CoOOH	$\text{Co}_3\text{O}_4 + \text{OH}^- + \text{H}_2\text{O} \rightarrow 3 \text{ CoOOH} + \text{e}^-$	1.146
7	Co(OH)₂/CoO₂	$\text{Co(OH)}_2 + 2 \text{ OH}^- \rightarrow \text{CoO}_2 + 2 \text{ H}_2\text{O} + 2 \text{ e}^-$	1.178
8	Co₃O₄/CoO₂	$\text{Co}_3\text{O}_4 + 4 \text{ OH}^- \rightarrow 3 \text{ CoO}_2 + 2 \text{ H}_2\text{O} + 4 \text{ e}^-$	1.401
9	CoOOH/CoO₂	$\text{CoOOH} + \text{OH}^- \rightarrow \text{CoO}_2 + \text{H}_2\text{O} + \text{e}^-$	1.486

The oxidation wave I_a has also been observed previously and was assigned to take part in the $\text{Co}^{2+} \leftrightarrow \text{Co}^{3+}$ transition^{135,137}, but a few reports also speculate about the origin of this feature to be the oxidation of adsorbed hydroxyl ions^{82,138}. However, it is remarkable that this wave is apparently expression of an irreversible process.

The third oxidation feature (III_a) at around 1.5 V appears as a broad and weak one in the case of the as-deposited sample and the sample heated at 100°C. This can be interpreted as an overlap

of the oxidation process with the faradaic current of the starting OER and is most likely related to the amorphous nature of the samples, characterized by energetically similar but not identical metal oxygen bonding states¹¹². When the samples are subjected to a temperature treatment at 200°C and above a significant change in the current-voltage behavior can be observed. The oxidation/reduction features I_a, II_a and II_c vanish completely. Instead, the waves at 1.5 V become more pronounced and sharper, which is attributed to the well-defined structure of the now crystalline thin film. Such a shape has been described in the past as fingerprint for the Co spinel Co₃O₄, but was so far only observed after annealing at temperatures higher than 300°C^{74,136}. Interestingly, the cathodic peak III_c shows a shoulder at lower potentials, which has been assigned to a splitting of the cathodic process¹³⁶ related to the reduction of Co⁴⁺ to Co³⁺. It has also been suggested that upon the formation of crystalline Co₃O₄ the Co²⁺ ions, located in the tetrahedral sites of the crystal, are less accessible for oxidation¹³⁹, which could be the reason for the vanishing of the redox features I and II.

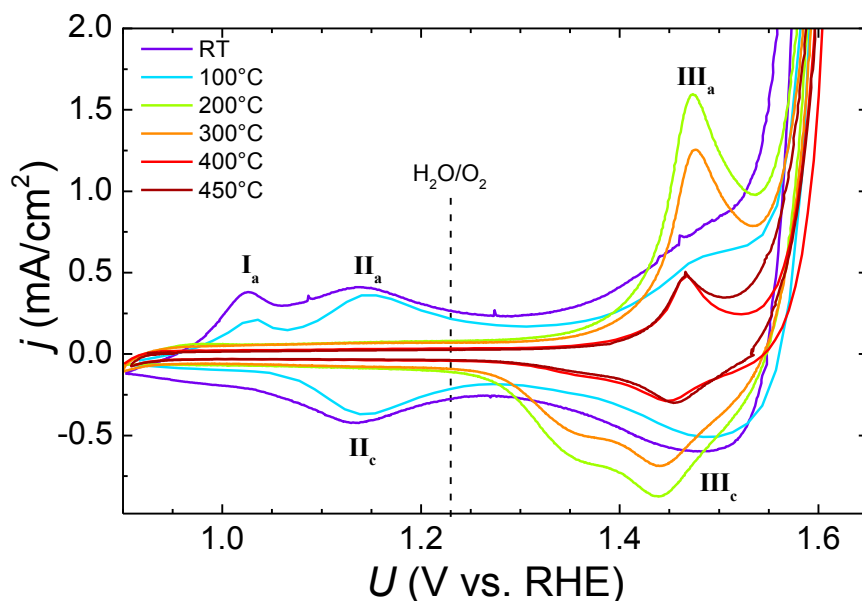


Figure 4.16: Current-voltage curves of different electrodes in the potential range from 0.9 to 1.65 V as a function of annealing temperature. The anodic waves I_a and II_a and the cathodic feature II_c disappear after annealing at 200°C and higher, while the redox pair III_a and III_c becomes sharper with increasing annealing temperature. The measurements have been corrected for the iR-drop and were carried out in 1 M KOH (pH 14) at a scan rate of 10 mV/s.

From the cyclic voltammogram it can also be assumed that the surface area of the films decreases with increasing temperature due to sintering effects and crystal growth¹³⁶. This becomes obvious by considering the shrinking oxidation wave at 1.5 V, which is a measure for the amount of Co ions that are oxidized. Also in this diagram there is no noticeable difference between the sample annealed at 400°C and that annealed at 450°C, which confirms the completed transformation process at 400°C.

A further evidence for the decrease in surface area can be seen in the SEM images in Figure 4.17. It can be deduced that the surface area of an as-deposited sample (left SEM image) is larger compared to a sample annealed at 450°C (right SEM image). The shrinking cracks, which are already characteristic for the as-deposited film, become much more pronounced after the heat treatment and large gaps in between the film patches reduce the overall available sample surface. Furthermore, also the conductive properties of the islets appear to have changed, because at the edges of the structures on the annealed film broad bright areas are visible, which result from sample charging effects indicating worse electrical conductivity in these zones.

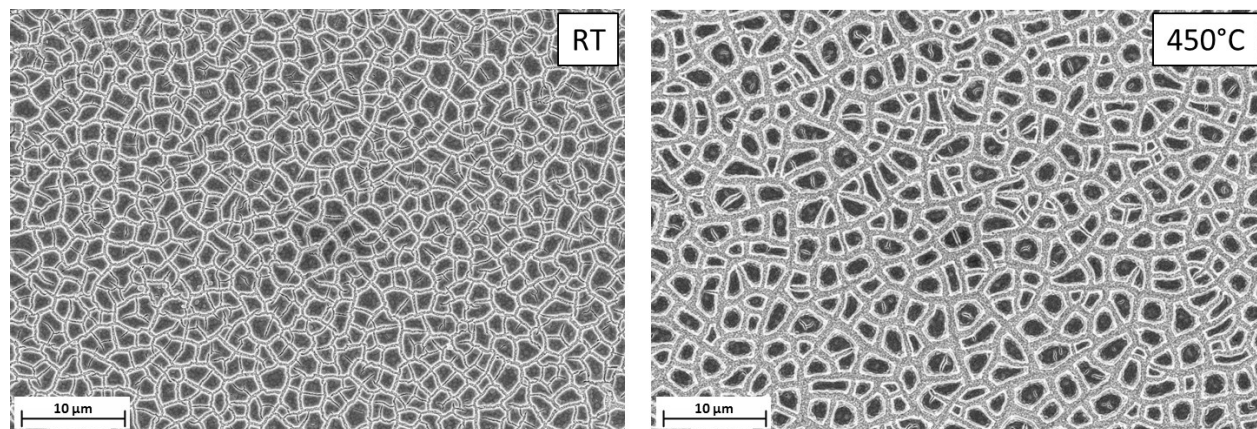


Figure 4.17: SEM images of electrodes dried at room temperature (left) and after annealing at 450°C (right).

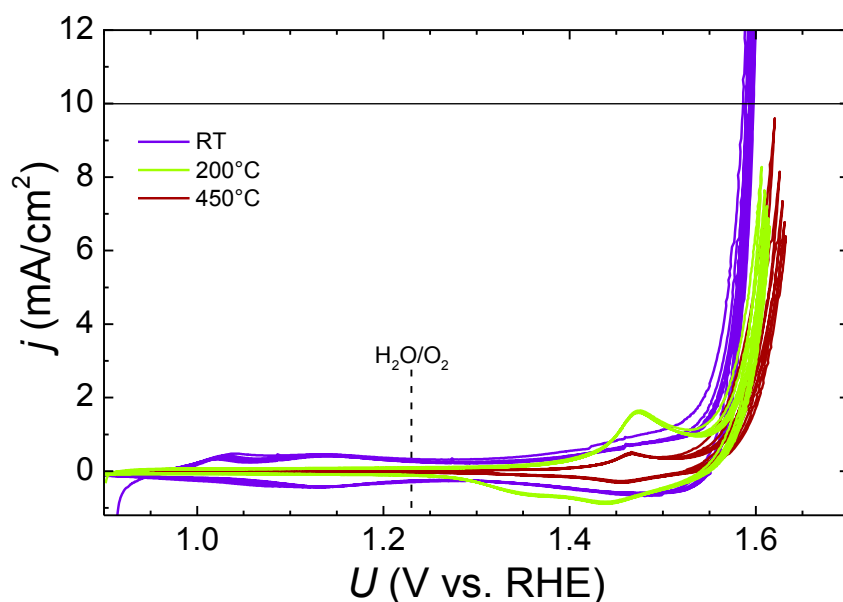


Figure 4.18: CV diagrams of cobalt oxide films annealed at different temperatures. OER activity decreases with increasing temperature accompanied by an increasing current loss from cycle to cycle. The measurements have been corrected for the iR-drop and were carried out in 1 M KOH (pH 14) at a scan rate of 10 mV/s.

The most important property of a catalyst in a photoelectrochemical device, however, is the overpotential necessary to reach a certain absolute current density, usually 10 mA/cm^2 . In Figure 4.18, therefore, CV diagrams of samples annealed at different temperatures are depicted in a larger current density range. A clear trend can be observed, namely that the overpotential increases with increasing annealing temperature. This might partly be related to the loss in catalyst surface area, but still represents a significant drawback of an annealing step at elevated temperatures, when absolute numbers are considered. Furthermore, the current density of 10 mA/cm^2 shifts to higher voltages with every cycle investigating annealed electrodes, which can be seen as a sign of bad stability of the catalytic film under electrochemical measurement conditions.

To prove, whether the annealed samples are indeed less stable than the not annealed ones, galvanostatic measurements have been performed at 10 mA/cm^2 in addition to the CV investigations. The results are depicted in Figure 4.19. In contrast to the CV measurements, this time the samples were immersed completely into the KOH electrolyte and rotated about the axis parallel to the thin film plane. Under these conditions the electrolyte was flowing continuously over the sample surface and a permanent supply of fresh reaction educts (namely OH^- ions) was guaranteed. Furthermore, gas bubbles formed at the catalyst surface could be removed quickly and inactivation of the surface area by stuck gas bubbles was prevented. The disadvantage of this setup is the large current flow between the working (i.e. the sample) and the counter electrode (i.e. a Pt-wire) due to the high sample area of 2 cm^2 taking part in the reaction. The ohmic losses of the setup are in the same range as for the CV measurements under stationary electrochemical conditions (see section 3.2.1.1), but the potential difference ΔU , which has to be corrected for, increases dramatically with increasing absolute current (i.e. 20 mA) during the experiment according to equation (9). Of course, every correction for the iR -drop is related to a more or less pronounced error and the smaller the correction the better the result. Therefore, the preferred measurement setup was the stationary electrochemical cell, where a smaller sample area (i.e. 0.31 cm^2) was subjected to the electrolyte and consequently smaller absolute currents have to be considered for the iR -correction.

Still, to measure the overpotential at 10 mA/cm^2 , where significant gas bubble formation can be expected, the rotating sample setup provides better reliability in some cases. In contrast to the CV measurements (Figure 4.18), also the annealed samples produce O_2 at constant rates over the investigated period of 10 minutes, but with increasing overpotentials (Figure 4.19). The strong scattering in the right diagram originates from the sample rotation and the average of these values has been taken to produce the data points in the left graph. The results shown in Figure 4.19 lead to the assumption that the annealed samples have indeed a similar electrochemical stability as the as-deposited ones, but most probably the gas bubble detachment is severely inhibited. That is why the current in the CV diagrams decreases strongly with each measured cycle. If the sample is rotated with a sufficient speed the performance stays constant over time.

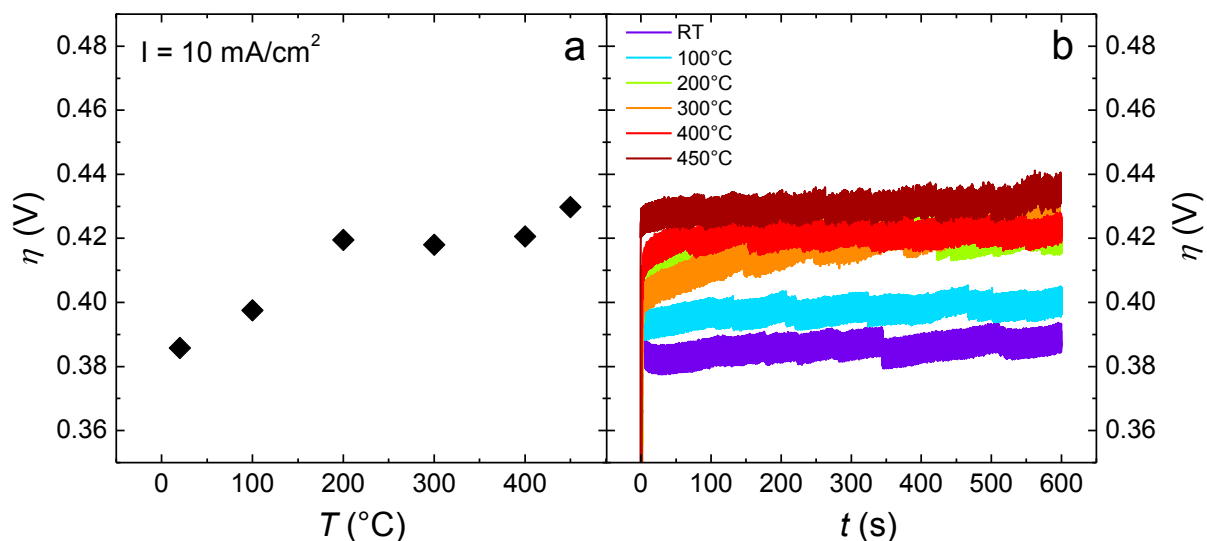


Figure 4.19: (a) Averaged overpotential η at 10 mA/cm^2 as function of the annealing temperature T . (b) Development of η at 10 mA/cm^2 over time t . The measurements have been corrected for the iR-drop and were performed in 1 M KOH.

It can be concluded that any annealing procedure is futile to improve activity and/or stability of electrodeposited cobalt oxide electrocatalysts. The elevated temperatures result in a crystallization of the initially amorphous samples to Co_3O_4 , which is related to a loss in surface area and consequently OER activity. Even though the effects are rather small and the increase of overpotential is limited to a few tens of mV, no benefit from the annealing procedure could be observed.

4.1.2. CoO_x films as oxygen evolution catalysts

In this chapter the oxygen evolution reaction (OER) at CoO_x film electrodes is investigated in more detail. Relations between amount of catalyst and activity as well as turnover frequency and other kinetic parameters are investigated and described. Furthermore, the influence of the electrolyte on electrocatalysis and the stability of the films are evaluated and compared, the reaction products are analyzed by mass spectroscopy.

4.1.2.1. Dependence of OER activity on the deposited amount of CoO_x

Elucidating the dependency of the catalytic activity or, to be more precise, the catalytic performance towards the OER, the amount of deposited cobalt oxide was varied. A series of samples was produced with deposition charges in the range from 0.01 to 5000 mC/cm². All samples were deposited from a standard solution at a deposition potential of 1.2 V vs. RHE. This potential lies just above the oxidation potential of the L₂Co₂²⁻ complex (see chapter 4.1.1.1) and was chosen to exclude side reactions as far as possible. Thus, it is assumed that all charges recorded during the deposition process are directly connected to the film deposition of CoO_x onto FTO.

Figure 4.20 shows exemplarily the CV diagrams of selected samples deposited with different charges. Obviously, the performance of the catalysts towards the OER gradually increases the higher the deposited charge is. Nevertheless, already a deposition charge of only 0.01 mC/cm² (violet solid curve), which corresponds to a film thickness of much less than a monolayer¹³⁰, leads to significantly higher faradaic current densities, compared to the blank FTO substrate (black line). Interestingly, not only the faradaic current density increases with the amount of deposited CoO_x, also the onset potential of the OER appears to be improved. This is misleading though, because the current densities for the thinner samples are too small to derive any conclusion from this graph and the faradaic current at the very beginning of the OER is significantly superimposed by other fractions of the total current density, such as capacitive and oxidative currents, which are of course more pronounced at higher amounts of deposited CoO_x. If the violet CV curve of the sample with the deposition charge of 0.01 mC/cm² is multiplied by a factor of 130 (violet dotted line) it matches almost perfectly the red curve corresponding to the sample with 100 mC/cm² deposition charge. The same procedure is possible for the other current voltage curves. This shows that the onset potential and the faradaic current behavior is the same for all thin films and follows the Butler-Volmer-relation, which describes an exponential growth of the current density after the onset of the OER. Taking into account that four orders of magnitude of deposited CoO_x lie in between the two compared samples, but the OER performance is only increased by about two orders of magnitude, it can be concluded already from this graph that the intrinsic activity is higher for the thinnest films. This effect is, however, more than compensated by the absolute increase in active centers. A more detailed analysis on this topic is given in chapter 4.1.2.5.

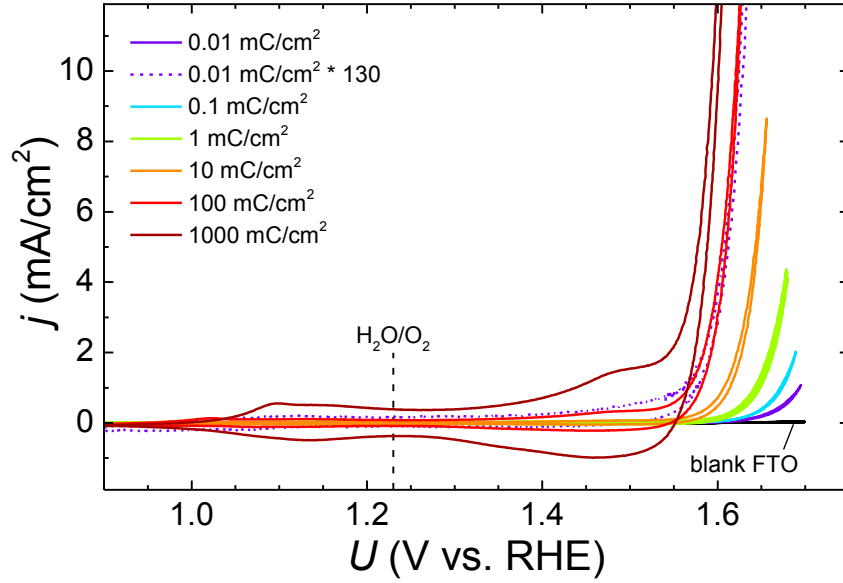


Figure 4.20: Selected CV diagrams of samples with deposited charges between 0.01 and 1000 mC/cm² and a blank FTO substrate as reference. The dotted violet line represents the current-voltage curve of the sample with the deposited charge of 0.01 mC/cm² multiplied by a factor of 130. All samples were deposited at 1.2 V (RHE). The measurements have been corrected with respect to the iR-drop and have been carried out in 1 M KOH (pH 14) at a scan rate of 10 mV/s.

A more quantitative examination is given in Figure 4.21. This graph shows the measured overpotential at the current density of 10 mA/cm² as function of the deposition charge and the amount of deposited Co ions, respectively. The latter was simply calculated from the charge, based on the assumed reaction (8), using the following equation:

$$M_{Co}(\mu\text{mol}) = \frac{3 * Q_{dep}}{n * e * N_A} * 10^6 \quad (12)$$

where Q_{dep} is the deposition charge in C/cm², n is the number of electrons transferred per unit Co₃O₄ (i.e. 2), e is the elementary charge (i.e. 1.602*10⁻¹⁹ C), N_A is Avogadro's constant (i.e. 6.022*10²³ mol⁻¹) and 10⁶ is the factor to convert mol in μmol.

As can be seen in the linear-log graph, the overpotential decreases continuously with increasing amount of catalyst on the substrate. The black squares represent the average overpotential of at least three samples and the red error bars show the standard deviations of the different measurements, respectively. Below the deposition charge of around 1 mC/cm² the differences between nominally identical samples increase significantly. This is caused by small deviations in the deposition parameters and the limited capability of the potentiostat for stopping the deposition after an exact amount of charge has passed the electrode/electrolyte interface. These factors become, of course, more significant and the relative errors increase the lower the amount of deposited catalyst is. Furthermore, it could be observed that very thin samples deposited with charges below 1 mC/cm² suffer from aging in air (not shown here), which also contributes to the

deviations in overpotential. Therefore, the actual values of the thinnest films are considered to be less reliable and one has to be cautious with deriving conclusions from them. Very thick films on the other hand become mechanically unstable and detach from the substrate after drying in air. Still, some OER activity can be detected even after the complete optically visibly detachment of the film (violet square). If drying of the samples is prevented, their stability under OER conditions can be improved (see also chapter 4.1.2.8).

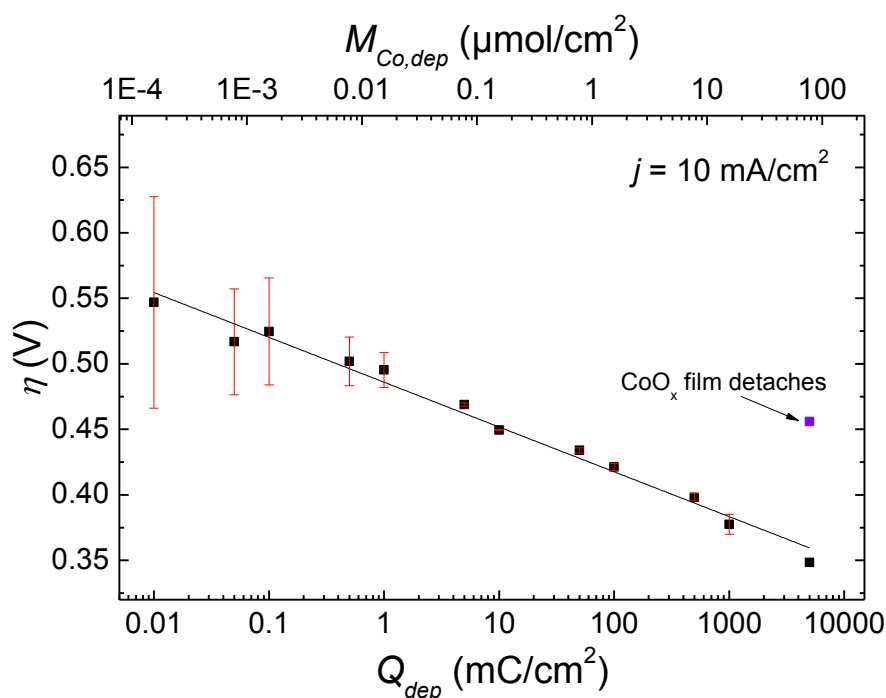


Figure 4.21: Overpotential η as function of the deposited charge Q_{dep} and the amount of deposited Co $M_{Co, dep}$.

The decrease of overpotential with deposition charge is evidence for a (micro-) porosity of the films, since in classical electrochemical considerations the current is proportional to the surface area of the catalyst in contact with the electrolyte. If CoO_x would form dense and compact films the surface area would stay constant and the reaction rate of the catalytically active centers at the surface would have to increase by orders of magnitude to show a behavior as given by Figure 4.21. This is rather unlikely. Instead, for a dense film the overpotential can be expected to be independent of the amount of deposited catalyst (i.e. film thickness). Moreover, an increase of overpotential could arise with increasing film thickness due to the presumably limited electrical conductivity of the CoO_x layers. An alternative explanation is given by Dau and coworkers⁹⁰, who recently proposed a volume activity model for an electrodeposited amorphous cobalt oxide catalyst without pores in neutral media. However, current densities and electrochemical conditions in that publication are very different compared to this work and (micro-) porosity is, supported by TEM images (Figure 4.26) the most convenient explanation for the dependence of the overpotential of CoO_x films on the deposition charge.

As already visible from Figure 4.20 also the very thin samples appear to have a significantly increased activity towards the OER compared to the blank FTO substrate, which has an overpotential of 1.26 V at 10 mA/cm² (not shown in the graph). Yeo and Bell¹³⁰ calculated a film thickness of about 0.4 monolayers after having deposited 0.095 mC/cm² of cobalt oxide on Au. They reported an overpotential (from CV) of around 540 mV at 10 mA/cm² in 0.1 M KOH, which is close to the value found in this work and shows that already a sub-monolayer film of cobalt oxide is capable to oxidize water at relatively high rates.

4.1.2.2. Film thickness

The results of the prior chapter have been leading to the assumption that the volume or in other words the sample thickness plays a role for the OER performance, since the overpotential decreases continuously with increasing amount of electrochemically deposited cobalt oxide. Hence, the sample thickness was estimated from SEM cross section and profilometer investigations. The results are summarized in Figure 4.22 and show the measured film thicknesses as function of flown charge during electrodeposition. As expected, the sample thickness increases with increasing deposition charge. However, the measurements with the profilometer did not always provide reliable results and showed a poor reproducibility as can be seen by the blue squares and green triangles, respectively. The results generally tend to underestimate the sample thickness compared to the SEM cross section measurements (cyan diamonds; see also Figure 4.23). Still, it can be noticed that samples deposited at 1.2 V are by trend thicker than samples deposited at 1.4 V.

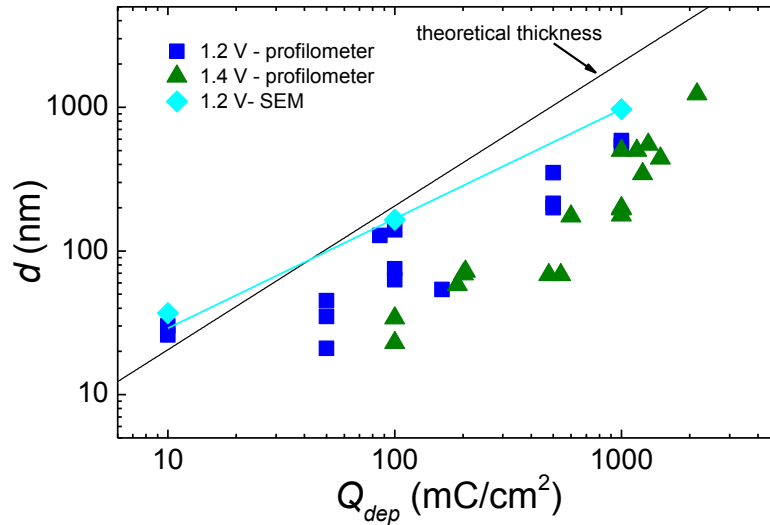


Figure 4.22. Sample thickness d as function of the deposition charge Q_{dep} . The blue squares and green triangles represent samples deposited at 1.2 V and 1.4 V (RHE) measured with a profilometer, respectively. The cyan diamonds are the results of cross section SEM investigations on samples deposited at 1.2 V, the black line shows the sample thickness calculated according to equation (13).

The black line in the graph represents the expected film thickness assuming a compound close to Co_3O_4 is formed and was calculated according to the equation:

$$d(\text{nm}) = \frac{Q_{dep} * M * 10^7}{n * e * N_A * \rho} \quad (13)$$

where Q_{dep} is the deposited charge in C/cm^2 , M is the molar mass of Co_3O_4 (240.8 g/mol)¹⁴⁰, n is number of transferred electrons per unit Co_3O_4 (i.e. 2) according to equation (8), ρ is the density of Co_3O_4 ($6.07 \text{ g}/\text{cm}^3$)¹⁴⁰ and e and N_A represent the elementary charge and Avogadro's constant,

respectively. Comparing the theoretical thickness of a Co_3O_4 film with the measured SEM cross section values (cyan line) it can be seen that the film grows slower than expected with respect to the deposition charge. This shows that the process of film formation is rather complex. Tentatively, a densification of the film with increasing thickness occurs as the pores far away from the sample surface become smaller and smaller. The film thickness can be expressed as function of the deposition charge by:

$$d = 5.02 * Q_{dep}^{0.76} \quad (14)$$

Samples with thicknesses below 10 nm could not be resolved neither by SEM nor by profilometer measurements. Even though, the interpolation from Figure 4.22 is based on only three data points, the coefficient of determination of $R^2 = 0.9997$ gives reason for the reliability of this fit. Therefore, for further considerations equation (14) was used for estimating the thicknesses of the very thin samples.

Cross section SEM images of samples with a deposition charge of 10 (a), 100 (b) and 1000 mC/cm^2 (c) can be found in Figure 4.23. They show the typical film thickness and morphology of the samples in detail. While at 10 mC/cm^2 (a) the CoO_x film is uniformly distributed over the FTO substrate and only a few nm thick, the dimension of the film grows to around 170 nm, when 100 mC/cm^2 are deposited (b). At this stage the film is still fully covering the substrate. Increasing the deposition charge by another order of magnitude (c) results in an islet structure, already observed and described previously (see Figure 4.11). Interestingly, from this images no significant change in the surface area or any porosity can be observed. Nevertheless, the resolution of the SEM is not high enough to exclude pores or features in the order of a few nanometers.

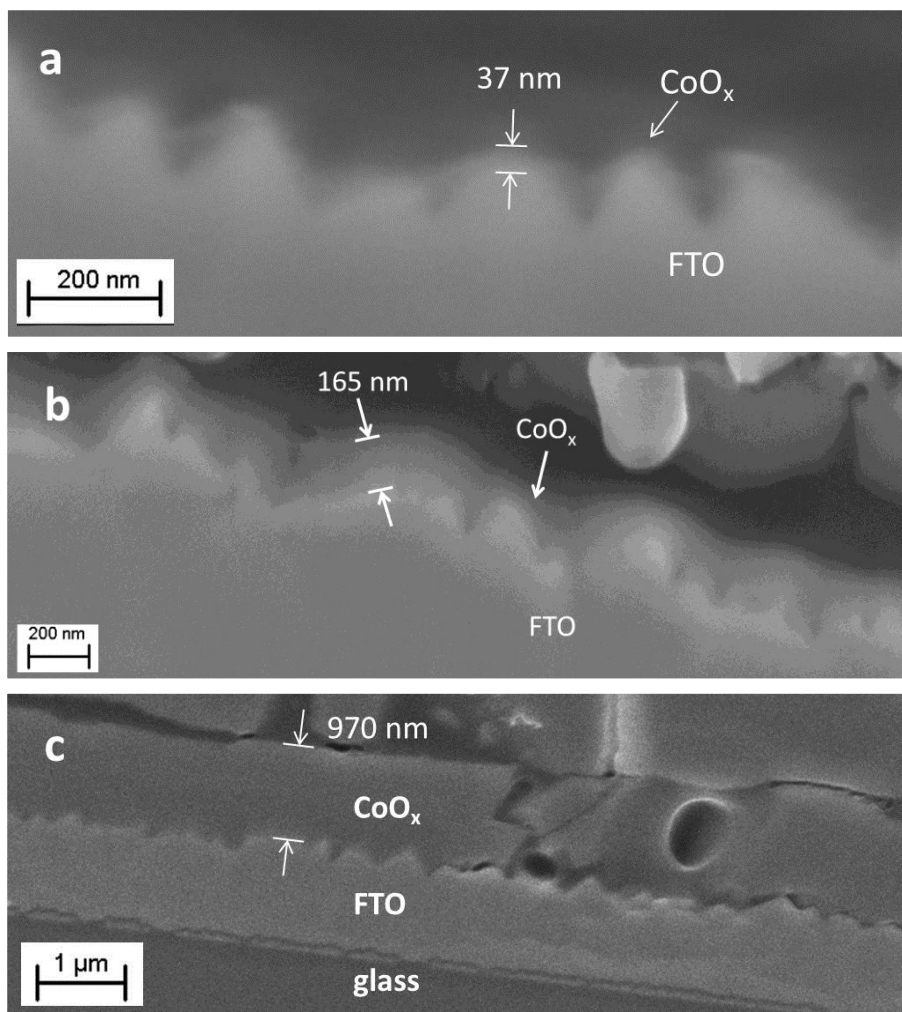


Figure 4.23: SEM images of samples deposited at 1.2 V (RHE) until 10 (a), 100 (b) and 1000 mC/cm^2 have passed the electrode/electrolyte interface. The samples were cut and prepared for cross section analysis in a sandwich alignment.

4.1.2.3. Determination of the electrochemically active surface area (ECASA)

In principal all considerations on electrocatalytic reactions are based on the assumption that charge transfer has to occur at the electrode/electrolyte interface^{22,141}. The electrochemically active surface area (ECASA) therefore plays a crucial role for characterizing the activity of a catalyst. This means that at a certain overpotential a catalyst with a weak intrinsic activity (i.e. a low reaction rate per active center), but a very high ECASA may have a better overall geometric faradaic current density than a catalyst with a very high intrinsic activity but a smooth surface. The estimation of the ECASA is one of the most challenging tasks in electrocatalysis, because there is no established and generally accepted method determining the ECASA of a solid electrode¹⁴¹. Several techniques have been developed, but they are only physically valid in narrow confinements or only applicable to allow a comparison within one material system.

In the following, it was tried to estimate the ECASA of the CoO_x catalysts by measuring the double layer capacitance of the films. This can be done by recording current-voltage curves at various scan rates in a small potential range, where no oxidative/reductive or faradaic current can be expected and the only contribution to the measured current comes from charging of the double layer capacitor at the electrode/electrolyte interface^{47,136,141–143}. The current density values of the anodic and cathodic scan, corresponding to a potential in the middle of the investigated range, are then plotted against the sweep rate and the mean of the slopes of the best-fit lines gives the double layer capacitance according to the equation:

$$C_{dl}(mF/cm^2) = \frac{dj_c}{dv} * 10^3 \quad (15)$$

where j_c is the measured capacitive current density in mA/cm² and v is the scan rate in mV/s (see also Figure 4.13). The calculated C_{dl} has then to be normalized with the C_{dl} of an “ideal smooth” film (i.e. real surface area = geometric surface area) of the same electrode material, in order to receive the roughness factor of the sample. Unfortunately, very few experimental data are available, describing the nature of “ideal smooth” electrodes, which is the main limitation for this method. In literature, values ranging from 40⁴⁷ to 80 μF/cm²¹³⁶ have been used for the calculation of roughness factors, assuming that the C_{dl} per unit area is approximately the same for all oxides. Most authors though refer to Levine and Smith¹⁴⁴, who calculated a value of 60 μF/cm². This approximation has been severely criticized¹⁴¹ and it can be doubted that the ESCAs of electrodes of different nature can be compared in absolute numbers.

In this work, it was tried, to investigate the relationship between ECASA and the amount of deposited cobalt oxide. Since all samples nominally consist of the same electrode material and only the deposition charge was varied, the voltammetric method described above should be applicable for at least an internal comparison. Figure 4.24a shows the CV diagram of one of the samples with the regions marked with dotted circles, where the capacitance measurements have

been performed. Already from this graph it becomes obvious that no pure “double-layer region” is available throughout the whole investigated anodic regime. A “double-layer region” is usually characterized by constant positive anodic and negative cathodic currents in a certain potential range. The absence of a “double-layer region” for cobalt oxide, which severely complicates the interpretation, has already been observed by others¹³⁶. The graphs in Figure 4.24b and (c) show typical capacitance measurements in the marked regions in more detail.

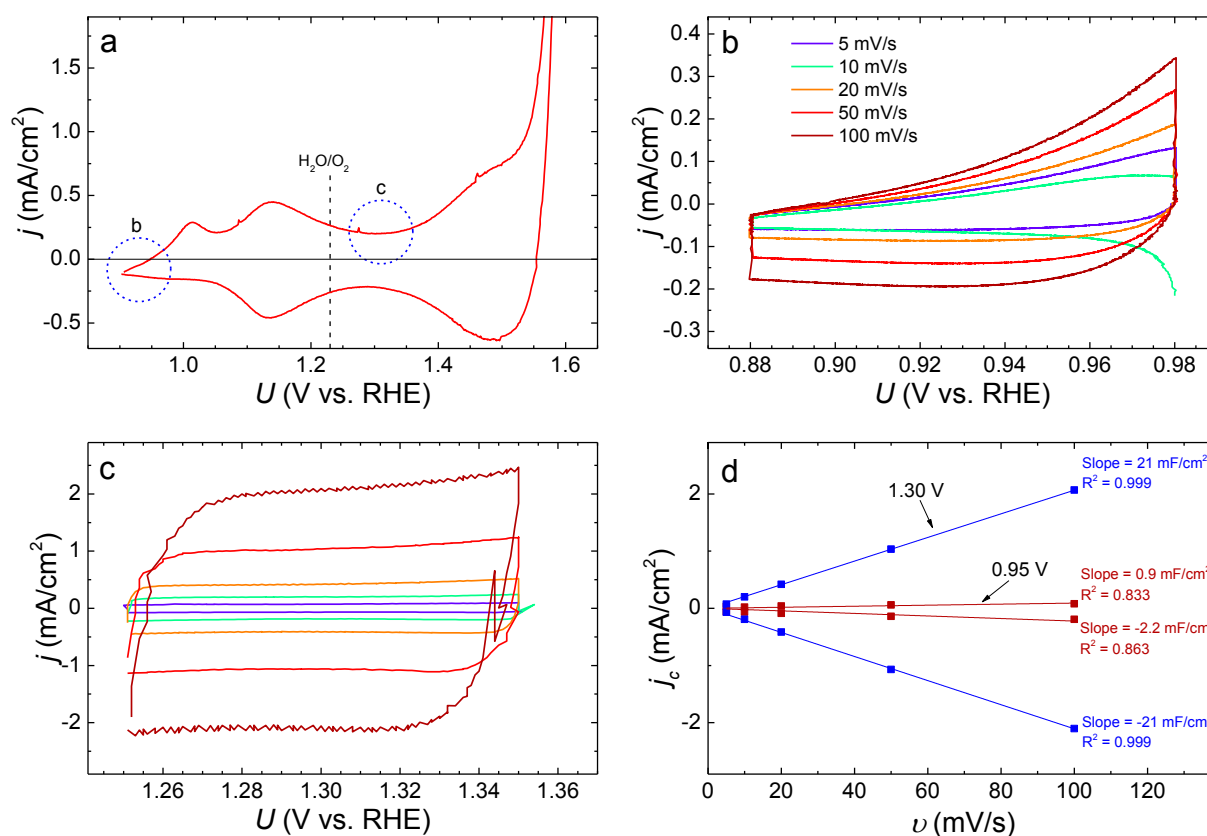


Figure 4.24: (a) CV diagram taken at 10 mV/s with the marked regions for possible capacitance measurements. The graphs in (b) and (c) show CV diagrams at different scan rates (5 – 100 mV/s) in the potential range from 0.88 to 0.98 V (b) and from 1.25 to 1.35 V (c). The diagram in (d) shows the plot of the anodic (positive) and cathodic (negative) current density vs. the scan rate at 0.95 V (brown) and 1.30 V (blue). All measurements were carried out in 1 M KOH.

In Figure 4.24b the potential range close to the open circuit potential (i.e. ca. 0.94 V) is measured with different scan rates. This potential interval is frequently used for capacitive measurements. Some dependence of the current density on the sweep rate is visible, but the oxidative current of the first oxidation peak at about 1.0 V (RHE) affects the measurements and does not allow any clear conclusions (cf. Figure 4.24d). A sneaky reduction of cobalt ions⁵⁸ in the anodic scan can also not be ruled out. In contrast to that, a clear linear relation between current density and sweep rate was found at around 1.3 V (Figure 4.24c and d), just in between the two oxidation peaks. This allows some analysis of the data, but due to the fact that the current densities are much higher

than in more cathodic potential regions it cannot be ruled out that the capacitive current is superimposed by other effects. In fact, as described in chapter 4.1.3.2 a significant electrochromic behavior can be observed for the CoO_x films, which is considered to be a volume electrochemical effect and would lead to a constant current density of about $30 \mu\text{A}/\text{cm}^2$ between 1.1 and 1.7 V at a scan rate of $10 \text{ mV}/\text{cm}^2$. However, at 1.3 V a current density of about $200 \mu\text{A}/\text{cm}^2$ or higher was recorded for $10 \text{ mV}/\text{s}$ (see Figure 4.24c), which supports the assumption that at least a great part of the current density can be ascribed to double layer charging and thus can be seen as a measure of the ECASA.

In Figure 4.25 the values for C_{dl} are plotted against the deposition charge Q_{dep} . Interestingly, a linear dependence between C_{dl} and Q_{dep} was found for samples with a Q_{dep} of about $1 \text{ mC}/\text{cm}^2$ or more. Below that deposition charge a constant capacitance was detected, but, as already mentioned in previous chapters, the reliability of these values is not as good as for the thicker samples, because of the low current densities in the CV diagrams and the strong increase in significance of possible errors in the measurements. For reasons of comparison, the capacitance of the blank FTO sample was added (with an arbitrary Q_{dep}) to the graph (violet square). If the double layer capacitance is accepted to be a relative measure for the electrode surface in contact with the electrolyte (with the reservations mentioned above), the slope of 0.8 shows that the relative share of ECASA decreases with increasing amount of deposited CoO_x . This supports the assumption that with increasing film thickness a densification of the inner parts of the film occurs (cf. section 4.1.2.2).

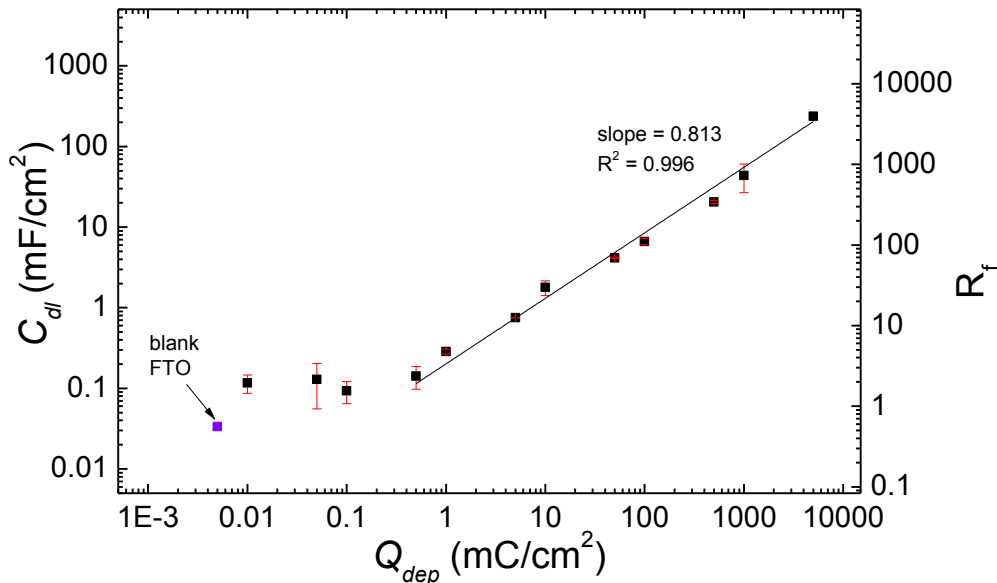


Figure 4.25: Double layer capacitance C_{dl} and roughness factor R_f as function of the deposition charge Q_{dep} .

Figure 4.25 also shows the roughness factor (right y-axis), computed by using $60 \mu\text{F}/\text{cm}^2$ as capacitance per unit real surface area¹⁴⁴ and plotted against Q_{dep} . The R_f was found to be between 1 and almost 4000. Depending on the preparation method, R_f values between 10 and several thousands have been published for cobalt oxides or mixed oxides containing cobalt^{47,67–69,72,76,134,136,143,145}. Of course, a detailed comparison to differently prepared samples from the literature is difficult and poorly reliable, but a rough estimation whether the obtained roughness factors are realistic or not should nevertheless be possible. Except for the thickest samples ($5000 \text{ mC}/\text{cm}^2$) the order of magnitude fits to the publications, even if an error of about a factor of two, due to the possible contribution of currents of other origin (see above), is taken into account.

The supposition that micro- or nanoporosity might be the explanation for the increasing double layer capacitance with film thickness is supported by TEM cross section images in Figure 4.26. The left images (a and c) show a sample, which was dried in air at room temperature and has been considered to be amorphous. The TEM high magnification image (c) shows that the sample consists of a loosely bound network of tiny grains with a diameter of 2 to 3 nanometers. This porous network becomes even more obvious from the overview image (a). The distinct particles do not seem to be of high crystallinity, because almost no lattice plains are visible. It has to be considered that during the sample preparation for the TEM measurements, the samples have been heated to 150°C . Therefore, it is thinkable that parts of the porous structures have been removed by particle movement and growth (see also Figure 4.16, where a dramatic change in the CV diagram is visible between 100 and 200°C) and that the original sample has an even higher internal surface area. It is thinkable that when immersed into the electrolyte, the sample behaves like a sponge and fills up all the space in between the grains with electrolyte.

In comparison to that the images on the right side (b and d) show a sample, which was tempered at 400°C . The big difference in grain size and crystallinity is obvious. On several grains in the high magnification image (d), the lattice planes of the crystallites can be seen. Also, it is apparent that the internal surface becomes much smaller due to the growth of the grains in the annealing step. This matches the differences in the CV diagrams between annealed and not annealed samples (Figure 4.16) very well.

Moreover, in the overview images in (a) and (b) the densification of the inner parts of the thin films, close to the substrate, can be seen. This is more obvious for the annealed sample in (b), where the grain size is significantly increased and the pores in between are less. The as-deposited sample (a) does not show such a clear effect, but still a slightly darker tone can be observed for areas in the inner part of the film, close to the interface with the substrate.

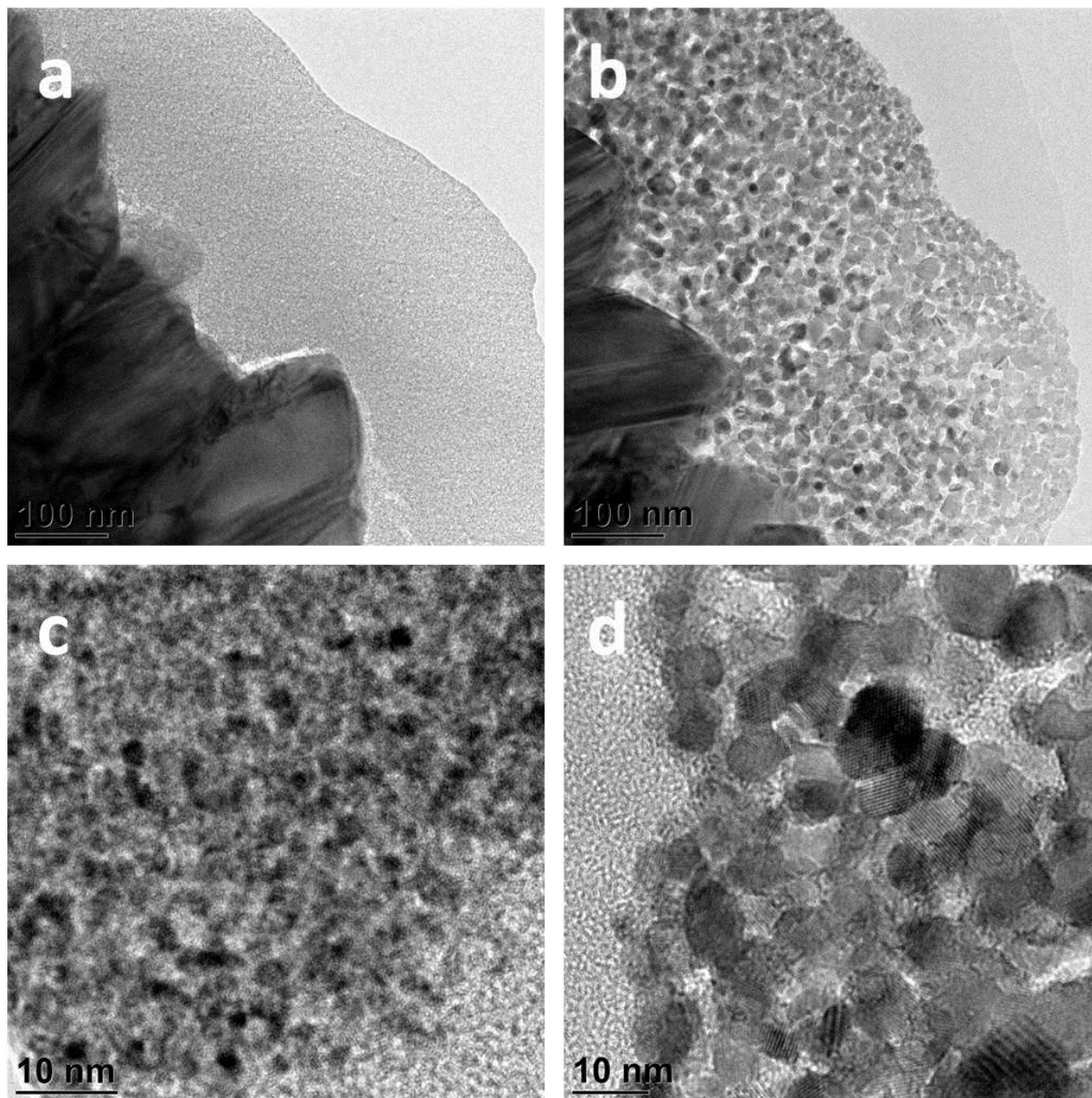


Figure 4.26: TEM images of a CoO_x sample dried in air at RT (a, c) and a Co₃O₄ sample heated to 400°C (b, d).

4.1.2.4. Magnitude of the reduction peaks

The oxidation and reduction waves in the CV diagrams are generally accepted to represent changes in the oxidation state of the cobalt ions^{112,83,116,81,134,135,80}. Furthermore, the feature at about 1.5 V (RHE), just before the onset of the OER is considered to be essential for activating the catalyst¹¹². If the species formed in this oxidation process, most probably Co⁴⁺ ions, represent the active centers for the OER, it is of great interest to which extent these species are formed, compared to the entire amount of catalyst. The oxidation and reduction processes are connected to the charge transfer of one electron per cobalt ion. Therefore, the total charge of the oxidation and reduction peaks is a measure for the amount of ions, which are oxidized and reduced and can be calculated, respectively. Since the oxidation feature at about 1.5 V turns directly over into the faradaic current of the OER, it is more convenient to take the corresponding reduction peak for calculating the amount of reduced ions⁹⁰. This is valid if the redox pair represents a (quasi-) reversible process, which is the case for this oxide and has been shown by several authors^{116,134,136}. In Figure 4.27a it is exemplarily shown, which areas of the cathodic scan have been integrated to estimate the amount of reduced cobalt ions. This method might not be exact, because the capacitive current cannot be taken out, but since the procedure was repeated in the same way for all samples and, again, the film thickness represents the only parameter to be varied within the samples series, the procedure is expected to be valid for an internal comparison.

In Figure 4.27b, the integrated reduction charges $Q_{red,peak}$ are illustrated as a function of sample thickness. Both reduction peaks have a linear relation towards the film thickness. The second one (blue squares) shows a slope of unity, while the integrated first reduction peak (red squares) has a slight, but significantly smaller slope. This is a first hint for the independence of the two reactions from one another. As already noticed in Figure 4.25, the trend stops at very low film thickness and the numbers for $Q_{red,peak}$ stay constant. In fact, the charge of the peaks even exceeds the total deposition charge in this region (not shown), which is physically impossible, if the assumptions made above are valid. Most probably this effect can be explained by the very small current densities and the fact that the capacitive current is also part of the measured current signal, which becomes of course more significant for very thin films showing the limitations of this method. In the right y-axis of Figure 4.27b the amount of cobalt ions, which undergo a reduction is plotted. These values were calculated according to the equation:

$$M_{Co}(nmol/cm^2) = \frac{Q_{red,peak}}{n * F} * 10^9 \quad (16)$$

where n is the number of electrons per reduced Co-ion (i.e. 1), $Q_{red,peak}$ is the charge of the reduction peaks (C/cm²) and F is the Faraday constant (96 485 C/mol), respectively. This calculation allows the estimation of turnover frequencies based on the amount of Co⁴⁺ ions (see below).

Figure 4.27c depicts the percentage of the cobalt ions, which undergo an oxidation and reduction, respectively. As can be seen from the graph, the fraction of cobalt ions decreases continuously with increasing deposition charge and ends up below 2% at the deposition charge of 5000 mC/cm^2 . It is somehow vexing that the fraction of oxidized/reduced ions stays constant in relation to the film thickness, but decreases when the total amount of deposited cobalt oxide is considered. This can tentatively be explained by the “densification” (see Figure 4.22) of the inner parts of the film, which are then not accessible for the electrolyte anymore. As a consequence the film thickness increased slower as one would expect from a homogeneously composed film. Of course, this effect is more pronounced for thick samples.

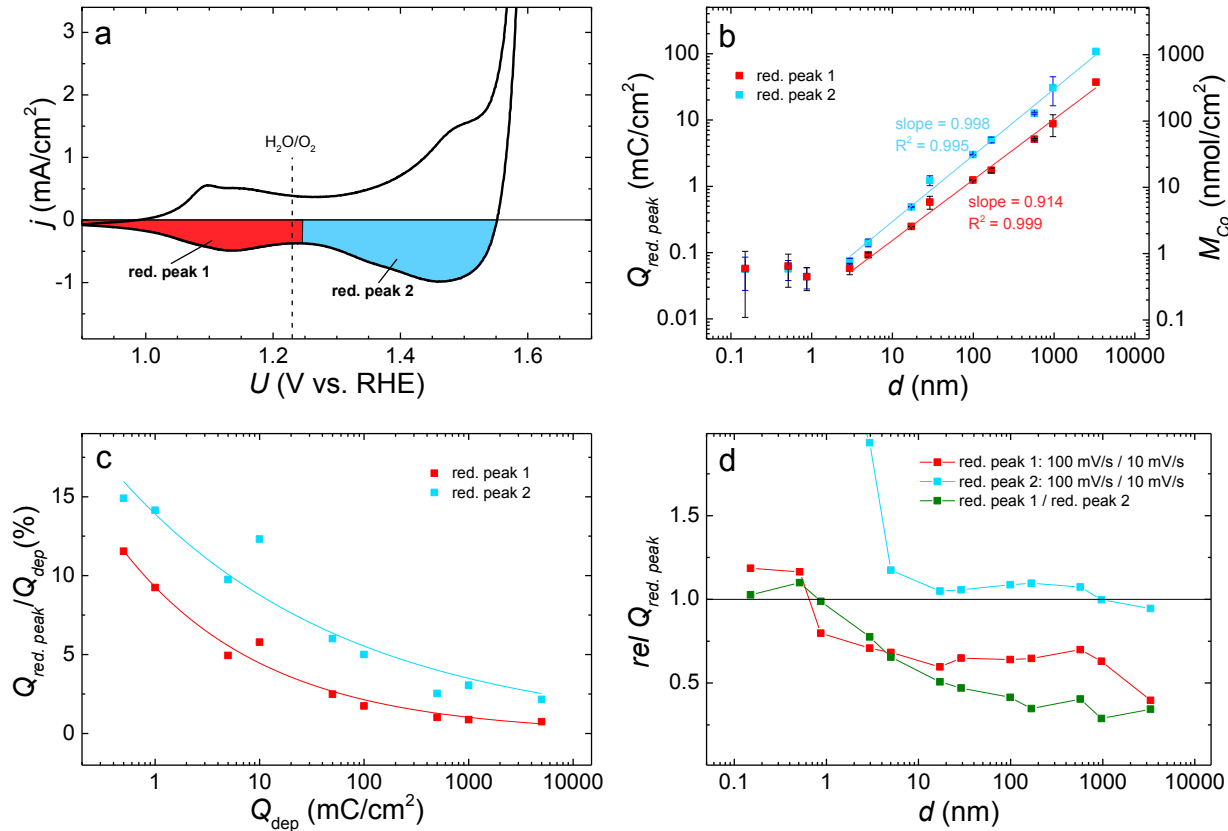


Figure 4.27: (a): CV diagram with the marked regions for the integration of the reductive current density. (b): Charge belonging to the reduction peaks $Q_{\text{red,peak}}$ (red and blue areas in a) and amount of reduced cobalt ions M_{Co} as function of film thickness d . (c): Fraction of the reduced cobalt ions $Q_{\text{red,peak}}/Q_{\text{dep}}$ as function of the deposition charge Q_{dep} . (d): Relative charges of the reduction peaks $\text{rel } Q_{\text{red,peak}}$ as function of film thickness d . The blue and red lines represent the relative charges between measurements conducted at 100 and 10 mV/s for reduction peak 1 and 2, respectively. The green line is the relative charge between reduction peak 1 and 2 measured at 100 mV/s.

Finally, in Figure 4.27d the dependence of the reduction peaks on the scan rate and the relation among them was investigated. The diagram shows the relative charges of peaks 1 and 2 calculated by dividing the integrated peak area measured at 100 mV/s by the integrated peak area measured at 10 mV/s, respectively (red and blue squares). The peak area (i.e. the charge) of the first

reduction peak (red) decreases when the sweep rate is increased from 10 to 100 mV/s, which is why the red curve declines below 1. This can be possibly associated with a slow step in the oxidation/reduction reaction^{74,136}. Most probably accessibility and/or potential dependent binding characteristics of OH⁻ ions are responsible for it. Still, it is surprising that the effect can only be observed on the first reduction peak, while magnitude of the second peak is independent of the sweep rate and the blue curve stays constant at numbers close to 1. The green line gives the relation of the charges of the two reduction peak as function of the film thickness. It was calculated by dividing the peak area of the first reduction peak by the area of the second one and shows that the first reduction peak becomes smaller relative to the second one as the samples become thicker. Possibly, the two redox processes are independent from one another and affect a different amount of cobalt ions. This is important, since the first redox feature is usually considered to represent the transition from Co²⁺ to Co³⁺ (see chapter 4.1.1.4) and could thus provide the trivalent cobalt ions for the oxidation to Co⁴⁺ in the second redox feature. But as the results from Figure 4.27d show, this is probably not the case and the Co³⁺ ions have to have their origin (partly) somewhere else.

4.1.2.5. Kinetics

Besides the apparent catalytic performance, which is expressed by the faradaic current density at a certain overpotential, also the “intrinsic” catalytic activity, which considers the reaction rate per active catalytic center, is of great interest. This “intrinsic” catalytic activity can be expressed by the turnover frequency (*TOF*), which is defined in this work as the number of O₂ molecules generated per active center (e.g. Co ion) and second. Figure 4.28 shows the *TOF* of various samples at different overpotentials as a function of the sample thickness. The *TOF* has been calculated in two different ways. First, potentiostatic measurements at various overpotentials have been carried out and the corresponding current density after one minute of equilibration was measured. Then, the *TOF* was calculated by

$$TOF_{Q_{dep}}(s^{-1}) = \frac{j}{n * Q_{dep}} * \frac{2}{3} \quad \text{and} \quad TOF_{red,peak}(s^{-1}) = \frac{j}{n * Q_{red,peak}} \quad (17a,b)$$

where *n* is the number of electrons needed for producing one O₂ molecule (i.e. 4), *j* is the measured current density in mA/cm² at various overpotentials, 2/3 is a factor coming from reaction (8) and *Q_{dep}* and *Q_{red,peak}* are the total deposition charge and the charge of the second reduction peak area in mC/cm² (see Figure 4.27a), respectively.

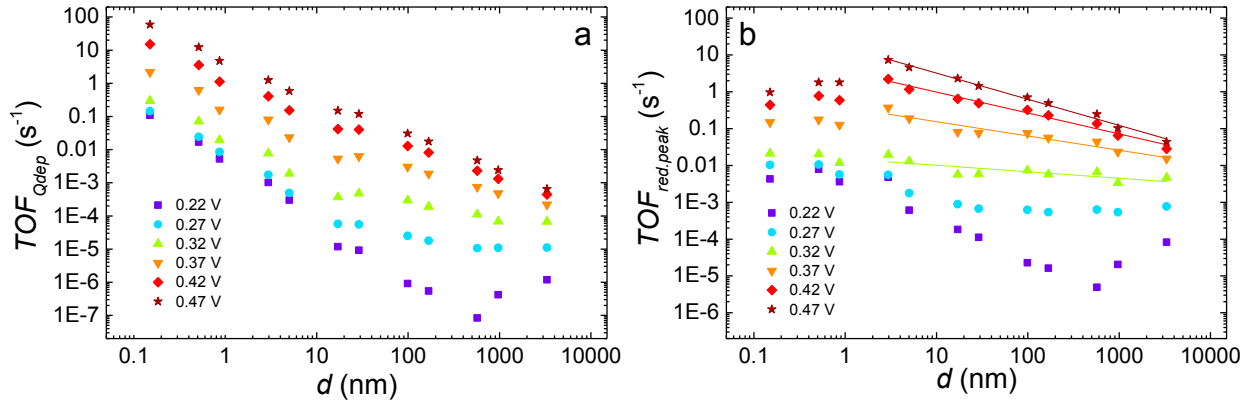


Figure 4.28: Turnover frequency calculated from the total deposition charge *TOF_{Qdep}* (a) and from the charge of the second reduction peak *TOF_{red,peak}* (b) vs. film thickness *d*.

As obvious from the graphs, the two equations lead to totally different results. In Figure 4.28a every Co ion is considered to be an active center and thus the total deposition charge of the sample is taken for the calculation. This is probably the more convenient method from an application point of view, because also the inactive or “buried” Co ions have to be taken into account when calculating the amount (and price) of a catalyst in a device. The *TOF_{Qdep}* continuously decreases with increasing film thickness. Only for the very small overpotential of 0.22 V, where barely any faradaic current is detectable, there are some deviations from the trend. These findings are in contrast to the results of Dau et al.⁹⁰, who reported constant turnover

frequencies for moderate overpotentials. Their experiments, however, have been carried out in a different electrolyte (phosphate buffer) and at lower current densities, which might be a reason for the differences.

From a scientific point of view the TOF of those sites, who actually take part in the catalytic reaction is of great interest as it is a measure for the intrinsic catalytic activity of the compound. If the Co^{4+} ions are assumed to be the catalytically active centers, the number of reduced Co ions (calculated from the peak area of the second reduction peak, see equation (16)) can be taken as base for the calculation of the “intrinsic” $TOF_{red,peak}$. A maximum in $TOF_{red,peak}$ can be deduced for samples with a thickness between 5 and 10 nm. At larger film thicknesses the $TOF_{red,peak}$ decreases, but at much lower rates compared to TOF_{Qdep} . Furthermore, the slope of the decrease of $TOF_{red,peak}$ becomes steeper at higher overpotentials. The thicker the sample and the higher the current density, the larger becomes the impact of hindered accessibility of the potentially active sites and diffusion limitations, which cause the $TOF_{red,peak}$ to decline.

Table 4.3: List of reported turnover frequencies (TOF) for cobalt oxides and other transition metal oxides. d , η , NP, NC, CoPi and mCo_3O_4 stand for sample thickness, overpotential, nanoparticles, nanoclusters, cobalt phosphate and mesoporous Co_3O_4 , respectively.

catalyst	electrolyte	d (nm)	η (mV)	TOF (s^{-1})	Ref.
Co oxide	0.1 M KOH	< 1	351	1.81	130
Co_3O_4 NP	water	4	photocatalysis	>3	40
Co oxide	0.1 M KPi	10-1000	0.383-0.583	0.0003-0.04 ^a	90
Co_3O_4 NC	aq. sol (pH 5.8)	65*130	350	0.01	48
Co_3O_4	1 M KOH	3 mg/cm ²	235	>0.006 ^b	48,72
CoPi	0.1 M KPi	n/a	410	>0.0007 ^b	48,84
Au/ mCo_3O_4	0.1 M KOH	n/a	400	0.048	133
Co oxide	0.1 M KPi	20	533	0.017	103
Mn oxide	0.1 M KPi	20	533	0.01	103
Ni-Fe- oxide	0.1 M KOH	25-70	300	0.008-87	50

^a Photocatalytic system ^b Data calculated by Ref.⁴⁸, the second Ref. denotes the original publication.

Table 4.3 shows a list of TOF values for cobalt oxide and other abundant transition metal oxides from the literature, along with some experimental data of these reports for comparison. Even though, a thorough evaluation might be difficult due to the great variation of electrode preparation and measurement conditions, it becomes clear that the electrocatalyst layers

presented in this work show a similar *TOF* compared to most cobalt oxide electrodes described by other authors. Only Ni-Fe-oxides have a *TOF* of up to four orders of magnitude higher⁵⁰. However, it has to be stated that the *TOF* does still not belong to the standard characterization parameters for electrocatalysts when present in the form of thin films. There is a debate ongoing about its use and definition⁴⁷.

The considerations above assume that the entire reaction of oxygen evolution occurs at one catalytic center only, despite the fact that reaction mechanisms involving two interacting neighboring sites have been proposed³⁰. However, DFT calculations have shown that direct recombination of oxygen atoms to form O_2 is related to large activation barrier and thus rather unlikely^{46,146}. Besides, inclusion of a second catalytic center would halve the *TOF* per site, which is negligible considering that the range of *TOFs* spreads over several orders of magnitude.

The fact that already at an overpotential of only 0.22 V a very small, but constant faradaic current has been observed and a *TOF* could be calculated supports the assumption made above that the kinetics of all samples are very similar and the differences in the apparent onset potential (see Figure 4.20) are caused by the very different magnitude of the (qualitatively) same or at least very similar shape of the current curve.

This property is further supported by Figure 4.29. It shows the Tafel slope of electrodes as a function of sample thickness as it has been calculated by plotting the log of the stationary current density against the overpotential. The slope of the fit in the linear region of that plot is the Tafel slope²² (see chapter 2.1). Apparently, the changes in the magnitude are small and comprise only a few mV/dec. This can be seen as confirmation for the assumption of the same reaction mechanism for all samples, since a fundamental change in the reaction mechanism (e.g. change of the rate determining step) can be expected to affect the Tafel slope to a much greater extent²². However, there is an optimum in the curve, which is consistent with the optimum in *TOF* (Figure 4.28b). Presumably, at the sample thickness between 1 and 50 nm the conditions for the “intrinsic” activity are best. Yet, this effect is more than overcompensated by the absolute increase of the ECASA, so that the apparent current density continuously increases with increasing sample thickness. A Tafel slope for cobalt oxide under basic conditions of around 40 to 50 mV/dec has often been reported in the literature^{49,51,64}, but also values below⁸⁰ and above^{68,134,147} were observed. Frequently also two regimes could be distinguished for low and high current densities^{68,148}. For comparison, the Tafel slope of the blank FTO substrate was added to the graph (violet diamond) at an arbitrary film thickness of 0.1 nm.

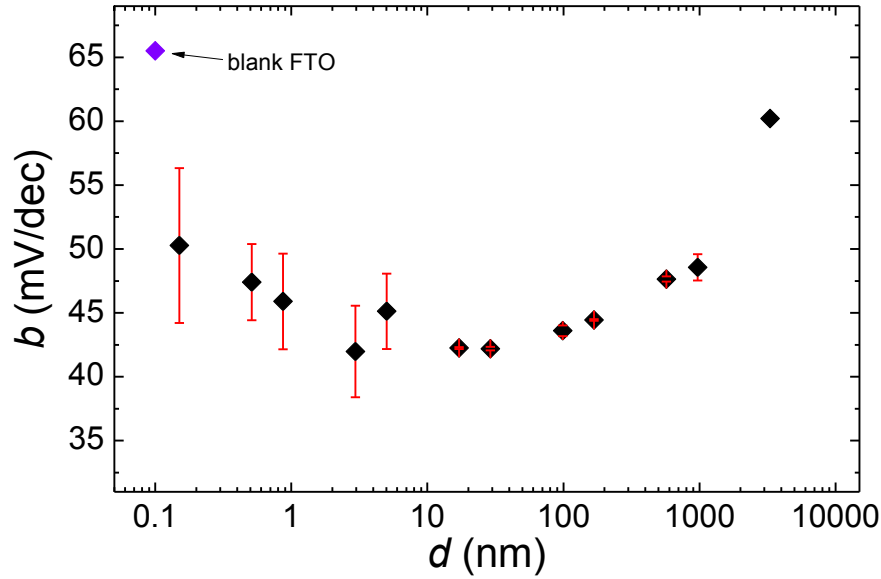


Figure 4.29: Tafel slope b as function of the sample thickness d . The violet diamond represents the blank FTO substrate, which was arbitrarily placed at 0.1 nm to show it in the graph.

Finally, the exchange current density and the charge transfer coefficient were calculated from the Tafel plot. This was done using the equation:

$$\log j_0 = \log j - \frac{1}{b} \eta \quad \text{and} \quad \alpha = \frac{2.3 * R * T}{b * n * F} \quad (18a,b)$$

where j and j_0 are the current density and the exchange current density in mA/cm^2 , b is the Tafel slope in V/dec , α is the charge transfer coefficient and R , T , n and F are the gas constant ($8.314 \text{ J}/(\text{K} * \text{mol})$), the absolute temperature (298 K), the number of exchanged electrons (4) and the Faraday constant ($96485 \text{ C}/\text{mol}$), respectively.

The results are shown in Figure 4.30. The exchange current density (red circles) turned out to be very low. Only the very thick samples have a higher j_0 of around $15 \text{ nA}/\text{cm}^2$ (not shown in the graph). This can be explained by the very complicated electrochemical oxygen evolution reaction involving four electrons for the formation of one O_2 molecule and the related theoretical overpotential of 0.2 to 0.4 V (see chapter 2.2.1). The order of magnitude for CoO_x electrodes is significantly lower than for Pt ($10^{-6} \text{ A}/\text{cm}^2$)²² and Mn oxide (10^{-7} - $10^{-9} \text{ A}/\text{cm}^2$)¹⁴⁹. Nevertheless, for electrodeposited amorphous cobalt oxide similar values were published by Koza et al⁸⁰.

The charge transfer coefficient has values in the range from 0.3 to 0.35 and is comparable to other transition metal oxides, like $\alpha\text{-Mn}_2\text{O}_3$ ¹⁴⁹. The deviations among the samples are not very pronounced, but a maximum at a sample thickness of 10 to 50 nm can be observed, which is consistent with *TOF* and Tafel slope observations. For anodic reactions, the activation energy of the transition state(s) is more affected by potential changes if the value of α is high²². An ideal

catalyst has therefore an α value close to 1. Thus, the results support the assumption that the best intrinsic catalytic conditions are fulfilled for catalysts with a thickness in the range from 1 to 50 nm (see above).

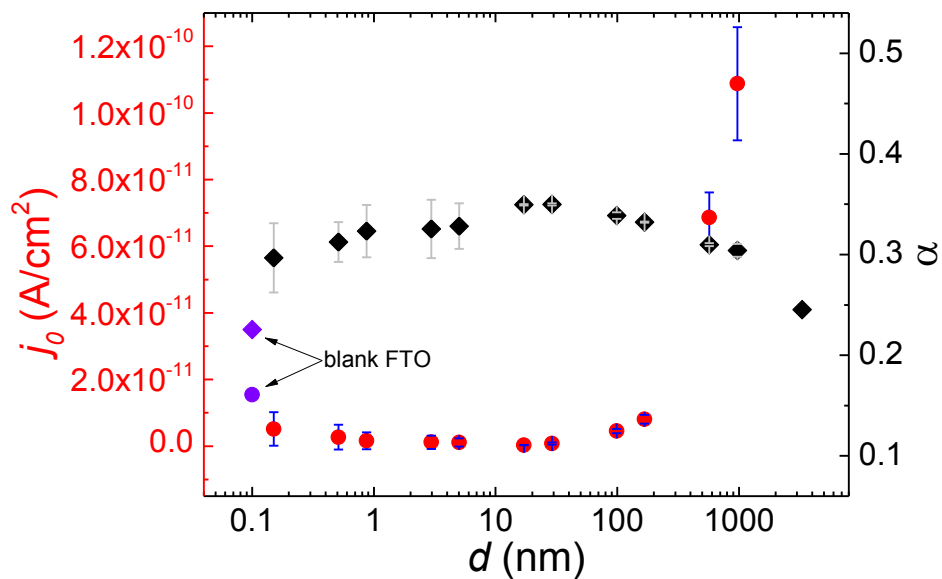


Figure 4.30: Exchange current density j_0 and charge transfer coefficient α versus sample thickness d . The violet diamond and circle represent α and j_0 of the blank FTO substrate.

4.1.2.6. Influence of the electrolyte

In the last years a great interest has grown in solar water splitting at near-neutral pH, since the environment for the photoabsorbers is less aggressive and many materials show a better stability⁹³. Especially potassium phosphate buffer solution (KPi) has attracted great attention and its influence on the catalytic performance has been studied intensively^{87,150}. Still, kinetics at neutral pH is by several orders of magnitude worse compared to strong acid or alkaline media, as illustrated in by Figure 4.31. It shows CV diagrams of several CoO_x electrodes deposited at 1.4 V vs. RHE (deposition charge: 1 C/cm²) from the standard KOH solution and successively measured under different concentrations of KPi. The large shift of the overpotential at 10 mA/cm² of about 190 to 265 mV compared to KOH is noteworthy. But also among the different KPi electrolytes significant differences can be observed. The difference between the brown and blue curves is caused by the addition of K₂SO₄ to increase the conductivity of the 0.1 M KPi electrolyte. The catalytic performance increases significantly. A feature, which all curves have in common, is a supposedly oxidative current starting at around 1.4 V (RHE). It has been suggested that this wave represents the formation of Co⁴⁺ ions^{87,90}, which seems consistent, since also a corresponding reduction wave can be observed and the oxidation potential approximately fits to the potential observed for measurements in KOH. The concentration of KPi possibly influences this redox reaction as indicated by the more pronounced oxidation peak at 1.4 V, which appears to be reproducible only in 1 M KPi (orange curve).

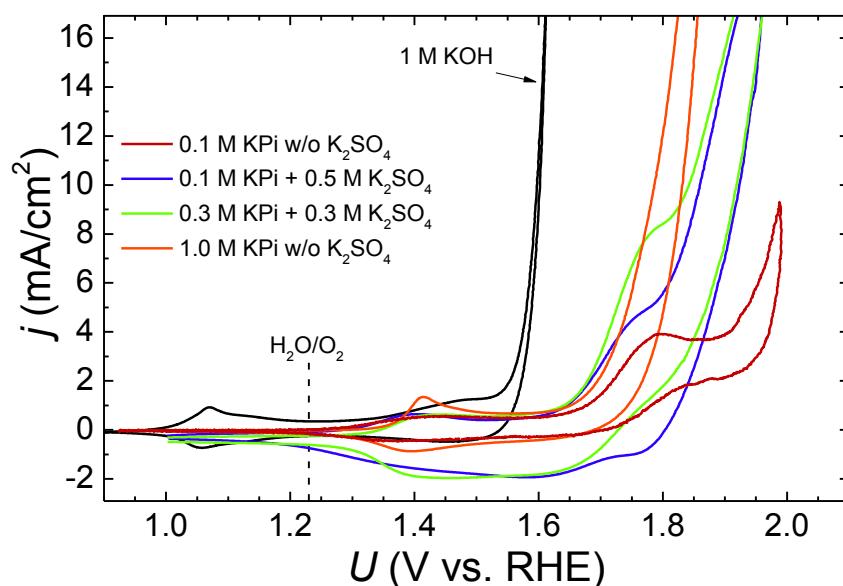


Figure 4.31: CV diagrams of CoO_x measured in 1 M KOH (black) and different concentrations of potassium phosphate buffer solution (KPi). All measurements were conducted at 10 mV/s and corrected for the iR-drop.

A further wave at about 1.75 V can be observed in all measurements except for the one in 1 M KPi. This feature is also heavily influenced by the concentration of the KPi electrolyte and its shape becomes less pronounced with increasing KPi concentration. It is in principle assumable that this wave represents a further oxidation of the catalyst, but it is rather unlikely, because only very few compounds containing Co^{5+} are known and they have to be synthesized under harsh conditions⁵⁴. Furthermore, the wave does not show the typical shape expected for redox reactions with a positive anodic and a negative cathodic current of approximately the same magnitude. Instead, the cathodic scan reveals a similar course as the anodic scan with a positive current. This can be seen best in the brown line scan.

Another possible explanation for this behavior is caused by the porous structure of the catalyst. Initially, at potentials below the onset of the OER, the electrolyte is homogeneously distributed over the entire ECASA. When the applied potential is increased and oxygen evolution starts, OH^- ions are consumed and H^+ ions are produced at the electrode/electrolyte interface due to the anodic OER reactions in neutral media (see chapter 2.1). Low buffer concentrations might not be able to stabilize the pH at 7 inside micro- and nanopores or other not very well accessible regions of the electrode and the pH there drops into the acidic regime. Consequently, the equilibrium potential of $\text{H}_2\text{O}/\text{O}_2$, if measured against the reference electrode, increases according to the Nernst equation (see equation (2)) and the rate of O_2 production (and thus the current) drops. The outer surface is not affected by this effect, since an “unlimited” amount of buffer molecules are available from the bulk of the electrolyte. This is why the O_2 production rates at the outer surface continuously grow with increasing potential. At a certain point (at around 1.82 V) the O_2 production rates inside the pores become negligible or constant (inactivation) and the only contribution to the current increase comes from the outer surface area. Therefore, the current density starts to increase again, but with a different and smaller slope, since the significantly smaller outer surface area of the catalyst now determines the O_2 production rates. This assumption is supported by the fact that because of the higher buffer capacity, the bending in the current curve for the measurement in 0.3 M KPi (green line) appears at a higher current density and after a larger faradaic charge has passed the electrochemical cell (i.e. a larger amount of O_2 has been produced). After the inactivation of the pores, the currents of the green and blue curve are almost the same, because the outer surfaces are nominally identical and the buffer concentration plays no role for the OER at the outer surface. When the concentration of KPi is increased to 1 M, the buffer capacity is high enough to compensate all H^+ ions produced inside the pores, at least for the investigated potential range, which is why the red curve does not show any bending and has a higher slope. It might also be possible that the buffer capacity of the 1 M KPi is high enough to overcome a “first stage” of the O_2 production, where H^+ are produced but mixing and supply of fresh electrolyte caused by O_2 bubble formation and release is not sufficient yet. It could be that at higher O_2 production rates an equilibrium between acidification and electrolyte supply can be formed and continuous OER is possible.

Further evidence for the assumption described above is given by Figure 4.32. The left graph (a) shows a potentiostatic measurement of CoO_x electrodes in KOH (black) and differently concentrated KPi (conductivity has been increased by the addition of K_2SO_4 , see Figure 4.31). The different applied potentials for KOH and KPi were selected to keep the current density approximately at the same level. The black (KOH) and the red line (1 M KPi) decrease very steeply (charging of the double layer capacitor) and turn into steady state very fast. In contrast to that, the blue (0.1 M KPi) and green curve (0.3 M KPi) decrease rather slow but continuously, which can be interpreted as the slow decrease of the O_2 production rates inside the pores due to the decrease of pH as consequence of the OER and the limited buffer capacity of the electrolytes. Unfortunately, the samples measured in 1 M KPi suffer from general degradation to a greater extent, which is why the measured current (red line) is lower than for the other samples. The right graph (b) shows CV diagrams of a sample in 0.1 M KPi with K_2SO_4 at different scan rates. Here, the rate of potential sweep is changed and consequently the bending in the current curve becomes less pronounced and moves to higher current densities the more the scan rate is increased. This is also consistent with the observations made above, because with increased scan rate the potential, where the portion of the current generated at the outer surface area becomes dominant is achieved faster and the effect of the inactivation of the pores cannot be represented by the current curve that well. It might also be that at higher scan rates the inactivation of the pores is not completed at 1.82 V and continues, which manifests as lower overpotential at 10 mV/s. The differences between 10 and 20 mV/s are, however, rather small. Furthermore, the oxidation process at around 1.4 V is shifted to higher potentials, when the scan rate is increased. This suggests that this reaction is not very fast.

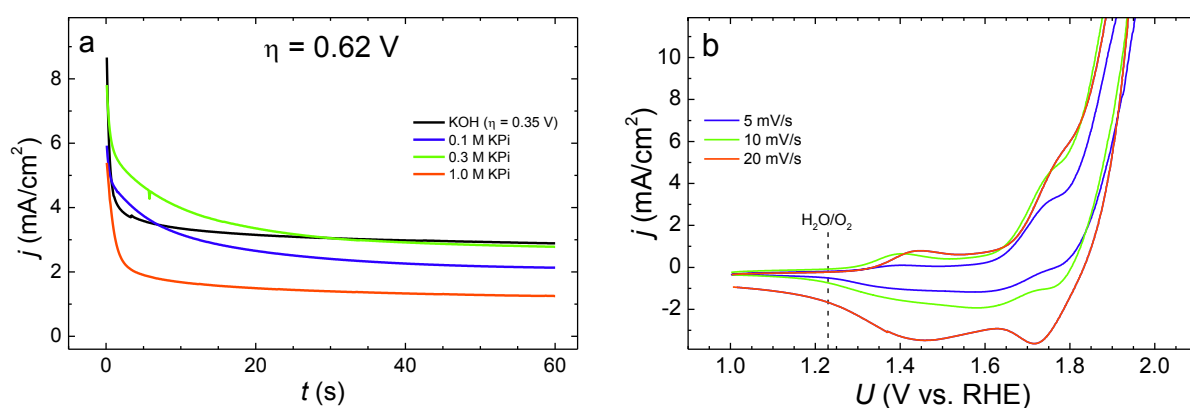


Figure 4.32: (a): Current density j vs. time t in different electrolytes at the overpotential of 0.62 (KPi) and 0.35 V (KOH), respectively. (b): CV diagram of CoO_x electrodes in 0.1 M KPi at different scan rates.

To get deeper insights into this observations DEMS measurements have been performed, the results of which are given in the next chapter.

Comparison to CoPi

The work of Kanan and Nocera⁸⁴, published in 2008, attracted high attention. They reported the synthesis of a highly active cobalt oxide catalyst by a simple electrochemical deposition from a phosphate buffer solution. This so called CoPi catalyst has been studied intensively for its structure and working principles^{87,86,151} and was applied in several systems to improve photoanodes in oxidizing water^{91,92}. This catalyst can therefore be used as a benchmark to estimate the quality of CoO_x presented in this work.

CoPi catalysts have been deposited on FTO from a potassium phosphate solution containing 0.5 mM Co(NO₃)₂, following the proposed protocol⁸⁴, but the potential to be applied has been reduced to 1.5 V (RHE), which is significantly below any oxygen evolving current and ensures that all charge passing the electrode/electrolyte interface is used for film formation⁸⁷. The deposition charge was limited to 100 mC/cm². This limitation was necessary, because a deposition charge of 1000 mC/cm², as it has been usually used in this work, would require the deposition of almost the complete amount of Co²⁺ ions present in the 50 ml of solution used for potentiostatic deposition. Of course, the CoO_x samples for comparison have also been limited to 100 mC/cm² and were deposited at 1.2 V.

Figure 4.33 compares the CoO_x films from this work with CoPi samples in 1 M KOH (a) and in 0.1 M KPi with 0.5 M K₂SO₄ added as conducting salt (b). As can be seen from the right diagram, the CoPi film (blue) is not stable at all in KOH and significantly loses activity within two scans. In comparison to that the CoO_x film (red) shows a very good chemical stability (see chapter 4.1.2.8). The depicted red line represents the second cycle.

In neutral electrolyte on the other hand (b) the activity of both catalysts is comparable to one another and to literature values^{87,152}. Both curves show the same bending at around 1.8 V as it has been described above. However, kinetics seem to be slightly better for CoPi, because of the steeper slope of the current after the OER onset, in return CoO_x might have a larger ECASA, since the capacitive portion of the current is higher. Further studies would have to be done to elucidate these questions, but this was not the scope of this thesis. As a result from this comparison it can be stated that the CoO_x electrodes presented here are far superior to CoPi, when measured in 1 M KOH electrolyte. At neutral pH, their activity is similar.

4. Results and discussion

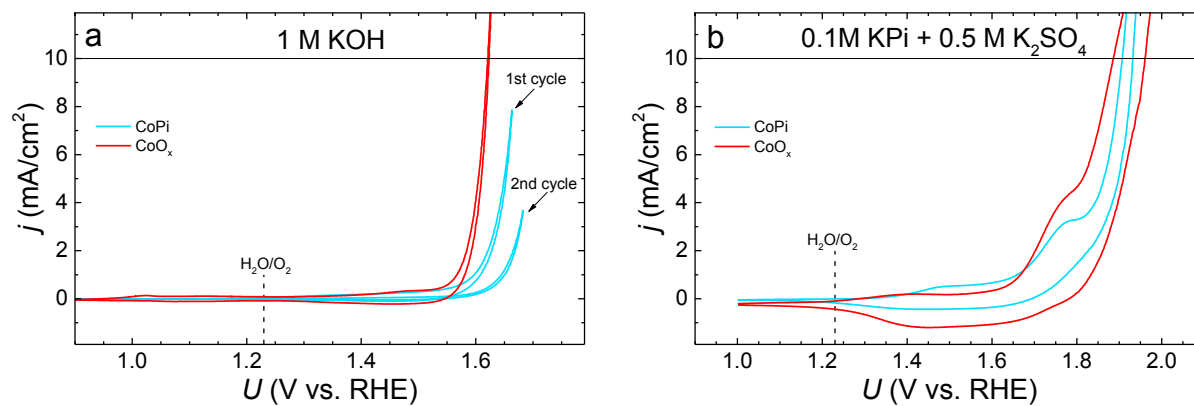


Figure 4.33: CV diagrams of CoO_x and CoPi in 1 M KOH (a) and 0.1 M KPi + 0.5 M K₂SO₄ (b), respectively. All samples had a deposition charge of 0.1 C/cm² and were deposited at 1.2 (CoO_x) and 1.5 V vs. RHE (CoPi), respectively. The scan rate was 10 mV/s and the potential was corrected with respect to the iR-drop.

4.1.2.7. Differential electrochemical mass spectroscopy (DEMS)

Selectivity and stability are two main criteria of catalysts and knowledge about the kind of the reaction products is crucial. Thus, differential electrochemical mass spectrometry (DEMS) measurements (see section 3.2.1.2) were carried out to investigate whether the current generated by CoO_x electrocatalysts in the anodic potential regime actually corresponds to O_2 formation or is related to corrosion phenomena of the catalyst itself.

In the course of electrochemical measurements on electrodeposited CoO_x electrodes of different thickness (see chapter 4.1.2.1) it was observed that after the samples were freshly immersed into the electrolyte, the first anodic scan of CV investigations always showed a significantly higher current density in the range before OER onset. This is exemplarily shown in Figure 4.34. From the consecutive cathodic scan on, the curve progression showed a very similar and reversible behavior for all following cycles. It is known from metallic electrodes such as platinum¹⁵³ that cycling in the anodic regime oxidizes species on the electrode surface and removes (organic) contaminations. This could also be the case for the CoO_x films investigated in this work, as an organic complexing agent (Na-gluconate) was used during the deposition of the catalysts. To elucidate this question DEMS measurements can contribute.

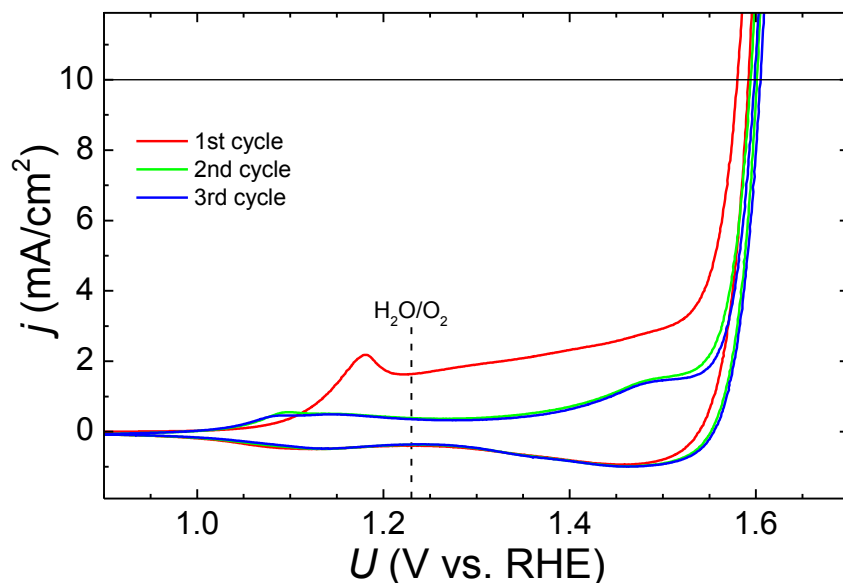


Figure 4.34: First, second and third cycle of a regular CV experiment. The deposition potential was 1.2 V, the deposition charge 1000 mC/cm². The measurement has been corrected for the iR-drop and was performed in 1 M KOH at 10 mV/s.

Figure 4.35 shows the current and the mass signals of O_2 and CO_2 as a function of the applied potential in a KOH electrolyte. As can be seen from the blue curve, the oxygen evolution starts at around 1.5 V and goes along with the start of the faradaic current. This is a clear evidence for the electrocatalytic character of the CoO_x films. Moreover, it can be seen that the slight current

increase at about 1.4 to 1.45 V (marked with an arrow) can be indeed attributed to an oxidation process within the CoO_x film, as it is not accompanied with any O_2 formation. The smaller magnitude of this feature compared to other CV diagrams in this work is caused by the very slow scan rate of 2 mV/s.

The CO_2 mass signal was also recorded, since it is a potential product from the oxidation of organic contaminations on the surface of the catalyst. As can be seen from the black curve no CO_2 was detected throughout the whole investigated potential regime. This, however, allows no final conclusion about the nature of the increased current in the first CV scan, since it is well known that CO_2 forms carbonates in contact with bases and it is possible that the formed CO_2 cannot reach the membrane fast enough to be detected in the mass spectrometer.

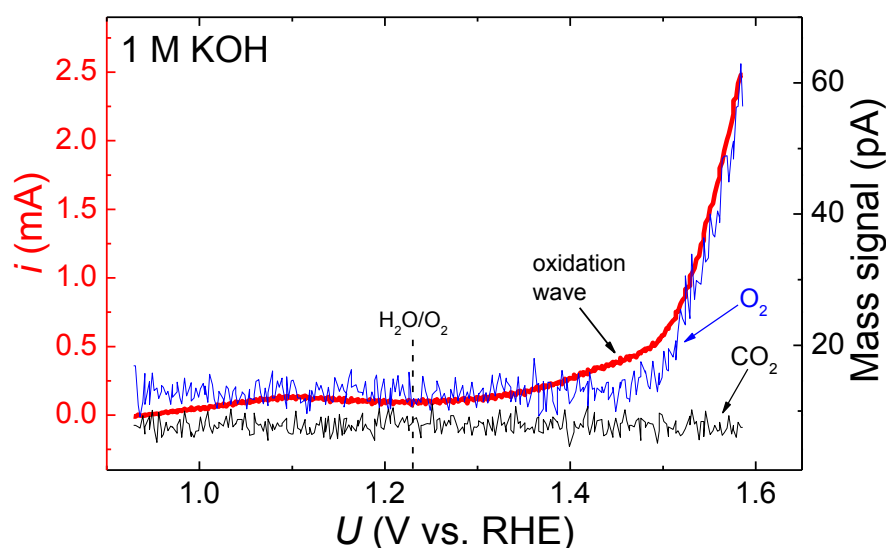


Figure 4.35: DEMS measurement performed in 1 M KOH at 2 mV/s. The red curve represents the current i as function of the applied potential U and the black and blue lines are the corresponding mass signals of CO_2 and O_2 , respectively.

Therefore, also measurements in 0.1 KPi with 0.5 M K_2SO_4 as conducting salt were performed. The black line in Figure 4.36a displays again the CO_2 mass signal and approves that in this electrolyte CO_2 can actually be detected in the first CV scan. The signal seems to correspond to the first peak in the current curve (red line), but has, however, a quite large delay. Nevertheless, the signal declines after a short time and in the second cycle (Figure 4.36b) no CO_2 evolution can be detected. This behavior can be regarded as confirmation of the oxidative removal of organic contaminations and/or residuals from the deposition process in the first cycle of the CV measurement.

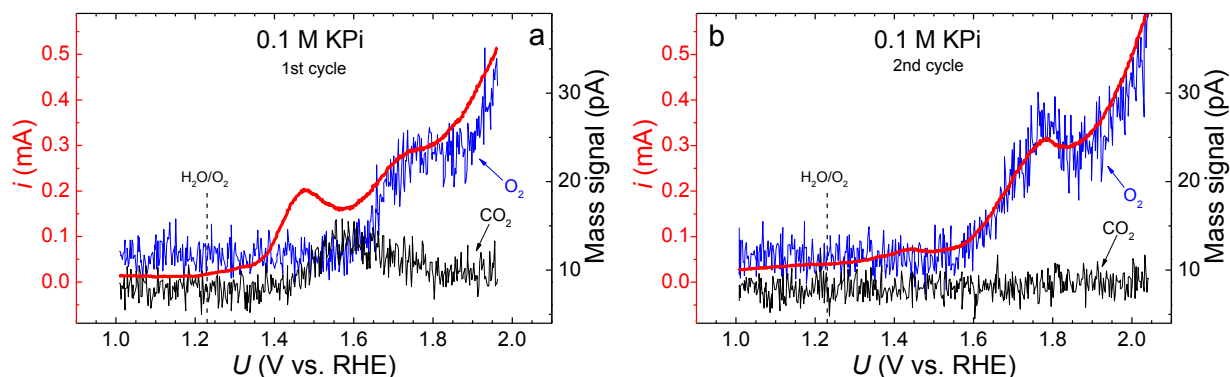


Figure 4.36: DEMS measurements of the first (a) and second (b) cycle of a CoO_x electrode measured in 0.1 M potassium phosphate buffer (KPi) solution at a sweep rate of 2 mV/s. The red curve represents the current i as function of the applied potential U and the black and blue lines are the corresponding mass signals related to CO_2 and O_2 , respectively.

The progress of the O_2 mass signal in Figure 4.36 is very interesting. As mentioned in the previous chapter the bending of the curve at around 1.8 V is attributed to an inactivation of less accessible sites of the catalyst due to a decrease of pH. Figure 4.36 supports this interpretation, because the O_2 mass signal follows almost exactly the course of the current. If the feature would be an internal oxidation process in the volume of the CoO_x catalyst, one should not expect such a correlation.

As a conclusion, it can be stated that oxygen evolution is possible at pH7, but at much lower rates compared to an alkaline electrolyte. One has to ensure that the buffer capacity of the electrolyte is high enough to compensate for produced H^+ ions in the course of OER, especially in poorly accessible sites. Unfortunately, it has also to be mentioned that the stability of the CoO_x electrodes in KPi is worse than in KOH. This property has not been investigated systematically in this work, but from the results and the condition of the films after the electrochemical measurements it can be concluded that the CoO_x catalyst presented here, is much more applicable in alkaline solutions. A more detailed study of the stability in KOH is presented in the next chapter.

4.1.2.8. Stability of CoO_x electrodes

Stability of the electrodes is one of the key issues in electrocatalysis. A catalyst being not stable for long periods of time is useless, no matter how high the catalytic activity initially might be. In this section two types of stability will be considered. First, the mechanical stability will be investigated, which is defined in this case as the strength of adhesion towards the substrate and the resistance to flaking off, respectively. On the other hand, the electrochemical stability will be examined, which comprises a continuously high activity towards the OER and the ability of keeping the oxygen production at constant rates under defined conditions.

Mechanical stability

The electrocatalytically active thin films investigated in this work have to perform under chemically and mechanically harsh conditions. It is crucial that they stay well attached to the substrate and do not dissolve or peel off from the support under operation. During the experiments it turned out that this mechanical stability is not given in every case. Figure 4.37 shows a photograph and a SEM image of partly detached film segments. Interestingly, the film comes partially off the substrate also outside the electrochemically investigated “round spot” in the middle of the sample (marked with an arrow). This happens only due to contact with KOH or during rinsing with deionized water after the electrochemical measurements. It could not be resolved which factors are responsible for the partial relieve of the films, since the phenomenon appeared seemingly at random, to very different extents and just on a minor number of samples, deposited under varying conditions. Possibly, the local quality of the substrate, some residual contaminations, the formation of shrinking cracks⁸⁰ and/or the gas bubble formation play a role, which is a problem especially when the sample is kept upside down as it is the case for DEMS and in-line XPS measurements.

The SEM image in Figure 4.37 shows that the film actually peels off the substrate and does not dissolve into the electrolyte, as a few patches of the film have indeed lost contact to the substrate, but appear in the same shape as the attached ones. On the other hand, the SEM image shows another very interesting fact, namely that the CoO_x film grows on a very well formed, tight connection to the substrate, which is crucial for a good electrical contact and reduction of ohmic losses. This can be seen from the islet turned upside down in the upper part of the image (marked with an arrow), which appears to have a replica of the FTO structure on its back side.

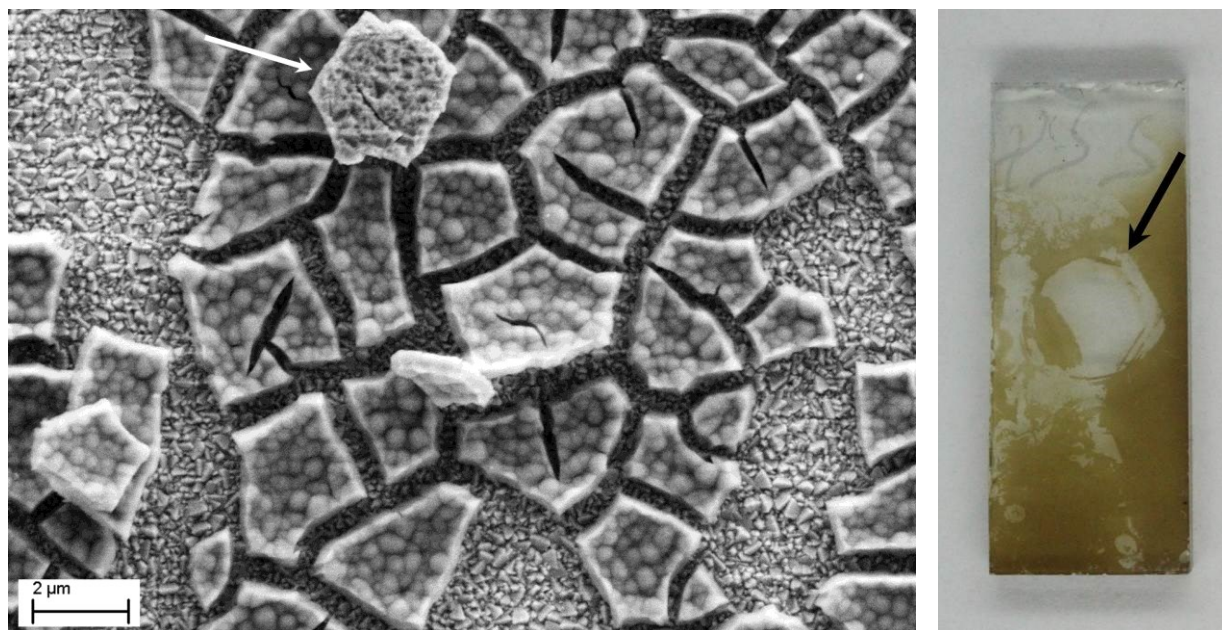


Figure 4.37: SEM image and photograph of a partially detached CoO_x thin film.

Interestingly, even if the film was optically fully detached from the FTO/glass substrate, there was still some OER activity detectable, as shown in Figure 4.38a. The red line represents a CV curve of a CoO_x film, which peeled off completely during the electrochemical measurement. Apparently, not all of the cobalt oxide is removed and the overpotential at 10 mA/cm^2 was in the range of films with a deposited charge of $10\text{--}50 \text{ mC/cm}^2$ (see Figure 4.21). It could not be resolved in the SEM, if this activity comes from a few residual islets of the original film or if a rather thin “underlayer” of CoO_x stays homogeneously connected to the FTO throughout the electrochemically active spot, but some catalyst material remains definitely well attached.

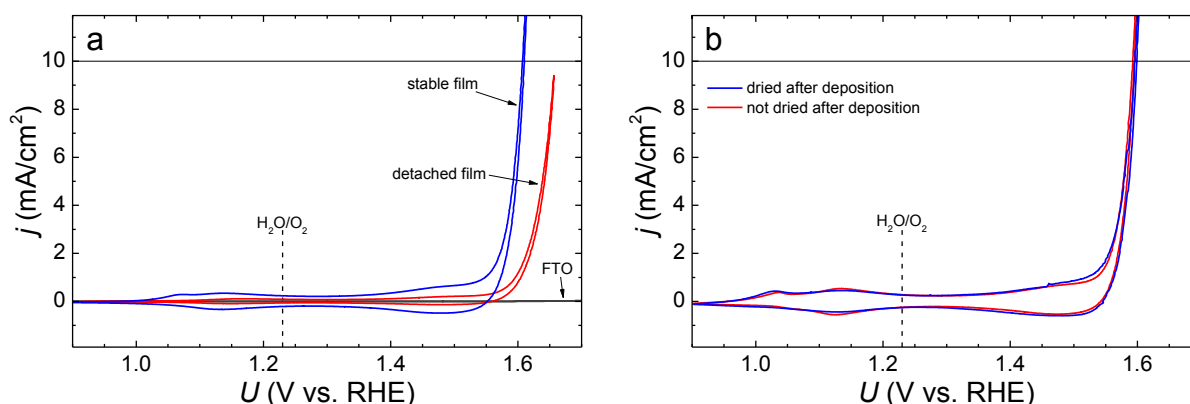


Figure 4.38: (a): Comparison of the CV diagrams of a stable CoO_x film and a film, which detached from the substrate in the electrochemically active spot. The films were deposited under the same conditions (1.4 V , 1000 mC/cm^2). (b): Comparison of the activity of a sample, which was dried at RT in air after the deposition (blue) and a sample, which was electrochemically characterized immediately after the deposition. The measurements have been corrected for the iR -drop and were carried out in 1 M KOH (pH 14) at a scan rate of 10 mV/s .

Finally, it was observed that the detachment of the films appeared only on some samples, which were completely dried between deposition and electrochemical characterization. Thus, the formation of shrinking cracks (see Figure 4.11) most likely has a strong influence on the adhesion of the film. Even though the mechanical stability of the thin films is possibly influenced by whether the sample was dried or not, the electrocatalytic activity is independent of that, as a comparison of a dried sample with one that was kept in the electrolyte shows (Figure 4.38b). For the application in a photoelectrochemical device, however, it is recommended to make sure the sample stays permanently in contact with the electrolyte to avoid film detachment.

Electrochemical stability

For being applicable in a photoelectrochemical device, an electrocatalyst has to keep working at the same efficiency for a long period of time. Therefore, some long term experiments were conducted on CoO_x electrocatalyst. Figure 4.39 shows a galvanostatic measurement at 10 mA/cm^2 for 48 hours. The sample ($A = 2 \text{ cm}^2$) was fully immersed in the electrolyte and rotated at a speed of around 400 rpm to prevent surface deactivation by gas bubbles and diffusion limitations. In addition, the electrolyte was continuously bubbled with N_2 . As can be seen from the graph the iR-corrected overpotential decreases slightly from around 400 to 385 mV during the investigated period of time. The scattering in the curve is attributed to sample rotation. Even though the activity of the electrode increases over time, the change in overpotential is too small to be a reliable evidence for a further activation of the catalyst by the ongoing water oxidation process. Instead, small deviations in the measurement parameters, e.g. in the potential of the reference electrode, may also play a role. A more detailed study on the long term performance of the catalysts, including measurements over several thousands of hours, might elucidate if there is a significant increase of the catalyst's activity. Such a study, however, is beyond the scope of this work and hence the CoO_x catalysts are considered to be electrochemically stable under alkaline conditions.

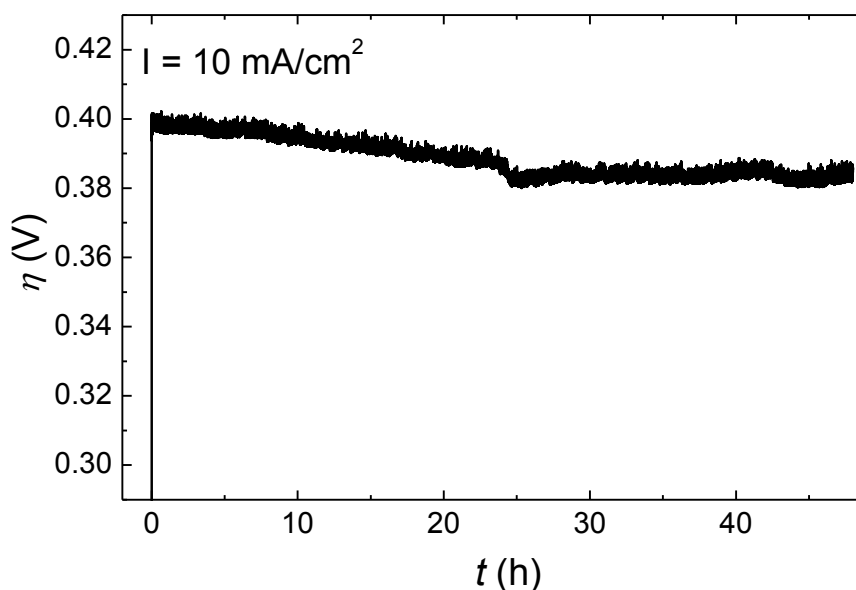


Figure 4.39: Overpotential η versus time t for a galvanostatic measurement at a current density of 10 mA/cm^2 . The potential has been corrected for the iR-drop; the electrolyte was 1 M KOH . The sample was fully immersed (2 cm^2) in the electrolyte and rotated with a speed of around 400 rpm .

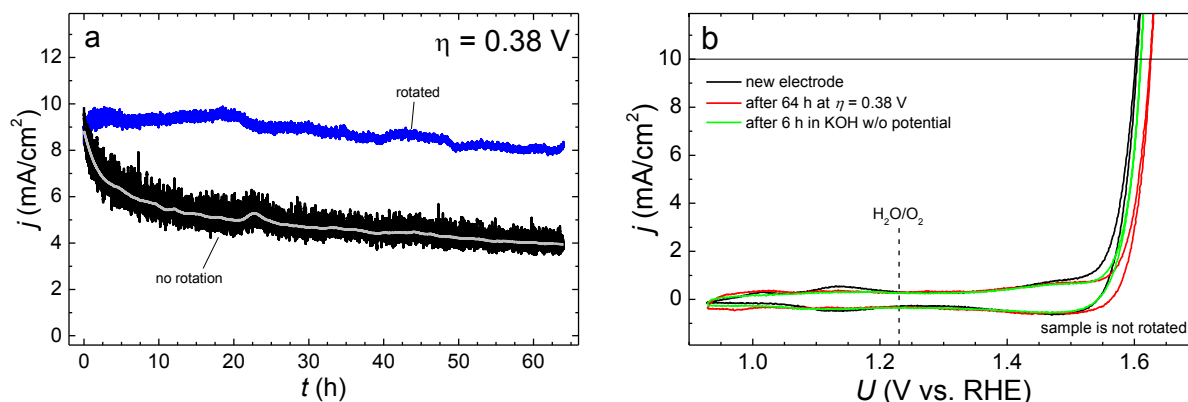


Figure 4.40: (a): Long term potentiostatic measurement (current density j versus time t) in 1 M KOH at an overpotential of $\eta = 0.38 \text{ V}$. The measurements were carried out with (blue curve) and without (black and gray curves) sample rotation and iR-compensation, respectively. (b): CV diagrams before and after the potentiostatic measurement shown in (a) (black curve). The measurements have been corrected for the iR-drop and were carried out in 1 M KOH (pH 14) at a scan rate of 10 mV/s .

For an application in a photoelectrochemical device it is of particular interest to know which current density can be generated by the electrocatalyst, if a constant potential is provided by the photoactive semiconductor and how stable that generated current density is over time. This is crucial for calculating the solar to hydrogen efficiency (STH) and for estimating the long term performance of the photoelectrochemical device. In Figure 4.40a potentiostatic measurements at an overpotential of 380 mV over 64 hours are depicted. It has been published that a maximum overpotential of $350\text{--}400 \text{ mV}$ for the OER at 10 mA/cm^2 is required for a high efficiency

photoelectrochemical device^{154–156}. Thus, the overpotential of 380 mV has been chosen, since it lies within the range mentioned above and the current of the CoO_x samples exceeds 10 mA/cm² in the CV diagrams approximately at this overpotential.

Two kinds of experiments have been compared. The blue curve shows the current density over time of a sample fully immersed in the electrolyte (2 cm²) and rotated at 400 rpm. Furthermore, the iR-drop of the setup has been corrected automatically and continuously by the potentiostat, to guarantee that the potential at the electrode/electrolyte interface stays constant. As can be seen in the graph, the current density decreases slightly from about 9 to 8 mA/cm² in a time period of 64 hours. The decrease however is not constant but interrupted by periods of increasing current density. Considering this and the slope of the CV diagram in the potential range around the overpotential of 0.38 V (the current density increases by 1 mA/cm² within 4 mV in this region) it is possible that the changes of the current density are again caused by experimental parameters (cf. Figure 4.39). Since the absolute current flow in this experiment is located in the range from 18 to 20 mA also very small errors in the iR-compensation might play a significant role. Again, further long term studies have to be performed to clarify if an effect of the applied potential actually exists, but for this work the electrocatalyst is considered to be stable.

The black curve on the other hand shows the development of the current density over time of a CoO_x electrocatalyst measured in a stationary electrochemical cell with an exposed sample area of 0.31 cm² and neither rotation of the sample nor any gas flow through the electrolyte to stir it. Obviously, the generated current density decreases by a factor of two over the investigated time of 64 hours. The current value scatters very much during the whole measurement, which is explained by gas bubble formation (low current density) and detachment (sudden increase in current density). Therefore, the black curve has been smoothed (gray line) subsequently to the measurement to follow the development of the current more easily. Interestingly, this deactivation of the electrocatalyst seems to be reversible as the CV diagrams in Figure 4.40b show. They correspond to the very same sample and show current-voltage measurements before (black) and after (red) the potentiostatic long term experiment and after 6 hours of rest in KOH (green) without any applied potential. While the red line has a significantly higher overpotential at 10 mA/cm², the green curve gives an overpotential very close to the one before the long term experiment. Apparently, the electrocatalyst is stable over time, but disadvantageous effects connected to the OER, most probably the gas bubble formation and consequently an increasing number of blocked active sites, result in a slow decrease of current density. Another fact, which has to be considered, is that during this potentiostatic experiment no iR-compensation was performed. Due to the relatively low absolute current flow of around 3 mA, the errors resulting from this might be relatively small, but it is possible that the actual potential at the electrode/electrolyte interface was not entirely constant throughout the experiment since the potential drop in the electrochemical cell depends on the current flow. However, this experiment resembles the actual conditions in a photoelectrochemical cell better than the potentiostatic

experiment with a rotated electrode (blue curve) and stresses out how important the design of a PEC is to its performance¹⁵⁷. Considering 10 hours of sunlight per day followed by 14 hours of weak or no light, the CoO_x might be applicable in a PEC if the design of the cells (constant electrolyte flow etc.) is optimized, even though a certain decrease in efficiency during the day can be expected. The “resting” time overnight should be sufficient to guarantee a constant efficiency every day.

4.1.3. Spectroscopic analysis

4.1.3.1. In-line SXPS

As described in more detail in chapter 3.2.2.1, in-line synchrotron XPS measurements were performed at the U49/2 beamline at Bessy II in Berlin Adlershof, to characterize the catalyst surface in dependence of the applied potential. The SoLIAS endstation (Technical University Darmstadt) has been used for the measurements. The samples were subjected to different constant anodic potentials in an electrochemical cell held under inert N_2 atmosphere and after removal of the electrolyte the samples could be transferred directly into the UHV system of the SoLIAS for XPS characterization, without any contact to the ambient atmosphere.

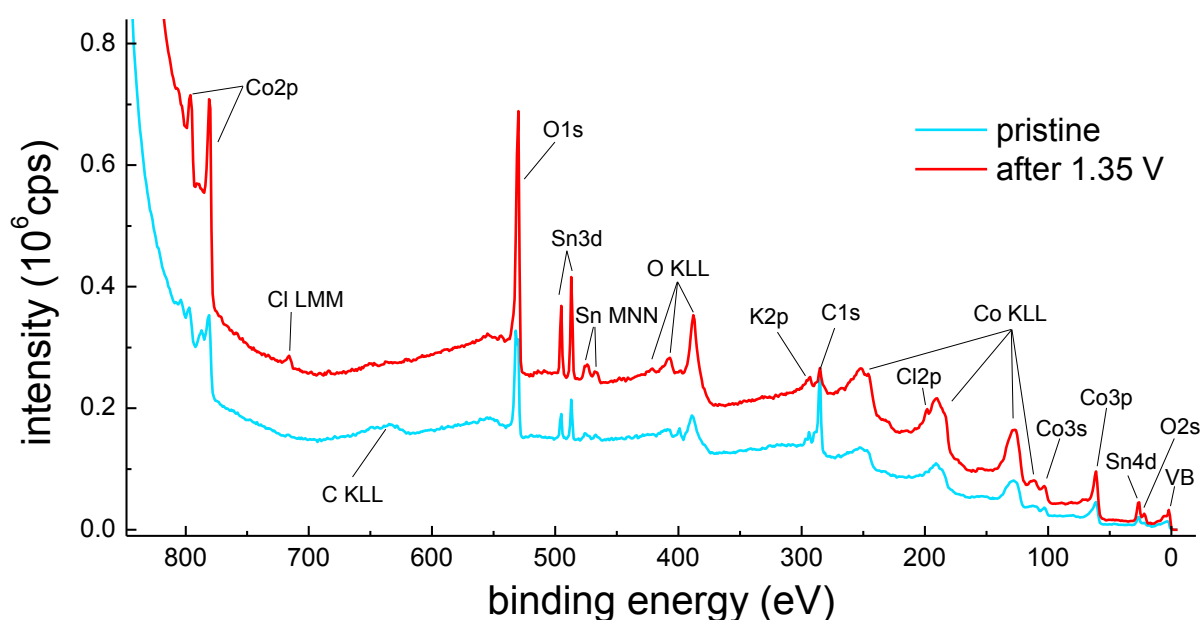


Figure 4.41: XPS overview spectra of the pristine CoO_x sample (blue) and after the sample has been subjected to a potential of 1.35 V vs. RHE (red). The most important features are marked within the graph. Excitation energy was 900 eV.

Figure 4.41 shows the XPS overview spectra of an as-deposited (pristine) sample and the same sample after it has been subjected to a potential of 1.35 V vs. RHE. The most prominent features of the spectra are marked in the graph. Obviously, the signal intensity increases after the application of 1.35 V, which is attributed to “electrochemical cleaning” of the sample surface (see also chapter 4.1.2.7). A significant amount of contamination can be expected on the sample surface, coming from both the deposition process (e.g. residuals of gluconate complexes) and the storage in air previous to the measurement. The considerably higher C1s and C KLL peaks in the pristine sample confirm that. Furthermore, small residuals from the KOH electrolyte can be observed in the K2p peak. Interestingly, chlorine appears after the electrochemical treatment. The only possible source for this impurity is the reference electrode containing KCl as electrolyte,

which might diffuse through the diaphragm at the tip of the electrode. However, since the measurement was conducted in 1 M KOH (pH 14) and the thermodynamic equilibrium potential of Cl^-/Cl_2 is pH independent at 1.36 V vs. NHE³⁰, compared to 0.404 V vs. NHE for $\text{H}_2\text{O}/\text{O}_2$ (cf. equation (2)), the effect of the chlorine at the sample surface is considered to be negligible.

In all measurements a pronounced Sn3d signal appears which originates from the FTO substrate indicating that the film is not completely closed. To check whether the FTO is actually inert towards the OER in the considered potential range, also measurements on a blank substrate have been performed which did not show any changes in the spectra (not shown).

Figure 4.42 depicts the CV diagram of a sample measured in the electrochemical cell (“glass cross”) attached to the UHV system of the SoLIAS endstation. The potentials, which were applied potentiostatically before SXPS investigations are marked with blue bars. The gray curve represents the actually measured current values as function of the potential, set by the potentiostat. However, due to the design of the glass cross and the long distance between the working (sample) and reference electrode a significant setup resistance of about 160 Ω was determined by impedance spectroscopy. Consequently, the black curve in the diagram represents the “real” potential values at the electrode/electrolyte interface after the correction for the iR -drop, according to equation (9). This leads to the fact that the applied potential of 1.9 V appears as only 1.6 V at the catalyst surface, which it is hence denoted as measurement point in the graphs.

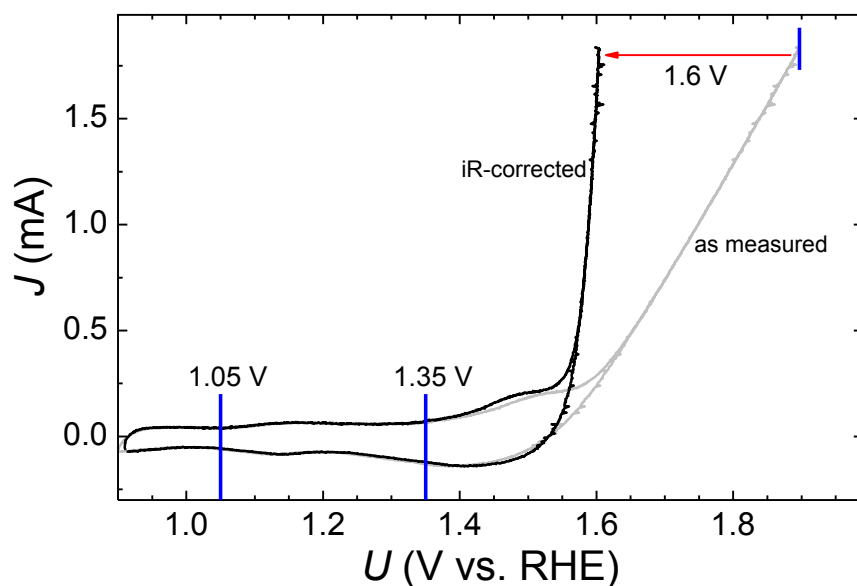


Figure 4.42: CV diagram of a CoO_x electrode recorded inside the glass cross without (grey) and after iR -correction (black). The measured cell resistance was 160 Ω . The position of the investigated potentials are marked with blue bars.

For the anodization of the samples, the denoted potentials have been applied to the electrocatalyst until a steady state current was achieved (usually 1 to 2 minutes). The contact of the sample to the electrolyte was then rapidly interrupted, while the potential was still applied. It is supposed that in this manner the surface state of the catalyst can be conserved. After a quick but thorough removal of residual electrolyte with deionized water, the sample was dried in a N₂ stream and immediately transferred into the UHV system to perform SXPS measurements. This procedure was repeated several times and different potentials have been applied to the thin film in the following order: first, a potential in between the two redox features was selected (1.35 V), followed by a potential in the OER regime (1.6 V). Successively, the potential was reduced to 1.05 V to proof the reversibility of the observed effects.

Excitation energies to monitor high resolution spectra were set to 900 eV for Co2p and 650 eV for O1s, respectively. These values represent a compromise between the intention to measure as surface sensitive as possible (maximum surface sensitivity would be achieved at excitation energies of about 830 eV and 580 eV, respectively) and the need to obtain a clear signal, which is superimposed by the rather well pronounced secondary electron tale at low electron kinetic energies (i.e. high binding energies), owing to the rough surface morphology and porosity of the CoO_x electrocatalysts. In Figure 4.41 the very steep intensity increase at the left end of the diagram is well visible. In general, thin films with a rough surface topography suffer from severe photoelectron scattering, which affects the signal intensity and impedes SXPS analysis.

First insights into the results are given by unmodified Co2p high resolution spectra of a CoO_x sample¹¹² in Figure 4.43. The pristine sample (bottom spectrum) reveals a surface oxidation state of predominantly Co²⁺, which is indicated by the peak position and the intense shake-up satellite (ss) at about 5.8 eV located at the left side of the main 2p_{3/2} peak^{55,158}. Shake-up satellites arise due to the interaction of photoelectrons with valence electrons in an outer shell of the atom or ion and lead to a defined kinetic energy loss (i.e. increase in binding energy) of the excited photoelectron. The intensity and position of the shake-up satellite depend on the investigated element, its oxidation state and the kind of photoelectron-valence electron interaction. After application of a potential of 1.35 V (RHE), cobalt ions at the surface oxidize to Co³⁺, which is expressed by a slight right shift of the Co2p_{3/2} main peak, but even more by a pronounced loss of intensity of the shake-up satellite and its shift to a position about 10 eV higher than the main 2p_{3/2} peak^{55,158}. In photoelectron spectroscopy it is unusual that the binding energy of an ion decreases at a higher oxidation state, but for Co³⁺ it is a well-known phenomenon, which is related to the larger relaxation energy of the Co³⁺ species after the photoexcitation process, compared to the Co²⁺ final state relaxation¹⁵⁹. These results are in agreement with similar measurements on native oxides grown on Co metal¹⁶⁰. However, it cannot be concluded definitively from this spectrum whether the oxidation towards Co³⁺ is complete or happened only to a large fraction and Co²⁺ is still partially present. A more detailed analysis is given below.

Further increase of the applied potential to 1.6 V, which is well above the onset potential of the OER, does not change the spectrum significantly. This is surprising, since the oxidation wave of CoO_x at about 1.5 V in Figure 4.42 suggests the formation of Co^{4+} species. But even in the very surface sensitive SXPS measurements no evidence for any significant amount of Co^{4+} could be found. Such a species would appear as a shoulder at the high energy side of the $\text{Co}2p_{3/2}$ main peak and, more indicative, a shake-up satellite at about 786.6 eV would become visible¹⁶¹. From this point of view, the Co^{3+} oxidation state might be responsible for the high activity of CoO_x ¹⁰³.

Moreover, a reduction of the applied potential to 1.05 V, which is even lower than the redox peak at about 1.15 V, does not change the $\text{Co}2p$ spectra either, even though a significant amount of Co^{2+} could be expected from the current voltage plot.

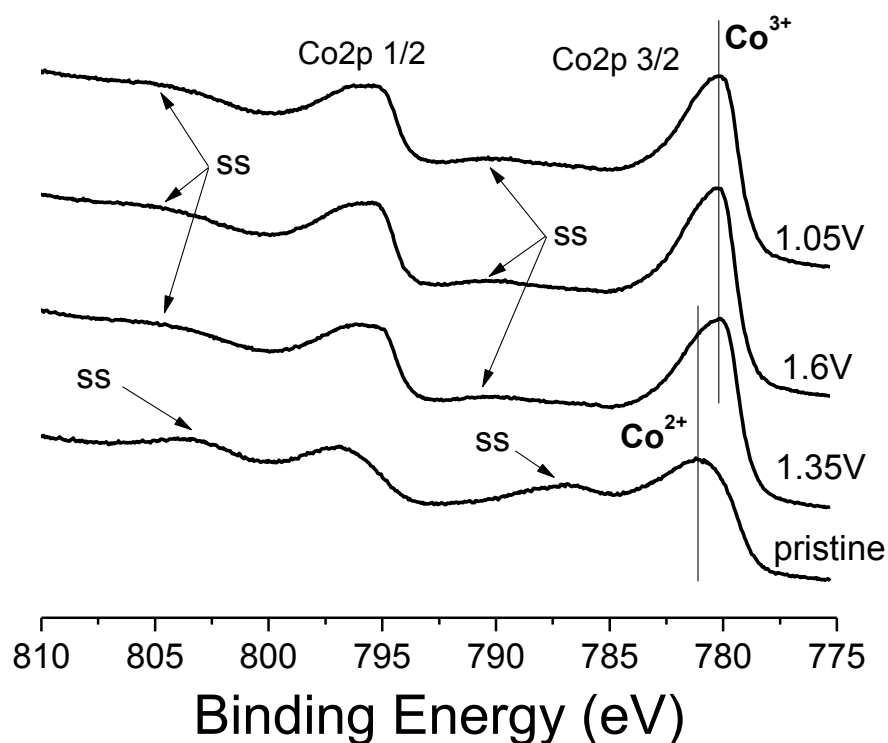


Figure 4.43: Co2p photoelectron spectra of CoO_x after the application of different anodic potentials. The binding energies of Co^{2+} and Co^{3+} are marked by vertical lines, shake-up satellites are indicated as ss.

In Figure 4.44 the high resolution spectra of $\text{Co}2p_{3/2}$ (a, c, e, g) and $\text{O}1s$ (b, d, f, h) have been analyzed in more detail. As usual for p orbitals, the $\text{Co}2p$ peak shows a spin-orbit splitting into two components, namely $2p_{1/2}$ at higher and $2p_{3/2}$ at lower binding energies. Both contain the same chemical information¹⁶², which is why peak-fitting was performed only on the $\text{Co}2p_{3/2}$ peak. Prior to the deconvolution of the peaks, the spectral background was calculated according to Shirley¹⁶³ and subtracted. In the deconvolution process, additive coupling of Gauß and Lorentz

functions was applied. All spectra were charge corrected towards an Au-standard ($\text{Au}4f_{5/2} = 84 \text{ eV}^{164}$) measured before and after the measurements on the sample. A comparison with the position of the $\text{C}1s$ peak of the samples, attributed to adventitious hydrocarbons ($\text{C-H}_2 = 284.8 \text{ eV}$), was in good agreement to that. The fitting parameters are summarized in Table 4.4.

As can be seen from Figure 4.44a, four peaks are necessary to deconvolute the pristine $\text{Co}2p_{3/2}$ spectrum. The contributions at 779.7 (orange) and 780.7 eV (cyan) can easily be assigned to lattice Co^{3+} and Co^{2+} , respectively^{55,158,159,165–169}. More difficult is the identification of the other two peaks. The feature at 781.7 (green) was attributed to (surface) Co-OH , even though most literature values for this peak are found at slightly lower binding energies^{166,168,170–173}. This assignment is justifiable, because the deconvoluted $\text{O}1s$ spectrum in Figure 4.44b gives strong evidence for OH groups (see below) and a distinction between Co^{2+} in the lattice of Co_3O_4 (and CoO) and Co(OH)_2 can be expected from the reported binding energies¹⁶⁶. A general shift of about 0.2 eV towards higher binding energies can furthermore be observed for the pristine sample compared to the other measurements, which might be an explanation for the high binding energy values of Co(OH)_2 . The origin of the peak at 783.0 (labeled as A, pink) on the other hand is rather unclear. The binding energy distance from the well documented Co^{3+} and Co^{2+} peaks seems rather large for being a chemical shift and it is in addition unlikely that further, very distinct chemical states of cobalt are present in the sample. The peak has previously been observed in Co(OH)_2 and Co_3O_4 nanoparticles¹⁷⁰. A description of its physical nature is missing, though. One can therefore speculate that some final state effects, probably related to interactions of some photoelectrons with the outer shell of the Co-ions, are responsible for the appearance of peak A.

However, it is obvious from Figure 4.44a that the pristine sample contains a significant amount of Co^{3+} . Considering the deposition process at 1.4 V (RHE) one would even expect a much higher content of Co^{3+} than it is actually the case. Nevertheless, lattice Co^{2+} and Co(OH)_2 represent the major part of the peak. A possible explanation for the presence of Co(OH)_2 on the surface of the pristine sample can be given by a dissolution precipitation mechanism¹⁶⁰ in the presence of Co^{2+} ions in solution, which transform from a $[\text{Co(OH)}_4]^{2-}$ complex to deposited Co(OH)_2 on the top of the catalyst. Another possible reason is related to the multi-step deposition mechanism (see chapter 3.1). If the decomposition of the $\text{Co}_2\text{L}_2^{3-}$ complex and the oxidation of the Co^{2+} ions happen consecutively and not simultaneously it is possible that a thin layer of not yet oxidized Co(OH)_2 remains at the top of the film, if the deposition potential is turned off rapidly.

The portion of lattice Co^{2+} is too high for representing only Co_3O_4 , as the relation of Co^{2+} to Co^{3+} in this compound is 1:2. As it is not possible to distinguish between Co^{2+} in the octahedral sites of CoO and Co^{2+} in the tetrahedral sites of Co_3O_4 a certain amount of CoO might be present too. Moreover, the pronounced shake-up satellite at around 778 eV (see Figure 4.43) is a strong evidence for the presence of CoO . This is quite surprising and was not expected, since CoO is known for being insulating and detrimental for the OER activity⁵⁸. However, as the peak area of

Co^{2+} significantly decreases after potential application, it is likely that CoO simply oxidizes to Co_3O_4 and plays no role in the OER.

The deconvolution of the O1s peak of the pristine layer in Figure 4.44b shows a strong peak at 531.4 eV (blue), which can be attributed to -OH groups^{166,170,174,175} and confirms the presence of $\text{Co}(\text{OH})_2$. However, the peak area is too large to represent only $\text{Co}(\text{OH})_2$, especially if compared to the relative fraction of the corresponding Co-OH peak (green) in Figure 4.44a. It is thus assumed that the -OH peak in Figure 4.44b also comprises some other hydroxides, most probably from residual gluconic acid and KOH electrolyte from the deposition process¹⁶⁴, which both cannot be resolved as distinct peaks. The other features in the O1s peak are assigned to lattice oxygen of cobalt oxide (529.5 eV, pink)^{55,159,166,175}, lattice oxygen of the FTO substrate (530.7 eV, gray) and a broad peak of rather undefined surface oxygen (533.2 eV, yellow), which probably contains components of water, carbonates, carboxyls¹⁶⁴ and other common organic pollutants. A distinction between differently bonded lattice oxygen is hardly possible for cobalt oxides, because of the rather small chemical shifts^{55,166,176} between oxygen bound to Co^{3+} and Co^{2+} , respectively.

After electrochemical treatment of the sample at 1.35 V, both the $\text{Co}2p_{3/2}$ and the O1s peak show substantial changes (Figure 4.44c and d). A small shift of all peaks of about 0.1 to 0.2 eV towards lower binding energies can be observed. The portion of Co^{3+} significantly increases in relation to lattice Co^{2+} . Furthermore, the relative amounts of Co-OH and peak A decrease. However, a complete oxidation to the trivalent state of cobalt does not occur, as Co^{2+} as well as -OH groups are still present in the sample. It might be that not all Co-ions at the sample surface are either accessible or capable for being oxidized to higher valences, but only a limited amount can take part in the reaction. Evidence for this assumption has already been given in Figure 4.27c (chapter 4.1.2.4), where it is shown that the overall portion of Co-ions undergoing a transition in the oxidation state is rather low. The relation of the peak areas of lattice Co^{3+} (orange) and Co^{2+} (cyan) is now approximately 2:1, which is a strong evidence for the presence of Co_3O_4 . This assumption is consistent with results from electrochemical investigations, which suggests an increased appearance of Co_3O_4 in the potential region around 1.35 V. The peak representing surface oxygen (yellow) on the other hand disappears upon electrochemical treatment. This can be interpreted as a result of the applied potential, “cleaning” the surface from contaminations.

After increasing the potential from 1.35 to 1.6 V (Figure 4.44e and f), both lattice Co oxidation states and Co-OH are still present in the sample, even in similar quantities. From the CV diagram (see Figure 4.42), one should expect the appearance of Co^{4+} ions, but no evidence for the rise of a new species is recognizable in the spectra. In this respect, it has to be noted that only very few reports have been published, which show XPS spectra of Co^{4+} species¹⁶¹ and to the best of the author’s knowledge no stable CoO_2 compound was successfully synthesized so far⁶⁰. Therefore it is possible that Co^{4+} ions are not stable when the applied potential is removed or that they dissolve into the Helmholtz layer just in front of the electrode/electrolyte interface and are washed away when the electrolyte is removed after the potentiostatic voltage application.

What is most surprising is the fact, that upon a potential decrease to 1.05 V (Figure 4.44g and h), below the redox feature at 1.15 V, neither Co^{2+} nor Co-OH show a significant intensity increase, but the spectra stay rather constant instead. The most likely explanation for this result is that in contrast to previous reports^{83,81,135,177}, the redox feature at about 1.15 V, does not correspond to the transition of Co^{2+} to Co^{3+} , but instead this transition occurs at a lower potential and/or is not (entirely) reversible. Evidence for this assumption is given by the CV diagram of CoO_x (see Figure 4.16), which shows an oxidation feature at 1.02 V, but no corresponding reduction wave.

It has to be stated at this point that especially the peak-fit of the O1s peak was not easy and the residual curves show a certain deviation from ideality. Therefore, it is possible that one or more unknown minor oxygen species are present at the surface of the electrocatalyst, but due to their apparently small portion in the overall oxygen amount the peak-fit is expected to represent all significant and relevant oxygen species

Table 4.4: Fit parameter of the peak fit of Co2p3/2 and O1s for CoO_x under different anodic potentials: binding energy, full width at half maximum (FWHM) and relative peak area (rel. area).

Peak	Pristine	1.35 V	1.6 V	1.05 V
Co^{3+} (eV)	779.7	779.6	779.6	779.7
FWHM (eV)	1.7	1.4	1.4	1.4
rel. area (%)	36.1	50.6	51.3	50.7
Co^{2+} (eV)	780.7	780.6	780.6	780.6
FWHM (eV)	1.7	1.4	1.4	1.4
rel. area (%)	34.1	27.4	27.2	27.7
A (eV)	781.7	781.5	781.5	781.5
FWHM (eV)	1.7	1.4	1.4	1.4
rel. area (%)	21.9	16.1	15.9	15.8
B (eV)	783.0	782.6	782.6	782.6
FWHM (eV)	1.7	1.4	1.4	1.4
rel. area (%)	7.9	5.8	5.6	5.7
Co-O (eV)	529.6	529.5	529.5	529.6
FWHM (eV)	1.2	1.6	1.6	1.4
rel. area (%)	40.6	71.1	69.2	62.7
-OH (eV)	531.6	531.4	531.4	531.3
FWHM (eV)	1.6	1.4	1.5	1.5
rel. area (%)	42.4	18.8	21.8	26.8
Sn-O (eV)	530.7	530.8	530.7	530.7
FWHM (eV)	1.0	0.9	0.9	0.9
rel. area (%)	5.6	10.1	9.1	10.5
surf-O (eV)	533.20	-	-	-
FWHM (eV)	1.9	-	-	-
rel. area (%)	11.4	-	-	-

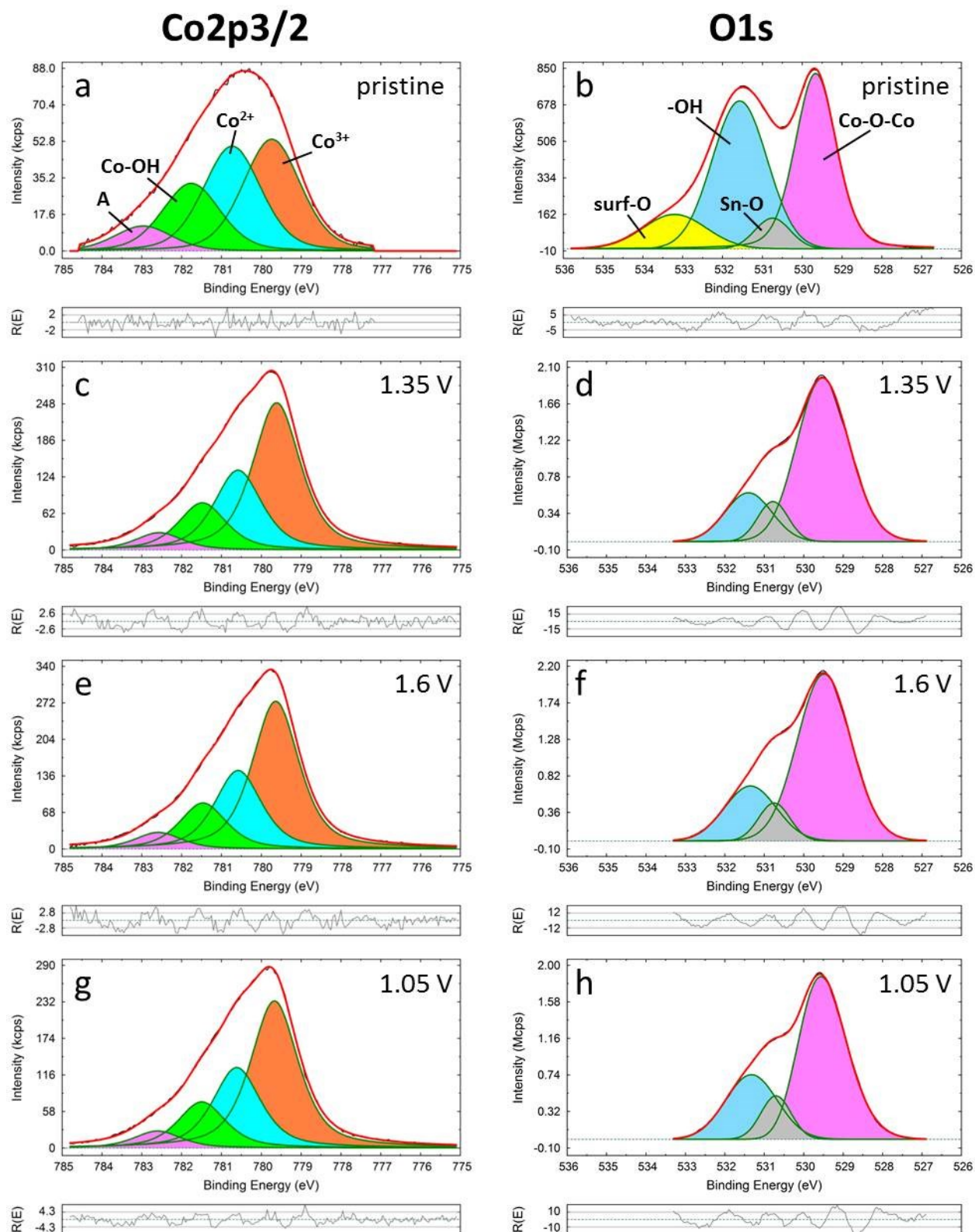


Figure 4.44: Deconvolution and residual function of Co₂p_{3/2} and O1s peaks of CoO_x after deposition (a, b) and the application of 1.35 V (c, d), 1.6 V (e, f) and 1.05 V (g, h). A Shirley background¹⁶³ has been subtracted. The potentials are given vs. RHE and the incident photon energies were 900 and 650 eV for Co₂p and O1s, respectively.

4.1.3.2. In-situ UV/Vis

During potential cycling experiments reversible coloration of the CoO_x thin films was observed. Figure 4.45 shows a series of photographs recorded at different applied potentials. A distinct and continuous darkening of the initially brown/greenish catalyst film with increasing anodic potentials can be seen in the images.

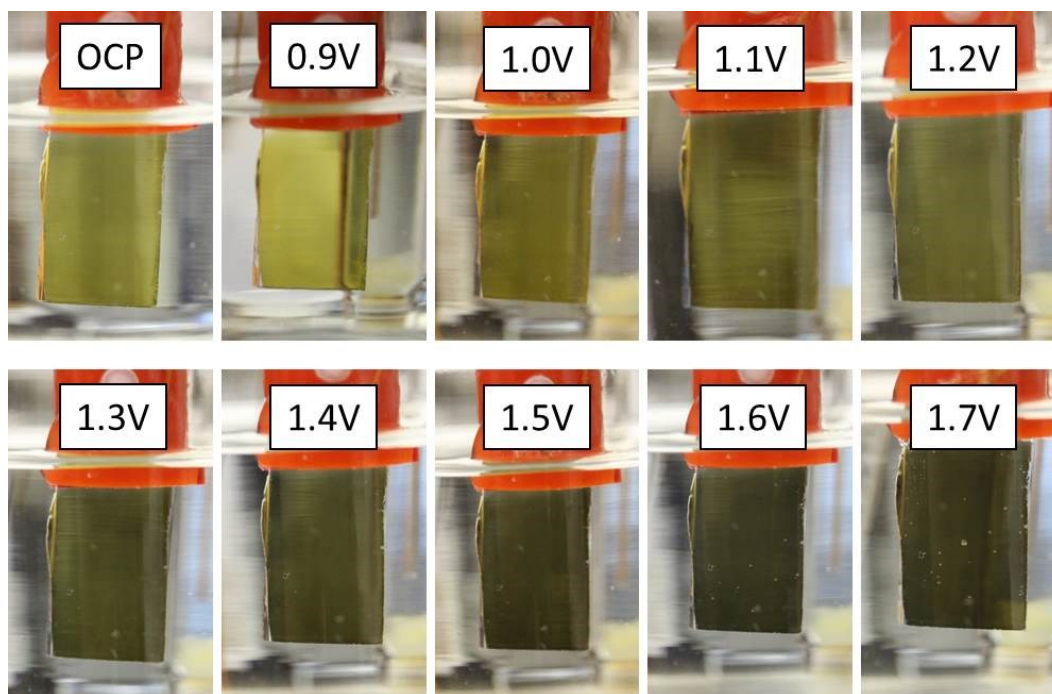
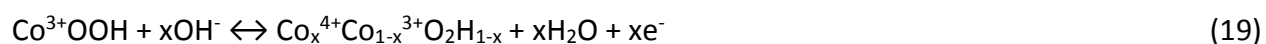


Figure 4.45: Photographs of an as-deposited CoO_x sample during the application of different potentials.

Electrochromic (potential dependent) color changes of cobalt hydroxide have already been observed in 1964^{56,178}. Since then, numerous studies were carried out regarding electrochromism on the different available cobalt oxides^{135,177,179–183}. Electrochromism is generally related to the intercalation (cathodic) or deintercalation (anodic) of ions into or out of a material, respectively, which is accompanied by a charge-balancing electron flow. This causes a change of the electron density and further a modulation of the optical properties of the material⁶⁰. For cobalt oxide in aqueous electrolytes, numerous redox reactions can be formulated in the anodic potential regime (see Table 4.2), which makes the system very complex. Regarding the anodic electrochromic effect the transition from Co^{3+} to Co^{4+} has been denoted as the most interesting reaction⁶⁰. It can be written as



But also other oxidation state transitions alter the electron density and can therefore cause electrochromic color changes.

To investigate the darkening of the cobalt oxide samples presented in this work, in-situ UV/Vis measurements have been carried out. As described in more detail in section 3.2.2.2, the samples were mounted into an electrochemical cell and the relative transmittance (normalized to the sample at OCP) was measured as a function of the applied potential (from the bottom to the top of the graph). Figure 4.46 shows three dimensional diagrams of as-deposited CoO_x (a, c, e) and annealed Co_3O_4 (b, d, f) samples of different thicknesses. As can be seen from the first image (Figure 4.46a), remarkable changes in the transmittance appear upon increasing the potential from 0.9 to 1.65 V (RHE) for CoO_x samples with 1000 mC/cm^2 deposition charge. The corresponding samples with deposition charges of 100 and 10 mC/cm^2 in (c) and (e) show qualitatively the same behavior, but to a much lower extend (see range of the color bar) and accordingly with more interferences. This is consistent with the general concept of electrochromism being a volume effect⁶⁰. The decrease in transmittance does not occur uniformly over the whole investigated light spectrum, but shows distinct features. A strong, but narrow absorption region can be observed between 300 and 380 nm and a broader one between 450 and 900 nm with decreasing magnitude at higher wavelengths. The transmittance minimum for all wavelengths is reached at the potential of 1.65 V (center of the graphs) and with the following potential decrease in the upper part of the diagram, the transmittance increases again until the original state is achieved at 0.9 V (top of the graph). Except for the section between about 350 and 450 nm, the electrochromic effect appears as fully reversible.

The annealed Co_3O_4 sample characterized in Figure 4.46b was synthesized with a deposition charge of 1000 mC/cm^2 as well, but shows a totally different transmittance behavior compared to the as-deposited sample in Figure 4.46a. At wavelengths below 580 nm no transmittance change can be observed at all, while at higher wavelengths the absorption is even more pronounced than in (a). This observation could in principle be explained by a significant change in the electrochemical mechanism after annealing at 450°C . But the annealed samples with the deposition charge of 100 (d) and 10 mC/cm^2 (f) again show qualitatively the same response to potential application as the not annealed ones in Figure 4.46c and (e). Since all results are reproducible it might be that for the thick film (b) a different effect superimposes the optical potential response. This is not unlikely, since the film is already very dark under OCP conditions (see Figure 4.15) and further darkening in the visible range might not be detectable by the spectrometer.

The crosscheck of an empty FTO substrate did not show any transmittance change throughout the whole investigated potential range (not shown). This was expected, because only transition metal compounds with more than one available oxidation state are known for electrochromic behavior⁶⁰.

4. Results and discussion

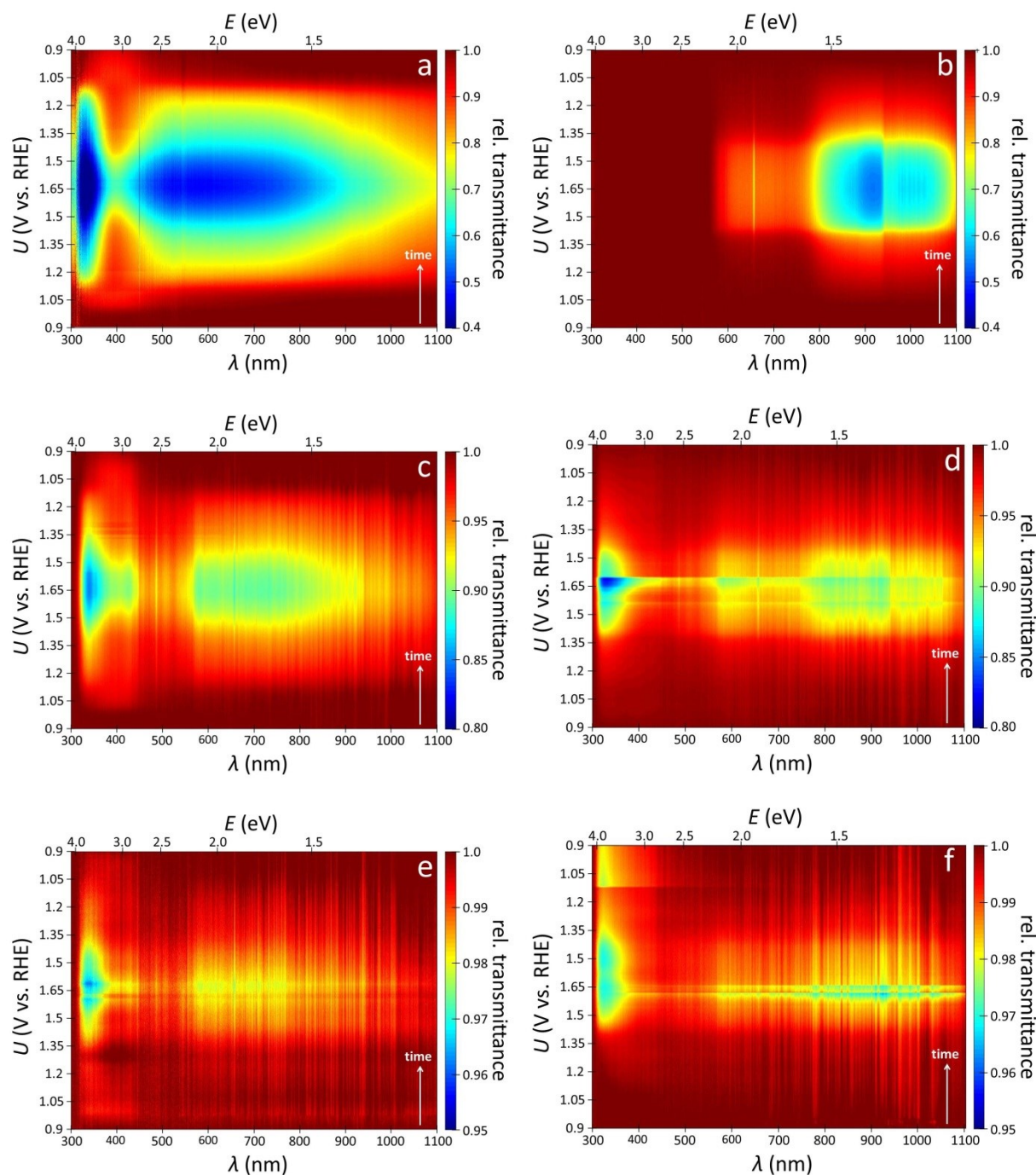


Figure 4.46: Applied potential U vs. wavelength λ of the incident light of in-situ UV-Vis measurements during potential cycling on as-deposited CoO_x (a, c, e) and annealed Co_3O_4 samples (b, d, f). The samples had a nominal deposition charge of 1000 (a, b), 100 (c, d) and 10 mC/cm^2 (e, f). The color bar gives the relative transmittance normalized to the samples under open circuit conditions; the scan rate was 1 mV/s in 1 M KOH electrolyte. The transmittance was integrated for 5 s, respectively, which results in a potential resolution of 5 mV.

Interestingly, once started, the darkening of the films seems to grow continuously with increasing potential. In contrast to that, the CV diagrams of CoO_x electrodes (see Figure 4.16) shows distinct

redox features at rather well defined potentials. If the electrochromic effect would be caused by these superficial redox transitions, one would rather expect a step-wise change in transmittance at the corresponding potentials. The 3d-plots in Figure 4.46, allow a good qualitative evaluation of the coloration effects, but it is rather hard to gain quantitative information from them. Therefore, the relative transmittance at certain selected wavelengths was plotted in Figure 4.47 as 2d-plot against the applied potential. The data were derived from Figure 4.46a. As can be seen from the curves, the loss in transmittance actually occurs continuously, but the starting potentials differ between the wavelengths. A first slight transmittance decrease of about 10% can be observed between 1.0 and 1.05 V (RHE) for the red triangles (400 nm), which represent a wavelength in between the two main absorption features in Figure 4.46a. This matches the first oxidation peak in the CV diagram (Figure 4.16) very well. Furthermore, similar to the oxidation peak, which does not show a corresponding reduction wave, also the transmission change of the red triangles is not entirely reversible, which can be seen from the values being roughly 0.9 at the right end of the graph. Considering the results from the XPS analysis (Figure 4.44) it can be concluded that a partial but not reversible oxidation of Co^{2+} to Co^{3+} occurs at around 1.05 V.

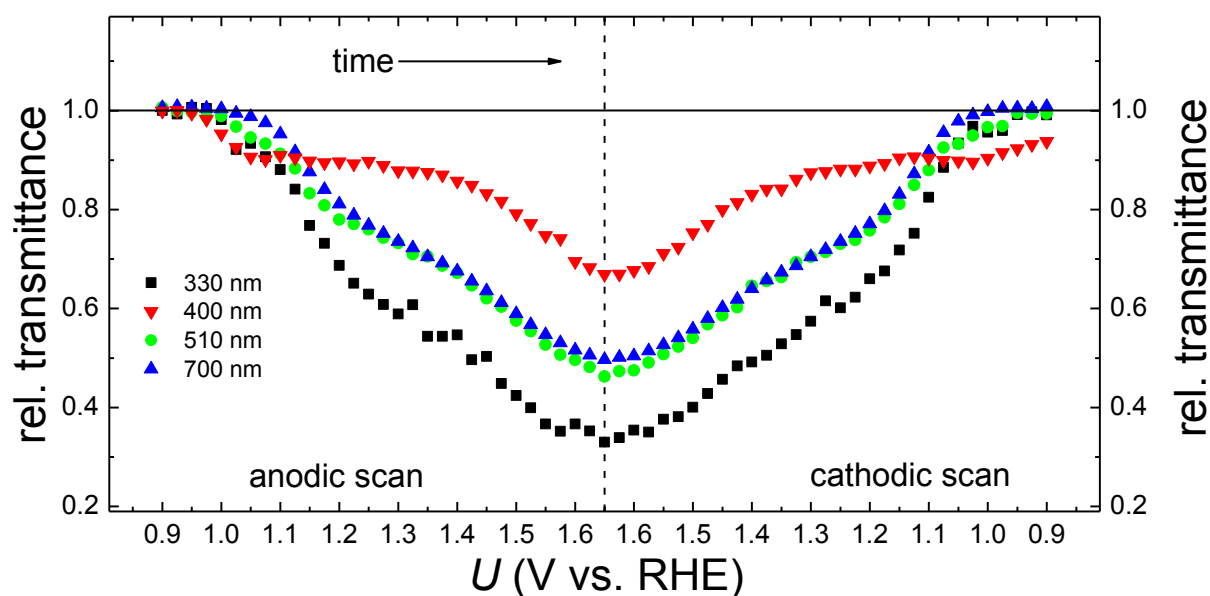


Figure 4.47: Relative transmittance (normalized to the sample transmittance at OCP) as function of the applied potential U of an as-deposited CoO_x electrode with a deposition charge of 1000 mC/cm^2 . The selected wavelengths correspond to the different absorption features in the 3d-plot in Figure 4.46a.

Between 1.05 and 1.4 V the transmission at 400 nm (red triangles in Figure 4.47) stays approximately constant, before decreasing again. The potential range and the less definite starting point of the decrease are fitting to the third redox feature in the CV diagram (Figure 4.16), which also appears a little smeared over a rather large potential range. Therefore, absorption at around 400 nm is seen as image of the third oxidation peak and represents, according to the

literature^{81,134,135}, the appearance of Co^{4+} due to equation (19). This feature is, in contrast to the first transmittance decay at 1.0 V, fully reversible and reaches its starting level at about 1.35 V in the cathodic scan.

The black squares (330 nm), green dots (510 nm) and blue triangles (700 nm) on the other hand represent the two main absorption features in Figure 4.46a and start decreasing at a potential between 1.05 and 1.15 V. This can be ascribed to the second redox peak in the CV diagram (Figure 4.16). Consequently, the relative transmittance at these wavelengths is fully reversible and reaches unity again at about 1.0 V in the cathodic scan. However, the relative transmittance decreases linearly with increasing potential between 1.1 and 1.65 V and rises again upon subsequent potential decrease. This is tentatively explained by the electrochromic effect being volume dependent. Once the oxidation potential for the cobalt ions at the large and rough surface is reached, the sudden oxidation of a great number of ions occurs, which is expressed by the oxidation peak centered at around 1.15 V in the CV diagram. However, the potential, which has to be applied to oxidize cobalt ions in the bulk of the thin film successively increases with distance of the ions to the surface, because there might be a potential drop inside the thin film and further the involved ions from the electrolyte (i.e. OH^-) have to be transported through the bulk to the relevant cobalt ions. In that way, the linear decrease of relative transmittance can be seen as progress of the cobalt oxidation through the bulk of the sample. In the CV diagram this effect is not visible, since it would result in a small constant current, which is overlapped by other effects. In the cathodic scan the phenomenon is accordingly reversed. The same model can be applied for the transmittance at 400 nm (red triangles) between 1.4 and 1.65 V, while the feature between 1.0 and 1.05 V seems to be superficial as it does not proceed at higher potentials.

Unlike the first and third oxidation peak in the CV diagram (Figure 4.16), the assignment of a particular oxidation reaction for the second peak is not trivial, because conflicting results have been obtained. From the electrochemical point of view one would expect the transition from Co^{2+} to Co^{3+} according to equation No. 6 in Table 4.2. However, XPS measurements (chapter 4.1.3.1) showed that this oxidation happens only partially and probably already at lower potentials, as a significant Co^{2+} portion persists also at potentials far above 1.15 V and an unchanged fraction of Co^{3+} can be measured at 1.05 V. It might be that part of the Co^{2+} ions in the tetrahedral sites of Co_3O_4 are not accessible for further oxidation to Co^{3+} to form CoOOH and that many different oxides, hydroxides and/or oxyhydroxides exist simultaneously in the sample, but at this point it has to remain speculation. Nevertheless, it could be shown that also oxidative transitions below the tetravalent state of Co ions show a considerable electrochromic effect¹⁷⁹.

To investigate the kinetics of the electrochromic effect, potential step experiments have been performed as well. The results are presented in Figure 4.48 for CoO_x (a) and annealed Co_3O_4 layers (b), both with a deposition charge of 1000 mC/cm^2 . The electrodes were subjected to different anodic potentials for 10 seconds each, interrupted by 10 seconds at 0.9 V (dark red areas), respectively. The coloration of the graphs approximately corresponds to the coloration in Figure

4.46a and (b) at the particular applied potential, with some minor deviations. Interestingly, the darkening of the samples occurs very fast, at time scales well below 2 seconds, which is much faster than observed for Co_3O_4 films prepared by sol-gel deposition¹⁷⁹. This requires a high ionic conductivity of the samples, since at high potentials the oxidation of large fractions of the bulk is expected. In fact, best electrochromic effects are obtained for highly disordered, yet not fully amorphous films with structural inhomogeneity on all scales⁶⁰ and a layered structure, which was shown to be the case for HCoO_2 ¹⁸⁴. Especially the CoO_x thin films meet these requirements very well.

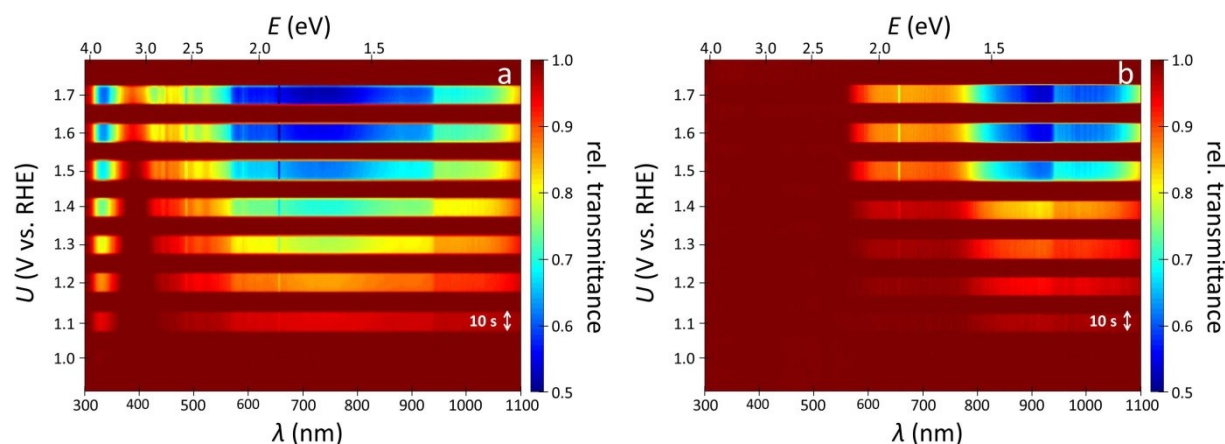


Figure 4.48: Applied potential U vs. wavelength λ of the incident light for in-situ UV/Vis measurements during rapid potentiostatic measurements at different potentials on as-deposited CoO_x (a) and annealed Co_3O_4 (b) electrodes. In between the different potential steps the samples were discharged at 0.9 V (RHE). The deposition charge was 1000 mC/cm^2 in both cases and the Co_3O_4 film has been annealed at 450°C. The color bar gives the relative transmittance normalized to the sample under open circuit conditions.

One could now argue that in the case of a very high ionic conductivity, water oxidation could occur in the volume of the catalyst⁹⁰ instead of the electrochemically active surface area. This might be possible, but is considered as unlikely, because the electrochromic effect and the OER are two considerably different processes. For the darkening of the whole bulk of the electrode a very limited amount of OH^- needs to be transported through the thin film to reach the desired cobalt ions, whereas for the OER a constant and very high ion flow, coming from the bulk of the electrolyte, needs to be maintained for a long period of time and, even more important, large and uncharged O_2 and H_2O molecules have to be transferred through the bulk of the electrode to the surface to be released into the electrolyte.

It is possible to estimate the number of OH^- involved in the darkening of the electrocatalysts by integrating the current density of the first two seconds (i.e. period of the darkening process) after a certain potential has been applied and subtracting the faradaic current fraction. At 1.7 V an approximate charge of roughly 2 mC/cm^2 was calculated, which is much lower than the deposition charge and shows that not the whole volume and/or not every cobalt ion is oxidized. If this charge

is evenly spread over the potential range from 1.0 (start of the color changes) to 1.7 V in a CV diagram at a scan rate of 10 mV/s, a constant current density of about $30 \mu\text{A}/\text{cm}^2$ is obtained to be necessary for the darkening of the volume of the sample. Integration of the current density of the first two seconds after the application of other potentials confirms this finding. Such a low current is indeed not distinguishable from values in a CV diagram (see Figure 4.16) as already mentioned above.

The in-situ UV/Vis measurements show light absorption at around 400 nm for potentials above 1.4 V, which was attributed to the appearance of Co^{4+} (Figure 4.47), while in the XPS measurements (Figure 4.44) no evidence for Co^{4+} could be found. It is therefore of great interest how this mismatch can be explained. Figure 4.49 shows the first two hours of relaxation of charged (colored) CoO_x electrodes in KOH (a) and in air (b) after 1.7 V have been applied for one minute. The reference spectrum, which was used for normalization of the spectra, was taken in KOH and air before potential application, respectively.

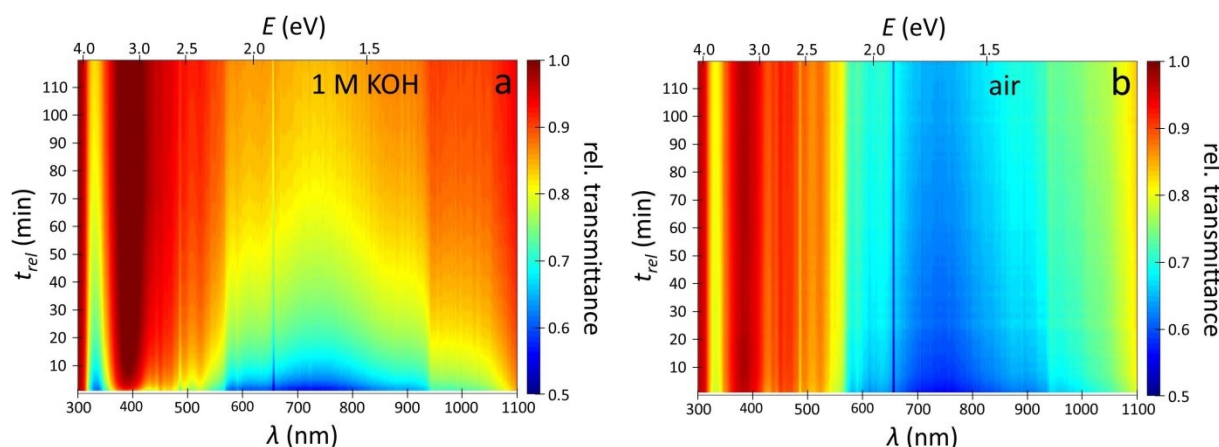


Figure 4.49: Relative transmittance, normalized to the status before the application of potential, as a function of relaxation time t_{rel} and wavelength λ during the relaxation process in 1 M KOH (a) and air (b). The samples were beforehand subjected to 1.7 V (RHE) for 1 min. The measurement was started as fast as possible after the applied potential was switched off and, in the case of (b), the electrolyte was removed. Integration time of the individual spectra was 1 min.

The sample in Figure 4.49a was simply kept in KOH after switching off the potentiostat, while for the relaxation in air (b), the electrolyte has been removed with deionized water and N_2 , just as it has been done for the in-line SXPS measurements. As can be seen from the figures, the dark state is not stable and the films brighten after some time. This is attributed to a certain electronic conductivity of the CoO_x films, which is indeed required for electrocatalysis, but detrimental for the continuity of electrochromic effects⁶⁰. Brightening occurs much faster in KOH due to the higher presence of potential reaction partners in the electrolyte. After about 10 hours the original state of the films, as it was before potential application, is achieved again (not shown). But also in air the electrochromic effect cannot be maintained and after about 48 hours the original color of the films is almost completely restored.

A very interesting fact can be seen in Figure 4.50. It shows a 2d-plot of the relaxation of a CoO_x film in air. The data have been derived from Figure 4.49b. The pink curve denotes the relative transmittance of the CoO_x electrode at a potential of 1.7 V, while the green curves represent the spectra after different relaxation times in air (1 minute to 2 hours). As obvious from the graph, the relative transmittance at about 400 nm is almost fully restored to unity immediately after the potential has been turned off (marked with a dashed arrow). Meanwhile, in other sections of the light spectrum the relaxation occurs much slower (see black arrow). If absorption at around 400 nm is accepted to represent the formation of Co^{4+} , the findings in this diagram can be taken as evidence for the instability of Co^{4+} species and explain why no such species could be found in the XPS spectra. Apparently, the time span between the removal of the potential and the XPS measurement is too long for the Co^{4+} ions to persist and they are removed or reduced meanwhile. Unfortunately, it has therefore to be concluded that in-line XPS is probably not the right tool to study the surface state of cobalt oxide as it appears during the OER. Possibly, ambient-pressure XPS, which allows real in-situ measurements, can help in this occasion¹⁸⁵.

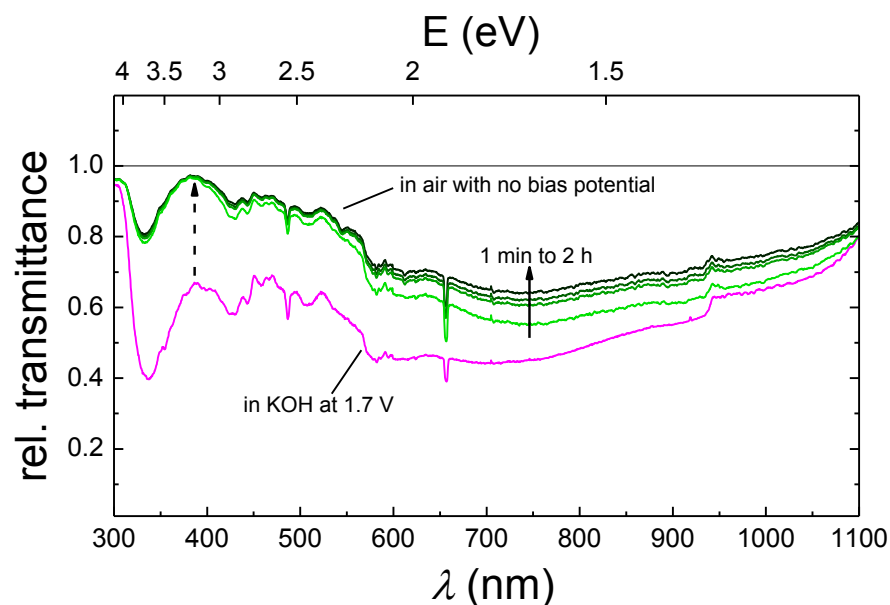


Figure 4.50: Relative transmittance, normalized to the status before the application of potential, as function of the wavelength λ at the applied potential of 1.7 V vs. RHE (pink) and in air after different relaxation times (green \rightarrow black).

4.2. Manganese Oxide

In this chapter manganese oxide as an alternative abundant OER electrocatalyst is presented briefly. It has been developed in our research group¹¹¹ and shows promising results concerning OER activity and stability. The first part of the chapter summarizes the findings about the activity of the different available phases, while in the second part in-line synchrotron photoelectron spectroscopy was applied to study the surface properties of the catalyst under OER conditions. The first part of the chapter is based on recent publications^{111,112}, while the second part presents some additions to them.

4.2.1. Catalytic activity

The synthesis of MnO_x catalyst thin films is described in chapter 3.1. Three types of manganese oxides have been produced by different heat treatments. Figure 4.51 shows the X-ray diffractograms of these phases. Besides the characteristic reflexes of the FTO/glass substrate (dashed lines) the as-deposited MnO_x films (blue line) did not show any diffraction lines and were therefore considered as being amorphous. An as-deposited sample annealed for 1 h in air at 500°C (red), transformed into $\alpha\text{-Mn}_2\text{O}_3$ (JCPDS # 73-1826), which has a crystal structure close to the cubic bixbyite phase¹¹⁰. After annealing of an amorphous MnO_x film for 1 h at 600°C in N_2 atmosphere (green) the X-ray diffractogram gave clear evidence for the presence of a pure Mn_3O_4 spinel-type phase (JCPDS # 24-0734).

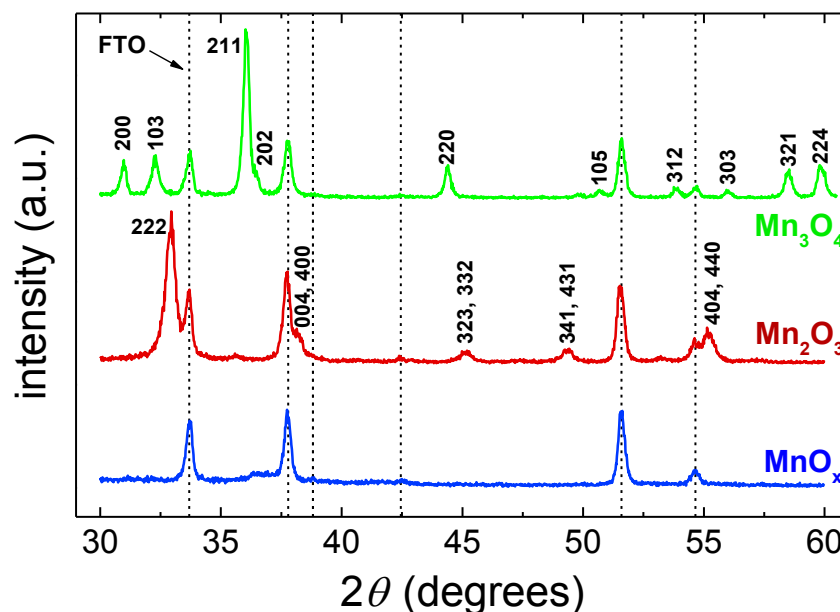


Figure 4.51: X-ray diffractogram of electrodeposited manganese oxide films after different annealing treatments. The blue curve represents as-deposited amorphous MnO_x ; the red line gives crystalline $\alpha\text{-Mn}_2\text{O}_3$ after treatment at 500°C in air and the green graph shows Mn_3O_4 after annealing at 600°C in N_2 . The most important reflexes are labeled with the corresponding hkl-indices and the dotted line denotes the reflexes belonging to the FTO substrate.

The catalytic performance of different manganese oxides towards the OER is illustrated in Figure 4.52. The by far highest activity could be achieved with α - Mn_2O_3 film electrodes (red), which were obtained by annealing amorphous MnO_x films at 500°C in air, after galvanostatic deposition. Similar to amorphous CoO_x films, the overpotential amounted to about 0.36 V at a current density of 10 mA/cm^2 , which is comparable to the best manganese oxides reported in the literature¹⁰². The reason for the extraordinarily high activity of α - Mn_2O_3 is assumed to originate from structural features of the bixbyite structure, which is characterized by regular and highly distorted $[\text{MnO}_6]$ octahedrons leading to different Mn-O bonds ranging from covalent to ionic^{110,111}. However, unlike CoO_x electrodes (Figure 4.16), the α - Mn_2O_3 current voltage curve does not show any redox peaks before the onset of the OER. Instead, a rather slow increase in current density was noticed below 1.5 V. This feature is interpreted in the way of a slow continuous oxidation of the film surface throughout a relatively wide potential range. The high activity of α - Mn_2O_3 was already observed in 1978 by Morita et al.¹⁸⁶, who investigated massive manganese oxide electrodes prepared by spray pyrolysis.

In contrast to that, the electrocatalytic activity of Mn_3O_4 electrodes (green), which have been formed by annealing amorphous MnO_x films in N_2 at 600°C , is rather low, while the as-deposited, amorphous MnO_x films (blue) are not stable at all in 1 M KOH and dissolve after a few scans. This is visible from the severe degradation of the corresponding curve in Figure 4.52.

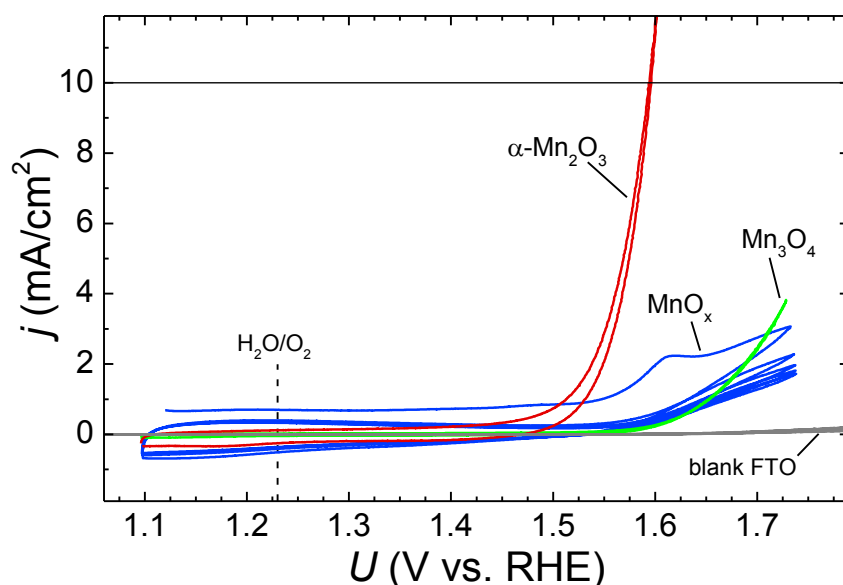


Figure 4.52: Cyclic voltammograms of different types of manganese oxide and a blank FTO substrate for comparison. The electrolyte was 1 M KOH and the scan rate 10 mV/s. All curves have been corrected for the iR-drop.

4.2.2. In-line SXPS

To investigate the oxidation state of the manganese and oxygen atoms on the surface of the catalyst electrode during oxygen evolution in contact with an electrolyte, in-line SXPS measurements have been carried out on the most active α - Mn_2O_3 compound (for experimental details see section 3.2.2.1). An overview spectrum of the pristine sample (blue) and the sample after it has been subjected to a potential of 1.55 V (red) is depicted in Figure 4.53.

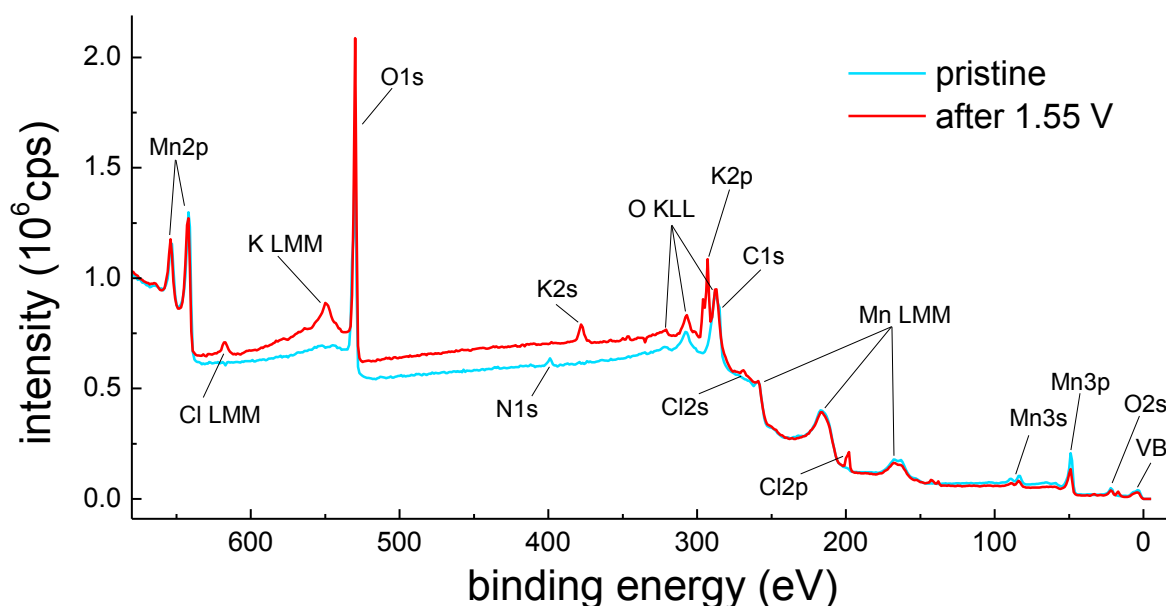


Figure 4.53: XPS overview spectra of the pristine α - Mn_2O_3 sample (blue) and the sample after it has been subjected to a potential of 1.55 V (red). The most important features are marked within the graph. Excitation energy was 800 eV.

As for the measurements on cobalt oxide, the high setup resistance of the electrochemical cell of about $150 \, \Omega$ (see Figure 4.42) called for an iR correction of the current-voltage curve, which led to a significant reduction of the applied potential of 1.7 V to the actual potential of 1.55 V at the electrode-electrolyte interface, which is denoted in the graph. This potential, however, is still high enough to ensure that oxygen evolution takes place at considerable rates. The most important features are labeled in the graph. Besides the main signals originating from Mn and O some impurities could be detected. On the pristine sample nitrogen and carbon represent the main impurities and are attributed to organics from the air. At the incident photon energy of 800 eV, as used to perform the XPS measurements for this graph, the C1s peak overlaps with Auger signals from oxygen. Nevertheless, measurements with other incident photon energies confirmed a notable amount of carbon at the surface of the sample. After the application of 1.55 V, the carbon is mostly oxidized and the surface has been electrochemically cleaned (cf. sections 4.1.2.7 and 4.1.3.1). On the other, hand a significant amount of potassium could be observed after electrochemical treatment, despite the removal of the electrolyte with deionized water. This

observation can tentatively be explained by the very porous structure of the films, which makes it difficult to remove the entire electrolyte inside the pores. As already observed for CoO_x (section 4.1.3.1), a minor chlorine contamination was observed for $\alpha\text{-Mn}_2\text{O}_3$ electrodes as well. Interestingly, the Cl signals vanish after prolonged X-ray radiation, which indicates the very volatile character of these species.

Figure 4.54 shows high resolution spectra of the Mn2p (a) and the Mn3s (b) peaks of the pristine sample and the same film after it has been subjected to a potential of 1.55 V. A clear difference can be observed in the Mn2p signal. The main 2p_{3/2} peak at 641.5 eV shifts slightly to higher binding energies and changes its shape with a shoulder at 640.9 eV. The published binding energies of Mn^{2+} (640.4-641.2 eV), Mn^{3+} (641.3-641.9 eV) and Mn^{4+} (641.8-642.5)^{187–194} are labeled in the graph. Obviously, the sample (partially) oxidizes from Mn^{3+} to Mn^{4+} upon potential application. But interestingly, the shoulder in the red spectrum seems to represent also Mn^{2+} . A more detailed analysis of this observation is given below.

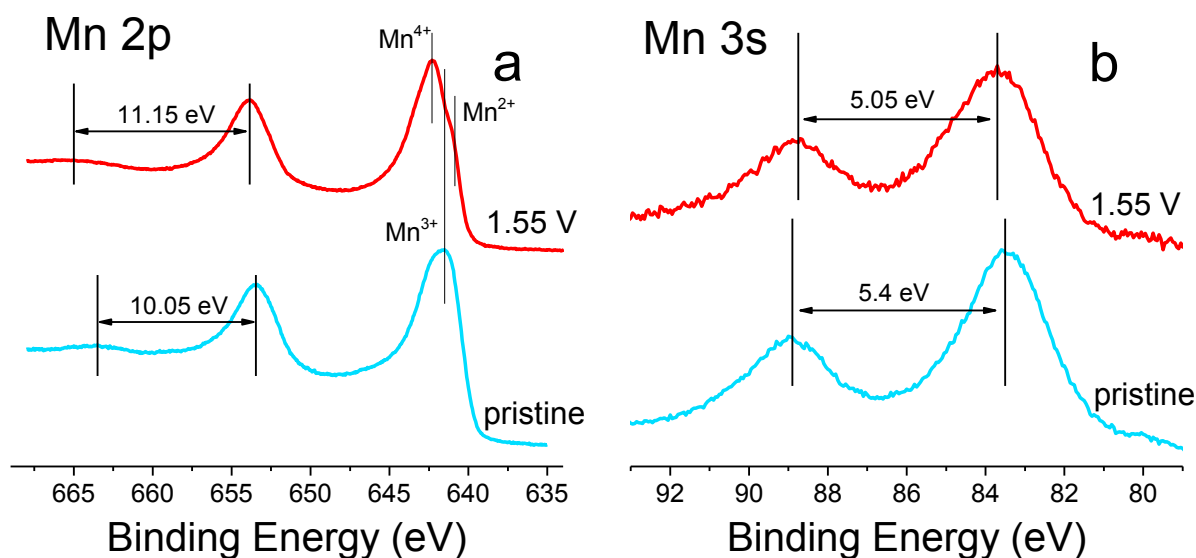


Figure 4.54: High resolution XPS spectra of Mn2p (a) and Mn3s (b) peaks before and after application of an anodic potential of 1.55 V. The characteristic distances in binding energy between the high energy shake-up satellite and the 2p_{1/2} peak (a) and the multiplet splitting of 3s (b) are labeled in the graphs. Excitation energies were 800 (a) and 450 eV (b), respectively.

The chemical shifts of Mn2p are rather small, which gives rise to considerable uncertainties. Therefore, further evidence for the actual change in oxidation state is desired. It has been reported^{101,191,195} that the distance between the Mn2p_{1/2} peak and a shake-up satellite at its higher binding energy side can be a characteristic and distinguishing feature between the oxidation states of Mn. The increase of the satellite's distance from the Mn2p_{1/2} peak from about 10 to more than 11 eV upon potential application is a clear indication for the appearance of the Mn^{4+} oxidation state (Figure 4.54a).

Furthermore, the multiplet splitting of the Mn3s peak can be taken to identify oxidation states of manganese as well. In transition metals with unpaired electrons in the valence shell, electron exchange interactions upon photoelectron ejection can cause a splitting of the s-orbitals¹²³. For manganese such an exchange occurs between 3s-3d levels and results in a characteristic distance of the 3s peaks (ΔE), which decreases for higher oxidation states¹⁸⁷. As can be seen from Figure 4.54b the distance between the 3s peaks of manganese decreases from 5.4 eV to 5.05 eV after a high anodic potential has been applied. This is a strong evidence for only a partial oxidation of Mn³⁺ to Mn⁴⁺, since for complete oxidation a ΔE of about 4.7 eV would be expected^{187–189,191}.

With the above information in mind, peak fitting can be done for the Mn2p_{3/2} and the O1s peaks, which contain all the chemical information of the sample. As it was the case for the investigations on cobalt oxide, also for the manganese oxide samples the electrode-electrolyte interface is of highest interest and consequently the excitation energy was set to a value, which allows highest possible surface sensitivity, but still provides a good signal to background relation as the peaks have a sufficient distance to the secondary electron tail at the high binding energy end of the spectrum. The chosen excitation energies are 800 eV for Mn2p and 700 eV for O1s, respectively. The results of the Mn2p_{3/2} peak fit are shown in Figure 4.55a and (c), the corresponding fit parameters are summarized in Table 4.5.

The pristine sample appears as almost pure Mn³⁺, as it was expected from the single phase XRD pattern (Figure 4.51). However, best fit results were achieved with a very small contribution of Mn⁴⁺ in the sample as well. It has to be noted here that the shape of the Mn³⁺ peak appears comparatively broad with a FWHM of 2.75 eV and furthermore shows some asymmetry to the high energy side. This is attributed to the complex structure of α -Mn₂O₃, which contains a large variety of different bond lengths and distorted [MnO₆] octahedrons sharing edges and corners among each other¹¹⁰. After application of 1.55 V, the fraction of Mn⁴⁺ increases dramatically (Figure 4.55c) and represents the main component of the sample. But a considerable amount of Mn³⁺ is still present and refused oxidation. However, to realize a good fit result, it was necessary to introduce a small third peak at the low binding energy side of the Mn³⁺ signal, which was attributed to Mn²⁺. This finding was not at all expected and is puzzling. Tentatively, its appearance is assigned to the OER itself, which is assumed to occur in a circular reaction involving a sequence of manganese oxidation states¹⁰⁵: Mn³⁺ → Mn⁴⁺ → Mn²⁺ (O₂ release) → Mn³⁺. Under the given conditions, namely high anodic potential (1.55 V) and strong alkaline electrolyte (1 M KOH), one would expect the Mn²⁺ ions to oxidize rapidly to Mn³⁺, especially since a comproportionation reaction was shown to occur in alkaline environment^{105,196}. It could be that the oxidation of Mn²⁺ occurs slower than expected (and Mn²⁺ can therefore be isolated by a rapid removal of the electrolyte) or is hindered in some regions of the sample. Similar effects have recently been observed by Gorlin et al.¹⁰⁶

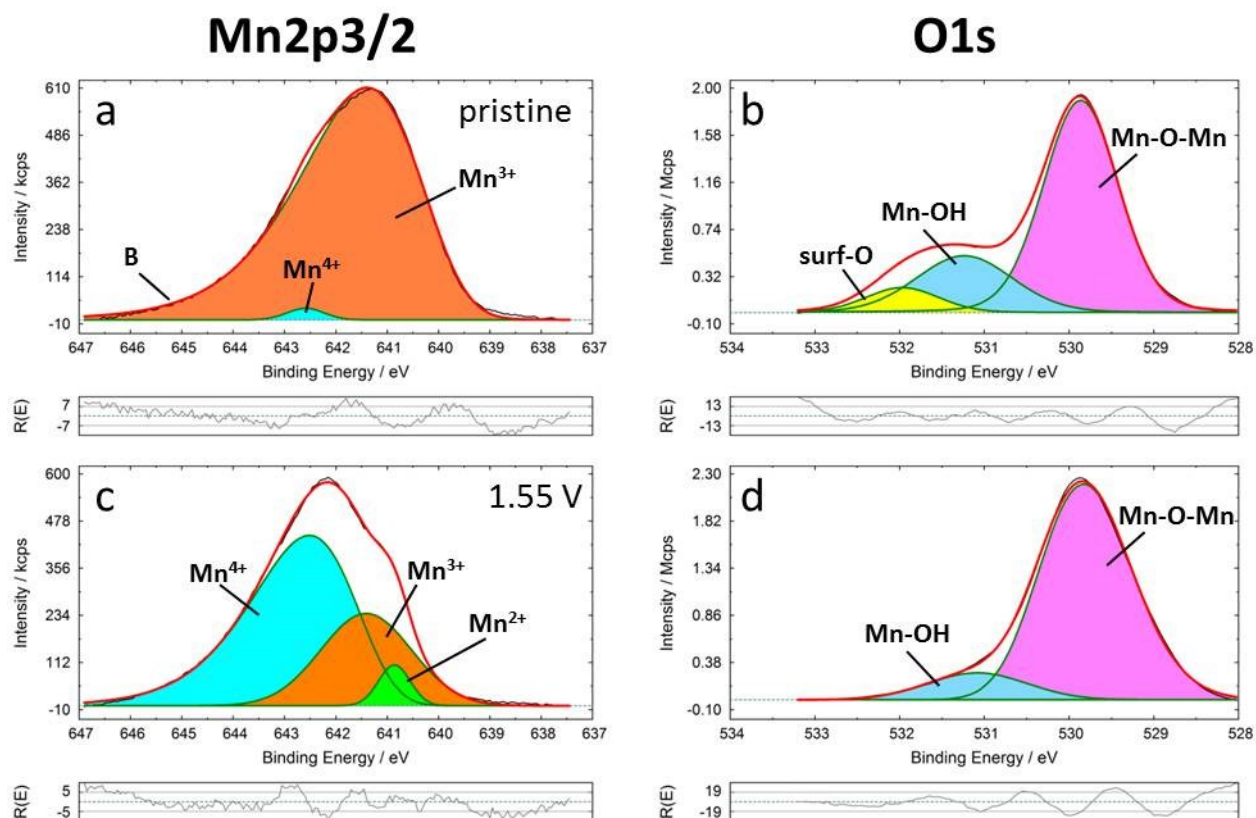


Figure 4.55: Deconvolution and residual function of Mn2p3/2 and O1s peaks of α -Mn₂O₃ after preparation (a, b) and after the application of a potential of 1.55 V (c, d). A Shirley background¹⁶³ has been subtracted. The potentials are given vs. RHE and the incident photon energies were 800 and 700 eV for Mn2p and O1s, respectively.

The O1s spectra of the pristine sample and after anodic potential application of 1.55 V are shown in Figure 4.55b and (d), respectively. A strong signal from the lattice oxygen at 529.8 eV dominates the O1s response in both graphs. This is in agreement with previous observations^{187–189}, which allow the conclusion that a clear distinction between lattice oxygen from α -Mn₂O₃ and MnO₂ is not possible. Both spectra also include a rather broad peak at 531.2 (pristine) and 531.1 eV (1.55 V) coming from OH-groups¹⁸⁷ (bluish colored curve). Most probably, they can be attributed to hydroxides or oxyhydroxides at the surface of the electrocatalyst. Such a peak has also been observed for cobalt oxide. Interestingly, the relative area of the OH-peak decreases after potential application, which is a sign for a more oxidized surface. However, since OH⁻ ions from the electrolyte are expected to adsorb on the catalyst's surface in the first step of OER, one could also expect a higher OH-signal under OER conditions, if the whole surface is accessible to OER. On the other hand, it has been suggested that under anodic potential in alkaline media water (or OH⁻) adsorbs as Mn-O⁻ instead of Mn-OH¹⁹⁷, which could explain the decrease of the OH-signal. A complete physical model is still missing, though.

4. Results and discussion

As already observed for cobalt oxide, the pristine α - Mn_2O_3 sample shows a rather undefined surface oxygen peak (Figure 4.55b), which disappears after electrochemical treatment. Accordingly, also the C1s peak vanishes, which leads to the conclusion that organic contaminations are the origin of this feature and its influence on the OER is negligible.

Table 4.5: Fit parameters of the peak fit of Mn2p3/2 and O1s for α - Mn_2O_3 in pristine state and after 1.55 V potential application: binding energy, full width at half maximum (FWHM) and relative peak area (rel. area).

Peak	Pristine	1.55 V
Mn⁴⁺ (eV)	642.6	642.5
FWHM (eV)	0.9	2.4
rel. area (%)	1.5	65.7
Mn³⁺ (eV)	641.4	641.4
FWHM (eV)	2.7	2.1
rel. area (%)	98.5	29.7
Mn²⁺ (eV)	-	640.9
FWHM (eV)	-	0.7
rel. area (%)	-	4.6
Mn-O (eV)	529.9	529.8
FWHM (eV)	1.0	1.3
rel. area (%)	68.6	88.1
-OH (eV)	531.2	531.1
FWHM (eV)	1.3	1.4
rel. area (%)	23.6	11.9
surf-O (eV)	532.0	-
FWHM (eV)	1.0	-
rel. area (%)	7.9	-

5. Summary and final remarks

In this work a systematic study was carried out on the catalytic activity of electrodeposited cobalt oxide towards the oxygen evolution reaction (OER) in alkaline medium. In a first step (chapter 4.1.1) several deposition parameters were varied and their influence on the performance of the catalyst was studied. It turned out that using potentiostatic deposition from a solution containing CoCl_2 , Na-gluconate and KOH the amount of precursors and OH^- in the solution do not affect the film properties if the deposition charge is kept constant, but had a strong influence on the deposition rate. The magnitude of the deposition potential had a great influence on the deposition rate too, as higher anodic potentials increase the driving force and speed up the thin film formation. However, the “deposition efficiency”, i.e. the portion of the deposition charge that led to actual film formation, was highest at potentials slightly above the oxidation potential ($> 1.1 \text{ V vs. RHE}$). Therefore, for systematic studies on the activity as function of deposition charge and film thickness, 1.2 V was the deposition potential of choice.

Film substrate and heat treatment after the electrochemical deposition had a significant influence on the performance of the catalysts. Despite their distinct morphology, films deposited on FTO, Au and Co sheets showed a similar OER activity, but on FTO best reproducibility and highest effective current densities (taking the surface roughness into account) were achieved. Ti is not suited as substrate, most probably due to insulating TiO_x barrier layers at the substrate/catalyst interface. As-deposited cobalt oxide films showed no XRD patterns beside the characteristic lines of the substrate and were therefore considered to be amorphous (CoO_x). Upon annealing above 300°C , characteristic reflexes of the spinel phase Co_3O_4 could be found by X-ray diffraction; crystallization was completed at 450°C . In CV diagrams, however, significant changes in the potential regime below the OER onset were observed already after annealing at 200°C . While as-deposited CoO_x films showed three characteristic oxidation and two reduction peaks, only one redox pair at about 1.5 V was observed after heat treatment. Furthermore, the magnitude of the peak decreased with increasing temperature. SEM images confirmed a significant loss of particle surface area caused by the annealing process and consequently also the catalytic performance decreased.

In the second part of the thesis (chapter 0), the OER on CoO_x films was investigated in more detail. Samples with deposition charges ranging from 0.01 to 5000 mC/cm^2 were synthesized and characterized. A logarithmic decrease in overpotential at 10 mA/cm^2 as function of the deposition charge was found. This was in a first moment an unexpected result, since the electrocatalytic activity is generally considered as a function of the surface area instead of the film thickness. Therefore, the electrochemically active surface area was evaluated and it could be shown that it is a function of the deposited charge as well. TEM images supported the suspected micro- and nanoporosity of the films, which can explain the increase in electrochemically active surface area,

even though a volume activity of the samples, as proposed recently⁹⁰, cannot be completely ruled out at this point.

Oxidation and reduction waves in the CV diagram of CoO_x are generally attributed to oxidation state transitions of the Co ions. As an oxidation peak appears at about 1.5 V, shortly before the onset of the OER, it is frequently proposed in the literature that it reflects the oxidation from Co^{3+} to Co^{4+} , which represents a crucial activation step for the cobalt oxide catalyst. The magnitude of the corresponding reduction wave was evaluated as a function of the film thickness and showed a 1:1 relation, which supports this statement. In contrast to that, the redox feature at about 1.15 V seems not to be directly related to the OER as it shows different kinetics and decreases in magnitude compared to the redox feature at 1.5 V as the samples become thicker.

If the Co^{4+} ions are seen as the active centers for the OER and the activity of the CoO_x film is proportional to their total number at the electrochemically active surface area (i.e. the magnitude of the reduction wave at 1.5 V), the highest relative activity is found for samples with a thickness ranging from 3 to 50 nm. Turnover frequencies (TOF) of up to 35 s^{-1} were derived for moderate overpotentials (0.42 V) and compared with values found in the literature. Even though values for TOFs are not easily accessible and/or difficult to compare, the values from this work are rather high. The maximum relative activity for samples between 3 and 50 nm thickness has been confirmed by Tafel slopes and charge transfer coefficients, which have their minimum and maximum in this range, respectively. However, the effect of the high activity per number of Co ions is more than overcompensated by the increase in absolute amount of catalyst for thicker samples. If, the whole amount of deposited CoO_x is taken as basis for TOF calculations, which is probably more convenient from an economical point of view, the numbers are significantly lower.

Since in recent years a growing interest for catalysts working under neutral conditions emerged for their use in photoelectrochemical devices, the activity of the CoO_x films towards the OER was investigated in phosphate buffer at pH7 too. Compared to 1 M KOH a significantly higher overpotential was found. Furthermore, a strong dependence of the activity on the concentration of the phosphate buffer appeared, including an interesting wave in the OER regime, which appeared for low buffer capacities. DEMS measurements showed that the O_2 production coincides with the shape of the wave in the current voltage curve leading to the assumption that the limited buffer capacity at low PO_4^{3-} concentrations causes a pH drop inside the nanopores of the CoO_x film electrode, which disables OER in the inner part of the porous film owing to the hindered diffusion of the electrolyte. At high phosphate concentrations this effect does not appear. A comparison to the very prominent CoPi catalyst⁸⁴ showed similar activity at pH7, but a significantly better performance at pH14.

Furthermore, electrochemical stability of CoO_x thin films was studied as a crucial property for a catalytically active material towards OER. Under optimal experimental conditions (fast removal of gas bubbles from the surface and rapid supply with fresh electrolyte by rotating the sample)

no activity loss has been observed for at least 64 hours. However, if the samples suffer from unfavorable experimental conditions (i.e. no movement of sample and/or electrolyte) as it probably is the case under photoelectrochemical working conditions in a light-driven electrolyzer, the catalytic activity decreases significantly over time. But interestingly, if the potential is removed for several hours, the catalyst can recover and the initial activity is restored. This is a very appropriate property of CoO_x film electrodes having the day and night cycles of such a PEC device in mind.

In chapter 4.1.3.1, the binding energies and oxidation states of cobalt and oxygen ions on the surface of CoO_x electrodes were investigated as a function of the applied potential using in-line synchrotron photoelectron spectroscopy (SXPS). Different anodic potentials were applied to the samples in an electrochemical cell held under inert N_2 atmosphere and after removal of the electrolyte a fast and direct transfer to UHV for surface characterization was possible without any contact to ambient atmosphere. The thin film showed a superficial partial oxidation of Co^{2+} species to Co^{3+} at moderate potentials. This partial oxidation appears to be irreversible even if the applied potential is decreased again, which gives evidence to doubt the frequently proposed interpretation of the redox feature at 1.15 V in the CV diagrams to be associated with a transition from Co^{2+} to Co^{3+} . Instead, it is proposed that a possible reduction of Co^{3+} species is occurring in a sneaky process over an extended potential region which is more cathodic than the investigated one.

Surprisingly, no Co^{4+} ions could be found after electrochemical treatment in the OER regime, although CV diagrams strongly suggested their presence. To evaluate the stability of possible Co^{4+} species on the surface of the films, in-situ UV/Vis measurements were carried out and clearly showed a feature, which could be related to Co^{4+} formation. Relaxation experiments however revealed that cobalt in the form of Co^{4+} is not stable in CoO_x films as soon as the potential is turned off and immediate reduction or removal of tetravalent ions from the film surface prevents their detection with SXPS.

Furthermore, a pronounced color change of the CoO_x catalyst films was observed and evaluated (chapter 4.1.3.2). Over a large range of wavelengths, an absorption increase of the thin film was monitored as function of the applied potential and a dependence of the darkening on the volume of the catalyst electrode was found. Even though this electrochromic behavior appears as volume effect, OER as a volume phenomenon is thought to be very unlikely since both processes are significantly different and the steady supply of educts (OH^-) and especially the release of uncharged products (H_2O and O_2) via ionic conduction through the volume of the film in the necessary rates is difficult to explain because of the large size of the migrating ions. Due to the pronounced electrochromic effect cobalt oxide is not suited as catalyst placed on the top of photoabsorbers, since a significant amount of the solar energy would be absorbed by the not photoactive catalyst. For the “artificial leaf” concept in superstrate configuration though, the

compound might be used as water oxidation catalyst since the light absorption happens at the opposite side of the photoelectrochemical cell.

Manganese oxide (chapter 4.2) is another candidate as cheap, abundant OER catalyst material for an application in PEC devices. It was shown that among the different oxide modifications crystalline $\alpha\text{-Mn}_2\text{O}_3$ is the most active and stable compound¹¹¹. In contrast to cobalt oxide, in-line SXPS measurements on $\alpha\text{-Mn}_2\text{O}_3$ gave a clear indication of a partial oxidation of Mn^{3+} to Mn^{4+} under OER conditions. This finding shows that a significant difference in the stability of the tetravalent ions exists between cobalt and manganese. Since in both cases a strong relation between the 4+ state and the activity towards the OER can be expected, the findings in this work give some evidence for possible crucial differences in the mechanism of the OER on these compounds.

Final remarks

Both compounds, CoO_x and $\alpha\text{-Mn}_2\text{O}_3$ prepared as thin film electrodes, presented in this work show a rather good electrocatalytic activity towards the oxygen evolution reaction in alkaline electrolytes. Nevertheless, as Figure 5.1 elucidates, there is still a long way to go to achieve the activities of noble metal containing catalysts like RuO_2 . On the other hand, RuO_2 is at least three to four orders of magnitude more expensive than cobalt and manganese.

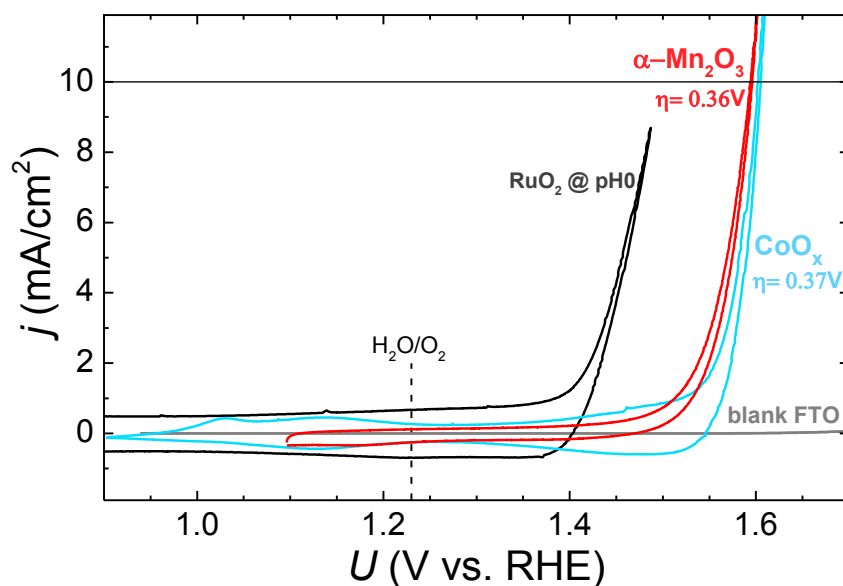


Figure 5.1: Cyclovoltammograms of CoO_x (blue) and $\alpha\text{-Mn}_2\text{O}_3$ (red) thin film electrodes in comparison to RuO_2 (black) and the blank FTO substrate (gray). Except for RuO_2 (measured in 0.5 M H_2SO_4), 1 M KOH has been used as electrolyte and a scan rate of 10 mV/s was applied.

The electrochemistry of both metal oxide systems is complex, as several oxide, hydroxide and oxyhydroxide phases appear in the investigated potential range^{177,178}. In case of cobalt oxide, this is reflected by a CV diagram, which shows several redox transitions, while oxidation state changes in manganese oxide occur in a more sneaky way. The large number of compositions and structural distortions, however, could actually be the key for the catalytic activity. Spectroscopic investigations may display only half of the truth, since a certain integration of signals and a lower resolution limit are unavoidable to obtain good signal intensity. Tiny differences in binding energy, atomic distance or coordination and lattice distortion are not resolvable, but possibly crucial for a good OER performance. The catalytic center of photosystem II is characterized by its flexibility and ability to change interionic distances to a large extent³⁵, which allows formation of optimized binding sites for every transition state during OER. The fact that amorphous CoO_x , which offers a great variety of binding sites, and $\alpha\text{-Mn}_2\text{O}_3$ with its strongly distorted $[\text{MnO}_6]$ octahedrons, are the most active compounds fit very well into this picture.

The strongly different stability of the tetravalent oxidation state in CoO_x and $\alpha\text{-Mn}_2\text{O}_3$ gives some evidence for the possibility of different reaction mechanisms for the two oxides with respect to OER. While it is widely accepted that Co^{4+} is essential for the catalytic activity of cobalt oxides, the role of Mn^{4+} is still under debate^{102,103,186} and also considered as being detrimental for the catalytic activity¹⁰³. Theoretical investigations place Mn_2O_3 on the strong binding site and Co_3O_4 and CoOOH on the weak binding side of the volcano activity plot, respectively^{37,38}. A combination of both transition metals on the atomic scale, might offer a possibility to overcome the scaling relations of the OER intermediate states, similar to the recently shown modification of RuO_2 with Ni and Co⁴⁵. Synthesis of mixed Mn-Co-O compounds published some years ago, showed promising catalytic results¹⁹⁸ and call for further investigations. However, catalysis of the oxygen evolution reaction remains one of the key issues for developing a highly efficient photoelectrochemical device for solar hydrogen production. Great efforts are currently made in the community to put this exciting topic onto a new level.

6. Appendix

6.1. References

- (1) McCrory, C. C. L.; Jung, S.; Ferrer, I. M.; Chatman, S.; Peters, J. C.; Jaramillo, T. F. Benchmarking HER and OER Electrocatalysts for Solar Water Splitting Devices. *J. Am. Chem. Soc.* **2015**, *137*, 4347–4357.
- (2) U.S. eia. International Energy Statistics
<http://www.eia.gov/cfapps/ipdbproject/iedindex3.cfm?tid=5&pid=62&aid=2&cid=regions&syid=2006&eyid=2010&unit=TBD>.
- (3) Nilsson, M.; Heaps, C.; Persson, Å. *Energy for a Shared Development Agenda : Global Scenarios and Governance Implications*; Stockholm, 2012.
- (4) British Petroleum. *BP Statistical Review of World Energy, June 2014*; 2014.
- (5) British Petroleum. *BP Energy Outlook 2035*; 2015.
- (6) Ahmed, N. M. Die Nächste Blase. *Le Monde Diplomatique*. April 12, 2013, pp 1, 5.
- (7) *Photoelectrochemical Hydrogen Production*; Roel, van de K., Grätzel, M., Eds.; Springer: New York, Dordrecht, Heidelberg, London, 2012.
- (8) Pachauri, R. K.; Allen, M. R.; Barros, V. R.; Broome, J.; Cramer, W.; Christ, R.; Church, J. a.; Clarke, L.; Dahe, Q.; Dasgupta, P.; et al. *IPCC Climate Change 2014: Synthesis Report*; 2014.
- (9) Allison, I.; Bindoff, N.; Bindschadler, R.; Cox, P.; de Noblet-Ducoudré, N.; England, M.; Francis, J.; Gruber, N.; Haywood, A.; Karoly, D.; et al. *The Copenhagen Diagnosis. Updating the World on the Latest Climate Science*; Sydney, 2009.
- (10) NOAA. Global Climate Change Indicators <https://www.ncdc.noaa.gov/indicators/> (accessed Apr 10, 2015).
- (11) International Energy Agency. *Energy Policies of IEA Countries: Germany 2013 Review*; 2013.
- (12) Verne, J. *L'île Mystérieuse*; 1874.
- (13) Wendt, H.; Vogel, G. H. Die Bedeutung Der Wasserelektrolyse in Zeiten Der Energiewende. *Chemie-Ingenieur-Technik* **2014**, *86* (1-2), 144–148.

- (14) Lewis, N. S.; Nocera, D. G. Powering the Planet: Chemical Challenges in Solar Energy Utilization. *Proc. Natl. Acad. Sci. U. S. A.* **2006**, *103* (43), 15729–15735.
- (15) Nocera, D. G. The Artificial Leaf. *Acc. Chem. Res.* **2012**, *45* (5), 767–776.
- (16) Iridiumpreis in Euro <http://www.goldseiten.de/kurse/Iridiumcharts-EUR.php?s=kg> (accessed Apr 13, 2015).
- (17) Rutheniumpreis in Euro <http://www.goldseiten.de/kurse/Rutheniumpreis.php?s=kg> (accessed Apr 13, 2015).
- (18) Metalprices.com <http://www.metalprices.com/dailyexchangedata/Exchange/LME/ALL> (accessed Apr 13, 2015).
- (19) 1 Year Manganese Prices and Price Charts <http://www.infomine.com/investment/metal-prices/manganese/1-year/> (accessed Apr 13, 2015).
- (20) Stellmach, D. Molybdänsulfid-Nanopartikel Als Wasserstoffentwickelnder Elektrokatalysator Für Die Lichtinduzierte Wasserspaltung, PhD- thesis, Technische Universität Berlin, 2014.
- (21) Hamann, C. H.; Vielstich, W. *Elektrochemie I*, second edi.; VCH Verlagsgesellschaft mbH: Weinheim, 1985.
- (22) Hamann, C. H.; Vielstich, W. *Elektrochemie II*; Verlag Chemie: Weinheim, 1981.
- (23) Atkins, P. W. *Physikalische Chemie*, first edit.; VCH Verlagsgesellschaft mbH: Weinheim, 1990.
- (24) Trasatti, S. 1799–1999: Alessandro Volta’s “Electric Pile.” *Journal of Electroanalytical Chemistry*, 1999, *460*, 1–4.
- (25) Trasatti, S. Water Electrolysis: Who First? *J. Electroanal. Chem.* **1999**, *476* (1), 90–91.
- (26) De Levie, R. The Electrolysis of Water. *J. Electroanal. Chem.* **1999**, *476*, 92–93.
- (27) Paets van Troostwijk, A.; Deiman, J. R. No Title. *J. Phys.* **1790**, *2*, 130.
- (28) Ortiz-Rivera, E. I.; Reyes-Hernandez, A. L.; Febo, R. a. Understanding the History of Fuel Cells. *2007 IEEE Conf. Hist. Electr. Power, HEP 2007* **2007**, *2* (2), 117–122.
- (29) Schmidt, T.; Wendt, H. Electrocatalysis of Cathodic Hydrogen and Anodic Oxygen Evolution in Alkaline Water Electrolysis by in Situ Activation Procedures. *Electrochim. Acta* **1994**, *39* (11-12), 1763–1767.

- (30) Trasatti, S.; Lodi, G. Oxygen and Chlorine Evolution at Conductive Metallic Oxide Anodes. In *Electrodes of conductive metallic oxides. Part B*; Trasatti, S., Ed.; Elsevier: Amsterdam, 1981; pp 521–626.
- (31) Matsumoto, Y.; Sato, E. Electrocatalytic Properties of Transition Metal Oxides for Oxygen Evolution Reaction. *Mater. Chem. Phys.* **1986**, *14* (5), 397–426.
- (32) Dau, H.; Limberg, C.; Reier, T.; Risch, M.; Roggan, S.; Strasser, P. The Mechanism of Water Oxidation: From Electrolysis via Homogeneous to Biological Catalysis. *ChemCatChem* **2010**, *2* (7), 724–761.
- (33) Ferreira, K. N.; Iverson, T. M.; Maghlaoui, K.; Barber, J.; Iwata, S. Architecture of the Photosynthetic Oxygen-Evolving Center. *Science* (80-.). **2004**, *303*, 1831–1839.
- (34) Dau, H.; Haumann, M. The Manganese Complex of Photosystem II in Its Reaction cycle—Basic Framework and Possible Realization at the Atomic Level. *Coord. Chem. Rev.* **2008**, *252* (3-4), 273–295.
- (35) Siegbahn, P. E. M. Structures and Energetics for O₂ Formation in Photosystem II. *Acc. Chem. Res.* **2009**, *42* (12), 1871–1880.
- (36) Siegbahn, P. E. M. Water Oxidation Mechanism in Photosystem II, Including Oxidations, Proton Release Pathways, O-O Bond Formation and O₂ Release. *Biochim. Biophys. Acta - Bioenerg.* **2013**, *1827* (8-9), 1003–1019.
- (37) García-Mota, M.; Bajdich, M.; Viswanathan, V.; Vojvodic, A.; Bell, A. T.; Nørskov, J. K. Importance of Correlation in Determining Electrocatalytic Oxygen Evolution Activity on Cobalt Oxides. *J. Phys. Chem. C* **2012**, *116* (39), 21077–21082.
- (38) Man, I. C.; Su, H.-Y.; Calle-Vallejo, F.; Hansen, H. A.; Martínez, J. I.; Inoglu, N. G.; Kitchin, J.; Jaramillo, T. F.; Nørskov, J. K.; Rossmeisl, J. Universality in Oxygen Evolution Electrocatalysis on Oxide Surfaces. *ChemCatChem* **2011**, *3* (7), 1159–1165.
- (39) Rossmeisl, J.; Qu, Z. W.; Zhu, H.; Kroes, G. J.; Nørskov, J. K. Electrolysis of Water on Oxide Surfaces. *J. Electroanal. Chem.* **2007**, *607* (1-2), 83–89.
- (40) Zhang, M.; de Respinis, M.; Frei, H. Time-Resolved Observations of Water Oxidation Intermediates on a Cobalt Oxide Nanoparticle Catalyst. *Nat. Chem.* **2014**, *6* (4), 362–367.
- (41) Trasatti, S. Electrocatalysis in the Anodic Evolution of Oxygen and Chlorine. *Electrochim. Acta* **1984**, *29* (11), 1503–1512.
- (42) Gattrell, M.; MacDougall, B. Chapter 30: Reaction Mechanisms of the O₂ Reduction/evolution Reaction. In *Handbook of Fuel Cells*; Vielstich, W., Lamm, A., Gasteiger, H. A., Eds.; John Wiley & Sons: West Sussex, 2003.

- (43) Greeley, J.; Jaramillo, T. F.; Bonde, J.; Chorkendorff, I. B.; Nørskov, J. K. Computational High-Throughput Screening of Electrocatalytic Materials for Hydrogen Evolution. *Nat. Mater.* **2006**, *5* (11), 909–913.
- (44) Koper, M. T. M. Thermodynamic Theory of Multi-Electron Transfer Reactions: Implications for Electrocatalysis. *J. Electroanal. Chem.* **2011**, *660* (2), 254–260.
- (45) Halck, N. B.; Petrykin, V.; Krtil, P.; Rossmeisl, J. Beyond the Volcano Limitations in Electrocatalysis - Oxygen Evolution Reaction. *Phys. Chem. Chem. Phys.* **2014**, *16*, 13682–13688.
- (46) Rossmeisl, J.; Logadottir, a.; Nørskov, J. K. Electrolysis of Water on (oxidized) Metal Surfaces. *Chem. Phys.* **2005**, *319* (1-3), 178–184.
- (47) McCrory, C. C. L.; Jung, S.; Peters, J. C.; Jaramillo, T. F. Benchmarking Heterogeneous Electrocatalysts for the Oxygen Evolution Reaction. *J. Am. Chem. Soc.* **2013**, *135* (45), 16977–16987.
- (48) Jiao, F.; Frei, H. Nanostructured Cobalt Oxide Clusters in Mesoporous Silica as Efficient Oxygen-Evolving Catalysts. *Angew. Chemie - Int. Ed.* **2009**, *48*, 1841–1844.
- (49) Trotochaud, L.; Ranney, J. K.; Williams, K. N.; Boettcher, S. W. Solution-Cast Metal Oxide Thin Film Electrocatalysts for Oxygen Evolution. *J. Am. Chem. Soc.* **2012**, *134* (41), 17253–17261.
- (50) Louie, M. W.; Bell, A. T. An Investigation of Thin-Film Ni-Fe Oxide Catalysts for the Electrochemical Evolution of Oxygen. *J. Am. Chem. Soc.* **2013**, *135* (33), 12329–12337.
- (51) Smith, R. D. L.; Prévot, M. S.; Fagan, R. D.; Zhang, Z.; Sedach, P. A.; Siu, M. K. J.; Trudel, S.; Berlinguette, C. P. Photochemical Route for Accessing Amorphous Metal Oxide Materials for Water Oxidation Catalysis. *Science* **2013**, *340* (6128), 60–63.
- (52) Armelao, L.; Barreca, D.; Gross, S.; Martucci, A.; Tieto, M.; Tondello, E. Cobalt Oxide-Based Films: Sol–gel Synthesis and Characterization. *J. Non. Cryst. Solids* **2001**, *293-295*, 477–482.
- (53) Armelao, L.; Barreca, D.; Gross, S.; Tondello, E. Nanoscale Cobalt Oxides Thin Films Obtained by CVD and Sol-Gel Routes. *J. Phys. IV* **2001**, *11*, Pr3–Pr438.
- (54) Riedel, E. *Anorganische Chemie*, 3rd ed.; de Gruyter: Berlin, New York, 1994.
- (55) Chuang, T. J.; Brundle, C. R.; Rice, D. W. Interpretation of the X-Ray Photoemission Spectra of Cobalt Oxides and Cobalt Oxide Surfaces. *Surf. Sci.* **1976**, *59* (2), 413–429.

- (56) Benson, P.; Briggs, G. W. D.; Wynne-Jones, W. F. K. The Cobalt Hydroxide electrode—I. Structure and Phase Transitions of the Hydroxides. *Electrochim. Acta* **1964**, *9* (3), 275–280.
- (57) Göhr, H. Über Anodisch Gebildete Oxidische Deckschichten Auf Kobalt in Wässriger Lösung - I. Zur Thermodynamik Des Systems Kobalt - Wässrige Lösung. *Electrochim. Acta* **1966**, *11*, 827–834.
- (58) Behl, W. K.; Toni, J. E. Anodic Oxidation of Cobalt in Potassium Hydroxide Electrolytes. *J. Electroanal. Chem.* **1971**, *31*, 63–75.
- (59) Wang, G.; Zhang, L.; Zhang, J. A Review of Electrode Materials for Electrochemical Supercapacitors. *Chem. Soc. Rev.* **2012**, *41* (2), 797.
- (60) Granqvist, C. G. *Handbook of Inorganic Electrochromic Materials*, 2nd ed.; Granqvist, C. G., Ed.; Elsevier: Amsterdam, 1995.
- (61) Fergus, J. W. Recent Developments in Cathode Materials for Lithium Ion Batteries. *J. Power Sources* **2010**, *195* (4), 939–954.
- (62) Li, W. Y.; Xu, L. N.; Chen, J. Co₃O₄ Nanomaterials in Lithium-Ion Batteries and Gas Sensors. *Adv. Funct. Mater.* **2005**, *15* (5), 851–857.
- (63) El Wakkad, S. E. S.; Hickling, A. The Anodic Behaviour of Metals. Part VI. Cobalt. *Trans. Faraday Soc.* **1950**, *46* (10), 820.
- (64) Nikolov, I.; Darkaoui, R.; Zhecheva, E.; Stoyanova, R.; Dimitrov, N.; Vitanov, T. Electrocatalytic Activity of Spinel Related Cobalties M_xCo_{3-x}O₄ (M = Li, Ni, Cu) in the Oxygen Evolution Reaction. *J. Electroanal. Chem.* **1997**, *429* (1-2), 157–168.
- (65) Tiwari, S.; Samuel, S.; Singh, R. N.; Poillerat, G.; Koenig, J. F.; Chartier, P. Active Thin NiCo₂O₄ Film Prepared on Nickel by Spray Pyrolysis for Oxygen Evolution. *Int. J. Hydrogen Energy* **1995**, *20* (1), 9–15.
- (66) De Chialvo, M.; Chialvo, A. Oxygen Evolution Reaction on Ni_xCo_(3-x)O₄ Electrodes with Spinel Structure. *Electrochim. Acta* **1993**, *38* (15), 2247–2252.
- (67) Singh, J. P.; Singh, R. N. New Active Spinel-Type M_xCO_{3-x}O₄ Films for Electro-Catalysis of Oxygen Evolution. *J. new Mater. Electrochem. Syst.* **2000**, *3*, 131–139.
- (68) Singh, R. N.; Pandey, J. P.; Singh, N. K.; Lal, B.; Chartier, P.; Koenig, J. F. Sol-Gel Derived Spinel M_xCo_{3-x}O₄ (M = Ni, Cu; 0 ≤ x ≤ 1) Films and Oxygen Evolution. *Electrochim. Acta* **2000**, *45*, 1911–1919.

- (69) Hamdani, M.; Singh, R. N.; Chartier, P. Co₃O₄ and Co-Based Spinel Oxides Bifunctional Oxygen Electrodes. *Int. J. Electrochem. Sci* **2010**, *5*, 556–577.
- (70) Singh, R. N.; Tiwari, S. K.; Singh, S. P.; Singh, N. K.; Poillerat, G.; Chartier, P. Synthesis of (La, Sr)CoO₃ Perovskite Films via a Sol-Gel Route and Their Physicochemical and Electrochemical Surface Characterization for Anode Application in Alkaline Water Electrolysis. *J. Chem. Soc. Faraday Trans.* **1996**, *92* (14), 2593.
- (71) Rasiyah, P.; Tseung, A. C. C. A Mechanistic Study of Oxygen Evolution on Li-Doped Co₃O₄. *J. Electrochem. Soc.* **1983**, *130* (2), 365.
- (72) Singh, R. N.; Mishra, D.; Sinha, A. S. K.; Singh, A. Novel Electrocatalysts for Generating Oxygen from Alkaline Water Electrolysis. *Electrochem. commun.* **2007**, *9* (6), 1369–1373.
- (73) Marsan, B.; Fradette, N.; Beaudoin, G. Physicochemical and Electrochemical Properties of CuCo₂O₄ Electrodes Prepared by Thermal Decomposition for Oxygen Evolution. *J. Electrochem. Soc.* **1992**, *139* (7), 1889.
- (74) Spinolo, G.; Ardizzone, S.; Trasatti, S. Surface Characterization of Co₃O₄ Electrodes Prepared by the Sol-Gel Method. *J. Electroanal. Chem.* **1997**, *423*, 49–57.
- (75) El Baydi, M.; Poillerat, G.; Rehspringer, J.-L.; Gautier, J. L.; Koenig, J.-F.; Chartier, P. A Sol-Gel Route for the Preparation of Co₃O₄ Catalyst for Oxygen Electrocatalysis in Alkaline Medium. *Journal of Solid State Chemistry*, 1994, *109*, 281–288.
- (76) Singh, N. K.; Sungh, J. P.; Singh, R. N. Sol-gel-Derived Spinel Co₃O₄ Films and Oxygen Evolution: Part II. Optimization of Preparation Conditions and Influence of the Nature of the Metal Salt Precursor. *Int. J. Hydrogen Energy* **2002**, *27* (9), 895–903.
- (77) Orel, B.; Kauc, V. Characterization of Spinel Co₃O₄ and Li-Doped Co₃O₄ Thin Film Electrocatalysts Prepared by the Sol – Gel Route. **2000**, *45*, 4359–4371.
- (78) Poillerat, G.; Chartier, P. Thin Films of Co₃O₄ and NiCo₂O₄ Prepared by the Method of Chemical Spray Pyrolysis for Electrocatalysis Part IV. The Electrocatalysis of Oxygen Reduction. *Thin Film.* **1991**, *314*, 241–257.
- (79) Singh, R. N.; Hamdani, M.; Koenig, J.-F.; Poillerat, G.; Gautier, J. L.; Chartier, P. Thin Films of Co₃O₄ and NiCo₂O₄ Obtained by the Method of Chemical Spray Pyrolysis for Electrocatalysis III. The Electrocatalysis of Oxygen Evolution. *J. Appl. Electrochem.* **1990**, *20*, 442–446.
- (80) Koza, J. A.; He, Z.; Miller, A. S.; Switzer, J. A. Electrodeposition of Crystalline Co₃O₄ —A Catalyst for the Oxygen Evolution Reaction. *Chem. Mater.* **2012**, *24* (18), 3567–3573.

- (81) Castro, E.; Gervasi, C.; Vilche, J. Oxygen Evolution on Electrodeposited Cobalt Oxides. *J. Appl. Electrochem.* **1998**, *28*, 835–841.
- (82) Casella, I. G. Electrodeposition of Cobalt Oxide Films from Carbonate Solutions Containing Co (II)–tartrate Complexes. *J. Electroanal. Chem.* **2002**, *520*, 119–125.
- (83) Casella, I. G.; Di Fonzo, D. A. Anodic Electrodeposition of Cobalt Oxides from an Alkaline Bath Containing Co-Gluconate Complexes on Glassy Carbon. An Electroanalytical Investigation. *Electrochim. Acta* **2011**, *56* (22), 7536–7540.
- (84) Kanan, M. W.; Nocera, D. G. In Situ Formation of an Oxygen-Evolving Catalyst in Neutral Water Containing Phosphate and Co^{2+} . *Science* **2008**, *321* (5892), 1072–1075.
- (85) Risch, M.; Khare, V.; Zaharleva, I.; Gerencser, L.; Chernev, P.; Dau, H. Cobalt-Oxo Core of a Water-Oxidizing Catalyst Film. *J. Am. Chem. Soc.* **2009**, *131* (20), 6936–6937.
- (86) Kanan, M. W.; Yano, J.; Surendranath, Y.; Dincă, M.; Yachandra, V. K.; Nocera, D. G. Structure and Valency of a Cobalt-Phosphate Water Oxidation Catalyst Determined by in Situ X-Ray Spectroscopy. *J. Am. Chem. Soc.* **2010**, *132* (39), 13692–13701.
- (87) Risch, M.; Klingan, K.; Ringleb, F.; Chernev, P.; Zaharieva, I.; Fischer, A.; Dau, H. Water Oxidation by Electrodeposited Cobalt Oxides--Role of Anions and Redox-Inert Cations in Structure and Function of the Amorphous Catalyst. *ChemSusChem* **2012**, *5* (3), 542–549.
- (88) McAlpin, J. G.; Surendranath, Y.; Dincă, M.; Stich, T. a.; Stoian, S. a.; Casey, W. H.; Nocera, D. G.; Britt, R. D. EPR Evidence for Co(IV) Species Produced during Water Oxidation at Neutral pH. *J. Am. Chem. Soc.* **2010**, *132* (20), 6882–6883.
- (89) Surendranath, Y.; Lutterman, D. a.; Liu, Y.; Nocera, D. G. Nucleation, Growth, and Repair of a Cobalt-Based Oxygen Evolving Catalyst. *J. Am. Chem. Soc.* **2012**, *134* (14), 6326–6336.
- (90) Klingan, K.; Ringleb, F.; Zaharieva, I.; Heidkamp, J.; Chernev, P.; Gonzalez-Flores, D.; Risch, M.; Fischer, A.; Dau, H. Water Oxidation by Amorphous Cobalt-Based Oxides: Volume Activity and Proton Transfer to Electrolyte Bases. *ChemSusChem* **2014**, *7*, 1301–1310.
- (91) Abdi, F. F.; Han, L.; Smets, A. H. M.; Zeman, M.; Dam, B.; van de Krol, R. Efficient Solar Water Splitting by Enhanced Charge Separation in a Bismuth Vanadate-Silicon Tandem Photoelectrode. *Nat. Commun.* **2013**, *4*, 2195.
- (92) Zhong, D. K.; Cornuz, M.; Sivula, K.; Grätzel, M.; Gamelin, D. R. Photo-Assisted Electrodeposition of Cobalt–phosphate (Co–Pi) Catalyst on Hematite Photoanodes for Solar Water Oxidation. *Energy Environ. Sci.* **2011**, *4* (5), 1759.

- (93) Reece, S. Y.; Hamel, J. A.; Sung, K.; Jarvi, T. D.; Esswein, A. J.; Pijpers, J. J. H.; Nocera, D. G. Wireless Solar Water Splitting Using Silicon-Based Semiconductors and Earth-Abundant Catalysts. *Science* **2011**, 334 (6056), 645–648.
- (94) Esswein, A. J.; Surendranath, Y.; Reece, S. Y.; Nocera, D. G. Highly Active Cobalt Phosphate and Borate Based Oxygen Evolving Catalysts Operating in Neutral and Natural Waters. *Energy Environ. Sci.* **2011**, 4 (2), 499.
- (95) Jiao, F.; Frei, H. Nanostructured Cobalt Oxide Clusters in Mesoporous Silica as Efficient Oxygen-Evolving Catalysts. *Angew. Chemie - Int. Ed.* **2009**, 48 (10), 1841–1844.
- (96) Jiao, F.; Frei, H. Nanostructured Cobalt and Manganese Oxide Clusters as Efficient Water Oxidation Catalysts. *Energy Environ. Sci.* **2010**, 3 (8), 1018.
- (97) Sun, Y.; Gao, S.; Lei, F.; Liu, J.; Liang, L.; Xie, Y. Atomically-Thin Non-Layered Cobalt Oxide Porous Sheets for Highly Efficient Oxygen-Evolving Electrocatalysts. *Chem. Sci.* **2014**, 5 (10), 3976.
- (98) Najafpour, M. M.; Ehrenberg, T.; Wiechen, M.; Kurz, P. Calcium manganese(III) Oxides ($\text{CaMn}_2\text{O}_4 \cdot x\text{H}_2\text{O}$) as Biomimetic Oxygen-Evolving Catalysts. *Angew. Chem. Int. Ed. Engl.* **2010**, 49 (12), 2233–2237.
- (99) Wiechen, M.; Zaharieva, I.; Dau, H.; Kurz, P. Layered Manganese Oxides for Water-Oxidation: Alkaline Earth Cations Influence Catalytic Activity in a Photosystem II-like Fashion. *Chem. Sci.* **2012**, 3 (7), 2330.
- (100) Ramírez, A.; Bogdanoff, P.; Friedrich, D.; Fiechter, S. Synthesis of $\text{Ca}_2\text{Mn}_3\text{O}_8$ Films and Their Electrochemical Studies for the Oxygen Evolution Reaction (OER) of Water. *Nano Energy* **2012**, 1 (2), 282–289.
- (101) Gorlin, Y.; Jaramillo, T. F. A Bifunctional Nonprecious Metal Catalyst for Oxygen Reduction and Water Oxidation. *J. Am. Chem. Soc.* **2010**, 132 (39), 13612–13614.
- (102) Fekete, M.; Hocking, R. K.; Chang, S. L. Y.; Italiano, C.; Patti, A. F.; Arena, F.; Spiccia, L. Highly Active Screen-Printed Electrocatalysts for Water Oxidation Based on B-Manganese Oxide. *Energy Environ. Sci.* **2013**, 6 (7), 2222.
- (103) Zaharieva, I.; Chernev, P.; Risch, M.; Klingan, K.; Kohlhoff, M.; Fischer, A.; Dau, H. Electrosynthesis, Functional, and Structural Characterization of a Water-Oxidizing Manganese Oxide. *Energy Environ. Sci.* **2012**, 5 (5), 7081.
- (104) Jiao, F.; Frei, H. Nanostructured Manganese Oxide Clusters Supported on Mesoporous Silica as Efficient Oxygen-Evolving Catalysts. *Chem. Commun.* **2010**, 46 (17), 2920–2922.

- (105) Takashima, T.; Hashimoto, K.; Nakamura, R. Mechanisms of pH-Dependent Activity for Water Oxidation to Molecular Oxygen by MnO₂ Electrocatalysts. *J. Am. Chem. Soc.* **2012**, *134* (3), 1519–1527.
- (106) Gorlin, Y.; Lassalle-Kaiser, B.; Benck, J. D.; Gul, S.; Webb, S. M.; Yachandra, V. K.; Yano, J.; Jaramillo, T. F. In Situ X-Ray Absorption Spectroscopy Investigation of a Bifunctional Manganese Oxide Catalyst with High Activity for Electrochemical Water Oxidation and Oxygen Reduction. *J. Am. Chem. Soc.* **2013**, *135* (23), 8525–8534.
- (107) Hocking, R. K.; Brimblecombe, R.; Chang, L.-Y.; Singh, A.; Cheah, M. H.; Glover, C.; Casey, W. H.; Spiccia, L. Water-Oxidation Catalysis by Manganese in a Geochemical-like Cycle. *Nat. Chem.* **2011**, *3* (6), 461–466.
- (108) Zaharieva, I.; Najafpour, M. M.; Wiechen, M.; Haumann, M.; Kurz, P.; Dau, H. Synthetic Manganese–calcium Oxides Mimic the Water-Oxidizing Complex of Photosynthesis Functionally and Structurally. *Energy Environ. Sci.* **2011**, *4* (7), 2400.
- (109) Shevchenko, D.; Anderlund, M. F.; Styring, S.; Dau, H.; Zaharieva, I.; Thapper, A. Water Oxidation by Manganese Oxides Formed from Tetranuclear Precursor Complexes: The Influence of Phosphate on Structure and Activity. *Phys. Chem. Chem. Phys.* **2014**, *16* (24), 11965.
- (110) Norrestam, R. Alpha-Manganese(III) Oxide --- a C-Type Sesquioxide of Orthorhombic Symmetry. *Acta Chem. Scand.* **1967**, *21* (10), 2871–2884.
- (111) Ramírez, A.; Hillebrand, P.; Stellmach, D.; May, M. M.; Bogdanoff, P.; Fiechter, S. Evaluation of MnO_x, Mn₂O₃, and Mn₃O₄ Electrodeposited Films for the Oxygen Evolution Reaction of Water. *J. Phys. Chem. C* **2014**, *118*, 14073–14081.
- (112) Hillebrand, P.; Ramírez-Caro, A.; Calvet, W.; Bogdanoff, P.; Fiechter, S. On the Structure-Function Relationship of Cobalt and Manganese Oxides as Oxygen Evolving Catalysts for Light-Driven Water Electrolysis: An In-Line Synchrotron Radiation Photoelectron Spectroscopy Study. *ECS Trans.* **2014**, *61* (14), 9–20.
- (113) Fiechter, S.; Bogdanoff, P. Oxygen Evolution and Reduction Catalysts: Structural and Electronic Aspects of Transition Metal Based Compounds and Composites. In *Photoelectrochemical Water Splitting: Materials, Processes and Architectures*; Lewerenz, H. J., Peter, L., Eds.; The Royal Society of Chemistry: Cambridge, 2013; pp 154–192.
- (114) Ramírez, a.; Friedrich, D.; Kunst, M.; Fiechter, S. Charge Carrier Kinetics in MnO_x, Mn₂O₃ and Mn₃O₄ Films for Water Oxidation. *Chem. Phys. Lett.* **2013**, *568-569*, 157–160.
- (115) Blomqvist, K.; Still, E. R. Solution Studies of Systems with Polynuclear Complex Formation: Copper(II) and Cadmium(II) D-Gluconate Systems. *Anal. Chem.* **1985**, *57*, 749–752.

- (116) Casella, I. G.; Contursi, M. Cobalt Oxide Electrodeposition on Various Electrode Substrates from Alkaline Medium Containing Co–gluconate Complexes: A Comparative Voltammetric Study. *J. Solid State Electrochem.* **2012**, *16* (12), 3739–3746.
- (117) Wu, M.-S.; Chiang, P.-C. J.; Lee, J.-T.; Lin, J.-C. Synthesis of Manganese Oxide Electrodes with Interconnected Nanowire Structure as an Anode Material for Rechargeable Lithium Ion Batteries. *J. Phys. Chem. B* **2005**, *109* (49), 23279–23284.
- (118) Bard, A. J.; Faulkner, L. R. *Electrochemical Methods. Fundamentals and Applications*, second edi.; John Wiley & Sons, 2001.
- (119) Heinze, J. Cyclovoltammetrie - Die “Spektroskopie” Des Elektrochemikers. *Angew. Chemie* **1984**, *96* (11), 823–916.
- (120) Bogdanoff, P.; Alonso-Vante, N. Online Determination via Differential Electrochemical Mass-Spectroscopy (DEMS) of Chemical-Products Formed in Photoelectrocatalytical Systems. *Berichte der Bunsen-Gesellschaft für Phys. Chemie* **1993**, *97* (7), 940–943.
- (121) Bogdanoff, P.; Alonso-Vante, N. A Kinetic Approach of Competitive Photoelectrooxidation of HCOOH and H₂O on TiO₂ Anatase Thin Layers via on-Line Mass Detection. *J. Electroanal. Chem.* **1994**, *379*, 415–421.
- (122) Hüfner, S. *Photoelectron Spectroscopy. Principles and Applications*, Third edit.; Springer-Verlag: Berlin, Heidelberg, 2003.
- (123) Ratner, B.; Castner, D. Electron Spectroscopy for Chemical Analysis. In *Surface Analysis: The Principal Techniques*; Vickerman, J. C., Gilmore, I. S., Eds.; John Wiley & Sons, 2009; pp 43–98.
- (124) Kaiser, B.; Jaegermann, W.; Fiechter, S.; Lewerenz, H.-J. Direct Photoelectrochemical Conversion of Sun Light Into Hydrogen for Chemical Energy Storage. *Bunsen-Magazin* **2011**, *4*, 104–111.
- (125) Stellmach, D.; Bogdanoff, P.; Gabriel, O.; Stannowski, B.; Schlattmann, R.; Krol, R. van de; Fiechter, S. Artificial Leaf for Solar Water Splitting Based on a Triple-Junction a-Si:H/ a-Si:H/ Mc-Si:H Thin Film Solar Cell and a PEDOT:PSS/Catalysts Blend. *Prep.* **2015**.
- (126) Djokic (Editor), S. S. *Electrodeposition*; Djokic, S. S., Ed.; Modern Aspects of Electrochemistry; Springer New York: New York, NY, 2010; Vol. 48.
- (127) Pergola, F.; Nucci, L.; Pezzatini, G.; Wei, H.; Guidelli, R. Direct Electro-Oxidation of D-Gluconic Acid to D-Arabinose. *Electrochim. Acta* **1994**, *39* (10), 1415–1417.
- (128) Vallières, C.; Matlosz, M. A Multisectioned Porous Electrode for Synthesis of D-Arabinose. *J. Electrochem. Soc.* **1999**, *146* (8), 2933.

- (129) Zachäus, C. *Unpublished Results*.
- (130) Yeo, B. S.; Bell, A. T. Enhanced Activity of Gold-Supported Cobalt Oxide for the Electrochemical Evolution of Oxygen. *J. Am. Chem. Soc.* **2011**, *133* (14), 5587–5593.
- (131) Barrera, E. C.; Viveros, T. G.; Morales, U. Preparation of Selective Surfaces of Black Cobalt by the Sol-Gel Process. *Renew. Energy* **1996**, *9* (1-4), 733–736.
- (132) Chaudhury, N. K.; Gupta, R.; Gulia, S. Sol-Gel Technology for Sensor Applications. *Def. Sci. J.* **2007**, *57* (3), 241–253.
- (133) Lu, X.; Ng, Y. H.; Zhao, C. Gold Nanoparticles Embedded within Mesoporous Cobalt Oxide Enhance Electrochemical Oxygen Evolution. *ChemSusChem* **2014**, *7* (1), 82–86.
- (134) Švegl, F.; Orel, B.; Grabec-Švegl, I.; Kaučič, V. Characterization of Spinel Co₃O₄ and Li-Doped Co₃O₄ Thin Film Electrocatalysts Prepared by the Sol-gel Route. *Electrochim. Acta* **2000**, *45* (25-26), 4359–4371.
- (135) Co, A. C.; Liu, J.; Serebrennikova, I.; Abel, C. M.; Birss, V. I. Structural and Electrochemical Studies of Co Oxide Films Formed by the Sol-Gel Technique. *J. Mater. Sci.* **2005**, *40* (15), 4039–4052.
- (136) Boggio, R.; Carugati, A.; Trasatti, S. Electrochemical Surface Properties of Co₃O₄ Electrodes. *J. Appl. Electrochem.* **1987**, *17* (August 1986), 828–840.
- (137) Burke, L. D.; Murphy, M. M. The Electrocatalytic Behavior of Cobalt (and Iron) Electrodes at Low Potential in Base. *Journal of The Electrochemical Society*, 1991, *138*, 88.
- (138) Casella, I. G.; Guascito, M. R. Electrochemical Preparation of a Composite Gold–cobalt Electrode and Its Electrocatalytic Activity in Alkaline Medium. *Electrochim. Acta* **1999**, *45*, 1113–1120.
- (139) Serebrennikova, I. Electrochemical and Structural Studies of Sol-Gel Formed Ni-Co Oxide Films, PhD-thesis, University of Calgary, 1999.
- (140) GESTIS-Stoffdatenbank. Cobalt(II,III)-oxid
[http://gestis.itrust.de/nxt/gateway.dll/gestis_de/500063.xml?f=templates\\$fn=document-frameset.htm\\$3.0](http://gestis.itrust.de/nxt/gateway.dll/gestis_de/500063.xml?f=templates$fn=document-frameset.htm$3.0) (accessed Feb 23, 2015).
- (141) Trasatti, S.; Petrii, O. A. Real Surface Area Measurements in Electrochemistry. *Pure and Applied Chemistry*, 1991, *63*, 711–734.
- (142) Tilak, B. V.; Rader, C. G.; Rangarajan S K. Techniques for Characterizing Porous Electrodes I : Determination of the Double Layer Capacity. *J. Electrochem. Soc.* **1977**, *124* (12), 1879–1886.

- (143) Bockris, J. O. M.; Otagawa, T. The Electrocatalysis of Oxygen Evolution on Perovskites. *J. Electrochem. Soc.* **1984**, *131* (2), 290–302.
- (144) Levine, S.; Smith, A. L. Theory of the Differential Capacity of the Oxide/Aqueous Electrolyte Interface. *Discuss. Faraday Soc.* **1971**, No. 52, 290–301.
- (145) Lal, B.; Singh, N. K.; Samuel, S.; Singh, R. N. Electrocatalytic Properties of $\text{Cu}_x\text{Co}_{(3-x)}\text{O}_4$ ($0 < x < 1$) Obtained by a New Precipitation Method for Oxygen Evolution. *J. New Mater. Electrochem. Syst.* **1999**, *2*, 59–64.
- (146) Nørskov, J.; Bligaard, T.; Logadottir, A.; Bahn, S.; Hansen, L. B.; Bollinger, M.; Bengaard, H.; Hammer, B.; Sljivancanin, Z.; Mavrikakis, M.; et al. Universality in Heterogeneous Catalysis. *J. Catal.* **2002**, *209* (2), 275–278.
- (147) Singh, S. P.; Samuels, S.; Tiwari, S. K.; Singh, R. N. Preparation of Thin Co_3O_4 Films on Ni and Their Electrocatalytic Surface Properties towards Oxygen Evolution. *Int. J. Hydrogen Energy* **1996**, *21* (3), 171–178.
- (148) Wu, G.; Li, N.; Zhou, D. R.; Mitsuo, K.; Xu, B. Q. Anodically Electrodeposited Co+Ni Mixed Oxide Electrode: Preparation and Electrocatalytic Activity for Oxygen Evolution in Alkaline Media. *J. Solid State Chem.* **2004**, *177*, 3682–3692.
- (149) Kratzig, A. Strukturelle Und Physikalisch-Chemische Eigenschaften von Übergangsmetallchalkogeniden Als Elektrokatalysatoren Für Die Sauerstoffentwicklung, PhD- thesis, Technische Universität Berlin, 2014.
- (150) Surendranath, Y.; Dincă, M.; Nocera, D. G. Electrolyte-Dependent Electrosynthesis and Activity of Cobalt-Based Water Oxidation Catalysts. *J. Am. Chem. Soc.* **2009**, *131* (7), 2615–2620.
- (151) Surendranath, Y.; Kanan, M. W.; Nocera, D. G. Mechanistic Studies of the Oxygen Evolution Reaction by a Cobalt-Phosphate Catalyst at Neutral pH. *J. Am. Chem. Soc.* **2010**, *132* (46), 16501–16509.
- (152) Ringleb, F. Elektrochemische Wasseroxidation an Einer Katalytischen Kobalt-Schicht : Belege Für Protonengekoppelten Elektronentransfer, Diploma thesis, Humbolt Universität zu Berlin, 2009.
- (153) Han, K. S.; Han, O. H. Influence of Metal Cleaning on the Particle Size and Surface Morphology of Platinum Black Studied by NMR, TEM and CV Techniques. *Electrochim. Acta* **2001**, *47*, 519–523.
- (154) Weber, M. F.; Dignam, M. J. Efficiency of Splitting Water with Semiconducting Photoelectrodes. *J. Electrochem. Soc.* **1984**, *131* (June), 1258.

- (155) Weber, M. F.; Dignam, M. J. Splitting Water with Semiconducting photoelectrodes — Efficiency Considerations. *Int. J. Hydrogen Energy* **1986**, *11*, 225–232.
- (156) Walter, M. G.; Warren, E. L.; McKone, J. R.; Boettcher, S. W.; Mi, Q.; Santori, E. a.; Lewis, N. S. Solar Water Splitting Cells. *Chem. Rev.* **2010**, *110*, 6446–6473.
- (157) Haussener, S.; Xiang, C.; Spurgeon, J. M.; Ardo, S.; Lewis, N. S.; Weber, A. Z. Modeling, Simulation, and Design Criteria for Photoelectrochemical Water-Splitting Systems. *Energy Environ. Sci.* **2012**, *5*, 9922–9935.
- (158) Langell, M.; Anderson, M.; Carson, G.; Peng, L.; Smith, S. Valence-Band Electronic Structure of Co₃O₄ Epitaxy on CoO(100). *Phys. Rev. B* **1999**, *59* (7), 4791–4798.
- (159) Petitto, S. C.; Langell, M. A. Surface Composition and Structure of Co₃O₄(110) and the Effect of Impurity Segregation. *J. Vac. Sci. Technol. A Vacuum, Surfaces, Film.* **2004**, *22* (4), 1690.
- (160) Foelske, A.; Strehblow, H. H. Structure and Composition of Electrochemically Prepared Oxide Layers on Co in Alkaline Solutions Studied by XPS. *Surf. Interface Anal.* **2002**, *34* (1), 125–129.
- (161) Dupin, J. C.; Gonbeau, D.; Benqlilou-Moudden, H.; Vinatier, P.; Levasseur, A. XPS Analysis of New Lithium Cobalt Oxide Thin-Films before and after Lithium Deintercalation. *Thin Solid Films* **2001**, *384* (1), 23–32.
- (162) Artyushkova, K.; Levendosky, S.; Atanassov, P.; Fulghum, J. XPS Structural Studies of Nano-Composite Non-Platinum Electrocatalysts for Polymer Electrolyte Fuel Cells. *Top. Catal.* **2007**, *46* (3-4), 263–275.
- (163) Shirley, D. A. High-Resolution X-Ray Photoemission Spectrum of the Valence Bands of Gold. *Phys. Rev. B* **1972**, *5* (12), 4709–4714.
- (164) Moulder, J. F.; Stickle, W. F.; Sobol, P. E.; Bomben, K. D. *Handbook of X-Ray Photoelectron Spectroscopy*; Chastain, J., Ed.; Perkin-Elmer Corporation: Eden Prairie, 1992.
- (165) Zafeiratos, S.; Dintzer, T.; Teschner, D.; Blume, R.; Hävecker, M.; Knop-Gericke, a.; Schlögl, R. Methanol Oxidation over Model Cobalt Catalysts: Influence of the Cobalt Oxidation State on the Reactivity. *J. Catal.* **2010**, *269* (2), 309–317.
- (166) Brundle, C. R.; Chuang, T. J.; Rice, D. W. X-Ray Photoemission Study of the Interaction of Oxygen and Air with Clean Cobalt Surfaces. *Surf. Sci.* **1976**, *60*, 286–300.
- (167) Haber, J.; Ungier, L. On Chemical Shifts of ESCA and Auger Lines in Cobalt Oxides. *J. Electron Spectros. Relat. Phenomena* **1977**, *12* (3), 305–312.

- (168) Tan, B. J.; Klabunde, K. J.; Sherwood, P. M. a. XPS Studies of Solvated Metal Atom Dispersed (SMAD) Catalysts. Evidence for Layered Cobalt-Manganese Particles on Alumina and Silica. *J. Am. Chem. Soc.* **1991**, *113* (3), 855–861.
- (169) Carson, G. A.; Nassir, M. H.; Langell, M. A. Epitaxial Growth of Co₃O₄ on CoO(100). *J. Vac. Sci. Technol. A Vacuum, Surfaces, Film.* **1996**, *14* (3), 1637.
- (170) Yang, J.; Liu, H.; Martens, W. N.; Frost, R. L. Synthesis and Characterization of Cobalt Hydroxide, Cobalt Oxyhydroxide, and Cobalt Oxide Nanodiscs. *J. Phys. Chem. C* **2010**, *114* (1), 111–119.
- (171) McIntyre, N. S.; Cook, M. G. X-Ray Photoelectron Studies on Some Oxides and Hydroxides of Cobalt, Nickel, and Copper. *Anal. Chem.* **1975**, *47* (13), 2208–2213.
- (172) Hu, C. C.; Hsu, T. Y. Effects of Complex Agents on the Anodic Deposition and Electrochemical Characteristics of Cobalt Oxides. *Electrochim. Acta* **2008**, *53*, 2386–2395.
- (173) Mattogno, G.; Ferragina, C.; Massucci, M. A.; Patrono, P.; La Ginestra, A. X-RAY PHOTOELECTRON SPECTROSCOPIC EVIDENCE OF INTERLAYER COMPLEX FORMATION BETWEEN Co(II) AND N-HETEROCYCLES IN Alpha-Zr(HPO₄)₂*H₂O. *J. Electron Spectros. Relat. Phenomena* **1988**, *46*, 285–295.
- (174) Grellner, F.; Klingenberg, B.; Borgmann, D.; Wedler, G. Electron Spectroscopic Study of the Interaction of Oxygen with Co (1120) and of Coadsorption with Water. *J. Electron Spectros. Relat. Phenomena* **1995**, *71*, 107–115.
- (175) Singh, H.; Sinha, a. K.; Singh, M. N.; Tiwari, P.; Phase, D. M.; Deb, S. K. Spectroscopic and Structural Studies of Isochronally Annealed Cobalt Oxide Nanoparticles. *J. Phys. Chem. Solids* **2014**, *75* (3), 397–402.
- (176) Petitto, S. C.; Marsh, E. M.; Carson, G. a.; Langell, M. a. Cobalt Oxide Surface Chemistry: The Interaction of CoO(100), Co₃O₄(110) and Co₃O₄(111) with Oxygen and Water. *J. Mol. Catal. A Chem.* **2008**, *281* (1-2), 49–58.
- (177) Burke, L. D.; Lyons, M. E.; Murphy, O. J. Formation of Hydrous Oxide Films on Cobalt under Potential Cycling Conditions. *J. Electroanal. Chem.* **1982**, *132* (JAN), 247–261.
- (178) Benson, P.; Briggs, G. W. D.; Wynne-Jones, W. F. K. The Cobalt Hydroxide electrode—II. Electrochemical Behaviour. *Electrochim. Acta* **1964**, *9* (3), 281–288.
- (179) Švegl, F.; Orel, B.; Hutchins, M. G.; Kalcher, K. Structural and Spectroelectrochemical Investigations of Sol-Gel Derived Electrochromic Spinel Co₃O₄ Films. *Journal of The Electrochemical Society*, 1996, *143*, 1532.

- (180) Burke, L. D.; Murphy, O. J. Electrochromic Behaviour of Oxide Films Grown on Cobalt and Manganese in Base. *J. Electroanal. Chem.* **1980**, *109*, 373–377.
- (181) Burke, L. D.; Murphy, O. J. Electrochromic Behaviour of Electrodeposited Cobalt Oxide Films. *J. Electroanal. Chem.* **1980**, *112*, 379–382.
- (182) Trotochaud, L.; Mills, T. J.; Boettcher, S. W. An Optocatalytic Model for Semiconductor-Catalyst Water-Splitting Photoelectrodes Based on in Situ Optical Measurements on Operational Catalysts. *J. Phys. Chem. Lett.* **2013**, *4* (6), 931–935.
- (183) Fonseca, C. N. P. da; Paoli, M.-A. De; Gorenstein, A. The Electrochromic Effect in Cobalt Oxide Thin Films. *Adv. Mater.* **1991**, *3* (11), 553–555.
- (184) Delaplane, R. G.; Ibers, J. a; Ferraro, J. R.; Rush, J. J. Diffraction and Spectroscopic Studies of the Cobaltic Acid System $\text{HCoO}_2\text{-DCoO}_2$. *J. Chem. Phys.* **1969**, *50* (5), 1920–1927.
- (185) Sanchez Casalongue, H. G.; Ng, M. L.; Kaya, S.; Friebe, D.; Ogasawara, H.; Nilsson, A. In Situ Observation of Surface Species on Iridium Oxide Nanoparticles during the Oxygen Evolution Reaction. *Angew. Chem. Int. Ed. Engl.* **2014**, *53* (28), 7169–7172.
- (186) Morita, M.; Iwakura, C.; Tamura, H. The Anodic Characteristics of Massive Manganese Oxide Electrode. *Electrochim. Acta* **1979**, *24* (4), 357–362.
- (187) Chigane, M.; Ishikawa, M. Manganese Oxide Thin Film Preparation by Potentiostatic Electrolyses and Electrochromism. *J. Electrochem. Soc.* **2000**, *147* (6), 2246.
- (188) Audi, A. A.; Sherwood, P. M. a. Valence-Band X-Ray Photoelectron Spectroscopic Studies of Manganese and Its Oxides Interpreted by Cluster and Band Structure Calculations. *Surf. Interface Anal.* **2002**, *33* (3), 274–282.
- (189) Oku, M.; Hirokawa, K.; Ikeda, S. X-Ray Photoelectron Spectroscopy of Manganese—oxygen Systems. *J. Electron Spectros. Relat. Phenomena* **1975**, *7* (5), 465–473.
- (190) Oku, M.; Hirokawa, K. X-Ray Photoelectron Spectroscopy of Co_3O_4 , Fe_3O_4 , Mn_3O_4 , and Related Compounds. *J. Electron Spectros. Relat. Phenomena* **1976**, *8* (5), 475–481.
- (191) Di Castro, V.; Polzonetti, G. XPS Study of MnO Oxidation. *J. Electron Spectrosc. Relat. Phenomena* **1989**, *48*, 117–123.
- (192) Foord, J. S.; Jackman, R. B.; Allen, G. C. An X-Ray Photoelectron Spectroscopic Investigation of the Oxidation of Manganese. *Philos. Mag. A* **1984**, *49* (5), 657–663.
- (193) Carver, J. C.; Schweitzer, G. K.; Carlson, T. a. Use of X-Ray Photoelectron Spectroscopy to Study Bonding in Cr, Mn, Fe, and Co Compounds. *J. Chem. Phys.* **1972**, *57* (2), 973.

- (194) Moses Ezhil Raj, A.; Victoria, S. G.; Jothy, V. B.; Ravidhas, C.; Wollschläger, J.; Suendorf, M.; Neumann, M.; Jayachandran, M.; Sanjeeviraja, C. XRD and XPS Characterization of Mixed Valence Mn₃O₄ Hausmannite Thin Films Prepared by Chemical Spray Pyrolysis Technique. *Appl. Surf. Sci.* **2010**, *256* (9), 2920–2926.
- (195) Hu, H.-K.; Rabalais, J. W. Chemisorption and the Initial Stage of Oxidation on Mn. *Surf. Sci.* **1981**, *107*, 376–390.
- (196) Lume-Pereira, C.; Baral, S.; Henglein, a; Janata, E. Chemistry of Colloidal Manganese Dioxide. 1. Mechanism of Reduction by an Organic Radical (a Radiation Chemical Study). *J. Phys. Chem.* **1985**, *89* (26), 5772–5778.
- (197) Takashima, T.; Yamaguchi, A.; Hashimoto, K.; Irie, H.; Nakamura, R. In Situ UV-Vis Absorption Spectra of Intermediate Species of Oxygen-Evolution Reaction on the Surface of MnO₂ in Neutral and Alkaline Media. *Electrochemistry* **2014**, *82* (5), 325–327.
- (198) Cheng, F.; Shen, J.; Peng, B.; Pan, Y.; Tao, Z.; Chen, J. Rapid Room-Temperature Synthesis of Nanocrystalline Spinel as Oxygen Reduction and Evolution Electrocatalysts. *Nat. Chem.* **2011**, *3* (1), 79–84.

6.2. List of figures

Figure 1.1: (left) Global atmospheric CO ₂ concentration in ppm over the last 800 000 years. Source: Ref. ¹⁰ . (right) Global final energy demand from 1990 to 2050 in EJ by source of energy under a “business as usual” scenario. Source: Ref. ³	1
Figure 2.1: (a) Volcano plot based on Trasatti ⁴¹ linking overpotential with transition enthalpy. Source: Ref. ⁴² . (b) Volcano plot using the difference in binding energy between the –O* and the –OH* transition state as descriptor. Source: Ref. ³⁸ . (c) Free energy diagram of intermediates during OER at –O* covered RuO ₂ for different potentials. Source: Ref. ³⁹	10
Figure 3.1: Electrochemical cell for sample preparation in operation mode (a) and working (sample) and counter (Pt) electrodes outside the cell (b). WE, CE and RE denote working, counter and reference electrode, respectively.	15
Figure 3.2: (a): Typical CV diagram of a CoO _x electrode with the most important features labeled. The red line represents the iR-corrected current curve, while the blue line depicts the current density as function of the applied potential without any iR-compensation. (b): Typical impedance spectrum of a CoO _x electrode, with the setup resistance R _Ω labeled. The Randles equivalent circuit is schematically illustrated on the right hand side of the graph.	17
Figure 3.3: Photographs of the unmounted (left) and mounted electrochemical cell (right).	19
Figure 3.4: Schematic illustration of a DEMS setup. The sample is turned upside down onto the gas permeable membrane where O ₂ can diffuse through it and be analyzed in the mass spectrometer. The diagram has been taken from Ref. ¹¹¹	20
Figure 3.5: (a): An X-ray photon interacts with a core electron, transfers its energy and leads to the ejection of a photoelectron from the <i>n</i> -electron initial state. (b): The ion, now in the (<i>n</i> -1) state reorganizes its electrons to a lower energy state by dropping an electron from an outer shell into the vacant core hole. (c): The excess energy from the process in (b) is released from the ion either by X-ray photon emission (X-ray fluorescence) or by emission of an Auger electron from an outer shell. Source: Ref. ¹²³	21
Figure 3.6: Electron mean free path length as function of their kinetic energy for various metals. Source: Ref ¹²²	23
Figure 3.7: (a): Photograph of the SoLIAS endstation at Bessy II. (b): Electrochemical cell (“glass cross”) attached to the UHV system of the SoLIAS, with all relevant components. (c): Sample in contact with the electrolyte (KOH) inside the electrochemical cell.	25
Figure 3.8: Schematic illustration of the in-situ UV/Vis spectroscopy measurement setup.	26
Figure 4.1: Deposition current density <i>j</i> as function of deposition time <i>t</i> at different applied deposition potentials from 1.1 V (dark blue, bottom curve) to 1.7 V vs. RHE (red, top curve) in steps of 0.1 V.	30
Figure 4.2: Photograph of samples deposited at different deposition potentials. Top row: samples were deposited for 30 minutes, bottom row: samples were deposited until a total charge of 1 C/cm ² had been recorded.	31
Figure 4.3: Cyclovoltammograms (CV diagrams) of cobalt oxide electrodes deposited at different deposition potentials for 30 minutes (a) and deposited until a charge of 1 C/cm ² has passed the electrode (b), respectively. The diagrams show opposing trends for the activity of the two series of samples. Measurements were carried out in 1 M KOH (pH 14) at a scan rate of 10 mV/s.	32
Figure 4.4: Overpotential η , recorded at the current density of 10 mA/cm ² in 1 M KOH as function of the deposition potential U_{dep} for the two group of samples with constant deposition time of 30 min (blue) and constant deposition charge of 1 C/cm ² (red), respectively.	33

- Figure 4.5: (a) Current density j vs. deposition potential U_{dep} recorded during the deposition of CoO_x on an FTO/glass substrate. The lines represent the 1st, 10th, 20th, 30th, 40th, 50th, 60th, 70th, 80th, 90th and 100th cycle at a scan rate of 100 mV/s. (b) CV diagram of a sample deposited with cycled potential (blue) in comparison to a sample deposited at the potential of 1.4 V and a deposited charge of 1 C/cm². CV measurements in (b) have been corrected for the iR-drop and were carried out in 1 M KOH (pH 14) at a scan rate of 10 mV/s.....34
- Figure 4.6: Deposition current density j vs. time t (a) and related cyclovoltammograms (b) of samples deposited from solutions containing different Co^{2+} concentrations. The deposited charge for all samples was 1 C/cm² at 1.4 V (RHE). CV measurements have been corrected for the iR-drop and were carried out in 1 M KOH (pH 14) at a scan rate of 10 mV/s.35
- Figure 4.7: Deposition current density j over time t (a) and CV diagrams (b) of samples deposited from solutions containing different cobalt salts. The deposition time was 30 minutes at 1.4 V (RHE). CV measurements have been corrected with respect to the iR-drop and were carried out in 1 M KOH (pH 14) at a scan rate of 10 mV/s.....36
- Figure 4.8: Deposition current density j over time t (a) and CV diagrams (b) of samples deposited from solutions containing different KOH concentrations. The deposited charge was 1 C/cm² at 1.4 V (RHE). CV measurements have been corrected with respect to the iR-drop and were carried out in 1 M KOH (pH 14) at a scan rate of 10 mV/s.....37
- Figure 4.9: Current density j over time t during the deposition of CoO_x films on different substrates at a potential of 1.4 V (RHE) until a charge of 1 C/cm² has passed the electrode, except for the ITO sample, where a film was deposited for 30 min.....38
- Figure 4.10: Photograph of CoO_x films deposited on different substrates.....39
- Figure 4.11: SEM images of CoO_x films on different substrates. Top left: Isolated CoO_x patches with high surface area on a FTO support, which is visible in between the islands. Top right: CoO_x on Au forming similar structures as on FTO. The bright areas show the blank substrate. Bottom left: CoO_x on a Ti-substrate does not form films, but rose-like structures. Bottom right: Loose and not uniformly covering network of CoO_x on a Co substrate.40
- Figure 4.12: CV diagrams of CoO_x films deposited on different substrates at 1.4 V (RHE) until the charge of 1 C/cm² has passed the electrochemical cell. The CVs of the corresponding blank substrates are given by black line scans. CV measurements have been corrected for the iR-drop and were carried out in 1 M KOH (pH 14) at a scan rate of 10 mV/s.42
- Figure 4.13: (a) Capacitive current density j_c vs. scan rate v for CoO_x on FTO, Au and Co recorded at 1.27 V (RHE) to determine the double layer capacitance of the samples. (b) Geometric current density j_{geom} (black) at 1.55 V (squares), 1.57 (circles) and 1.6 V (triangles) in comparison with the relative current density j_{rel} (blue), which has been normalized for the double layer capacitance.43
- Figure 4.14: X-ray diffractograms of electrodeposited cobalt oxide films after annealing at different temperatures. The spinel type Co_3O_4 phase appears at annealing temperatures of 300°C and higher. At 450°C no further change in the diffractogram can be observed and the crystallization process is considered to be completed. 45
- Figure 4.15: Photograph of CoO_x films annealed at different temperatures.....46
- Figure 4.16: Current-voltage curves of different electrodes in the potential range from 0.9 to 1.65 V as a function of annealing temperature. The anodic waves I_a and II_a and the cathodic feature II_c disappear after annealing at 200°C and higher, while the redox pair III_a and III_c becomes sharper with increasing annealing temperature. The measurements have been corrected for the iR-drop and were carried out in 1 M KOH (pH 14) at a scan rate of 10 mV/s.....48
- Figure 4.17: SEM images of electrodes dried at room temperature (left) and after annealing at 450°C (right).49

- Figure 4.18: CV diagrams of cobalt oxide films annealed at different temperatures. OER activity decreases with increasing temperature accompanied by an increasing current loss from cycle to cycle. The measurements have been corrected for the iR-drop and were carried out in 1 M KOH (pH 14) at a scan rate of 10 mV/s.49
- Figure 4.19: (a) Averaged overpotential η at 10 mA/cm² as function of the annealing temperature T . (b) Development of η at 10 mA/cm² over time t . The measurements have been corrected for the iR-drop and were performed in 1 M KOH.51
- Figure 4.20: Selected CV diagrams of samples with deposited charges between 0.01 and 1000 mC/cm² and a blank FTO substrate as reference. The dotted violet line represents the current-voltage curve of the sample with the deposited charge of 0.01 mC/cm² multiplied by a factor of 130. All samples were deposited at 1.2 V (RHE). The measurements have been corrected with respect to the iR-drop and have been carried out in 1 M KOH (pH 14) at a scan rate of 10 mV/s.54
- Figure 4.21: Overpotential η as function of the deposited charge Q_{dep} and the amount of deposited Co $M_{Co, dep}$55
- Figure 4.22: Sample thickness d as function of the deposition charge Q_{dep} . The blue squares and green triangles represent samples deposited at 1.2 V and 1.4 V (RHE) measured with a profilometer, respectively. The cyan diamonds are the results of cross section SEM investigations on samples deposited at 1.2 V, the black line shows the sample thickness calculated according to equation (13).57
- Figure 4.23: SEM images of samples deposited at 1.2 V (RHE) until 10 (a), 100 (b) and 1000 mC/cm² have passed the electrode/electrolyte interface. The samples were cut and prepared for cross section analysis in a sandwich alignment.59
- Figure 4.24: (a) CV diagram taken at 10 mV/s with the marked regions for possible capacitance measurements. The graphs in (b) and (c) show CV diagrams at different scan rates (5 – 100 mV/s) in the potential range from 0.88 to 0.98 V (b) and from 1.25 to 1.35 V (c). The diagram in (d) shows the plot of the anodic (positive) and cathodic (negative) current density vs. the scan rate at 0.95 V (brown) and 1.30 V (blue). All measurements were carried out in 1 M KOH.61
- Figure 4.25: Double layer capacitance C_{dl} and roughness factor R_f as function of the deposition charge Q_{dep}62
- Figure 4.26: TEM images of a CoO_x sample dried in air at RT (a, c) and a Co₃O₄ sample heated to 400°C (b, d).64
- Figure 4.27: (a): CV diagram with the marked regions for the integration of the reductive current density. (b): Charge belonging to the reduction peaks $Q_{red, peak}$ (red and blue areas in a) and amount of reduced cobalt ions M_{Co} as function of film thickness d . (c): Fraction of the reduced cobalt ions $Q_{red, peak}/Q_{dep}$ as function of the deposition charge Q_{dep} . (d): Relative charges of the reduction peaks $rel\ Q_{red, peak}$ as function of film thickness d . The blue and red lines represent the relative charges between measurements conducted at 100 and 10 mV/s for reduction peak 1 and 2, respectively. The green line is the relative charge between reduction peak 1 and 2 measured at 100 mV/s.66
- Figure 4.28: Turnover frequency calculated from the total deposition charge $TOF_{Q_{dep}}$ (a) and from the charge of the second reduction peak $TOF_{red, peak}$ (b) vs. film thickness d68
- Figure 4.29: Tafel slope b as function of the sample thickness d . The violet diamond represents the blank FTO substrate, which was arbitrarily placed at 0.1 nm to show it in the graph.71
- Figure 4.30: Exchange current density j_0 and charge transfer coefficient α versus sample thickness d . The violet diamond and circle represent α and j_0 of the blank FTO substrate.72
- Figure 4.31: CV diagrams of CoO_x measured in 1 M KOH (black) and different concentrations of potassium phosphate buffer solution (KPi). All measurements were conducted at 10 mV/s and corrected for the iR-drop.73
- Figure 4.32: (a): Current density j vs. time t in different electrolytes at the overpotential of 0.62 (KPi) and 0.35 V (KOH), respectively. (b): CV diagram of CoO_x electrodes in 0.1 M KPi at different scan rates.75

Figure 4.33: CV diagrams of CoO _x and CoPi in 1 M KOH (a) and 0.1 M KPi + 0.5 M K ₂ SO ₄ (b), respectively. All samples had a deposition charge of 0.1 C/cm ² and were deposited at 1.2 (CoO _x) and 1.5 V vs. RHE (CoPi), respectively. The scan rate was 10 mV/s and the potential was corrected with respect to the iR-drop.	77
Figure 4.34: First, second and third cycle of a regular CV experiment. The deposition potential was 1.2 V, the deposition charge 1000 mC/cm ² . The measurement has been corrected for the iR-drop and was performed in 1 M KOH at 10 mV/s.	78
Figure 4.35: DEMS measurement performed in 1 M KOH at 2 mV/s. The red curve represents the current <i>i</i> as function of the applied potential <i>U</i> and the black and blue lines are the corresponding mass signals of CO ₂ and O ₂ , respectively.....	79
Figure 4.36: DEMS measurements of the first (a) and second (b) cycle of a CoO _x electrode measured in 0.1 M potassium phosphate buffer (KPi) solution at a sweep rate of 2 mV/s. The red curve represents the current <i>i</i> as function of the applied potential <i>U</i> and the black and blue lines are the corresponding mass signals related to CO ₂ and O ₂ , respectively.	80
Figure 4.37: SEM image and photograph of a partially detached CoO _x thin film.....	82
Figure 4.38: (a): Comparison of the CV diagrams of a stable CoO _x film and a film, which detached from the substrate in the electrochemically active spot. The films were deposited under the same conditions (1.4 V, 1000 mC/cm ²). (b): Comparison of the activity of a sample, which was dried at RT in air after the deposition (blue) and a sample, which was electrochemically characterized immediately after the deposition. The measurements have been corrected for the iR-drop and were carried out in 1 M KOH (pH 14) at a scan rate of 10 mV/s.....	82
Figure 4.39: Overpotential η versus time <i>t</i> for a galvanostatic measurement at a current density of 10 mA/cm ² . The potential has been corrected for the iR-drop; the electrolyte was 1 M KOH. The sample was fully immersed (2 cm ²) in the electrolyte and rotated with a speed of around 400 rpm.	84
Figure 4.40: (a): Long term potentiostatic measurement (current density <i>j</i> versus time <i>t</i>) in 1 M KOH at an overpotential of $\eta = 0.38$ V. The measurements were carried out with (blue curve) and without (black and gray curves) sample rotation and iR-compensation, respectively. (b): CV diagrams before and after the potentiostatic measurement shown in (a) (black curve). The measurements have been corrected for the iR-drop and were carried out in 1 M KOH (pH 14) at a scan rate of 10 mV/s.....	84
Figure 4.41: XPS overview spectra of the pristine CoO _x sample (blue) and after the sample has been subjected to a potential of 1.35 V vs. RHE (red). The most important features are marked within the graph. Excitation energy was 900 eV.	87
Figure 4.42: CV diagram of a CoO _x electrode recorded inside the glass cross without (grey) and after iR-correction (black). The measured cell resistance was 160 Ω . The position of the investigated potentials are marked with blue bars.	88
Figure 4.43: Co2p photoelectron spectra of CoO _x after the application of different anodic potentials. The binding energies of Co ²⁺ and Co ³⁺ are marked by vertical lines, shake-up satellites are indicated as ss.....	90
Figure 4.44: Deconvolution and residual function of Co2p3 and O1s peaks of CoO _x after deposition (a, b) and the application of 1.35 V (c, d), 1.6 V (e, f) and 1.05 V (g, h). A Shirley background ¹⁶³ has been subtracted. The potentials are given vs. RHE and the incident photon energies were 900 and 650 eV for Co2p and O1s, respectively.	94
Figure 4.45: Photographs of an as-deposited CoO _x sample during the application of different potentials.	95

- Figure 4.46: Applied potential U vs. wavelength λ of the incident light of in-situ UV-Vis measurements during potential cycling on as-deposited CoO_x (a, c, e) and annealed Co_3O_4 samples (b, d, f). The samples had a nominal deposition charge of 1000 (a, b), 100 (c, d) and 10 mC/cm^2 (e, f). The color bar gives the relative transmittance normalized to the samples under open circuit conditions; the scan rate was 1 mV/s in 1 M KOH electrolyte. The transmittance was integrated for 5 s, respectively, which results in a potential resolution of 5 mV.....97
- Figure 4.47: Relative transmittance (normalized to the sample transmittance at OCP) as function of the applied potential U of an as-deposited CoO_x electrode with a deposition charge of 1000 mC/cm^2 . The selected wavelengths correspond to the different absorption features in the 3d-plot in Figure 4.46a.....98
- Figure 4.48: Applied potential U vs. wavelength λ of the incident light for in-situ UV/Vis measurements during rapid potentiostatic measurements at different potentials on as-deposited CoO_x (a) and annealed Co_3O_4 (b) electrodes. In between the different potential steps the samples were discharged at 0.9 V (RHE). The deposition charge was 1000 mC/cm^2 in both cases and the Co_3O_4 film has been annealed at 450°C. The color bar gives the relative transmittance normalized to the sample under open circuit conditions.....100
- Figure 4.49: Relative transmittance, normalized to the status before the application of potential, as a function of relaxation time t_{rel} and wavelength λ during the relaxation process in 1 M KOH (a) and air (b). The samples were beforehand subjected to 1.7 V (RHE) for 1 min. The measurement was started as fast as possible after the applied potential was switched off and, in the case of (b), the electrolyte was removed. Integration time of the individual spectra was 1 min.101
- Figure 4.50: Relative transmittance, normalized to the status before the application of potential, as function of the wavelength λ at the applied potential of 1.7 V vs. RHE (pink) and in air after different relaxation times (green- > black).....102
- Figure 4.51: X-ray diffractogram of electrodeposited manganese oxide films after different annealing treatments. The blue curve represents as-deposited amorphous MnO_x ; the red line gives crystalline $\alpha\text{-Mn}_2\text{O}_3$ after treatment at 500°C in air and the green graph shows Mn_3O_4 after annealing at 600°C in N_2 . The most important reflexes are labeled with the corresponding hkl-indices and the dotted line denotes the reflexes belonging to the FTO substrate.103
- Figure 4.52: Cyclic voltammograms of different types of manganese oxide and a blank FTO substrate for comparison. The electrolyte was 1 M KOH and the scan rate 10 mV/s . All curves have been corrected for the iR-drop.104
- Figure 4.53: XPS overview spectra of the pristine $\alpha\text{-Mn}_2\text{O}_3$ sample (blue) and the sample after it has been subjected to a potential of 1.55 V (red). The most important features are marked within the graph. Excitation energy was 800 eV.105
- Figure 4.54: High resolution XPS spectra of Mn2p (a) and Mn3s (b) peaks before and after application of an anodic potential of 1.55 V. The characteristic distances in binding energy between the high energy shake-up satellite and the 2p_{1/2} peak (a) and the multiplet splitting of 3s (b) are labeled in the graphs. Excitation energies were 800 (a) and 450 eV (b), respectively.106
- Figure 4.55: Deconvolution and residual function of Mn2p_{3/2} and O1s peaks of $\alpha\text{-Mn}_2\text{O}_3$ after preparation (a, b) and after the application of a potential of 1.55 V (c, d). A Shirley background¹⁶³ has been subtracted. The potentials are given vs. RHE and the incident photon energies were 800 and 700 eV for Mn2p and O1s, respectively.108
- Figure 5.1: Cyclovoltammograms of CoO_x (blue) and $\alpha\text{-Mn}_2\text{O}_3$ (red) thin film electrodes in comparison to RuO_2 (black) and the blank FTO substrate (gray). Except for RuO_2 (measured in 0.5 M H_2SO_4), 1 M KOH has been used as electrolyte and a scan rate of 10 mV/s was applied.....114

6.3. List of tables

Table 1.1: Gravimetric and volumetric energy densities of different fuels (at 1 bar). Source: Ref. ⁷	2
Table 4.1: Setup resistance and capacitance for samples deposited on different substrates. The resistance values have been taken from the high frequency end of electrochemical impedance measurements at open circuit conditions and the capacitance was calculated from the capacitive current values at different scan rates at 1.27 V (RHE).....	39
Table 4.2: Redox couples, half-cell reactions and corresponding electrode equilibrium potentials of cobalt oxide/hydroxide under anodic potential conditions in alkaline solution. Data have been derived from Ref ⁵⁸	47
Table 4.3: List of reported turnover frequencies (<i>TOF</i>) for cobalt oxides and other transition metal oxides. <i>d</i> , <i>η</i> , NP, NC, CoP _i and mCo ₃ O ₄ stand for sample thickness, overpotential, nanoparticles, nanoclusters, cobalt phosphate and mesoporous Co ₃ O ₄ , respectively.	69
Table 4.4: Fit parameter of the peak fit of Co2p3/2 and O1s for CoO _x under different anodic potentials: binding energy, full width at half maximum (FWHM) and relative peak area (rel. area).	93
Table 4.5: Fit parameters of the peak fit of Mn2p3/2 and O1s for α-Mn ₂ O ₃ in pristine state and after 1.55 V potential application: binding energy, full width at half maximum (FWHM) and relative peak area (rel. area).	109

6.4. List of publications

Publications

- (1) Didden, A.; Hillebrand, P.; Wollgarten, M.; Dam, B.; van de Krol, R. Deposition of Conductive TiN Shells on SiO₂ Nanoparticles with a Fluidized Bed ALD Reactor. *J. Nanoparticle Res.* **2015**, (submitted).
- (2) Didden, A.; Hillebrand, P.; Dam, B.; van de Krol, R. Photocorrosion Mechanism of TiO₂-Coated Photoanodes. *Int. J. Photoenergy* **2015**, 457980.
- (3) Hillebrand, P.; Ramírez-Caro, A.; Calvet, W.; Bogdanoff, P.; Fiechter, S. On the Structure-Function Relationship of Cobalt and Manganese Oxides as Oxygen Evolving Catalysts for Light-Driven Water Electrolysis: An In-Line Synchrotron Radiation Photoelectron Spectroscopy Study. *ECS Trans.* **2014**, 61 (14), 9–20.
- (4) Ramírez, A.; Hillebrand, P.; Stellmach, D.; May, M. M.; Bogdanoff, P.; Fiechter, S. Evaluation of MnO_x, Mn₂O₃, and Mn₃O₄ Electrodeposited Films for the Oxygen Evolution Reaction of Water. *J. Phys. Chem. C* **2014**, 118, 14073–14081.
- (5) Emmeler, T.; Gutzmann, H.; Hillebrand, P.; Schieda, M.; Just, R.; Gärtner, F.; Bogdanoff, P.; Herrmann-Geppert, I.; Klassen, T. Cold Gas Spraying of Semiconductor Coatings for the Photooxidation of Water. In *Proc. SPIE 8822, Solar Hydrogen and Nanotechnology VIII*; **2013**; p 88220C.

Conferences

- ECS – 225th Meeting, Orlando, FL, May 2014:
On the Structure-function Relationship of Cobalt and Manganese Oxides as Oxygen Evolving Catalysts for Light-driven Water Electrolysis: An in-line Synchrotron Radiation Photoelectron Spectroscopy Study
- IPS 20, Berlin, DE, July 2014:
On the Relationship between Surface State and Activity of Cobalt and Manganese Oxides towards the Oxygen Evolution Reaction in Photoelectrochemical Devices

Posters

- E-MRS Spring Meeting 2014, Lille, FR, May 2014
In-line Synchrotron Radiation Photoelectron Spectroscopy Study on the Relationships between structure and function of Cobalt and Manganese Oxides for the oxygen evolution reaction
- Bessy Usermeeting 2013, Berlin, DE, December 2013
On the structure-function relationship between surface chemistry and catalytic activity of cobalt and manganese oxides towards oxygen evolution reaction (OER)
- International Summer School on Basic Concepts and First-Principles Computations for Surface Science: Applications in Chemical Energy Conversion and Storage, Norderney, DE, July 2013
Catalytic activity of cobalt oxides and manganese oxides towards the oxygen evolution reaction